DEVELOPMENT OF AUTOMATED PULSED EDDY CURRENT FOR INSPECTION OF F-35 WING STRUCTURES AT LIFT-OFF

DÉVELOPPEMENT D'UN SYSTÈME AUTOMATISÉ DE COURANTS DE FOUCAULT PULSÉS POUR L'INSPECTION DES STRUCTURES D'AILES DU F-35 À L'ENTREFER

A Thesis Submitted to the Division of Graduate Studies
of the Royal Military College of Canada
by

Tarrynne Jayde Kassidie Barr, BSc
Captain

In Partial Fulfillment of the Requirements for the Degree of
Master of Science in Physics

April, 2026

ROYAL MILITARY COLLEGE OF CANADA
COLLÈGE MILITAIRE ROYAL DU CANADA

DIVISION OF GRADUATE STUDIES AND RESEARCH
DIVISION DES ÉTUDES SUPÉRIEURES ET DE LA RECHERCHE

This is to certify that the thesis prepared by / Ceci certifie que la thèse rédigée par

Tarrynne Jayde Kassidie Barr

entitled / intitulée

DEVELOPMENT OF AUTOMATED PULSED EDDY CURRENT FOR INSPECTION OF F-35 WING STRUCTURES AT LIFT-OFF /
DÉVELOPPEMENT D'UN SYSTÈME AUTOMATISÉ DE COURANTS DE FOUCAULT PULSÉS POUR L'INSPECTION DES STRUCTURES D'AILES DU F-35 À L'ENTREFER

complies with the Royal Military College of Canada regulations and that it meets the accepted standards of the Graduate School with respect to quality, and, in the case of a doctoral thesis, originality / satisfait aux règlements du Collège militaire royal du Canada et qu'elle respecte les normes acceptées par la Faculté des études supérieures quant à la qualité et, dans le cas d'une thèse de doctorat, l'originalité

for the degree of / pour le diplôme de

Master of Science / Maîtrise ès Science

Signed by the final examining committee: /
Signée par les membres du comité examinateur de la soutenance de thèse

_____, Chair / Président

_____, External Examiner / Examinateur externe

_____, Main Supervisor / Directeur de thèse principal

Approved by the Head of Department /
Approuvée par le Directeur du Département: _____ Date: _____ To the

Librarian: This thesis is not to be regarded as classified. /
Au Bibliothécaire: Cette thèse n'est pas considérée comme à publication restreinte.

_____
Main Supervisor / Directeur de thèse principal

Acknowledgements

I would like to express my sincere gratitude to Dr. Thomas Krause, my thesis supervisor, for his guidance, patience, and support over the past two years. His unwavering commitment to the field of NDT, along with his thoughtful feedback and encouragement, has been instrumental to the success of this work.

I am also deeply grateful to Dr. Ross Underhill for his steadfast support throughout this project. His assistance in designing custom probes, developing LabVIEW interfaces, and implementing key algorithms was invaluable. His deep expertise in statistical methods provided essential insights that greatly strengthened the analytical components of this thesis.

Finally, I would like to thank my husband, Neil, for his enduring patience and understanding. Your love and unwavering support helped me navigate the many challenges along the way, and I could not have accomplished this without you by my side. I would also like to acknowledge our son, Archer, whose arrival during this journey brought perspective, motivation, and immeasurable joy.

Abstract

This thesis, completed by Barr, Tarrynne Jayde Kassidie, in partial fulfillment of the requirements for the degree of Master of Science in Physics at the Royal Military College of Canada, is entitled DEVELOPMENT OF AUTOMATED PULSED EDDY CURRENT FOR INSPECTION OF F-35 WING STRUCTURES AT LIFT-OFF, and was conducted under the supervision of Dr. Thomas Krause.

The Royal Canadian Air Force's future F-35 fleet presents a significant inspection challenge due to composite wing skins and radar-absorbing materials (RAM), precluding direct access to critical structural components, such as the inner wing spars. These constraints necessitate the development of a non-contact Non-Destructive Testing (NDT) method capable of detecting stress corrosion cracking (SCC) adjacent to both ferrous and non-ferrous fasteners at large lift-off distances.

To address this need, a pulsed eddy current (PEC) inspection system was developed, integrating custom probes, time-domain signal processing, and a modified principal component analysis (MPCA) classification framework. Four custom PEC probes, labelled ZEUS, ARES, THOR, and ODIN, were designed to explore trade-offs among magnetic sensitivity, lift-off tolerance, and modelling complexity. ZEUS, with its vertically differential pickup configuration and ferrite-cored pickup coils, demonstrated the most robust flaw separation, achieving accurate classification up to 17.7 mm above an angled aluminum surface. An analytical model, describing vertically differential PEC responses, was validated using ARES, which employs air-cored pickup coils for simplified modelling. THOR, with a ferrite-cored driver and axisymmetric pickups positioned on either side of the driver, performed well on titanium fasteners but showed sensitivity to geometric and edge effects. ODIN, featuring an air-cored driver and axisymmetric pickup coils, proved effective in ferromagnetic stainless steel, but exhibited elevated false positives near the 99% confidence threshold in thicker titanium samples.

Conventional Eddy Current Testing (ET) was assessed to benchmark performance under realistic aerospace conditions. While effective at identifying near-surface cracks and mapping fastener locations at low lift-offs, conventional ET performance degraded markedly beyond 11 mm of lift-off. Signal quality diminished due to broadened magnetic field distributions, limiting its ability to resolve flaws in high lift-off or through-layer inspection scenarios.

To overcome the limitations of scalar signal features in PEC, such as peak amplitude or decay slope, gated signals were projected into a reduced eigenspace using MPCA, followed by linear discriminant analysis of the principal component scores. Family-based eigenvectors consistently improved generalization and reduced false positives. HLT265 samples showed the strongest class separation, while titanium-based HLT313 samples posed greater classification challenges.

A rigorous thresholding strategy, based on discriminant score distributions, was developed, with 95% and 99% confidence levels enabling statistically grounded decisions for re-inspection or repair. ZEUS maintained clean class separation under elevated lift-off conditions, indicating strong potential for integration into automated or field-deployable systems.

A time-domain modelling framework was developed using analytical derivation and Finite Element Method (FEM) simulation. PEC excitation was modelled as a unipolar square wave via a truncated Fourier series, and frequency-dependent complex inductances were used to reconstruct coil-current responses through inverse harmonic summation. Simulated signals showed strong agreement with experimental data in waveform shape, polarity, and timing across various aerospace-relevant metals and lift-offs of up to 10 mm. Minor deviations at higher lift-offs were attributed to unmodelled boundary effects and surface imperfections.

This work demonstrates the feasibility of a non-contact PEC inspection system for detecting subsurface flaws in aircraft with stealth coatings. The combined analytical, numerical, and experimental approach provides a robust platform for PEC probe development, signal interpretation, and implementation in aerospace maintenance environments, where conventional ET techniques fall short.

Résumé

Thèse complétée par Barr, Tarrynne Jayde Kassidie, en vue de l'obtention partielle du grade de Maîtrise ès sciences en physique au Collège militaire royal du Canada, intitulée DÉVELOPPEMENT D'UN SYSTÈME AUTOMATISÉ DE COURANTS DE FOUCAULT PULSÉS POUR L'INSPECTION DES STRUCTURES D'AILE DU F-35 À L'ENTREFER, sous la supervision du Dr Thomas Krause.

La future flotte de F-35 de l'Aviation royale canadienne présente un défi majeur en matière d'inspection en raison des revêtements d'aile composites et des matériaux absorbants les ondes radar (RAM), lesquels empêchent l'accès direct à des composants structuraux critiques tels que les longerons internes d'aile. Ces contraintes exigent le développement d'une méthode de contrôle non destructif (CND) sans contact capable de détecter la fissuration par corrosion sous contrainte (CSC) à proximité de fixations ferreuses et non ferreuses à grande distance de décollage.

Afin de répondre à ce besoin, un système d'inspection par courants de Foucault pulsés (CFP) a été développé, intégrant des sondes personnalisées, un traitement des signaux dans le domaine temporel ainsi qu'un cadre de classification fondé sur une analyse en composantes principales modifiée (ACPM). Quatre sondes CFP personnalisées, désignées ZEUS, ARES, THOR et ODIN, ont été conçues afin d'explorer les compromis entre sensibilité magnétique, tolérance à la distance de décollage et complexité de modélisation.

La sonde ZEUS, dotée d'une configuration de bobines réceptrices différentielles verticales et de noyaux en ferrite, a démontré la séparation de défauts la plus robuste, permettant une classification précise jusqu'à 17,7 mm au-dessus d'une surface d'aluminium inclinée. Un modèle analytique décrivant les réponses CFP différentielles verticales a été validé à l'aide de la sonde ARES, laquelle utilise des bobines réceptrices à noyau d'air afin de simplifier la modélisation. La sonde THOR, munie d'une bobine excitatrice à noyau en ferrite et de bobines réceptrices axisymétriques disposées de part et d'autre de celle-ci, a offert de bonnes performances sur des fixations en titane, mais a montré une sensibilité accrue aux effets géométriques et aux effets de bord. La sonde ODIN, équipée d'une bobine excitatrice à noyau d'air et de bobines réceptrices axisymétriques, s'est révélée efficace pour l'acier inoxydable ferromagnétique, bien qu'elle ait présenté un taux plus élevé de faux positifs à proximité du seuil de confiance de 99 % dans des échantillons en titane plus épais.

Les essais conventionnels par courants de Foucault (CF) ont été évalués afin d'établir la perfor-

mance de référence dans des conditions aérospatiales réalistes. Bien qu'efficaces pour l'identification de fissures de surface et la localisation des fixations à faible distance de décollage, les performances des CF conventionnels se sont nettement détériorées au-delà de 11 mm. La qualité du signal diminuait en raison de l'élargissement de la distribution du champ magnétique, limitant ainsi la capacité à résoudre les défauts dans des scénarios d'inspection à grande distance ou à travers plusieurs couches structurales.

Afin de surmonter les limites des caractéristiques scalaires des signaux CFP, telles que l'amplitude maximale ou la pente de décroissance, les signaux fenêtrés ont été projetés dans un espace propre réduit au moyen de l'ACPM, puis analysés par une analyse discriminante linéaire appliquée aux scores en composantes principales. L'utilisation de vecteurs propres fondés sur des familles d'échantillons a systématiquement amélioré la capacité de généralisation et réduit le nombre de faux positifs. Les échantillons HLT265 ont présenté la séparation de classes la plus marquée, tandis que les échantillons HLT313 à base de titane ont posé davantage de défis en matière de classification.

Une stratégie rigoureuse d'établissement de seuils, fondée sur les distributions des scores discriminants, a été élaborée. Des niveaux de confiance de 95 % et 99 % ont permis de formuler des décisions statistiquement fondées quant à la réinspection ou à la réparation. La sonde ZEUS a maintenu une séparation nette des classes à des distances de décollage élevées, démontrant un fort potentiel d'intégration dans des systèmes automatisés ou déployables sur le terrain.

Un cadre de modélisation dans le domaine temporel a été développé au moyen d'une dérivation analytique et de simulations par la méthode des éléments finis (MEF). L'excitation CFP a été modélisée comme une onde carrée unipolaire à l'aide d'une série de Fourier tronquée, et des inductances complexes dépendantes de la fréquence ont été utilisées afin de reconstruire les réponses en courant des bobines par sommation harmonique inverse. Les signaux simulés ont présenté une forte concordance avec les données expérimentales en termes de forme d'onde, de polarité et de synchronisation, pour divers métaux pertinents en aérospatiale et pour des distances de décollage allant jusqu'à 10 mm. Les écarts mineurs observés à des distances plus élevées ont été attribués à des effets de frontière non modélisés ainsi qu'à des imperfections de surface.

Ce travail démontre la faisabilité d'un système d'inspection CFP sans contact pour la détection de défauts sous-surface sur des aéronefs munis de revêtements furtifs. L'approche combinant modélisation analytique, simulation numérique et validation expérimentale constitue une plateforme robuste pour le développement de sondes CFP, l'interprétation des signaux et leur implantation dans les environnements de maintenance aérospatiale, où les techniques conventionnelles de CF atteignent leurs limites.

Table of Contents

List of Tables

List of Figures

List of Abbreviations

ASM	American Society for Metals
AWG	American Wire Gauge
BHEC	Bolt-Hole Eddy Current
BVP	Boundary Value Problem
CFRP	Carbon Fibre Reinforced Polymer
CNN	Convolutional Neural Network
DAQ	Data Acquisition
DC	Direct Current
DTW	Dynamic Time Warping
EDM	Electrical Discharge Machining
emf	Electromotive Force
ET	Eddy Current Testing
FEM	Finite Element Method
GDK	Galil Design Kit
GMR	Giant Magnetoresistance
ICA	Independent Component Analysis
KVL	Kirchhoff's Voltage Law
LabVIEW	Laboratory Virtual Instrument Engineering Workbench
LOI	Lift-Off Point of Intersection
LPI	Liquid Penetrant Inspection
LTI	Linear Time-Invariant
MD	Mahalanobis Distance
MPCA	Modified Principal Component Analysis
MPI	Magnetic Particle Inspection
MQS	Magnetoquasistatic
NAVAIR	Naval Air Systems Command
NDE	Non-Destructive Evaluation
NDT	Non-Destructive Testing

NI	National Instruments
NRMSE	Normalized Root-Mean-Square Error
ODE	Ordinary Differential Equation
Op-Amp	Operational Amplifier
PCA	Principal Component Analysis
PDE	Partial Differential Equation
PEC	Pulsed Eddy Current
POD	Probability of Detection
RAM	Radar-Absorbing Material
RCAF	Royal Canadian Air Force
RMSE	Root-Mean-Square Error
RSS	Residual Sum of Squares
RT	Radiographic Testing
SCC	Stress Corrosion Cracking
SHM	Structural Health Monitoring
SNR	Signal-to-Noise Ratio
SS	Stainless Steel
SVD	Singular Value Decomposition
SVM	Support Vector Machine
Ti	Titanium
TREE	Truncated Region Eigenfunction Expansion
USAF	United States Air Force
UT	Ultrasonic Testing

1 Introduction

1.1 General

The aviation industry has made significant progress in reducing the risk of in-flight component failure through rigorous inspection programs [1], [2]. These inspections, essential for ensuring operational safety, fall into two primary categories: destructive testing and Non-Destructive Testing (NDT) [3], [4]. NDT offers several advantages over its destructive counterpart, including cost-effectiveness, reduced downtime, and preservation of component integrity for continued service. Recognizing these benefits, the aerospace sector has widely adopted NDT as a fundamental quality control process during manufacturing. Its application enables the identification of defects, discontinuities, and structural imperfections, as well as the detection of damage, material degradation, and deterioration in critical aircraft components throughout their service life.

To standardize NDT practices in aviation, the Canadian General Standards Board certifies five conventional NDT techniques for inspecting aircraft materials, components, and structures: Ultrasonic Testing (UT), Radiographic Testing (RT), Liquid Penetrant Inspection (LPI), Magnetic Particle Inspection (MPI), and Eddy Current Testing (ET) [5]. While each technique is effective within its respective domain, all have inherent limitations. Therefore, selecting the most appropriate method requires careful consideration of a component's material properties, geometry, and anticipated failure modes. Despite continued technological advancements, many inspection challenges still exceed the capabilities of existing techniques, underscoring the need for ongoing research and development in Non-Destructive Evaluation (NDE) [6].

Within the Royal Canadian Air Force (RCAF), crack detection for fastener holes involves removal, followed by conventional Bolt-Hole Eddy Current (BHEC) inspections [7]. Radiographic methods [8] are often impractical due to extended inspection times, high costs, limited reliability, and strict safety requirements, such as the need to clear hangar facilities because of radiation hazards. While BHEC testing remains an effective technique, the associated maintenance procedures are highly labour-intensive. This process requires fastener removal by a metal technician, potential disassembly of skins or substructures, and hole reaming or oversizing, all of which significantly increase inspection time. Considering that aircraft wings can contain tens of thousands of fasten-

ers, traditional ET methods demand extensive personnel hours, driving up costs for the RCAF and reducing aircraft availability for operations.

These limitations are further magnified in advanced fighter platforms, such as the F-35. The F-35 incorporates Radar-Absorbing Material (RAM) and low-observable structural coatings to minimize radar cross-section and enhance stealth capabilities. These materials are highly sensitive to environmental degradation and mechanical damage, rendering them unsuitable for contact-based inspection or repeated disassembly. In addition, Stress Corrosion Cracking (SCC) and fatigue damage are known to initiate between fasteners on the aluminum inner wing spars, which secure the Carbon Fibre Reinforced Polymer (CFRP) wing skins [9], [10]. These critical structural zones must be routinely monitored to ensure continued airworthiness. However, their inaccessibility beneath bonded skins and RAM coatings presents a significant barrier to conventional NDT methods.

To overcome these challenges, there is a growing demand for remote through-panel inspection techniques that eliminate the need for fastener removal or direct probe contact. Such systems would reduce inspection time and labour, while preserving the integrity of low-observable coatings, which are essential to stealth performance. Prior research [9], [11], [12], [13], [14] has demonstrated the feasibility of Pulsed Eddy Current (PEC)-based crack detection and statistical classification at small lift-off distances. However, extending these techniques to automated remote inspection at lift-offs exceeding $20\,\mathrm{mm}$—such as those required for through-panel inspection of stealth aircraft—has not been previously demonstrated. Differential PEC probe designs are particularly well suited to this application, as they exhibit tolerance to lift-off variations, while remaining sensitive to eddy current field distortions caused by cracks. Two configurations are of particular interest: a vertically differential probe optimized for lift-off measurement and an axisymmetric pickup configuration that enhances sensitivity to localized discontinuities.

This thesis is motivated by the need for non-invasive crack detection in the F-35 inner wing spar. It aims to advance PEC technology by developing an analytical model and hardware implementation that enables remote, non-contact flaw detection through skin and RAM coatings. Integrating automated scanning with differential probe configurations supports periodic Structural Health Monitoring (SHM), while preserving surface integrity and reducing inspection overhead. The proposed solution aligns with the broader objectives of third-line maintenance by reducing invasive inspection procedures and supporting condition-based asset management for fifth-generation stealth aircraft.

1.2 Eddy Current Testing

As described by Faraday's law, eddy currents are circulating electrical currents induced in a conductor by a time-varying magnetic field. These currents form closed loops perpendicular to the direction of the applied magnetic field in a conducting surface. ET is an NDT technique that leverages electromagnetic induction to detect flaws and discontinuities in conductive materials by monitoring

changes in the induced electromagnetic response.

ET employs a probe containing one or more electromagnetic coils to generate and sense an alternating magnetic field that induces eddy currents within the test specimen. The magnitude and distribution of these currents depend on the material's conductivity, permeability, geometry, and the presence of discontinuities. When a defect disrupts the eddy current flow, it alters the associated magnetic field, changing the impedance of the pickup coil. This impedance variation is interpreted as an eddy current signal, which can be displayed on an impedance plane to identify flaws and other discontinuities, including changes in geometry. ET is widely used for detecting surface and near-surface cracks, measuring properties such as resistivity and conductivity, and evaluating the thickness of thin metals and coatings [15].

Despite its advantages, ET has notable limitations, particularly when inspecting ferromagnetic and highly conductive materials. The high relative permeability of ferromagnetic materials restricts eddy current penetration, limiting detection to surface or near-surface regions. Similarly, while eddy currents penetrate to greater depths in good conductors, the penetration depth remains limited by conductivity. In both cases, permeability variations can cause false flaw indications, reducing inspection reliability [15]. Since conductivity and permeability govern eddy current penetration depth, ET is inherently constrained in applications involving ferromagnetic components [16].

To address these limitations, PEC has emerged as an effective alternative [17]. Unlike conventional ET methods that use sinusoidal excitation, PEC employs square-wave excitation, encompassing a broad range of discrete frequency components and giving rise to a transient electromagnetic response. Rather than relying on skin-depth principles to increase penetration, PEC exploits transient electromagnetic diffusion, whereby abruptly applied fields induce eddy currents that generate magnetic fields progressively diffusing into the volume of the conducting and potentially ferromagnetic material [17], while being dissipated by resistive losses. Early-time responses are confined near the surface, whereas later-time behaviour probes deeper regions of the material as the diffusing fields spread throughout the sample. This diffusion-driven mechanism enables the detection of deeper flaws, including in materials with complex geometries and ferromagnetic properties, for which conventional eddy current techniques are often limited. The combined effects of the excitation frequency spectrum and transient diffusion enable them to meet the increasing demands of modern industry standards.

The practical implications of PEC are particularly relevant to the inspection of both legacy aircraft platforms, such as the CF-188, and future Canadian fleets, including the F-35. The F-35 employs RAM coatings to minimize radar signatures, but environmental exposure and accidental damage can degrade their effectiveness, compromising stealth performance. Minimizing panel removal and replacement during maintenance is, therefore, a priority, motivating the development of non-contact PEC probe technology. An automated scanning system capable of remote through-panel assessment could detect subsurface corrosion or cracking beneath the skin, significantly re-

ducing inspection time, while preserving RAM and skin integrity. Conventional PEC approaches, previously applied to the CF-188, relied on manual probe placement and direct surface contact—an approach that is not viable for the F-35.

This thesis builds upon the PEC probe design investigated by Horan *et al.* [9], [10], who demonstrated that SCC could be detected in CF-188 inner wing spars using Modified Principal Component Analysis (MPCA). MPCA reduces PEC signals to a series of eigenvectors and scores that capture the maximum signal variance. However, this earlier method required manual probe positioning and physical contact with the wing surface. Given the design sensitivities and operational requirements of the F-35, this work advances Horan *et al.*'s [9], [10] methodology by developing a reliable, non-contact inspection solution that incorporates remote scanning and lift-off-tolerant probe designs.

PEC is uniquely suited for non-contact inspection, maintaining sensitivity at lift-off distances of several millimetres or greater, depending on material properties and excitation parameters [18]. This capability enables SHM through thin coatings or surface layers, reducing inspection time, while preserving surface integrity. The central motivation of this research is, therefore, to develop a PEC probe system capable of remote flaw detection without direct physical contact with the surface.

This work investigates three novel PEC probe configurations, classified into two design categories. The first is a vertically differential probe optimized for precise lift-off measurement, particularly at large lift-offs exceeding $10\,\mathrm{mm}$. The second employs differential pickup-coil connections to identify variations in response caused by discontinuities in the induced eddy current field, notably those arising from crack formation. An analytical model for a vertically differential PEC probe above a conducting plate is developed to enable probe optimization. The plate model serves as an idealized approximation of the local electromagnetic response encountered in aerospace structure inspection, enabling systematic evaluation of probe geometry and lift-off effects. The model characterizes the electromagnetic behaviour of the vertically differential probe by solving the electromagnetic Boundary Value Problem (BVP) for the coil–plate system and embedding the resulting frequency-dependent self and mutual inductances within an equivalent circuit framework. This formulation enables systematic optimization of probe dimensions to enhance sensitivity and accuracy at elevated lift-offs.

1.3 Objective

The objective of this master's research is to evaluate and enhance the equipment and analytical techniques used for PEC inspection of the CF-188 and the future Canadian F-35 inner wing spar, which is covered by a nonconductive skin and contains both ferrous and non-ferrous fasteners. This study compares two distinct differential probe designs to determine their effectiveness in detecting structural flaws. By integrating automated scanning and remote through-panel assessment with differential PEC probes, this research aims to detect subsurface cracks in the F-35 inner wing spar

without requiring fastener removal or direct probe contact. This technology enables non-invasive periodic monitoring, while preserving structural integrity and stealth performance.

A signal analysis framework incorporating MPCA is employed to capture maximum signal variation, followed by discriminant analysis, which reduces the data to one dimension. An analytical model is developed to describe transient eddy current behaviour in driver–pickup coil circuits, focusing on a vertically differential probe positioned above a conductive plate. The model is formulated from differential circuit equations incorporating complex self- and mutual inductance functions and is solved using Fourier series and Fourier transform techniques to analyze transient signal behaviour in both the time and frequency domains. BVPs are solved to represent the system's physical properties, and experimental validation is performed to assess model accuracy.

The results are used to optimize probe design for NDT applications, particularly in fastener geometries. This research contributes to the development of a new inspection technique for third-line maintenance, enabling SHM of F-35 aircraft. The anticipated outcome is reduced inspection time and cost, coupled with improved reliability and efficiency in flaw detection.

1.4 Research Survey

A comprehensive literature review was conducted in the field of PEC for aircraft structural inspection, beginning with fundamental analytical developments that establish the theoretical basis for the transient diffusion of magnetic fields into conductive media. Early transient eddy current models trace back to Wwedensky [19], who first described the time-dependent electromagnetic diffusion resulting from an abruptly applied uniform magnetic field (a step increase in the applied field). His solution [19] treated the diffusion of abruptly applied magnetic fields into an infinitely long conducting rod. Later, major advances in the time-harmonic domain were made by Dodd and Deeds [20], whose analytical solution for coaxial coils above conducting plates under sinusoidal excitation has become foundational to modern ET. However, the Dodd and Deeds model [20] applies strictly to the time-harmonic case and assumes constant-amplitude current excitation with the pick-up coil operating under high-resistance conditions. As a result, induced pick-up coil currents are negligible, and driver feedback effects present in voltage-controlled systems can be neglected.

Subsequent analytical advances have extended both transient and time-harmonic formulations. Bowler [21], Theodoulidis [22], [23], and others [24], [25], [26], [27] expanded the classical framework by incorporating voltage-controlled excitation and more complex geometries using time-harmonic analysis. In the transient domain, early formulations by Morozova [28] and later approaches such as Bi *et al.* [29] advanced transient modelling for single conducting layers, primarily by improving numerical tractability and computational efficiency. A substantially more advanced and physically accurate transient framework was developed by Desjardins *et al.* [30], [31], who enforced boundary conditions and source–conductor coupling, yielding improved accuracy across the

full transient response. Prior to this work, hybrid analytical–numerical approaches had been proposed by Fan *et al.* [32] and Chen and Lei [33] to address limitations of purely analytical transient models. Later developments by Sun *et al.* [34] and Theodoulidis and Skarlatos [35] extended transient modelling methods for multi-layer cylindrical conductive media, enabling efficient analysis of more intricate configurations.

Signal-processing strategies in PEC inspections have also evolved to mitigate lift-off variation and enhance feature reliability. Early contributions include Lift-Off Point of Intersection (LOI) point analysis by Giguère *et al.* [36], [37], normalization algorithms introduced by Tian and Sophian [38], derivative-based feature enhancement by Tian *et al.* [39], and flux-invariant approaches by Huang and Wu [40]. More recent developments have leveraged advanced computational methods such as wavelet scattering for denoising [41] and Convolutional Neural Networks (CNNs) for automated defect classification and lift-off compensation [42].

Publications concerning PEC signal analysis using statistical and machine-learning techniques were also reviewed. These include studies employing multivariate approaches such as Support Vector Machine (SVM) [43], [44] for supervised defect classification, Principal Component Analysis (PCA) [43], [44], [45] for unsupervised dimensionality reduction, and MPCA [9], [10], [11], [46], [47], which omits mean-centering to better preserve transient waveform characteristics. Complementary methods include Independent Component Analysis (ICA) [44] for independent component extraction and Mahalanobis Distance (MD) [9], [10], [11], [46] for quantifying statistical deviation from reference distributions to support anomaly detection. Collectively, these techniques have been applied to the detection of cracks and material degradation in multi-layer, fastener-containing aerospace assemblies [12], [48], [49], [50], [51].

The following sections outline key developments in analytical modelling, signal processing, and defect detection that underpin this thesis. Together, these studies highlight the evolution of PEC from fundamental field theory toward advanced inspection methodologies for multi-layer and fastener-containing aerospace structures.

1.4.1 Analytical Foundations of Pulsed Eddy Current

While conventional eddy current techniques employing sinusoidal excitation have been widely adopted for defect identification [52], [53], recent research has increasingly focused on advancing PEC methods. One of the earliest instances of pulsed or transient ET, utilizing square-wave excitation, was presented by Wwedensky [19], who described the time-dependent diffusion of eddy currents resulting from the abrupt application of a uniform magnetic field into a long cylindrical conductor.

Although Wwedensky's [19] assumption of an infinitely extending uniform field was later recognized as a violation of Gauss's law for magnetism, specifically the condition of no monopoles [14], his work [19] nevertheless established a foundational framework for transient excitation analysis.

However, the resulting solution was valid only at later times, as it treated the externally applied field as independent of the induced eddy currents in the conductor, thereby neglecting boundary conditions and drive coil feedback that are critical during the early stages of eddy current diffusion. His simplification [19] further constrained subsequent analytical developments by limiting the applicability of the formulation to idealized excitation conditions, reducing its suitability for finite coils, voltage-controlled sources, and the more complex or layered structures encountered in practice.

A significant advancement was achieved in the 1960s when Dodd and Deeds [20] introduced a pioneering analytical model based on the magnetic vector potential formalism. The work of Dodd and Deeds [20] provided closed-form solutions for eddy currents induced by cylindrical coils in planar and cylindrical conductors under constant harmonic excitation. Despite its impact, the Dodd and Deeds model [20] assumed open-circuit pickup coils and constant-amplitude sinusoidal drive currents, presenting challenges in voltage-controlled systems where feedback from nearby conductors perturbs coil behaviour [21]. Furthermore, its reliance on high input impedance limited its applicability in practical measurement scenarios involving finite pickup coil currents [54].

Building upon these foundations, substantial theoretical progress was made by Morozova [28], Bowler [21], [55], [56], Theodoulidis [22], [23], [57], and others [24], [25], [26], [27], who refined the modelling of induced voltages and coil impedance variations for NDT applications. Fan *et al.* [32] advanced analytical modelling by characterizing transient responses of air-cored coils near layered conductors subjected to step-function voltage excitation, improving upon earlier current-driven approaches.

Expanding this framework, Desjardins *et al.* [14] developed an analytical model for transmit–receive PEC probes with encircling coils positioned around cylindrical rod geometries. The model by Desjardins *et al.* [14] incorporated finite coil impedances and voltage-controlled excitations, effectively addressing feedback effects and improving transient electromagnetic field predictions.

In recent years, Chen and Lei [33] investigated transient PEC fields surrounding ferromagnetic pipes, while Sun *et al.* [34] provided detailed analyses of ferromagnetic casings, contributing to a deeper understanding of transient Electromotive Force (emf) behaviour relevant to NDE applications. Recognizing the limitations of purely analytical methods, Theodoulidis and Skarlatos [35] introduced a hybrid analytical–numerical approach employing Laplace inversion to efficiently model transient eddy current responses in multi-layer cylindrical media.

More recently, Bi *et al.* [29] enhanced PEC modelling efficiency through an adaptive interpolation-based Fourier transform method, supporting integration with machine learning frameworks. Fu *et al.* [42] further highlighted the role of data-driven approaches in PEC, emphasizing automated defect classification, lift-off compensation, and predictive maintenance through deep-learning architectures. Yan and Chen [58] addressed dynamic modelling challenges under pulsed excitation involving relative motion, providing further insight into transient coupling behaviour.

While analytical models established the theoretical framework for transient field behaviour, signal-processing advancements were essential to translate these responses into reliable defect indicators under practical inspection conditions.

1.4.2 Signal Processing Techniques in Pulsed Eddy Current Inspections

Lift-off variations pose a significant challenge in eddy current NDT, including PEC inspections, impacting signal reliability and hindering defect detection accuracy. Various techniques have been developed to address these challenges, each tailored to specific PEC applications and material configurations.

One of the most widely used methods is the LOI, introduced by Giguère *et al.* [37], which identifies a point in the transient response that remains largely insensitive to probe coupling or lift-off changes. By analyzing transient signals across various lift-offs, Giguère *et al.* [36], [59] determined the LOI time at which amplitude variation most reliably indicates defect presence. This approach is particularly effective under conditions of unknown or varying lift-off, such as CF-188 inner wing inspections [36]. However, the analysis was initially limited to sub-millimetre lift-offs typical of corrosion detection in aircraft lap joints, where variations often arise from protruding rivets, uneven skin panels, or differences in paint thickness.

Subsequent research expanded LOI applications to diverse structural configurations. Angani *et al.* [60] employed LOI-based features for plate thickness evaluation, Liu *et al.* [61] applied the approach to defect quantification in layered structures, and Lefebvre *et al.* [62] demonstrated that both LOI time and amplitude follow characteristic curves governed by conductivity and thickness. These studies confirmed that LOI-based analysis provides a robust indicator of material properties and defect signatures in the presence of lift-off variation.

Another widely adopted strategy for lift-off mitigation is signal normalization. Tian and Sophian [38] introduced a normalization algorithm using reference signals to improve metal loss quantification and subsurface slot detection, though their method was validated only for small lift-offs between 0 to $0.4\,\mathrm{mm}$. Subsequent investigations by Lefebvre and Mandache [63] identified LOI effects in conductive, non-ferrous layers over ferromagnetic substrates, while Mandache and Lefebvre [18] established that LOI is a fundamental property of eddy currents, not limited to transient responses. Kral *et al.* [64] further modelled LOI formation using a linear transformer approach, relating it to time derivatives of signals from Giant Magnetoresistance (GMR)-based probes.

Beyond LOI, further normalization-based methods have been explored. Tian *et al.* [39] confirmed that lift-off invariance applies to pickup coils and magnetic sensors, which led to theoretical modelling techniques for lift-off estimation, including potential applications in sensor arrays. Yu *et al.* [65] investigated indirect lift-off compensation through differential signal slope analysis for surface defect depth measurements. At the same time, Huang and Wu [40] demonstrated that the relative rate of magnetic flux change is independent of lift-off, offering a reliable metric for es-

timating ferromagnetic plate thickness. Additionally, Tian *et al.* [66] applied frequency-domain normalization techniques to mitigate lift-off effects effectively.

Recent advancements in PEC signal processing have expanded beyond traditional normalization and LOI methodologies. Sudirman *et al.* [41] employed the wavelet scattering transform to enhance transient signal denoising and improve ferromagnetic material thickness measurements. Fu *et al.* [42] integrated machine-learning frameworks, particularly CNNs, to facilitate automated defect classification and depth estimation, enabling fully integrated PEC analysis in complex environments. Developments in PEC array probe configurations, as demonstrated by Demers-Carpentier *et al.* [67], introduced spatial filtering capabilities to improve sensitivity and inspection coverage.

Building on signal-processing advancements, several studies [9], [10], [30], [31], [42], [50] have explored data-driven feature extraction and classification techniques to enhance PEC sensitivity in layered and multi-material aerospace structures.

1.4.3 Defect Detection in Multi-Layer Aircraft Structures

PCA has been one of the most widely used feature extraction techniques in PEC signal analysis, since its introduction by Sophian *et al.* [68], who proposed a novel PCA-based feature for defect classification. This approach was further expanded by Tian *et al.* [38], who refined the extraction process to improve sensitivity and dimensionality reduction.

In 2013, He *et al.* [43], [44] investigated the use of PCA for feature extraction and SVM for automated defect classification in two-layer specimens. He *et al.* [43] observed that defects at different depths influence the PEC signal at distinct times, with deeper defects primarily affecting later portions of the transient response owing to diffusion-controlled field penetration, thereby altering the waveform shape. However, these temporal variations were often subtle compared to the dominant amplitude component, which primarily depends on defect width. This finding aligns with the numerical results of Cadeau *et al.* [13], who demonstrated through experiments that PEC signal amplitude is strongly influenced by defect depth and probe geometry, emphasizing the importance of optimized probe design for improved depth sensitivity.

He *et al.* [43] showed that signal normalization amplifies defect-related differences, while mitigating lift-off and air-gap effects, thereby enhancing PCA's sensitivity to changes in the transient response associated with defects. When PCA was applied without normalization, classification accuracy reached $83.4\,\%$ using the first two principal components, improving to $100\,\%$ after normalization. Under variable lift-off conditions ranging from 0 to $1.4\,\mathrm{mm}$, accuracy increased from $61.4\,\%$ before normalization to $91.7\,\%$ [43]. He *et al.* [43] emphasized that SVM performance depends heavily on a sufficiently diverse training dataset to ensure reliable classification.

In a complementary study, He *et al.* [44] compared PCA and ICA for feature extraction when coupled with SVM. Their analysis [44] transformed the PEC signal into the frequency domain prior to feature extraction, showing that while PCA captures correlated variations, ICA separates statis-

tically independent components, producing clearer clustering and superior classification. Specifically, PCA alone achieved $82\,\%$ accuracy, improving to $98.9\,\%$ with SVM; ICA achieved $85.4\,\%$ alone and $100\,\%$ when integrated with SVM [44]. He *et al.* [44] concluded that independent components form tighter clusters than principal components, confirming the advantage of ICA for defect classification. Furthermore, they [44] found that time-domain responses were more effective for detecting bottom-layer defects, whereas frequency-domain features offered improved detection of top-layer defects.

While He *et al.* [43], [44] focused on enhancing feature extraction through normalization and machine learning, Pan *et al.* [45] advanced PEC defect classification by leveraging selected frequency responses and PCA to address air-gap challenges in two-layer structures. Pan *et al.* [45] conducted experiments to classify surface defects, subsurface defects, and material thickness variations, emphasizing that inter-layer corrosion—complicated by lift-off and air gaps—remains a key challenge in multi-layer inspections.

Unlike earlier studies that primarily used time-domain signals for PCA, Pan *et al.* [45] demonstrated that frequency-domain features extracted via Fourier series analysis of the square-wave excitation provided complementary diagnostic information. Pan *et al.* [45] reported that frequencies between $3.7\,\mathrm{kHz}$ and $5.4\,\mathrm{kHz}$ were optimal for classifying second-layer defects, whereas higher frequencies from $12\,\mathrm{kHz}$ to $25\,\mathrm{kHz}$ were more effective for first-layer detection. Moreover, Pan *et al.* [45] successfully classified surface and subsurface defects in layered samples with inter-layer air gaps ranging from 0 to $1.4\,\mathrm{mm}$, confirming the utility of frequency-domain PCA for multi-layer PEC inspection.

Although defect detection in planar multi-layer specimens has matured, detecting cracks around fasteners remains a major challenge due to geometric complexity and magnetic field distortion. The following studies chronicle progressive efforts to overcome these limitations using ferrite-cored and differential PEC probes.

1.4.4 Pulsed Eddy Current Crack Detection in Fastener-Containing Structures

Numerous studies have investigated the feasibility of using PEC techniques to detect subsurface cracks in multi-layer aircraft components, particularly around fasteners, where conventional ET techniques are often limited by geometric and material complexities.

In 2010, Whalen [48] demonstrated that a PEC probe with a ferrite-cored central driving coil and differentially paired pickups could detect subsurface notches located at the edge of multi-layer aluminum structures containing ferrous fasteners. The fastener acted as a magnetic flux conduit, thereby enhancing eddy current penetration and improving flaw detectability [48]. Whalen [48] further proposed that enlarging the ferrite core diameter relative to the fastener head would improve flux transfer, optimizing detection performance.

In 2012, Desjardins *et al.* [49] investigated PEC inspection at fastener locations in aluminum plates, concluding that transient fields enhance flux transfer due to fastener magnetization. They [49] showed that inserting a steel rod into the bolthole amplified induced currents and extended transient decay, thereby improving crack detection. Desjardins *et al.* [49] also examined a PEC probe with a transmit coil and two lateral differential pickups, demonstrating that concentrated flux along the ferrous fastener—intensified by the steel rod—produced strong angular signal variation when detecting cracks located $1.3\,\mathrm{mm}$ beneath the surface. Their findings [49] confirmed that flux enhancement from ferrous fasteners enables deeper eddy current penetration and improves subsurface crack detection in lap-joint structures.

In 2013, Horan *et al.* [9], [10] explored PEC for detecting SCC in CF-188 wing spars with thick CFRP skins, extending the probe developed by Desjardins *et al.* [49] by incorporating a ferrite-cored central driving coil and two 180° opposed differential pickups. Their [9], [10] experimental setup simulated an inner wing spar using a $3.2\,\mathrm{mm}$ thick 7075-T6 aluminum strip with ferrous fasteners beneath a $13\,\mathrm{mm}$ thick Nylon-6 overlayer. The test configuration included blank and notched fastener sites with $0.2\,\mathrm{mm}$ wide notches of varying lengths extending from borehole edges toward adjacent fasteners [9], [10]. An acrylic alignment tool ensured consistent probe positioning, and measurements were collected at each fastener site. Horan *et al.* [9], [10] introduced MPCA formalism for defect classification, using the first four eigenvectors to project the PEC signals into score plots. Clustering of the third versus second MPCA score (s_3 vs. s_2) effectively distinguished cracked from defect-free fastener sites. Despite the alignment tool, transient responses remained highly sensitive to axial misalignment, while perpendicular offsets of up to $0.5\,\mathrm{mm}$ had negligible effects, prompting Horan *et al.* [9], [10] to implement MD for real-time outlier detection based on misalignment.

In 2014, Babbar *et al.* [50] developed Finite Element Method (FEM) models to simulate PEC-based notch detection in lap-joint structures representative of the CP-140 Aurora wing. Their [50] simulated probe configuration—a central ferrite-cored driving coil surrounded by eight differentially paired pickup coils—became a standard layout for later experimental validation. Their [50] two-layer aluminum sample included cracks of various sizes and orientations. Even in defect-free samples, lap-joint edges significantly influenced differential signals, particularly when located at 270° on the top layer and 90° on the second layer [50]. Second-layer cracks produced weaker signals representing delayed time, consistent with observations by Horan *et al.* [9], [10], who found that displacements perpendicular to the lap-joint edge had minimal signal variation, whereas shifts along the edge altered the signal shape and amplitude [50]. Babbar *et al.* [50] applied MPCA to isolate defect-related signals from probe misalignment, showing that displacement effects were captured by the first eigenvector, while second-layer cracks appeared in the second. Their [50] results confirmed the potential of PEC for detecting cracks and inferring their depth and orientation in multi-layered aluminum structures with ferrous fasteners.

In 2015, Stott *et al.* [46] experimentally validated the probe design previously simulated by Babbar *et al.* [50], assessing crack detection in multi-layer aluminum lap-joint structures representative of a CP-140 Aurora wing. Samples containing blank fastener sites and Electrical Discharge Machining (EDM) notches of varying sizes and orientations were inspected using the same ferrite-cored probe layout [46]. PEC signals were analyzed using MPCA; however, due to notch diversity, conventional discriminant analysis [69] proved ineffective. Stott *et al.* [46] instead applied MD to quantify score separation, revealing a direct correlation with crack size and enabling effective sizing. This approach achieved a $97\,\%$ detection rate at $99\,\%$ confidence, with a $4\,\%$ false-call rate and $100\,\%$ detection at $95\,\%$ confidence when the threshold was increased to $10\,\%$. Although false calls required follow-up BHEC inspection, they [46] emphasized that PEC-based screening reduced unnecessary fastener removal and inspection time. Stott *et al.* [46] ultimately validated PEC as an effective technique for detecting cracks in layered aluminum and improving aircraft maintenance efficiency.

In 2016, Butt *et al.* [11], [70], [71] demonstrated that PEC can detect second-layer cracks in multi-layer aluminum lap-joint structures without fastener removal. Four probe configurations were evaluated to assess the influence of the driving-coil core diameter on magnetic flux transfer, as postulated by Whalen [48]. Each design featured a ferrite-cored driving coil and eight symmetrically positioned pickup coils paired at 180° intervals [11]. An $8\,\mathrm{mm}$ core, slightly larger than the $7\,\mathrm{mm}$ fastener head, enhanced magnetic flux transfer and eddy current induction [48], while a non-inverting op-amp improved signal quality. Butt *et al.* [11] examined seven Naval Air Systems Command (NAVAIR) samples representative of the CP-140 Aurora wing lap-joint structure, incorporating 2024-T3 aluminum plates joined by ferrous fasteners, deliberately introducing inter-layer gaps to simulate lap-joint separation, and EDM notches positioned at 45° angles. An acrylic alignment tool ensured concentric probe positioning over each fastener. Transient signals were gated, and MD was computed from blank fastener scores to classify defects. Additional processing mitigated environmental, repeatability, and geometric inconsistencies. Detection rates ranged from $81\,\%$ to $99\,\%$ at a $5\,\%$ false-call rate [11], validating PEC as a viable technique for inspecting multi-layered aircraft structures without fastener removal, while reducing inspection time and costs.

In 2018, Uemura *et al.* [12] expanded upon the work of Butt *et al.* [11], [70], [71] by evaluating the impact of parameter variability—including probe misalignment, temperature fluctuations, and fastener-to-lap-joint edge distance—on PEC inspection performance. Building on observations by Horan *et al.* [9], [10] and Babbar *et al.* [50], they [12] found that off-centre displacements of up to $2\,\mathrm{mm}$ shifted signal variation from the first to the second MPCA score (s_1 to s_2), reducing second-layer crack detection and increasing false calls. Temperature fluctuations between 10 and $30\,^\circ\mathrm{C}$ introduced electrical noise but had minimal impacts on detection rates. Improved fastener-to-lap-joint edge positioning enhanced overall detection accuracy from $86.0\,\%$ to $93.4\,\%$, while reducing the false-call rate from $5.5\,\%$ to $4.2\,\%$. A Probability of Detection (POD) analysis using

MH1823 software yielded an $a_{90/95}$ of $1.98\,\mathrm{mm}$, which was further reduced to $1.70\,\mathrm{mm}$ with image processing. Based on these findings, Uemura *et al.* [12] recommended standardizing PEC as an approved NDT method for bolt-hole crack detection, citing its ability to support localized BHEC confirmation, while minimizing fastener extractions, maintenance time, and inspection frequency.

In 2024, Punter and Hughes [51] investigated the feasibility of implementing a permanently installed PEC SHM system for continuous defect detection in aerospace structures containing fasteners. Building upon the flux-enhancement principles demonstrated by Desjardins *et al.* [49] and the finite-element modelling framework established by Babbar *et al.* [50], Punter and Hughes [51] examined the influence of bolt and nut material properties on eddy current generation in defective regions using FEM. Their analysis [51] demonstrated that ferrous bolts increased eddy current generation by $30.2\,\%$ compared to non-ferrous bolts due to enhanced magnetic-flux conduction, while ferrous nuts introduced magnetic shielding effects that reduced current density around defects. Punter and Hughes [51] emphasized the importance of optimizing sensor configurations, particularly pickup-coil placement, to maximize detection sensitivity in environments with varying fastener materials. Although their study was primarily simulation-based, Punter and Hughes [51] proposed future experimental validation to confirm detection capabilities and assess the practical integration of embedded PEC sensors within aerospace components. Their work [51] underscored the potential of PEC-based SHM systems to enable continuous, real-time monitoring of crack initiation and growth around fasteners, offering a pathway to reduced aircraft downtime, enhanced maintenance efficiency, and improved structural-integrity management.

1.5 Thesis Scope and Methodology

This section summarizes the organization and methodology of the thesis.

Chapter 2 establishes the theoretical foundation for PEC inspection, beginning with a review of electromagnetic fundamentals—Maxwell's equations, Ohm's law, and the diffusion equation under the Magnetoquasistatic (MQS) approximation. Analytical tools such as integral transforms and Fourier series are introduced to solve BVPs and to reconstruct time-domain responses from frequency-domain formulations. Equivalent circuit models, convolution theory, and statistical methods—including PCA, MPCA, and discriminant analysis—are presented for flaw classification and signal interpretation. The chapter concludes with resistivity measurement techniques used for model calibration and material characterization.

Chapter 3 describes the experimental methodology used to validate analytical and numerical models through measurements from four custom-designed probes—ZEUS, ARES, THOR, and ODIN—tested under varying lift-off and flaw conditions. ZEUS and ARES are vertically differential probes optimized for lift-off sensitivity, while THOR and ODIN employ radially offset pickup coils to detect field asymmetries. The chapter details probe construction, sample configurations,

and the automated Laboratory Virtual Instrument Engineering Workbench (LabVIEW) -based data-acquisition system developed for signal data capture and export.

Chapter 4 outlines the signal-processing framework used to extract, classify, and interpret PEC signals. The approach combines time-domain gating with MPCA and discriminant analysis to isolate features sensitive to material discontinuities. A calibration model composed of principal-component vectors and regression coefficients is applied to new measurements for automated classification, enabling real-time visualization and flaw detection in LabVIEW.

Chapter 5 introduces the analytical model for a vertically differential PEC probe above a conductive plate. Complex self- and mutual inductances are derived from circuit equations and evaluated via Fourier and Hankel transforms. The frequency-domain formulation is converted to the time domain using inverse-Fourier summation of a square-wave excitation, enabling parametric analysis of probe geometry, lift-off, and material effects.

Chapter 6 presents analytical-model results validated against FEM simulations and experimental measurements. Time-domain PEC responses are reconstructed from complex inductances to assess the influence of lift-off, conductivity, and thickness. Quantitative agreement across analytical, numerical, and experimental datasets confirms the model's predictive capability for probe optimization and signal interpretation.

Chapter 7 extends the validation through a coded experimental design to propagate uncertainty and identify dominant contributors to signal variability. Results demonstrate the model's ability to reproduce waveform morphology, amplitude, and lift-off sensitivity accurately, confirming its robustness for parametric studies.

Chapter 8 evaluates conventional ET for crack detection around fasteners under variable lift-off and material conditions. Using the ZEUS, THOR, and ODIN probes, the study quantifies alignment effects and compares flaw visibility across stainless-steel and titanium specimens. Limitations of sinusoidal excitation are highlighted, motivating the adoption of multivariate, PCA-based classification for enhanced sensitivity in low-conductivity or high lift-off scenarios.

Chapter 9 summarizes flaw-classification results using principal component–based discriminant analysis. The impact of probe architecture, eigenvector selection, and lift-off height on detection accuracy is examined, confirming the superior performance of vertically differential probes and family-based eigenspaces.

Chapter 10 integrates experimental, analytical, and computational findings to evaluate the feasibility of a PEC system for detecting stress-corrosion cracking in aerospace fasteners. Comparative results demonstrate the advantages of broadband, pulsed excitation over conventional ET. The chapter concludes with recommendations to expand material coverage, refine classification algorithms, and integrate PEC within automated aerospace NDT platforms.

2 Theory

2.1 General

This chapter presents the theoretical background underpinning PEC inspection. It begins with Maxwell's equations and the constitutive relationships that describe the interaction between electric and magnetic fields in conductive media. From these, the diffusion equation is derived to represent the time-dependent behaviour of magnetic fields and current densities in the presence of a conductor. The magnetic vector potential formulation is introduced to simplify the governing equations in axisymmetric geometries, and the vector Laplacian in cylindrical coordinates is derived for BVPs. Eddy current theory is then reviewed, including the formation of induced currents under alternating excitation, the skin effect, and the dependence of penetration depth on material properties and excitation frequency. The PEC method is introduced as a transient extension of classical ET, utilising square-wave excitation to generate broadband responses. Equivalent circuit models are developed to describe the time-domain behaviour of both driver and pickup coils, incorporating the effects of self- and mutual inductance. Mathematical tools, including the Fourier transform, the Fourier cosine transform, and the Hankel transform, are presented as methods for solving the associated Partial Differential Equation (PDE) in geometries involving infinite domains or layered structures. Signal processing approaches for interpreting PEC responses are then described, followed by a discussion of PCA and discriminant analysis methods for flaw detection and classification. These theoretical foundations form the basis for the modelling, simulation, and analysis methods developed throughout this thesis.

2.2 Electromagnetic Theory

Maxwell's equations express the fundamental principles of electromagnetism, describing how electric and magnetic fields interact with charges and currents in space. Maxwell's four equations in free space are given as [72]:

$$\nabla \cdot \mathbf{E} = \frac{1}{\epsilon_0}\rho, \tag{2.1}$$

$$\nabla \times \mathbf{E} = -\frac{\partial \mathbf{B}}{\partial t}, \tag{2.2}$$

$$\nabla \cdot \mathbf{B} = 0, \tag{2.3}$$

$$\nabla \times \mathbf{B} = \mu_0 \mathbf{J} + \mu_0 \epsilon_0 \frac{\partial \mathbf{E}}{\partial t}. \tag{2.4}$$

Here, t represents time, $\mathbf{E}$ denotes the electric field, $\mathbf{B}$ represents the magnetic field, $\mathbf{J}$ is the current density, ρ is the charge density, ϵ_0 is the permittivity of free space, and μ_0 is the permeability of free space. Equation 2.1 is Gauss's law for electricity; Equation 2.2 is Faraday's law of induction; Equation 2.3 is Gauss's law for magnetism; and Equation 2.4 is Ampère's law with Maxwell's correction.

Ohm's law, which relates the current density to the electric field, is expressed as [73]:

$$\mathbf{J} = \sigma \mathbf{E}, \tag{2.5}$$

where σ is the electrical conductivity of the medium. For linear and isotropic media, the following relationships hold [72]:

$$\mathbf{B} = \mu \mathbf{H}, \tag{2.6}$$

$$\mathbf{D} = \epsilon \mathbf{E}, \tag{2.7}$$

where $\mathbf{H}$ is the magnetic field intensity related to $\mathbf{B}$ through the permeability μ, and $\mathbf{D}$ is the electric displacement field related to $\mathbf{E}$ through the permittivity ϵ.

Using these relationships, Maxwell's equations in matter for linear and isotropic media become [72]:

$$\nabla \cdot \mathbf{D} = \rho_f, \tag{2.8}$$

$$\nabla \times \mathbf{E} = -\frac{\partial \mathbf{B}}{\partial t}, \tag{2.9}$$

$$\nabla \cdot \mathbf{B} = 0, \tag{2.10}$$

$$\nabla \times \mathbf{H} = \mathbf{J}_f + \frac{\partial \mathbf{D}}{\partial t}, \tag{2.11}$$

where ρ_f is the free charge density and $\mathbf{J}_f$ is the free current density.

From the vector calculus identity $\nabla \cdot (\nabla \times \mathbf{A}) = 0$ and Equation 2.10, the magnetic flux density $\mathbf{B}$ can be expressed as the curl of a magnetic vector potential:

$$\mathbf{B} = \nabla \times \mathbf{A}. \tag{2.12}$$

Substituting Equation 2.12 into Equation 2.9 gives:

$$\nabla \times \mathbf{E} = -\frac{\partial (\nabla \times \mathbf{A})}{\partial t} = -\nabla \times \frac{\partial \mathbf{A}}{\partial t}. \tag{2.13}$$

Using the vector identity $\nabla \times \nabla V = 0$, Equation 2.13 simplifies to:

$$\mathbf{E} = -\frac{\partial \mathbf{A}}{\partial t} - \nabla V, \tag{2.14}$$

where V is a scalar potential. In the absence of a potential gradient ($\nabla V = 0$), Ohm's law can be expressed in terms of the magnetic vector potential as:

$$\mathbf{J} = -\sigma \frac{\partial \mathbf{A}}{\partial t}. \tag{2.15}$$

Assuming the Coulomb–gauge condition $\nabla \cdot \mathbf{A} = 0$ and substituting Equation 2.12, Equation 2.14, and Equation 2.15 into Equation 2.4, the full wave equation is obtained:

$$\nabla^2 \mathbf{A} = \mu\sigma \frac{\partial \mathbf{A}}{\partial t} + \mu\epsilon \frac{\partial^2 \mathbf{A}}{\partial t^2}. \tag{2.16}$$

Under the MQS approximation [73], the second term on the right-hand side of Equation 2.16, which arises due to displacement currents, can be neglected for frequencies below approximately $10\,\mathrm{MHz}$ [20]. Assuming isotropic conductivity and permeability, Equation 2.16 simplifies to:

$$\nabla^2 \mathbf{A} \approx \mu\sigma \frac{\partial \mathbf{A}}{\partial t}. \tag{2.17}$$

Equation 2.17 is the electromagnetic analog of heat diffusion in solids, where electromagnetic field variations occur in three dimensions. Substituting Equation 2.5 into Equation 2.17, the current density in the drive coil can be determined as:

$$\nabla^2 \mathbf{A} = -\mu \mathbf{J}. \tag{2.18}$$

The vector Laplacian ∇^2 of the magnetic vector potential $\mathbf{A}$ in cylindrical coordinates (r, ϕ, z) takes the form [74]:

$$\nabla^2 \mathbf{A} = \begin{bmatrix} \frac{\partial^2 A_r}{\partial z^2} + \frac{\partial^2 A_r}{\partial r^2} + \frac{1}{r}\frac{\partial A_r}{\partial r} - \frac{A_r}{r^2} + \frac{1}{r^2}\frac{\partial^2 A_r}{\partial \phi^2} - \frac{2}{r^2}\frac{\partial^2 A_\phi}{\partial \phi^2} \\ \frac{\partial^2 A_\phi}{\partial z^2} + \frac{\partial^2 A_\phi}{\partial r^2} + \frac{1}{r}\frac{\partial A_\phi}{\partial r} - \frac{A_\phi}{r^2} + \frac{1}{r^2}\frac{\partial^2 A_\phi}{\partial \phi^2} + \frac{2}{r^2}\frac{\partial^2 A_r}{\partial \phi^2} \\ \frac{\partial^2 A_z}{\partial z^2} + \frac{\partial^2 A_z}{\partial r^2} + \frac{1}{r}\frac{\partial A_z}{\partial r} + \frac{1}{r^2}\frac{\partial^2 A_z}{\partial \phi^2} \end{bmatrix} \begin{matrix} \hat{r} \\ \hat{\phi} \\ \hat{z} \end{matrix} \tag{2.19}$$

For most coil problems, the current density in Equation 2.18 is axially symmetric and circulates in the circumferential (ϕ) direction. This implies that $\mathbf{A}$ is also oriented in the ϕ-direction, giving $A_r = A_z = 0$ and $\frac{\partial A_\phi}{\partial \phi} = 0$. Under these assumptions, the vector Laplacian reduces to:

$$\nabla^2 \mathbf{A}_\phi = \left[\frac{\partial^2 A_\phi}{\partial z^2} + \frac{\partial^2 A_\phi}{\partial r^2} + \frac{1}{r}\frac{\partial A_\phi}{\partial r} - \frac{A_\phi}{r^2} \right] \hat{\phi}. \tag{2.20}$$

The diffusion equation (Equation 2.17) and the vector Laplacian in cylindrical coordinates (Equation 2.19), together with appropriate boundary conditions, form the basis of the eddy current BVP.

2.2.1 Diffusion Equations

The diffusion of magnetic fields in conducting media governs eddy current behaviour at frequencies below approximately 10^8 Hz [20]. Applying the curl operator to Equation 2.9 yields:

$$\nabla \times (\nabla \times \mathbf{E}) = -\nabla \times \frac{\partial \mathbf{B}}{\partial t}. \tag{2.21}$$

Using the vector identity for second derivatives [72]:

$$\nabla \times (\nabla \times \mathbf{E}) = \nabla(\nabla \cdot \mathbf{E}) - \nabla^2 \mathbf{E}, \tag{2.22}$$

Equation 2.21 can be expressed as:

$$\nabla(\nabla \cdot \mathbf{E}) - \nabla^2 \mathbf{E} = -\frac{\partial}{\partial t}\left(\nabla \times \mathbf{B}\right). \tag{2.23}$$

For a good conductor (i.e., one where $\sigma \gg \omega\epsilon$), surface charges dissipate rapidly, leading to $\rho = 0$ [72]. Thus, Equation 2.8 simplifies to $\nabla \cdot \mathbf{E} = 0$. With this and Equation 2.11, Equation 2.23 becomes:

$$\nabla^2 \mathbf{E} = \frac{\partial}{\partial t}\left(\mu\sigma\mathbf{E} + \mu\epsilon\frac{\partial \mathbf{E}}{\partial t}\right). \tag{2.24}$$

Rearranging Equation 2.24 yields:

$$\nabla^2 \mathbf{E} = \mu\sigma\frac{\partial \mathbf{E}}{\partial t} + \mu\epsilon\frac{\partial^2 \mathbf{E}}{\partial t^2}. \tag{2.25}$$

Equation 2.25 represents Maxwell's modified wave equation [72]. A similar expression can be derived for the magnetic field **B** [72]:

$$\nabla^2 \mathbf{B} = \mu\sigma\frac{\partial \mathbf{B}}{\partial t} + \mu\epsilon\frac{\partial^2 \mathbf{B}}{\partial t^2}. \tag{2.26}$$

For good conductors under time-harmonic conditions where $\epsilon\omega \ll \sigma$, and ω is the angular frequency, the first term can be neglected for frequencies below approximately 10 MHz [20]. Assuming isotropic conductivity and permeability, Equation 2.25 and Equation 2.26 simplify to

$$\frac{\partial \mathbf{E}}{\partial t} = \frac{1}{\mu\sigma}\nabla^2 \mathbf{E}, \tag{2.27}$$

$$\frac{\partial \mathbf{B}}{\partial t} = \frac{1}{\mu\sigma}\nabla^2 \mathbf{B}. \tag{2.28}$$

In a conducting volume, where Ohm's law applies, the time-dependent electric fields are proportional to current densities, which can be described using Equation 2.5. Substituting Equation 2.5 into Equation 2.27 gives the diffusion equation [20]:

$$\nabla^2 \mathbf{J} = \mu\sigma\frac{\partial \mathbf{J}}{\partial t}. \tag{2.29}$$

This form closely resembles Equation 2.17, indicating that **A** and **J** are in the same direction. Under time-harmonic conditions, the time-dependent current density can be expressed as [20]:

$$\mathbf{J}(t) = \mathbf{J}_0 e^{\mathrm{j}\omega t}, \tag{2.30}$$

where $\mathbf{J}_0$ represents the maximum current amplitude. When a plane wave travels into a conducting half-space perpendicular to the z-axis, the solution to Equation 2.29 becomes [75]:

$$\mathbf{J} = \mathbf{J}_s e^{-z/\delta} e^{\mathrm{j}\left(\frac{z}{\delta} - \omega t\right)}, \tag{2.31}$$

where $\mathbf{J}_s$ is the surface current density and δ is the skin depth. The first exponential term in Equation 2.31 represents the attenuation of current density into the material. The second term accounts for the increasing phase lag of the sinusoidal signal as it penetrates deeper into the conductor.

These diffusion characteristics directly determine eddy current penetration depth, a key parameter in electromagnetic inspection. The penetration and density of eddy currents within a sample are crucial considerations in any ET application. Eddy current density, as given by Equation 2.31, decreases exponentially with depth, known as the skin effect. The depth at which the current density has reduced to $1/e$ of the surface density is termed the standard depth of penetration (δ) [76]. Under time-harmonic conditions, the skin depth δ is given by:

$$\delta = \sqrt{\frac{2}{\omega\mu\sigma}}, \tag{2.32}$$

Under conditions where the field excitation is not time-harmonic but a single square pulse, as in PEC, the transient decay of the induced eddy currents occurs. Rough estimates for solutions to the diffusion equations can be made as [77]:

$$\frac{\partial \mathbf{B}}{\partial t} \sim \frac{\mathbf{B}}{\tau_D}, \quad \nabla^2 \mathbf{B} \sim \frac{\mathbf{B}}{\ell^2}, \tag{2.33}$$

where τ_D is the characteristic magnetic diffusion time constant, and ℓ is the representative characteristic length of the conductor. The diffusion time τ_D for these transient eddy currents in a given material can be expressed as [73], [77]:

$$\tau_D \sim \mu\sigma\ell^2. \tag{2.34}$$

Here, ℓ depends on the conductor's geometry and measurement configuration. The magnetic and electric fields will dissipate from the conductor's volume in a characteristic diffusion time, τ_D, which depends on both conductivity and permeability. The complete transient response can be understood as a series of discrete relaxation times, with the longest relaxation time described by Equation 2.34, resulting in greater penetration depth by eddy current fields. The general time-domain solutions to the differential Equation 2.28 for pulse excitations are of the form [77]:

$$\mathbf{B} = f\left(e^{-t/\tau_D}\right), \tag{2.35}$$

Hence, an increase in conductivity leads to a longer diffusion time. Alternatively, Equation 2.34 can estimate the distance ℓ over which fields exist in a conductor subjected externally to transient fields [78]:

$$\ell \sim \sqrt{\frac{\tau_D}{\mu\sigma}}, \tag{2.36}$$

This equation highlights how changes in the sample's electrical conductivity, magnetic permeability, or diffusion time affect the signal output. An equivalent expression for the largest skin depth under transient conditions can be obtained by using Equation 2.34 [75]:

$$\delta \sim \sqrt{\frac{\tau_D}{\mu\sigma}}. \tag{2.37}$$

Equation 2.37 has the same dimensions as the characteristic length, ℓ, in Equation 2.36. Equation 2.32 reveals that penetration depth depends on the sample's excitation frequency, magnetic permeability, and electrical conductivity, while Equation 2.37 depends on the sample's diffusion time, magnetic permeability, and electrical conductivity. Notably, lower frequencies result in deeper penetration, while higher frequencies yield shallower penetration. This relationship is depicted in Figure 2.1. At 3δ, the strength of the eddy currents has decreased by approximately $95\,\%$ compared to that induced at the sample surface.

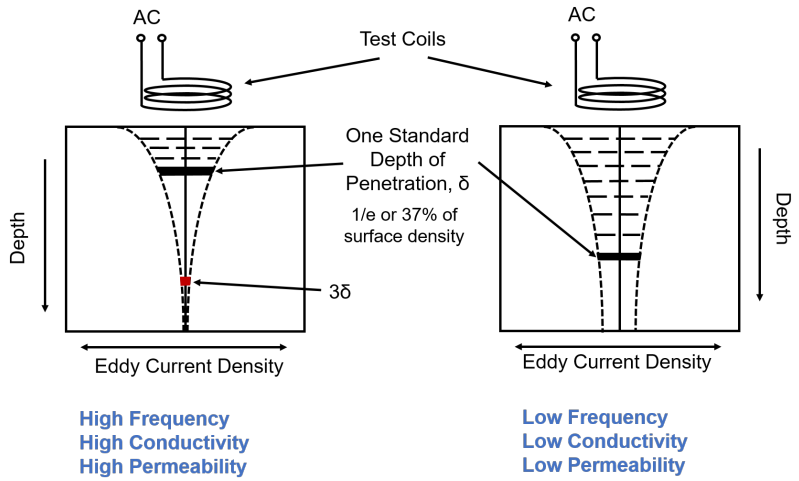

Figure 2.1: Penetration depth changes as frequency changes for conventional ET.

2.3 Eddy Current Theory

ET is a NDT technique widely used for examining conducting structures [79]. It relies on Faraday's law of induction, which describes how a changing magnetic field interacts with an electric circuit to produce an emf [72]. Eddy currents are electrical currents induced in a conductor when an alternating current passes through one or more coils in a probe assembly near the surface of the

specimen [16]. According to Faraday's law, the alternating current induces an oscillating magnetic field within the conductor. Lenz's law, contained within Faraday's law, states that the induced current opposes the change in magnetic flux caused by the time-varying field [72], as illustrated in Figure 2.2.

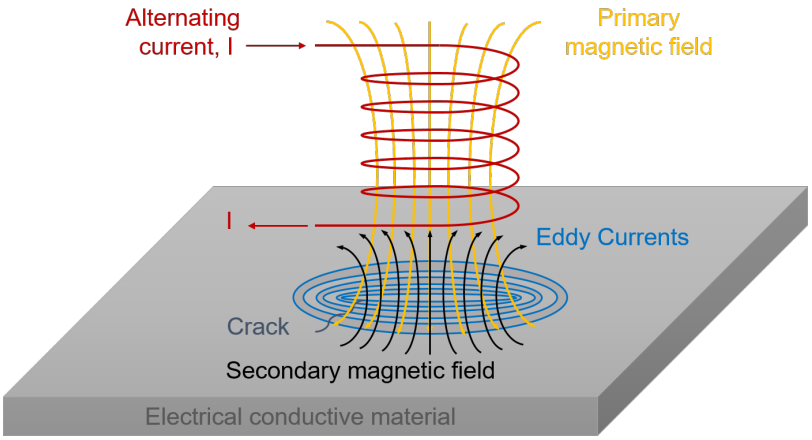

Figure 2.2: Illustration of eddy current formation based on Faraday's law of induction.

Faraday's law can be expressed as:

$$\varepsilon = -\frac{d\Phi_B}{dt} = \oint \mathbf{E} \cdot d\mathbf{l}, \tag{2.38}$$

where ε is the induced emf, Φ_B is the magnetic flux, $d\mathbf{l}$ is an incremental length element around a closed path, and $\frac{d\Phi_B}{dt}$ is the rate of change of magnetic flux. Lenz's law provides the direction of the induced emf: the resulting current always opposes the change in magnetic flux that produced it.

The magnetic flux through a surface S is given by:

$$\Phi_B = \int \mathbf{B} \cdot d\mathbf{a}, \tag{2.39}$$

where $d\mathbf{a}$ is the incremental vector area element. Substituting into Faraday's law yields its integral form:

$$\oint \mathbf{E} \cdot d\mathbf{l} = -\int \frac{\partial \mathbf{B}}{\partial t} \cdot d\mathbf{a}. \tag{2.40}$$

By applying Stokes' theorem, this relation becomes the differential form of Faraday's law, presented as Maxwell's Equation 2.2.

An induced emf will appear whenever the magnetic flux through a circuit changes. A sensing element, such as a coil or magnetic sensor, detects these field variations. Any deviation from the reference signal output can therefore indicate the presence of discontinuities or changes in material properties that impede the eddy current flow.

A key factor influencing ET is *lift-off*—the distance between the excitation coil surface and the conducting material surface. This separation affects the mutual inductance between the conductors and, consequently, the magnitude of the induced emf in the pickup coil. As lift-off increases, the induced signal amplitude decreases due to reduced magnetic coupling. When lift-off becomes sufficiently large, the induced emf in the secondary coil diminishes below the detectable limit, thereby reducing inspection sensitivity.

2.4 Pulsed Eddy Current Theory

The PEC technique differs from conventional ET in that it employs a voltage step function to excite the coil. As illustrated in Figure 2.3, step voltage excitation is applied to the coil to generate a transient electromagnetic field. The square shape of the excitation waveform, shown in Figure 2.3(a), provides broadband frequency content, enabling simultaneous data collection across a wide range of frequencies and penetration depths as the pulse propagates through the test specimen.

The drive current response is influenced by the back emfs generated in the drive coil, test specimen, and any neighbouring pickup coils. At the rising and trailing edges of the pulse, transient changes in the drive current occur (Figure 2.3(b)), producing induced eddy currents within the test object. As these eddy currents and associated magnetic fields diffuse through the material, they are attenuated and dispersed according to the sample's conductivity and magnetic permeability, as described by Equation 2.35. The solution to the corresponding BVP determines the precise temporal shape of the response.

According to Lenz's law, the induced eddy currents produce a secondary magnetic field that opposes the primary excitation field. The decay characteristics of this magnetic field are influenced by the material's electromagnetic properties and the presence of structural anomalies or discontinuities. A pickup coil or magnetic sensor detects the resulting time-varying magnetic field, as shown in Figure 2.3(c). The measured time-dependent voltage response provides valuable information regarding the specimen's electromagnetic properties, defect characteristics, and depth variations.

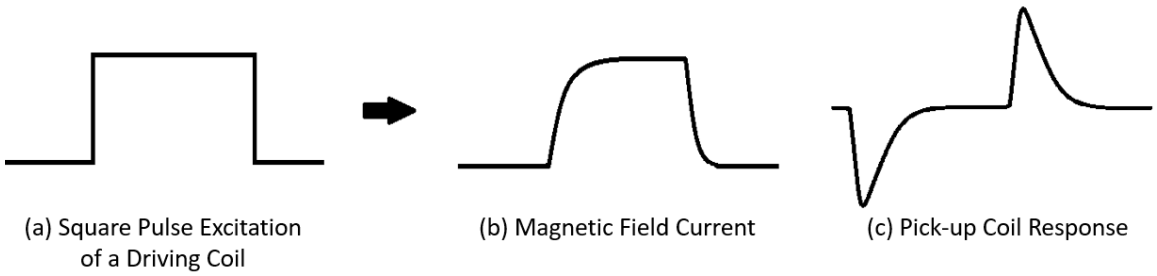

Figure 2.3: Illustration of the PEC technique: (a) Square-wave voltage excitation applied to the driving coil, (b) resulting transient magnetic field response, and (c) pickup-coil voltage signal.

2.4.1 Equivalent Circuit Analysis

When a voltage is applied to the excitation coil, the resulting current approaches a constant value governed by the circuit's resistance and inductance. The excitation coil's transient response can be represented by a simple $R-L$ circuit, as shown in Figure 2.4. This configuration models the PEC driver coil under a square-wave excitation.

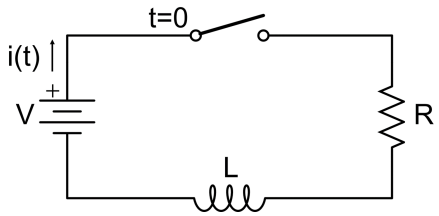

Figure 2.4: An $R-L$ circuit representing a typical PEC excitation coil.

Kirchhoff's Voltage Law (KVL) states that the algebraic sum of the electrical potential differences around any closed loop is zero [80]. Applying KVL to the circuit in Figure 2.4 gives [81]:

$$V - i(t)R - L\frac{di(t)}{dt} = 0, \tag{2.41}$$

where V is the applied voltage, R is the circuit resistance, $i(t)$ is the time-dependent current, and the self-inductance L is treated as a lumped circuit element defined by the ratio of magnetic flux linkage to current [72],

$$L = \frac{\mathrm{d}\Phi}{\mathrm{d}i}, \tag{2.42}$$

where Φ denotes the total magnetic flux linked by the circuit. Although the underlying magnetic field and associated flux distribution are spatially distributed, their net effect is represented by a single equivalent inductance under the quasi-static approximation. Solving Equation 2.41 for $i(t)$ under the initial condition $i(0) = 0$ yields the transient current expression [72]:

$$i(t) = \frac{V}{R}\left(1 - e^{-\frac{R}{L}t}\right). \tag{2.43}$$

Analyzing the system's steady-state response, as shown in Figure 2.5, involves taking the limit as $t \to \infty$:

$$\lim_{t\to\infty} i(t) = \frac{V}{R}. \tag{2.44}$$

The relaxation time, τ_c, defines the time required for the current to reach approximately $63\,\%$ of its final steady-state value:

$$\tau_c = \frac{L}{R}. \tag{2.45}$$

Figure 2.5 illustrates the exponential rise of current with time for an $R-L$ circuit driven by a step voltage.

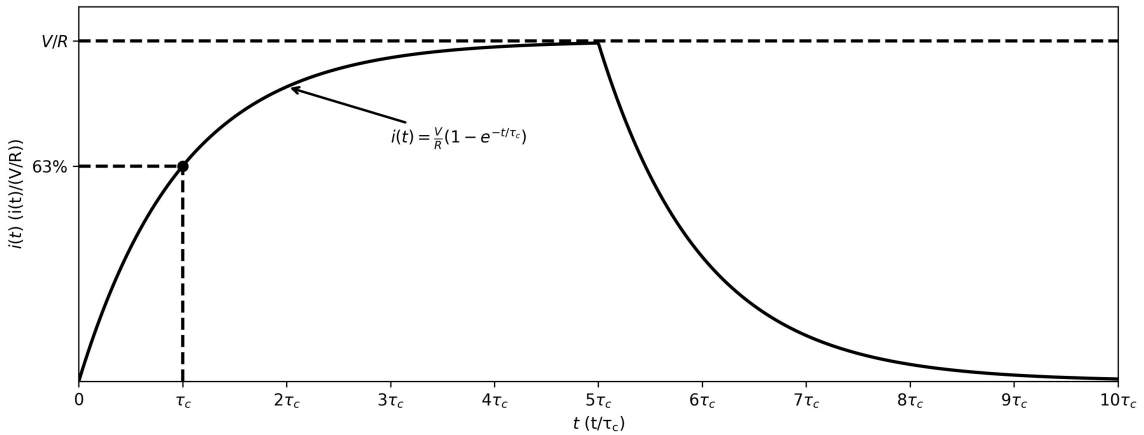

Figure 2.5: Transient current response of an $R-L$ driver circuit following the application of a square-wave excitation.

To simulate the coupling between the driver and pickup coils in a PEC probe, a second loop can be introduced. Figure 2.6 illustrates the expanded circuit, where Loop 1 represents the driving coil, and Loop 2 represents the pickup coil. Mutual inductance M arises between the two coils due to their magnetic coupling.

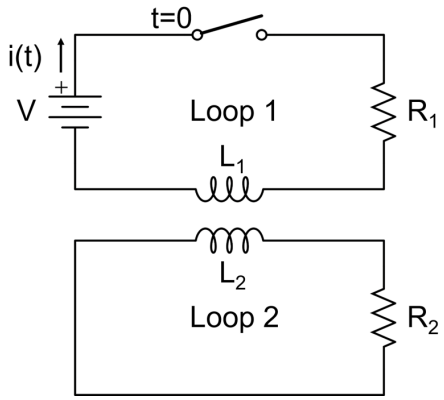

Figure 2.6: Equivalent circuit diagram for PEC driving (Loop 1) and pickup (Loop 2) coils including mutual inductance.

The mutual coupling between coils produces induced emfs given by [80]:

$$\varepsilon_1 = -M_{12}\frac{di_2(t)}{dt}, \qquad \varepsilon_2 = -M_{21}\frac{di_1(t)}{dt}, \tag{2.46}$$

where $M_{12} = M_{21} = M$ is achieved by reciprocity. Applying KVL to each loop in Figure 2.6 yields [82]:

$$L_1\frac{di_1(t)}{dt} + R_1 i_1(t) + M\frac{di_2(t)}{dt} = V\,U(t), \tag{2.47}$$

$$L_2 \frac{di_2(t)}{dt} + R_2 i_2(t) + M \frac{di_1(t)}{dt} = 0, \tag{2.48}$$

where $U(t)$ is the unit step function, and subscripts 1 and 2 denote the driver and pickup coils, respectively.

Taking the Laplace transform of Equation 2.47 and Equation 2.48 and solving for $i_2(t)$ gives the transient current flowing in the pickup coil [82]:

$$i_2(t) = \frac{MV(e^{-\alpha_2 t} - e^{-\alpha_1 t})}{(\alpha_1 - \alpha_2)(L_1 L_2 - M^2)}, \tag{2.49}$$

where α_1 and α_2 represent the inverse relaxation time constants defined as:

$$\alpha_1 = \frac{1}{\tau_1}, \qquad \alpha_2 = \frac{1}{\tau_2}. \tag{2.50}$$

Solving for α_1 and α_2 yields [82]:

$$\alpha_{1,2} = \frac{(L_1 R_2 + L_2 R_1) \pm \sqrt{(L_1 R_2 + L_2 R_1)^2 - 4 R_1 R_2 (L_1 L_2 - M^2)}}{2(L_1 L_2 - M^2)}. \tag{2.51}$$

The transient current described by Equation 2.49 comprises two exponential components corresponding to fast and slow relaxation processes governed by α_1 and α_2. Figure 2.7 shows a representative waveform of the pickup coil's transient response to square-wave excitation.

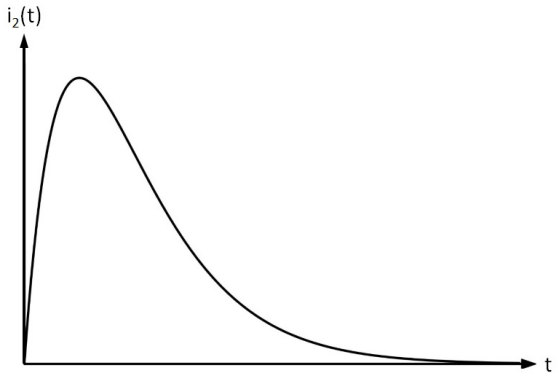

Figure 2.7: Representative pickup-coil transient current response following square-wave excitation.

When a conductive specimen is introduced near the probe, it acts as a third coupled circuit, modifying both the self- and mutual inductance parameters. This interaction is illustrated in Figure 2.8. Desjardins *et al.* [83] provided analytical solutions for simple cylindrical geometries, demonstrating how such coupling affects the system response.

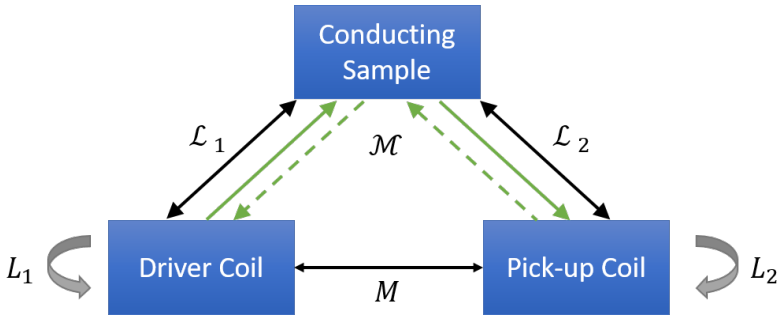

Figure 2.8: Mutual inductance relationships among the driving coil, pickup coil, and conductive specimen. L_1 and L_2 represent the intrinsic self-inductances; M is the mutual inductance coefficient; $\mathcal{L}_1$ and $\mathcal{L}_2$ are the complex-valued self-inductances due to electromagnetic coupling between elements; and $\mathcal{M}$ is the complex-valued mutual inductance modified by the specimen.

The quantities $\mathcal{L}_1$, $\mathcal{L}_2$, and $\mathcal{M}$ depend on the geometry and material properties of the test sample and the probe. Specifically, $\mathcal{L}_1$ and $\mathcal{L}_2$ represent the modified self-inductances of the driver and pickup coils, respectively, while $\mathcal{M}$ accounts for the additional mutual coupling introduced by the specimen. These complex inductance terms are central to the analytical and numerical models presented in subsequent chapters.

2.5 Analysis of Pulsed Eddy Current Signals

Signal processing plays a pivotal role in PEC inspections, as factors such as the probe–defect distance introduce time shifts in the PEC response [84]. A common approach in PEC analysis involves extracting differential signals by subtracting a reference signal—typically obtained from a defect-free sample—from the measured response. Various signal-processing techniques, including time-domain, frequency-domain, and time–frequency analysis, are employed to extract meaningful defect characteristics [85].

In time-domain analysis of differential pickup signals (Figure 2.9), key parameters such as peak amplitude, peak arrival time, time to zero-crossing, secondary peak amplitude, and secondary peak arrival time are frequently used. These features provide critical information regarding defect size and depth within the inspected material [83]. However, many time-domain features are sensitive to probe lift-off; in some cases, a LOI can be identified where responses acquired at different lift-off distances intersect, providing a degree of lift-off invariance for defect characterization [60], [62]. Conversely, frequency-domain analysis leverages the skin effect, wherein higher-frequency components exhibit greater sensitivity to surface defects, while lower-frequency components penetrate deeper into the material, facilitating the detection of subsurface anomalies [86].

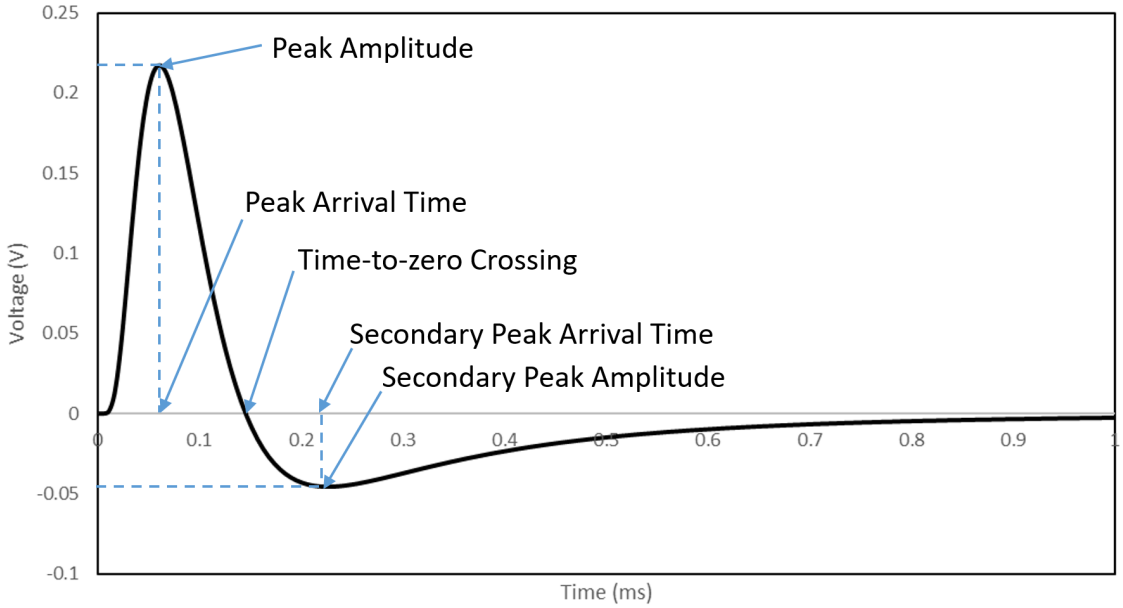

Figure 2.9: Typical PEC time-domain response for a differential pickup configuration.

Additionally, PEC excitation signals are inherently periodic, making them well-suited for spectral decomposition. Fourier transform techniques enable the extraction of frequency components associated with different defect depths, enhancing inspection capabilities beyond conventional ET. However, electromagnetic feedback can alter the excitation waveform and frequency spectrum, influencing signal interpretation [31].

Mathematically, a periodic PEC excitation can be expressed as a Fourier series—that is, a sum of sinusoidal components with varying frequencies and amplitudes. Beyond time- and frequency-domain approaches, time–frequency analysis provides a three-dimensional representation of signal behaviour in the time–frequency–amplitude domain. Although typically visualized as a two-dimensional time–frequency plot with amplitude variations indicated via grayscale intensity, this method enhances defect characterization by revealing transient features that may be overlooked in conventional analyses [87].

2.6 Integral Transforms

Integral transforms are a powerful analytical tool for addressing PDEs, such as the diffusion equation, particularly in geometries that incorporate planar and tubular structures with infinite domains and parallel interfaces. This section examines four principal transforms: the Fourier transform, the Laplace transform, the Fourier cosine transform, and the first-order Hankel transform. These transforms are adeptly matched to specific boundary conditions and symmetries, facilitating the simplification and solution of PDEs encountered in PEC modelling.

The Fourier transform [88], in its non-unitary angular-frequency form, is defined as:

$$X(\omega) = \mathcal{F}\{x(t)\} = \int_{-\infty}^{\infty} x(t) e^{-\mathrm{j}\omega t} \mathrm{d}t, \tag{2.52}$$

where $X(\omega)$ represents the frequency-domain counterpart of the time-domain function $x(t)$. The corresponding inverse Fourier transform is given by [88]:

$$x(t) = \mathcal{F}^{-1}\{X(\omega)\} = \frac{1}{2\pi} \int_{-\infty}^{\infty} X(\omega) e^{\mathrm{j}\omega t} \mathrm{d}\omega. \tag{2.53}$$

Table 2.1 summarizes several Fourier transform pairs relevant to the analytical formulations developed in this work.

Table 2.1: Fourier transform pairs.

Function	**Fourier transform**	**Notes**
$\frac{\mathrm{d}^k x(t)}{\mathrm{d}t^k}$	$(\mathrm{j}\omega)^k X(\omega)$	Differentiation property (integer $k \geq 1$)
$x(t) * g(t)$	$X(\omega)G(\omega)$	Convolution ($*$)
$u(t)$	$\frac{1}{\mathrm{j}\omega} + \pi\delta(\omega)$	Heaviside step function ($u(t) = 0$ for $t < 0$)
$\delta(t)$	1	Dirac delta (impulse)
1	$2\pi\delta(\omega)$	Constant (DC component)
$\sin(\varpi t)$	$-\mathrm{j}\pi[\delta(\omega - \varpi) - \delta(\omega + \varpi)]$	Harmonic at angular frequency ϖ
$\cos(\varpi t)$	$\pi[\delta(\omega - \varpi) + \delta(\omega + \varpi)]$	Harmonic at angular frequency ϖ

The Laplace transform [88], in its unilateral form, is defined as:

$$X(s) = \mathcal{L}\{x(t)\} = \int_{0}^{\infty} x(t) e^{-st} \mathrm{d}t, \tag{2.54}$$

where $X(s)$ represents the Laplace-domain counterpart of the time-domain function $x(t)$, defined for all real numbers $t \geq 0$, and $s = \sigma + \mathrm{j}\omega$ is the complex frequency-domain parameter, with real numbers σ and ω.

The Fourier cosine transform [88] is particularly useful for problems exhibiting symmetry about the origin. It is defined as:

$$X(k_z) = \int_{0}^{\infty} x(z) \cos(k_z z) \mathrm{d}z, \tag{2.55}$$

where $X(k_z)$ is the spatial-frequency representation of $x(z)$. The corresponding inverse Fourier cosine transform is expressed as [88]:

$$x(z) = \frac{1}{\pi} \int_{0}^{\infty} X(k_z) \cos(k_z z) \mathrm{d}k_z. \tag{2.56}$$

Table 2.2 lists several Fourier cosine transform pairs that are applicable to this work.

Table 2.2: Fourier cosine transform pairs.

Function	Fourier cosine transform (angular frequency)
$\dfrac{\mathrm{d}^2 x(z)}{\mathrm{d}z^2}$	$-k_z^2 X(k_z)$
$\delta(z)$	1
$\delta(z-h)$	$\cos(k_z h)$

For problems involving axial symmetry, the first-order Hankel transform [89] is particularly effective. The forward Hankel transform is defined as:

$$X(k_r) = \int_0^\infty r J_1(k_r r)\, x(r) \mathrm{d}r, \tag{2.57}$$

where $J_1(k_r r)$ is the first-order Bessel function of the first kind [90], and $X(k_r)$ is the first-order Hankel transform of $x(r)$. The corresponding inverse transform is given by [89]:

$$x(r) = \int_0^\infty k_r J_1(k_r r)\, X(k_r) \mathrm{d}k_r. \tag{2.58}$$

Table 2.3 summarizes several first-order Hankel transform pairs relevant to the analysis of axisymmetric eddy current problems.

Table 2.3: First-order Hankel transform pairs.

Function	First-order Hankel transform
$\dfrac{\mathrm{d}^2 x(r)}{\mathrm{d}r^2} + \dfrac{1}{r}\dfrac{\mathrm{d}x(r)}{\mathrm{d}r} - \dfrac{x(r)}{r^2}$	$-k_r^2 X(k_r)$
$\delta(r-a)$	$J_1(k_r a)$

These integral transforms provide a rigorous framework for solving eddy current BVPs in infinite domains with parallel interfaces. They are applicable to rods, boreholes, tubes, plates, half-spaces, and multilayered structures and are fundamental to the analytical modelling methods developed in subsequent sections.

2.7 Fourier Series

The Fourier series [88] is a powerful tool in harmonic analysis that enables the decomposition of a periodic function into an infinite sum of sine and cosine terms. This method leverages the orthogonality of trigonometric functions, making it particularly effective for representing periodic phenomena. For a periodic function $f(t)$ with a period of $2T_0$ (where T_0 represents half the period), the Fourier series expansion over the interval $[0, 2T_0]$ can be expressed as:

$$f(t) = \frac{a_0}{2} + \sum_{k=1}^{\infty} \left[a_k \cos\left(\frac{k\pi t}{T_0}\right) + b_k \sin\left(\frac{k\pi t}{T_0}\right) \right], \tag{2.59}$$

where a_k and b_k are the Fourier coefficients that quantify the contribution of each harmonic frequency. These coefficients are defined as:

$$a_0 = \frac{1}{T_0} \int_0^{2T_0} f(t)\, dt, \tag{2.60}$$

$$a_k = \frac{1}{T_0} \int_0^{2T_0} f(t) \cos\left(\frac{k\pi t}{T_0}\right)\, dt, \tag{2.61}$$

$$b_k = \frac{1}{T_0} \int_0^{2T_0} f(t) \sin\left(\frac{k\pi t}{T_0}\right)\, dt. \tag{2.62}$$

In this formulation, a_0 denotes the average or Direct Current (DC) component of the function, while a_k and b_k capture the amplitudes of the cosine and sine components associated with higher harmonics. The sine and cosine terms represent harmonic components of the fundamental frequency. This decomposition is particularly valuable in signal processing, communications, and vibration analysis, where periodicity is a fundamental characteristic.

The Fourier series converges pointwise to $f(t)$ at all points where $f(t)$ is continuous. At jump discontinuities, it converges to the midpoint of the discontinuity, a property known as the Dirichlet condition [91]. However, near discontinuities, the Fourier series exhibits oscillatory behaviour known as the Gibbs phenomenon [88]. This results in an overshoot near the discontinuity that does not diminish in amplitude as additional harmonic terms are included, although the oscillations become increasingly localized. In the context of square-wave excitation used in PEC systems, this may introduce minor ringing near sharp transitions in the reconstructed time-domain signal. Moreover, the convergence behaviour and decay rate of the Fourier coefficients provide insights into the smoothness and regularity of the original function.

For example, the Fourier series representation of a square wave with a $50\,\%$ duty cycle, amplitude v_0, and pulse duration T_0 can be expressed as:

$$v(t) = \frac{v_0}{2} + \frac{2v_0}{T_0} \sum_{k=1}^{\infty} \frac{\sin(\varpi_k t)}{\varpi_k}, \tag{2.63}$$

where $\varpi_k = \frac{(2k-1)\pi}{T_0}$.

The Fourier transform of Equation 2.63, using the transform pairs summarized in Table 2.1, is given by:

$$v(\omega) = \pi v_0 \delta(\omega) - \frac{2\pi v_0}{T_0} \sum_{k=1}^{\infty} \frac{\delta(\omega - \varpi_k) - \delta(\omega + \varpi_k)}{\mathrm{j}\varpi_k}, \tag{2.64}$$

which will be used in subsequent analytical formulations in this work.

2.8 Convolution

Convolution theory [88] provides a comprehensive framework for analyzing transient eddy current phenomena and plays a pivotal role in the problems addressed in this work. Combined with KVL, convolution enables precise modelling of feedback effects between conducting or ferromagnetic test objects and the driving and pickup coils in electromagnetic systems.

The impulse response of a system, denoted by $h(t)$, characterizes the system's output in response to a unit impulse applied at time $t = 0$. In causal systems, where the output cannot precede the input, the impulse response satisfies $h(t) = 0$ for $t < 0$. If an impulse is introduced at $t = \tau$, the system responds with a delayed output of $h(t - \tau)$.

Consider an arbitrary continuous input signal, $x(t)$, which can be decomposed into a series of infinitesimal rectangular pulses of width $d\tau$. Each pulse may be approximated by the Dirac delta function. For a pulse centered at $t = \tau$, the magnitude is $x(\tau)d\tau$, and the system's response to this pulse is $x(\tau)d\tau h(t - \tau)$. The total system response, as the summation of individual responses to all such pulses, can be expressed as:

$$y(t) = \sum x(\tau)d\tau h(t - \tau). \tag{2.65}$$

By taking the limit as the pulse width approaches zero, the summation transitions into an integral, yielding the continuous-time convolution integral:

$$y(t) = x(t) * h(t) = h(t) * x(t) = \int_{-\infty}^{\infty} x(\tau)h(t - \tau)\, d\tau. \tag{2.66}$$

For causal systems, where $x(t)$ and $h(t)$ vanish for $t < 0$, the limits of integration reduce to

$$y(t) = \int_0^t x(\tau)h(t - \tau)\, d\tau = \int_0^t h(\tau)x(t - \tau)\, d\tau, \tag{2.67}$$

since $h(t - \tau) = 0$ for $\tau > t$.

A key property of convolution is its relationship to the Fourier transform. Specifically, the Fourier transform of a convolution equals the product of the Fourier transforms of the individual functions. This property, critical for analyzing Linear Time-Invariant (LTI) systems, simplifies analysis by converting convolution in the time domain into multiplication in the frequency domain:

$$\int_{-\infty}^{\infty} (x(t) * h(t))e^{\mathrm{j}\omega t}\, dt = H(\omega)X(\omega), \tag{2.68}$$

where $H(\omega)$ and $X(\omega)$ are the Fourier transforms of the impulse response $h(t)$ and the input $x(t)$, respectively. This relationship simplifies the spectral analysis of system responses, enabling efficient evaluation of feedback effects in electromagnetic systems, as demonstrated by Desjardins *et al.* [14].

2.9 Principal Component Analysis

PCA is a powerful statistical technique used to uncover meaningful patterns in high-dimensional datasets that might otherwise be obscured by noise or redundancy [92]. Its strength lies in reducing the dimensionality of multivariate data, while preserving directions of maximum variance [93]. In PEC signal analysis, where detecting subtle variations across hundreds of data points is challenging, PCA provides a means to distill the data into a small number of principal components, facilitating more effective differentiation of underlying patterns.

By leveraging the assumption that neighbouring data points exhibit high correlation, PCA isolates variations associated with key parameters, such as defects or structural inconsistencies within the inspected material [94]. In aerospace structures, however, signal variations in PEC measurements may also arise from factors intrinsic to the technique's sensitivity, including variations in conductor or wing-skin thickness, fastener spacing, proximity to lap-joint edges, lift-off, and probe misalignment over fastener heads.

Transforming transient response signals into a space defined by principal components enables PCA to represent dominant sources of signal variance in orthogonal directions, which may correspond to defects or other physical parameters, while reducing the influence of confounding factors such as lift-off or misalignment [92]. This transformation enhances flaw detection accuracy by filtering out irrelevant signal artefacts, ultimately providing a robust and reliable method for defect characterization in complex aerospace geometries [46].

2.9.1 MPCA

The MPCA method differs from conventional PCA in that it does not subtract the average response before processing the data [92]. It can be shown that MPCA is equivalent to minimizing the Residual Sum of Squares (RSS) between the fitting functions and the original data [69], [93]. The objective of MPCA is therefore to determine an optimal set of basis vectors that best represents a given dataset by minimizing the RSS. From a linear algebra perspective, both PCA and MPCA may be formulated using the Singular Value Decomposition (SVD), with conventional PCA applying SVD to mean-centered data and MPCA applying SVD directly to the uncentered data matrix.

Consider a series of p signal measurements, denoted as $\mathbf{T}_i$, where each measurement consists of n data points. Here, n represents the number of data points in a single measurement, and p denotes the total number of measurements. The resulting data matrix $\mathbf{T}$ is thus of size $n \times p$ [94]. The goal is to find a column vector $\mathbf{v}$ that optimally represents $\mathbf{T}$ by minimizing the residual sum of squares, as formulated for mean-centered principal component analysis in the context of pulsed eddy current signal processing by Horan *et al.* [9], [10]. Each column vector $\mathbf{T}_i$ can be expressed as:

$$\mathbf{T}_i \approx c_i \mathbf{v}, \tag{2.69}$$

where $\mathbf{v}$ is determined by minimizing the RSS, defined as:

$$\text{RSS} = \sum_{i=1}^{n}\sum_{j=1}^{p}(T_{ij} - c_j v_i)^2. \tag{2.70}$$

Expanding Equation 2.70 yields:

$$\text{RSS} = \sum_{i=1}^{n}\sum_{j=1}^{p} T_{ij}^2 - 2\sum_{i=1}^{n}\sum_{j=1}^{p} T_{ij} c_j v_i + \sum_{i=1}^{n}\sum_{j=1}^{p} c_j^2 v_i^2. \tag{2.71}$$

Here, T_{ij} denotes the i^{th} element of the j^{th} column vector $\mathbf{T}_j$, and v_i is the i^{th} element of $\mathbf{v}$. To ensure a unique solution, $\mathbf{v}$ is constrained to be normalized such that [92]:

$$\sum_{i=1}^{n} v_i^2 = 1. \tag{2.72}$$

Without this constraint, if $\mathbf{v}$ is a solution, then $a\mathbf{v}$, where a is any scalar, would also be a solution, resulting in an infinite number of equivalent solutions.

The coefficient c_i in Equation 2.69 can be obtained as the dot product:

$$c_j = \sum_{i=1}^{n} T_{ij} v_i, \tag{2.73}$$

which can be rewritten in matrix notation as:

$$\mathbf{c} = \mathbf{T}^\mathsf{T}\mathbf{v}. \tag{2.74}$$

Using the normalization condition (Equation 2.72) and substituting Equation 2.73 into Equation 2.71, the RSS reduces to:

$$\text{RSS} = \sum_{i=1}^{n}\sum_{j=1}^{p} T_{ij}^2 - \sum_{j=1}^{p} c_j^2. \tag{2.75}$$

Thus, minimizing the RSS is equivalent to maximizing:

$$\sum_{j=1}^{p} c_j^2 = \mathbf{c}^\mathsf{T}\mathbf{c} = \mathbf{v}^\mathsf{T}\mathbf{T}\mathbf{T}^\mathsf{T}\mathbf{v}, \tag{2.76}$$

subject to the constraint:

$$\mathbf{v}^\mathsf{T}\mathbf{v} = 1. \tag{2.77}$$

This optimization problem can be solved using the method of Lagrange multipliers, which leads directly to an eigenvalue problem. The Lagrangian function is defined as:

$$\mathscr{L} = \mathbf{v}^\mathsf{T}\mathbf{T}\mathbf{T}^\mathsf{T}\mathbf{v} - \lambda(\mathbf{v}^\mathsf{T}\mathbf{v} - 1), \tag{2.78}$$

with λ being the Lagrange multiplier. Taking the derivative with respect to $\mathbf{v}$ and setting it equal to zero gives:

$$\frac{\partial L}{\partial \mathbf{v}} = 2\mathbf{T}\mathbf{T}^{\mathsf{T}}\mathbf{v} - 2\lambda\mathbf{v} = 0, \tag{2.79}$$

which can be rearranged to yield:

$$\mathbf{T}\mathbf{T}^{\mathsf{T}}\mathbf{v} = \lambda\mathbf{v}, \tag{2.80}$$

which is the standard eigenvalue problem.

This result shows that the optimal vector $\mathbf{v}$ corresponds to an eigenvector of $\mathbf{T}\mathbf{T}^{\mathsf{T}}$, with the best single representation given by the eigenvector associated with the largest eigenvalue. The eigenvector with the second-largest eigenvalue best represents the residual variance in $\mathbf{T}$ after the first eigenvector is removed. The deflation process forms a new dataset $\mathbf{T}'$ by subtracting the first principal component [92]:

$$\mathbf{T}' = \mathbf{T} - \mathbf{v}\mathbf{c}^{\mathsf{T}}. \tag{2.81}$$

This process is repeated for successive eigenvectors. The first m eigenvectors thus form an optimal basis that best represents $\mathbf{T}$ in the least-squares sense [94]. Since the sum of eigenvalues represents the total variance in the dataset, the extra sum of squares method—commonly used in multiple regression—can determine the number of significant eigenvectors required to capture meaningful signal content over random noise [69], [94]. In practice, three to four eigenvectors are typically sufficient to achieve an accurate representation of the original data.

In conventional PCA, the average signal is subtracted before constructing the covariance matrix $\mathbf{A}$, which is then scaled by $(n-1)^{-1}$ [92]. The eigenvalues of this covariance matrix quantify the variance explained by each eigenvector.

2.9.2 Calibration Eigenvectors

The MPCA method was applied to analyze PEC signals obtained from various fasteners, both with and without notches at their bores, under controlled laboratory conditions. The collected data were compiled into a larger matrix, $\mathbf{A}$, as defined in Equation 2.80, and its corresponding eigenvectors, $\mathbf{v}$, were computed. These calibration eigenvectors were subsequently utilized in Equation 2.74, where a dot product operation was performed to generate principal component scores during inspection. The resulting scores were then analyzed and compared to facilitate flaw discrimination.

With regard to this work, the lower CF-188 and F-35 inner wing spars contain multiple types of ferrous–nonferrous fasteners, as discussed in Chapter 3. To ensure robust calibration, eigenvectors must be derived from a sufficiently large dataset that captures variations in fastener type, size, and length, while also accounting for different measurement conditions. This approach ensures that the calibration eigenvectors generalize effectively across inspection scenarios, thereby improving defect detection accuracy.

2.9.3 Principal Component Scoring

The set of coefficients c_j obtained in Equation 2.73 for a given signal represents its principal component scores. These coefficients weight their associated uncorrelated eigenvectors in a linear combination that reconstructs the original signal [95], serving as unique descriptors that capture progressively smaller proportions of the total variance. The goal of this process is to reduce the dataset's dimensionality by analyzing only the first m principal components (typically two or three) rather than hundreds of gated voltage samples. This dimensionality reduction enables the identification of variations attributable to independent parameters, such as the presence of a crack in a wing spar, as demonstrated by Horan *et al.* [9], [10].

Figure 2.10 illustrates this process, where a scatter plot in PCA space—constructed using the second and third principal components (Z_2 and Z_3)—demonstrates clustering behaviour in the principal component domain. These clusters differentiate fastener locations containing borehole notches or simulated cracks from those without defects.

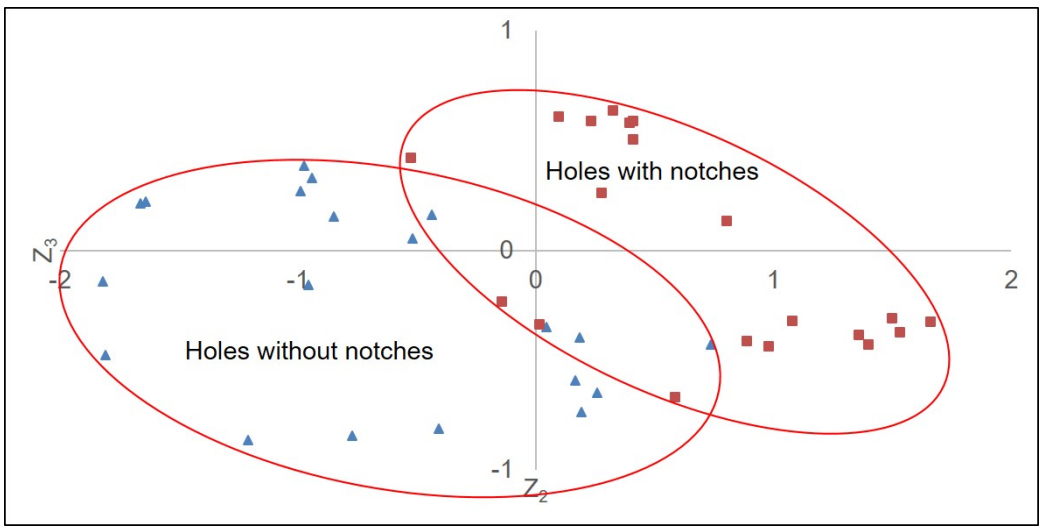

Figure 2.10: Sample PCA score scatter plot illustrating notch or simulated crack identification through cluster separation in principal component space. The axes represent the second and third principal component scores, Z_2 and Z_2, respectively.

Visual representations, such as Figure 2.10, provide an intuitive means of identifying defects by the degree of separation between score clusters. However, distinct separation may not always occur, as overlapping clusters can hinder confident notch or simulated crack identification. To address this limitation, a quantitative method is required to evaluate the separation between PCA score groupings relative to a known calibration dataset. This evaluation is performed using discriminant analysis, as described in Section 2.10.

2.10 Discriminant Analysis Method

Discriminant analysis is a statistical technique that quantifies the maximum separation, or discrimination, between predefined groups using known information about independent variables [69]. It is widely used to reduce complex multivariate datasets into a single discriminant dimension that best distinguishes between classes.

In the context of PEC analysis for CF-188 and F-35 inner wing spar inspections, a notch in a specimen represents a controlled parameter and therefore serves as the dependent variable. In contrast, the PEC signal and its corresponding principal component scores are independent variables. This known notch information is incorporated into the discriminant analysis process to map each signal's position within multi-dimensional PCA space, as shown in Figure 2.11, onto a single discriminant score determined solely by the presence or absence of a notch. This process is analogous to a two-group multiple linear regression [69].

This approach is advantageous when the grouping of PCA scores exhibits overlap in any projection, or when no single principal component reliably differentiates notches. For example, as illustrated in Figure 2.10, although there is an overall separation between scores corresponding to notched and unnotched fasteners, neither principal component (Z_2 or Z_3) alone provides reliable discrimination between the two groups.

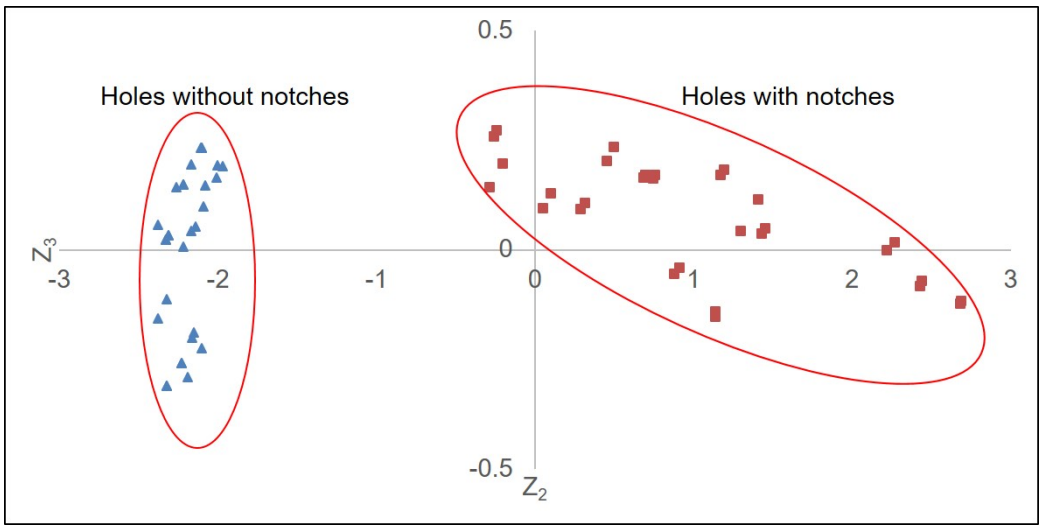

Figure 2.11: Representative PCA score scatter plot illustrating group overlap between notched and unnotched fastener signals. The axes represent the second and third principal component scores, Z_2 and Z_2, respectively.

2.10.1 Multiple Linear Regression Model

Fisher's [96] approach to discriminant analysis employs a linear combination of independent variables that maximizes separation between groups, producing a discriminant score [69]. When there

are only two groups to classify—such as distinguishing between fasteners with or without simulated cracks or notches—this method is mathematically equivalent to multiple linear regression when the response variable is coded as a binary indicator. In this case, the model assumes a linear relationship of the form [69]:

$$y_i = b_0 + \sum_{k=1}^{m} b_k x_{ik}, \tag{2.82}$$

where y_i represents the discriminant score for a given signal, $[x_{i1}, x_{i2}, x_{i3}, \ldots, x_{im}]$ are the m principal component scores describing the signal, and $[b_0, b_1, b_2, \ldots, b_m]$ are the best-fit regression coefficients. During model calibration, the presence of a notch or simulated crack serves as the dependent variable, assigned a binary value of one for a notched or simulated crack fastener and zero otherwise.

This transformation effectively linearly projects the multi-dimensional PCA space—illustrated in Figure 2.11—such that an initial projection, where no clear separation between groups is visible, becomes a transformed projection, where two distinct clusters emerge, corresponding to fastener locations with and without defects. Figure 2.12 illustrates this effect: in Figure 2.12(a), a scatter plot of the first three principal components shows overlap between the two groups, whereas in Figure 2.12(b), after applying discriminant analysis, two well-defined clusters are visible.

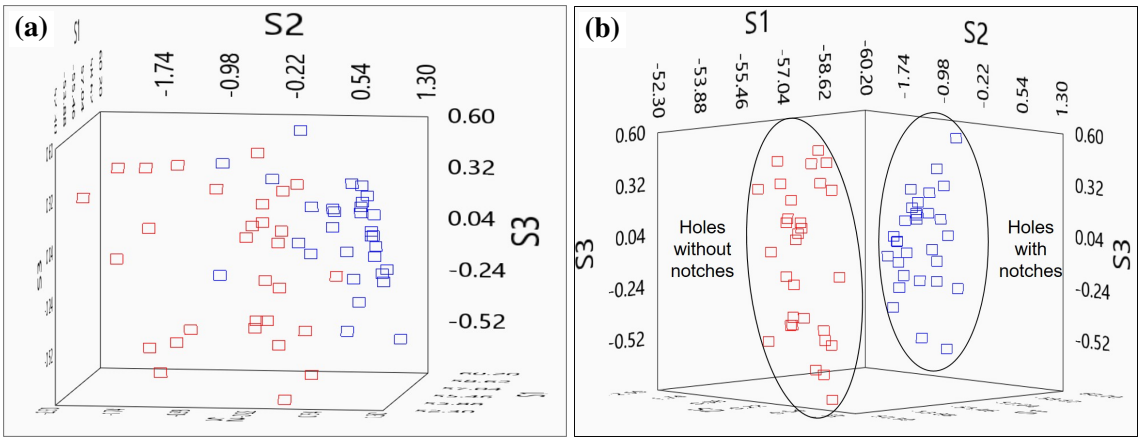

Figure 2.12: PCA scatter plots showing (a) no distinct separation between groups and (b) the effect of multiple linear regression in two-group discriminant analysis, revealing clear class separation.

Following this projection, each signal is assigned a discriminant score, wherein discriminant scores for simulated crack fastener locations cluster near one, and those for intact locations cluster near zero. This behaviour is illustrated in Figure 2.13, where discriminant scores from multiple fastener inspections exhibit a clear binary distribution. The best-fit coefficients from Equation 2.82 can then be stored and subsequently applied during real-time discriminant analysis for future PCA-based inspections.

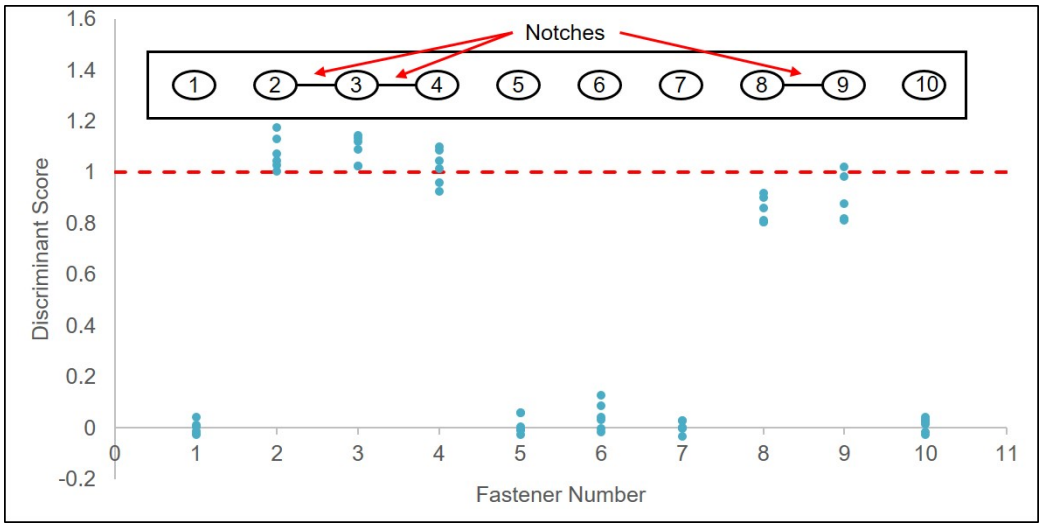

Figure 2.13: Example of discriminant analysis results showing discriminant score distribution of fastener locations with and without simulated cracks.

2.10.2 Confidence Intervals

Analysis of Figure 2.13 shows that a discriminant score decision threshold, $\hat{D}_{\text{decision}}$, can be established based on the relative spread of scores for unnotched fasteners. Any score below this threshold can be reasonably assumed to indicate the absence of a crack. This threshold, effectively a confidence interval, is determined by the distribution and position of the scores for unnotched fasteners. In this inspection scenario, it is preferable to have false positives (i.e., false calls—incorrectly classifying undamaged fasteners as notched) rather than false negatives (misses—incorrectly classifying notched fasteners as undamaged), as the latter could allow defects to go undetected. Chapter 9 discusses potential remedial steps for false calls. False calls are defined as NDE system responses that indicate a flaw when none is present at the inspection location [97].

The confidence interval for a given fastener is calculated based on the measured standard deviation, S, and the sample size of measurements from unnotched fasteners. When the true standard deviation, σ, of a dataset is unknown and the sample size is relatively small (typically fewer than 50), the t-distribution provides a reasonable approximation for confidence interval estimation [98]. The confidence interval is determined using the following equation [98]:

$$\hat{D}_{\text{decision}} = \bar{X} + kS \tag{2.83}$$

where $\bar{X}$ is the expected mean of the discriminant scores for unnotched fasteners (assumed to be zero based on the regression process), S represents the standard deviation of those scores about the mean, k is the critical value from the t-distribution corresponding to the desired confidence level, and n denotes the sample size (or degrees of freedom). Confidence intervals are presented at both $95\,\%$ and $99\,\%$ levels, as illustrated in Figure 2.14.

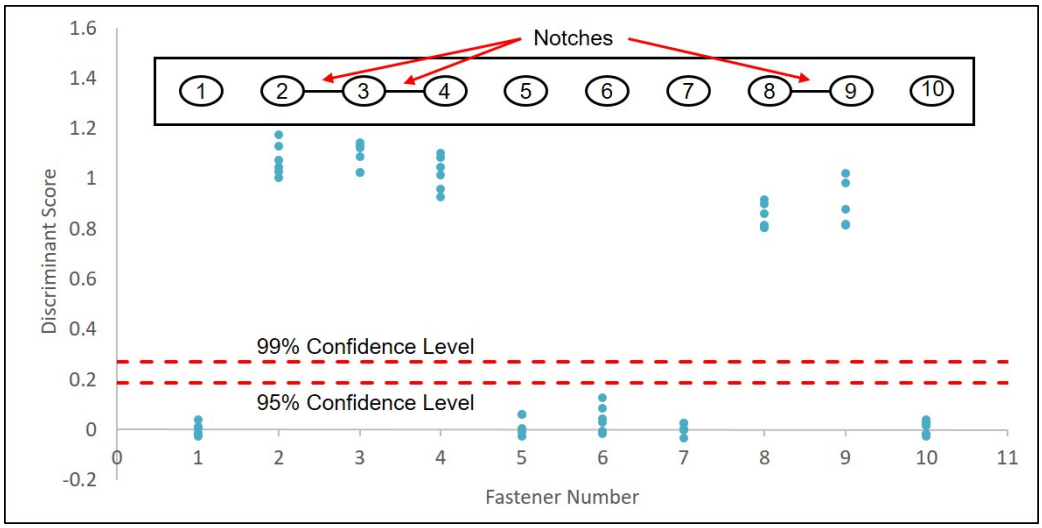

Figure 2.14: Example of discriminant analysis for fastener locations with and without simulated cracks, showing $95\,\%$ and $99\,\%$ confidence levels.

These confidence intervals represent the frequency with which the discriminant score of an unnotched fastener location will fall within the interval, rather than the probability that an inspector will detect a given flaw. The intervals derived in this study adhere to, or exceed, the guidelines established in United States Air Force (USAF) MIL-HDBK-1823 [97] for NDE POD studies. MIL-HDBK-1823 defines the $a_{90/95}$ parameter, representing the minimum detectable flaw size corresponding to a $90\,\%$ POD with a $95\,\%$ confidence interval, based on extensive testing by multiple inspectors [97].

Although a full POD study is beyond the scope of this thesis, the confidence intervals presented here are designed to align with these threshold guidelines. In POD studies, confidence intervals—based on the Wald and Delta methods [97]—typically assume a normal distribution of detectable flaw sizes due to large datasets. However, since the sample sizes in this study are smaller, the assumption that discriminant score variance follows a t-distribution is both reasonable and conservative. This approach increases sensitivity to cracks, as the t-distribution accounts for greater variability in its tails than a normal distribution, thereby improving defect detection [98].

3 Experimental Technique

3.1 Introduction

This chapter describes the experimental setup employed for data acquisition in this study. Two distinct PEC probe configurations were developed, each designed to meet a specific measurement objective. The first design is a vertically differential probe, developed primarily to achieve high sensitivity to lift-off variations. This configuration enables precise measurement of the lift-off distance between the probe and the sample surface, with the differential output accurately reflecting small variations in lift-off. Such probes are particularly well suited for acquiring raw time-domain responses suitable for detecting subsurface defects through non-conductive coatings. In this work, machined notches were introduced into representative test samples to simulate surface-breaking and subsurface cracks. These artificial cracks served as controlled flaw analogues for evaluating probe sensitivity and signal discrimination performance. Such capabilities would be especially valuable for inspecting aircraft such as the F-35, which incorporate RAM coatings and therefore require non-contact inspection methods.

Two versions of the vertically differential probe were fabricated, as shown schematically in Figure 3.1. The first incorporated ferrite cores in the pickup coils to enhance magnetic coupling and improve lift-off sensitivity during measurements over notched regions between fasteners. The second, an air-cored version, was developed to simplify comparison with analytical and numerical models by eliminating nonlinear magnetic effects introduced by ferrite materials. Both configurations share the same overall geometry, differing only in core material and magnetic coupling characteristics.

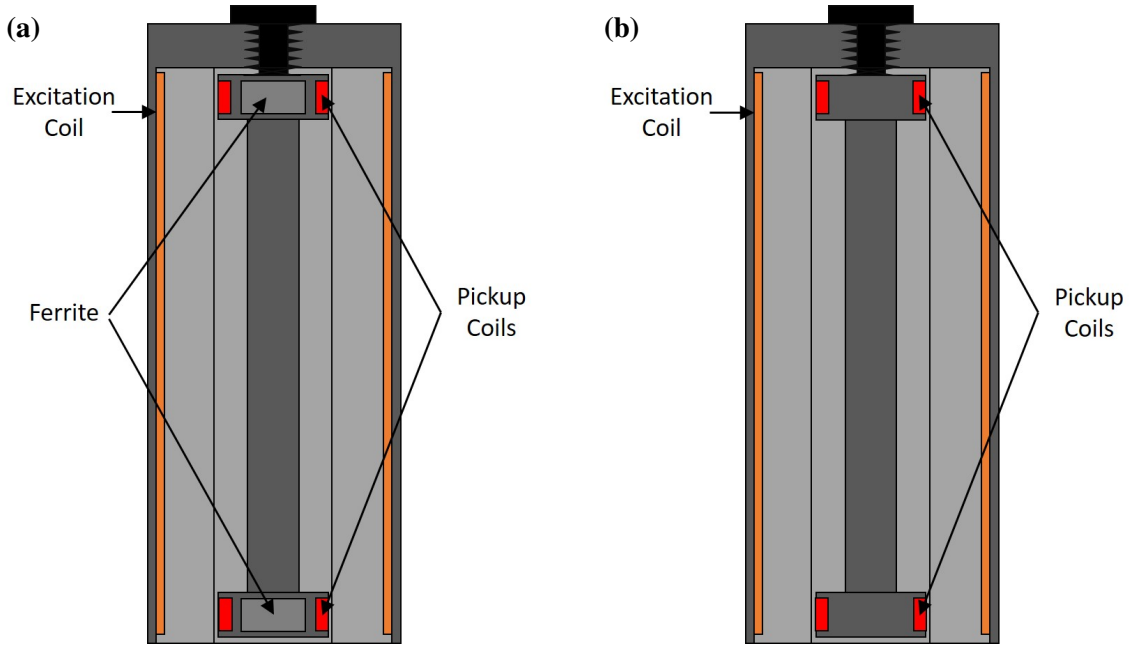

Figure 3.1: Cross-sectional schematics of vertically differential PEC probes: (a) ZEUS and (b) ARES.

The second probe design employs a pair of axisymmetric opposed pickup coils oriented such that their axes of sensitivity are normal to the surface of the aluminum spar and skin, as illustrated in Figure 3.2. This configuration is optimized to detect asymmetries in the eddy current field distribution caused by surface or subsurface notches that replicate crack-like behaviour. By comparing the differential responses of the opposed pickup coils, the system enhances sensitivity to localized defects. The PCA-based signal processing framework described in Section 2.9 is used to analyze the differential response, enabling detection of subtle variations indicative of structural anomalies. Two variations of this probe were also fabricated: one with the excitation coil wound around a ferrite core to enhance magnetic field concentration, and another with a solid plastic core to assess potential performance trade-offs. This design comparison aims to determine whether incorporating a ferrite core provides a measurable advantage in detecting simulated cracks represented by machined notches in the test specimens, as predicted in the literature [99], [100].

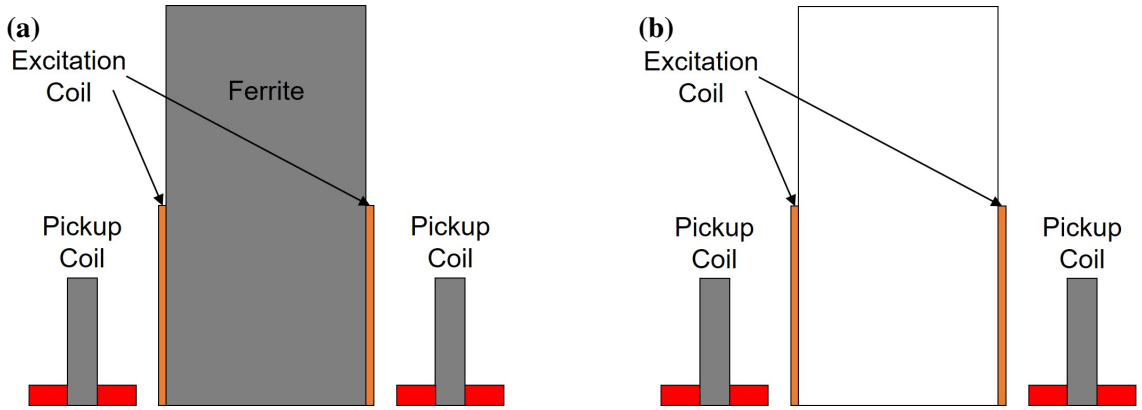

Figure 3.2: Cross-sectional schematics of the PEC probes: (a) THOR and (b) ODIN.

This section also describes the test samples and the Data Acquisition (DAQ) system used to control and record experimental measurements. The DAQ system triggers the excitation pulse to the driving coil and digitizes the voltage response from the pickup coils with high temporal resolution. The experimental setup also includes a programmable motion control platform for probe positioning, enabling precise alignment and repeatability during automated scans. Test specimens comprise simple metallic plates and fastener assemblies representative of aircraft structural components. Notably, each probe body was fabricated using high-resolution three-dimensional printing to ensure dimensional accuracy and reproducibility.

3.2 PEC Probe Design

3.2.1 ZEUS and ARES

The PEC probes ZEUS and ARES were engineered for precise measurement of the lift-off distance over metallic substrates. Each probe incorporates a primary excitation coil that generates transient electromagnetic fields through pulsed voltage excitation. These fields induce secondary electromagnetic responses within the test material, which are measured by vertically offset pickup coils. The differential signal between the pickup coils accurately reflects the lift-off distance [101].

Figure 3.1 presents cross-sectional schematics of (a) ZEUS and (b) ARES. In both probe designs, the excitation coil is wound around a central tube and secured by two end caps. The primary distinction between the two probes lies in the pickup coil core material: ZEUS incorporates ferrite cores within its pickup coils to enhance electromagnetic coupling, whereas ARES employs air-cored pickup coils. The inclusion of ferrite in ZEUS improves magnetic field concentration and signal amplitude but introduces nonlinear magnetic behaviour and increased boundary condition complexity, which complicate analytical modelling and FEM simulation. In contrast, the ARES probe's air-cored configuration simplifies the electromagnetic environment, providing an ideal ref-

erence for validating analytical and numerical models.

In the ZEUS probe, the pickup coils and ferrite cores are mounted along a central spindle that threads into the top cap. A plastic locking nut allows fine adjustment of the pickup coil position along the excitation axis. Although earlier vertically differential probe designs [102] employed more conservative geometries with larger excitation coil diameters and wider pickup coil separations, the geometrical parameters selected in this study were optimized for the specific fastener configurations under investigation—namely, the HLT53, HLT265, and HLT313 fasteners described in Section 3.3.1, with nominal shank diameters of $6.4\,\mathrm{mm}$ and $7.9\,\mathrm{mm}$.

The pickup coil diameter was selected to be comparable to or larger than the fastener head diameter, ensuring that the sensing region fully encompasses the fastener and promotes consistent magnetic coupling while reducing sensitivity to positional variation. This configuration enables the ferrite core within ZEUS to channel magnetic flux efficiently through the fastener to the underlying aluminum substrate, improving signal amplitude and sensitivity to lift-off variations. The resulting concentrated flux path enhances the detection of subsurface discontinuities, such as simulated crack notches beneath the coating layer.

The ARES probe adopts a similar mechanical design, with pickup coils mounted on a threaded spindle and secured using a plastic nut for precise axial positioning. All coils in both probes are wound with 36 American Wire Gauge (AWG) wire. Table 3.1 summarizes the electrical and geometrical specifications of the ZEUS and ARES probes. ZEUS was not modelled in COMSOL due to the inclusion of ferrite cores and the associated nonlinear magnetic behaviour; therefore, no simulated values are reported. For ARES, the pickup coil inductance is not provided, as it resulted in an unbounded (infinite) inductance value in the simulation.

Table 3.1: ZEUS and ARES PEC probe specifications.

Parameter	**ZEUS**		**ARES**	
	Driver	Pickup 1–2	Driver	Pickup 1–2
Number of turns	951	406	966	417
Length (mm)	76.2	6	76.2	6
Inner diameter (mm)	23.9	11.05	23.9	11.05
Outer diameter (mm)	24.41	14.48	24.41	14.48
Resistance (measured, Ω)	102	22.8 / 23.0	102	24.5 / 24.3
Resistance (COMSOL, Ω)	—	—	101.71	22.71
Self-inductance (measured, mH)	6.37	6.92	6.27	2.09
Self-inductance (COMSOL, mH)	—	—	6.02	—
Self-inductance (analytical, mH)	—	—	6.27	2.02

These vertically differential PEC probes enable accurate measurement of lift-off variations over non-conductive or low-conductive coatings and facilitate the detection of subsurface discontinuities

represented by simulated crack notches. Their performance is further analyzed in Chapter 6, where experimental measurements are compared against analytical and FEM simulations to evaluate lift-off sensitivity and signal consistency.

3.2.2 THOR and ODIN

The THOR and ODIN probes employ a distinct axisymmetric configuration consisting of a central driver coil and four pickup coils positioned at 90° intervals. Figure 3.2 shows cross-sectional schematics of (a) THOR and (b) ODIN. THOR includes a ferrite driver core, whereas ODIN employs a solid plastic core to evaluate the influence of ferrite on magnetic field distribution and overall probe performance. Both probes were designed to detect crack-like discontinuities represented by machined notches in test specimens, providing a controlled framework for comparing flaw sensitivity and magnetic coupling efficiency.

Figure 3.3 illustrates the probe faces used during experimental measurements. The driver coil is wound with 36 AWG wire around a $12.7\,\mathrm{mm}$ diameter core in both probes. The pickup coils are wound with 400 turns of 44 AWG wire around $1.9\,\mathrm{mm}$ ferrite cores. Each probe includes two differential pairs (180° opposing) and two single pickup channels for individual signal acquisition.

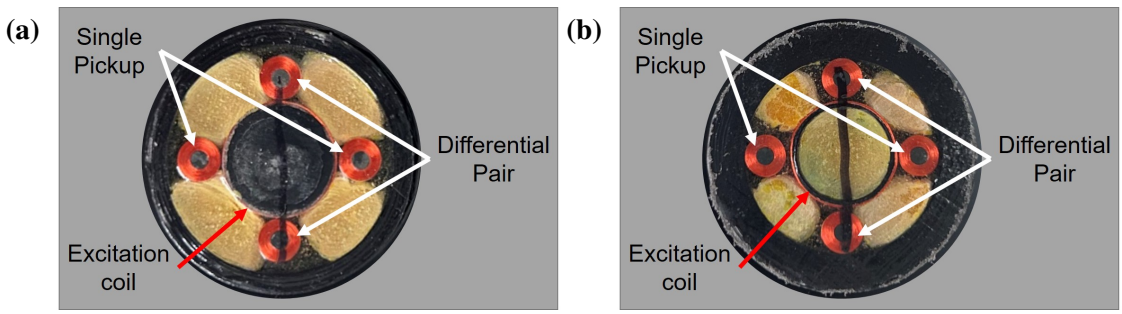

Figure 3.3: Probe faces of (a) THOR and (b) ODIN showing axisymmetric pickup coil configurations.

Table 3.2 summarizes the physical and electrical specifications of the THOR and ODIN probes, including measured and calculated self-inductance values for the driver, pickup, and differential coil configurations.

Table 3.2: THOR and ODIN PEC probe specifications and measured/calculated self-inductance values.

Parameter	THOR			ODIN		
	Driver	Pickup	Differential Pair	Driver	Pickup	Differential Pair
Number of turns	178.3	400	400	151.1	400	400
Wire gauge (AWG)	36	44	44	36	44	44
Length (mm)	12.7	1.2	1.2	12.7	1.2	1.2
Inner diameter (mm)	12.7	1.9	1.9	12.7	1.9	1.9
Outer diameter (mm)	13.21	4.9	4.9	13.21	4.9	4.9
Resistance (measured, Ω)	21.7	43.0, 42.2	83.1	11.2	42.1, 42.4	83.0
Self-inductance(measured, mH)	1.85	1.26	2.58	0.19	1.22	2.44
Self-inductance(calculated, mH)	0.26	—	—	0.19	—	—

3.3 Samples

This section describes the test specimens used in two distinct experimental investigations, each employing different sample types tailored to specific research objectives. The first set of samples was designed to emulate aerospace structures, specifically the CF-188 and F-35 inner wing spars. These specimens feature non-conductive skin materials with countersunk holes for HI-LOK™/HI-TIGUE™ fastener installation and incorporate notches machined into a piece of angle aluminum backing plate to simulate SCC within the wing spar. This sample set was used for fastener detection using conventional ET and notch detection between fasteners at various lift-off distances using PEC.

The second set consists of homogeneous metal plates representing aerospace-relevant materials with varying electrical conductivities and thicknesses. These specimens were used to provide controlled test conditions for benchmarking analytical models and validating FEM simulations across a range of electromagnetic diffusion regimes.

3.3.1 Fastener Samples for Fastener and Notch Detection Experiments

Fasteners

In the region of interest, three distinct HI-LOK™/HI-TIGUE™ fastener types [103] were evaluated: solid Stainless Steel (SS) fasteners (HLT53), hollow stainless steel fasteners (HLT265), and solid Titanium (Ti) fasteners (HLT313). The fasteners evaluated in this thesis, also used in the study by Horan *et al.* [9], [10], differ in basic part number, finish code, nominal diameter, and maximum grip length, as summarized in Table 3.3.

As an example, the part number HLT313TA10-13 can be broken down as follows: HLT313 indicates the basic part number; TA represents the finish code; the first dash number, 10, denotes the nominal diameter in $1/32$ $^{\mathrm{nd}}$ of an inch ($0.8\,\mathrm{mm}$); and the second dash number, 13, denotes

the maximum grip length in $1/16^{\text{th}}$ of an inch ($1.6\,\text{mm}$). Additional specifications, including finish codes and thread styles for each fastener, are provided in Appendix A.

Table 3.3: Fastener designations and properties.

Part Number	**Material**	**Style**	**Nominal Diameter** (mm**(in))**	**Maximum Grip Length** (mm**(in))**	**Sample Thickness** (mm)
HLT53DL8-10	SS	Solid	6.4 (1/4)	15.9 (5/8)	6.4
HLT53TB10-8	SS	Solid	7.9 (5/16)	12.7 (1/2)	6.4
HLT53YC10-13	SS	Solid	7.9 (5/16)	20.6 (13/16)	13.4
HLT265TB8-6	SS	Hollow	6.4 (1/4)	9.5 (3/8)	6.4
HLT265TB10-12	SS	Hollow	7.9 (5/16)	19.1 (3/4)	6.4
HLT265TB10-18	SS	Hollow	7.9 (5/16)	28.6 (9/8)	13.4
HLT313DL8-16	Ti	Solid	6.4 (1/4)	25.4 (1)	13.4
HLT313DL8-9	Ti	Solid	6.4 (1/4)	14.3 (9/16)	6.4
HLT313TA10-13	Ti	Solid	7.9 (5/16)	20.6 (13/16)	13.4

Skin Materials

Simple plastic materials were used to simulate the F-35 wing skin, although the actual material is likely CFRP, similar to the CF-188, with RAM. Of note, stacking multiple single-ply layers with varying fibre orientations is commonly employed to increase the overall thickness of CFRP. However, due to the insulating epoxy matrix and the highly anisotropic conductivity of individual plies, single-ply CFRP does not readily support closed-loop eddy current paths in the same manner as isotropic metallic materials. The thickness of the CFRP on the underside of the CF-188 inner wing varies depending on the location. According to the statement of requirements from the CF-188 third-line maintenance contractor for an NDT technique designed to detect SCC, the nominal skin thickness is specified as $12.7\,\text{mm}$; however, it can vary within the area of interest from 9 to $21\,\text{mm}$ [104].

In addition to the composite skin, RAM is applied to the outer surface of the F-35 structure. The exact composition of RAM is not publicly disclosed, and its electromagnetic properties are therefore uncertain. If the material is non-conductive and non-magnetic, its effect on the PEC response is expected to be minimal, acting primarily as an increase in effective lift-off. However, if RAM contains magnetically permeable or ferritic components, it may alter the local magnetic field distribution and transient diffusion behaviour, potentially enhancing magnetic coupling and increasing signal amplitude. As a result, RAM introduces uncertainty in the inspection response and must be considered in the interpretation of measured signals.

Sample Layout

Eight test standards were fabricated using $6.4\,\mathrm{mm}$ thick acrylic and $12.7\,\mathrm{mm}$ nylon to simulate different skin thicknesses. Each sample contained countersunk holes for fastener installation and included a $25.4\,\mathrm{mm} \times 25.4\,\mathrm{mm}$ piece of 6061-T6 angle aluminum backing plate to simulate the wing spar. Although the 6061-T6 aluminum alloy differs from the 7050-T73 aluminum alloy used in the CF-188 airframe [105], previous research by Horan *et al.* [9], [10] indicates that this distinction does not significantly influence the electromagnetic response within the frequency range investigated. The electrical properties of these aluminum alloys are summarized in Table 3.4, as reported in the *American Society for Metals (ASM) Specialty Handbook: Aluminum and Aluminum Alloys* [106].

Table 3.4: Electrical properties of aluminum alloys used in test specimens [106].

Alloy	**IACS** (%)	**Resistivity** ($\mu\Omega \cdot \mathrm{cm}$)	**Conductivity** ($\mathrm{S/m}$)
6061-T6	43.0	4.00	2.49×10^7
7050-T73	40.5	4.26	2.35×10^7

Longitudinal slits of $0.18\,\mathrm{mm}$ width and full penetration depth were machined into the aluminum backing plates to represent simulated SCC, as illustrated in Figure 3.4.

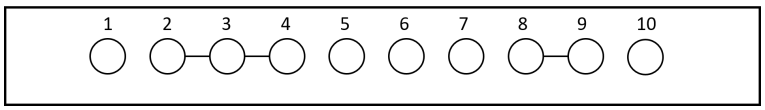

Figure 3.4: Schematic illustration of machined notch arrangement representing simulated SCC.

3.3.2 Samples for Pulsed Eddy Current Signal Modelling and Validation

A separate set of plates was used to validate the analytical PEC models and FEM simulations, ensuring the results were representative of aerospace-relevant materials. These samples included high-conductivity alloys such as aluminum 2024-T4 and 6061-T6, as well as copper, included as a high-conductivity reference material with well-established electromagnetic properties. In addition, lower-conductivity structural metals—commercially pure Titanium Grade 2 and the titanium alloy Ti-6Al-4V—were included to assess model performance under conditions of higher resistivity and, therefore, modified electromagnetic diffusion. The samples also vary in thickness and surface area to capture a broad range of electromagnetic behaviours. Resistivity measurements were performed using a four-point probe method to ensure accurate and repeatable characterization. Table 3.5 summarizes the measured physical and electrical properties of each specimen.

Table 3.5: Measured physical and electrical properties of test specimens.

Sample	**Material**	**Dimensions** (mm)	**Thickness**(mm)	**Conductivity** ($\mathrm{S/m}$)	**Resistivity** ($\mu\Omega \cdot \mathrm{cm}$)
1	2024-T4	197 × 201	5.30	1.67×10^7	5.99
2	2024-T4	200 × 200	2.87	1.67×10^7	5.99
3	6061-T6	164 × 330	9.55	2.55×10^7	3.92
4	6061-T6	148 × 297	3.12	2.55×10^7	3.92
5	Cu	612 × 445	3.30	5.88×10^7	1.72
6	Ti-2	307 × 305	4.06	2.10×10^6	47.7
7	Ti-6Al-4V	427 × 496	3.80	5.75×10^5	174

3.4 DAQ

Signal acquisition was conducted using dedicated hardware and software designed to ensure high-fidelity measurement of the probe responses. A custom-built amplifier circuit was used to condition and amplify the pickup coil signals immediately upon connection, improving the Signal-to-Noise Ratio (SNR) prior to digitization. The amplified signals were then digitized using a National Instruments (NI) USB-6361 data acquisition module operating at an effective sampling rate of $100\,\mathrm{kHz}$ per channel.

The same LabVIEW 2021 interface that controlled the probe positioning and motion platform also governed all acquisition parameters, including drive voltage, timing, and sampling rate. A $10\,\mathrm{V}$ step excitation was applied to the driver coil, while the pickup coils measured the transient voltage response induced by the resulting time-varying magnetic flux within the test specimen.

The digitized waveforms were routed through analog input channels, synchronized with motion-control signals, and automatically stored for subsequent post-processing and analysis. Figure 3.5 summarizes the complete signal acquisition and control workflow.

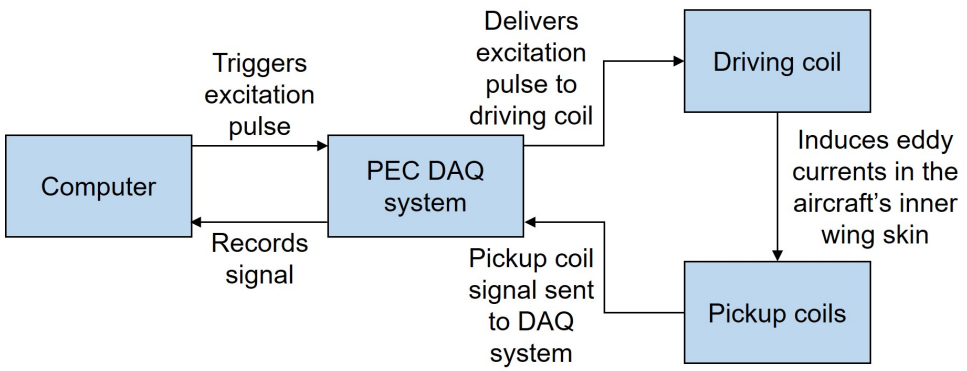

Figure 3.5: Flowchart illustrating the DAQ and control process used for automated PEC measurements.

3.5 Driver Operational Amplifier (Op-Amp) Circuit

To enhance the strength and fidelity of the driver signal—critical for accurate pulse reproduction and reliable MPCA performance—a PA75 dual power Op-Amp was implemented in a noninverting configuration, as shown in Figure 3.6 [11]. This configuration provides a wide bandwidth and high current output, making it well suited for driving low-impedance PEC excitation coils, while preserving signal fidelity in the early transient response.

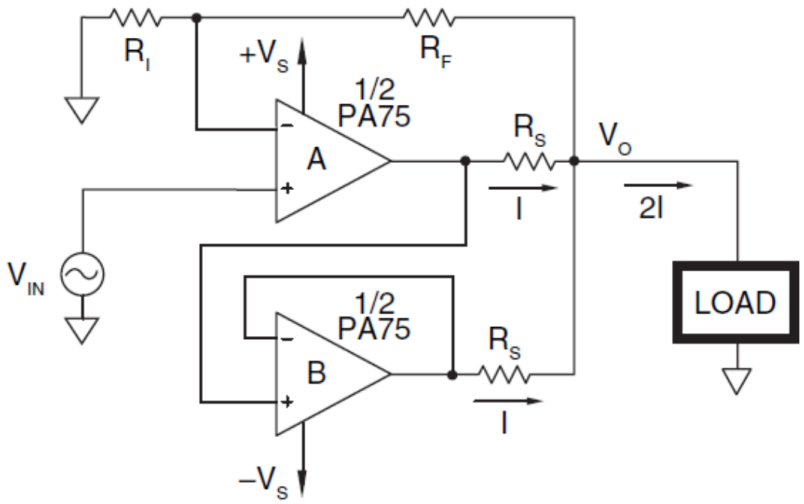

Figure 3.6: Circuit diagram of the PA75 dual power Op-Amp configured as a noninverting amplifier for PEC excitation.

The use of this amplifier significantly improved the clarity and repeatability of the pickup coil signals, particularly within the first few tens of microseconds following pulse excitation. These enhancements improved the SNR in the early transient region, resulting in clearer separation in the first five eigenvectors extracted during MPCA analysis, as illustrated in Figure 3.7. Such improvements are essential for detecting subtle variations in the PEC response.

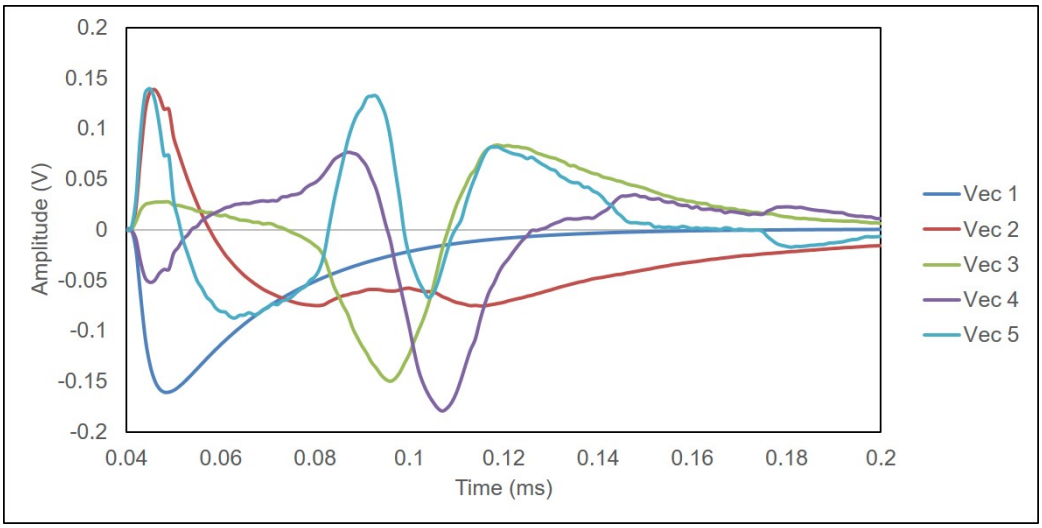

Figure 3.7: First five eigenvectors produced from MPCA of a pickup coil response using a noninverting Op-Amp driver configuration.

3.6 Experimental Setup

The experimental system, illustrated schematically in Figure 3.8, was designed to support two primary modes of operation: fastener-based localization and automated lift-off scanning. A programmable triple-axis motion control platform, Type GL206+800L, manufactured by THK Company Limited (Tokyo, Japan), controlled via the Galil Design Kit (GDK), enabled sub-millimetre probe positioning and automated stepping across predefined scan paths. This configuration ensured consistent lift-off spacing for sensitivity measurements and precise alignment during fastener scanning.

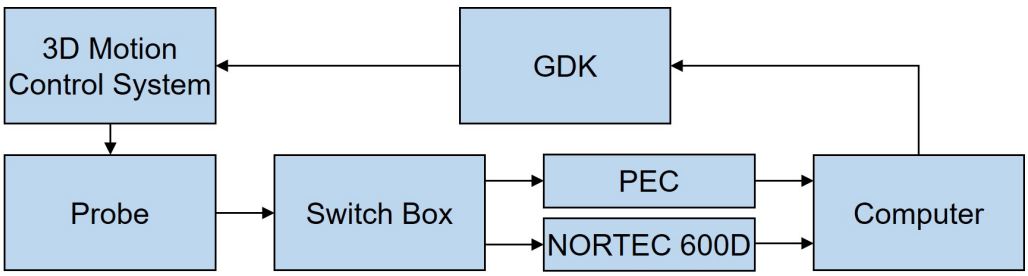

Figure 3.8: Schematic of the experimental setup incorporating automated three-axis motion control for PEC probe positioning.

Complementing the schematic in Figure 3.8, Figure 3.9 presents a photograph of the complete experimental setup. The key components are annotated from left to right, including the three-axis

motion control system, PEC probe, test standard, switch box, NORTEC 600D, PEC DAQ system with Op-Amp, and the LabVIEW interface connected via the GDK.

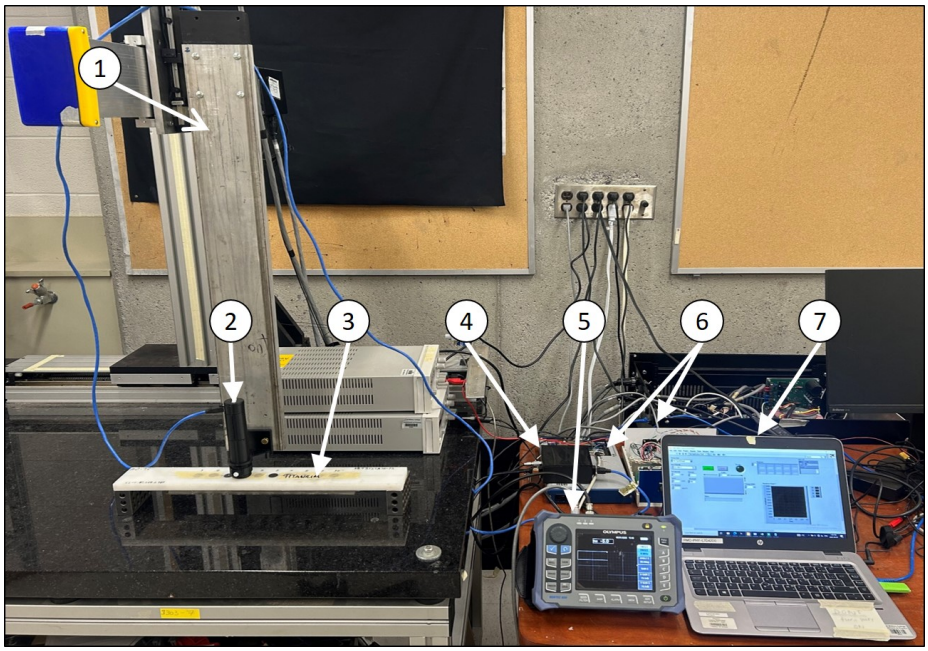

Figure 3.9: Photograph of the experimental setup. From left to right: (1) motion control system, (2) PEC probe, (3) test standard, (4) switch box, (5) NORTEC 600D, (6) PEC DAQ system and Op-Amp, and (7) LabVIEW interface (via GDK).

For fastener inspection experiments, initial localization was performed using conventional ET techniques with the NORTEC 600D. Once the fastener centres were identified, the LabVIEW 2021-controlled motion platform using the automated peak-detection algorithm applied to the eddy current signal. Motion parameters such as speed, acceleration, target spacing, and scan resolution were fully configurable within the LabVIEW interface, ensuring reproducibility and precise control throughout data acquisition.

3.7 Resistivity

Electrical resistivity, denoted by the symbol ρ, is a fundamental physical property that quantifies a material's intrinsic opposition to the flow of electric current [15]. It is defined as the resistance encountered by a unit length of a material with a unit cross-sectional area when an electric field is applied. Mathematically, resistivity is expressed as [15]:

$$\rho = R\frac{A}{L}, \tag{3.1}$$

where R is the electrical resistance, A is the cross-sectional area, and L is the sample length. The SI unit of resistivity is the ohm-meter ($\Omega \cdot \mathrm{m}$); however, for convenience, values in this work are reported in $\mu\Omega \cdot \mathrm{cm}$.

Resistivity is independent of a material's geometry but is strongly influenced by its atomic structure and the presence of impurities or defects [15]. Several factors—including alloy composition, processing conditions, and environmental effects such as temperature and humidity—can alter resistivity [107]. For most conductive materials, resistivity increases with temperature due to enhanced electron–phonon scattering [15].

Ti–6Al–4V is a titanium alloy characterized by relatively low electrical conductivity (i.e., high resistivity) owing to its alloying elements in solid solution. The measured value reported in Table 3.5 is $174\,\mu\Omega\cdot\mathrm{cm}$. Reported values range from approximately $130\,\mu\Omega\cdot\mathrm{cm}$ at $20\,\mathrm{K}$ to $190\,\mu\Omega\cdot\mathrm{cm}$ at $1000\,\mathrm{K}$ [107], indicating that impurity- and defect-related residual resistivity dominates over thermal contributions. Heat treatment, cold work, and impurity levels all influence the absolute resistivity of Ti–6Al–4V [107].

By comparison, commercially pure titanium, such as Ti–2, exhibits substantially lower resistivity owing to the absence of strong substitutional alloying elements. The measured value in Table 3.5 is $47.7\,\mu\Omega \cdot \mathrm{cm}$, which falls slightly below typical room-temperature resistivity values for Ti–2 of 50 to $55\,\mu\Omega \cdot \mathrm{cm}$ reported for impurity contents below 0.18 wt% Fe and 0.20 wt% O [107]. This reduction is consistent with decreased electron scattering associated with lower impurity levels. Of note, at room temperature, the resistivity of titanium is slightly lower than that of 18Cr–8Ni stainless steel; however, titanium exhibits a more rapid increase in resistivity with temperature, exceeding that of steel above approximately $200\,^{\circ}\mathrm{C}$ [107].

Two independent techniques were employed to measure resistivity: ET [15] and the four-point probe method [108]. Results from both techniques were compared to evaluate measurement accuracy and repeatability.

3.7.1 Resistivity Measurements Using Eddy Current Testing

ET uses an alternating current in a probe coil to generate a time-varying magnetic field, which induces circulating currents in a nearby conductor. The distribution and strength of these eddy currents depend on the material's electrical conductivity, which is inversely proportional to resistivity, as described by the skin-depth relationship in Equation 2.32 [76].

Since ET is inherently comparative, calibration against reference standards is required. The probe response, measured as a voltage signal, is influenced by the induced eddy currents, which depend on the electrical conductivity of the material. As ET does not directly measure resistivity, a calibration procedure is required to relate the measured voltage to the material property of interest. By measuring the probe voltage for reference samples with known resistivity, a relationship between

voltage and resistivity can be established and subsequently used to determine the resistivity of unknown samples.

Accurate measurement necessitates minimal lift-off, stable temperature, and sufficient sample thickness (typically $\geq 3\delta$), ensuring that at least $95\,\%$ of the eddy current density is confined within the material [15]. Optimized ET setups often employ ferrite-cupped or send–receive coil configurations to enhance signal contrast and reduce error. Impedance-plane plots are then used to identify the optimal test frequency near the curve's sensitivity knee [15].

Skin-Depth Verification

ET measurements were performed on titanium fasteners using comparative calibration. The measurements employed an eddy current probe with an outer coil diameter of $3.2\,\mathrm{mm}$ [109]. Additional probe specifications are reported by Van Barr *et al.* [109]. This diameter is significantly smaller than the lateral dimensions of the calibration reference plates, ensuring that the induced eddy currents remain well within the sample boundaries and minimize potential edge effects during calibration. The fasteners were also measured using the same pencil probe positioned at the centre of the fastener head. The material properties used for the skin-depth calculations are summarized in Table 3.6. The resistivity values for Grade 2 titanium and Ti–6Al–4V were adopted from Luloff's thesis [110], in which these materials were characterized at room temperature ($20\,^{\circ}\mathrm{C}$). The resistivity of Ti–5Al–5V–5Mo–3Cr (Ti–5553) was previously determined experimentally in the laboratory and is included here for completeness. The value listed for commercially pure titanium corresponds to a calibration reference standard.

Table 3.6: Electrical properties used for skin-depth calculations.

Material	**Thickness** (mm)	**Resistivity** ($\mu\Omega \cdot \mathrm{cm}$)
Titanium	12.2	53.8
Grade 2 Ti	3.2	54.0
Ti–6Al–4V	3.8	174
Ti–5Al–5V–5Mo–3Cr	30	179

The calculated triple skin depths (3δ) for selected excitation frequencies are shown in Table 3.7, obtained from Equation Equation 2.32.

Table 3.7: Calculated triple skin depth (3δ) in mm at selected frequencies.

Material	$100\,\mathrm{kHz}$	$200\,\mathrm{kHz}$	$300\,\mathrm{kHz}$	$400\,\mathrm{kHz}$	$500\,\mathrm{kHz}$
Titanium	3.48	2.46	2.01	1.74	1.56
Grade 2 Ti	3.49	2.46	2.01	1.74	1.56
Ti–6Al–4V	6.26	4.42	3.61	3.13	2.80
Ti–5Al–5V–5Mo–3Cr	6.38	4.51	3.68	3.19	2.85

For the Ti–6Al–4V fasteners with a minimum thickness of $3.8\,\mathrm{mm}$, the 3δ values at 300 to $500\,\mathrm{kHz}$ range from 3.61 to $2.80\,\mathrm{mm}$. This satisfies the $t \geq 3\delta$ criterion across the operating frequency range, confirming that the eddy current field remains effectively confined within the material and that back-surface contributions are negligible.

Calibration Results

Calibration results are plotted in Figure 3.10, showing the voltage–resistivity relationship between probe voltage and electrical resistivity used to extrapolate resistivity values for HLT313TA10-13 and HLT313DL8-16.

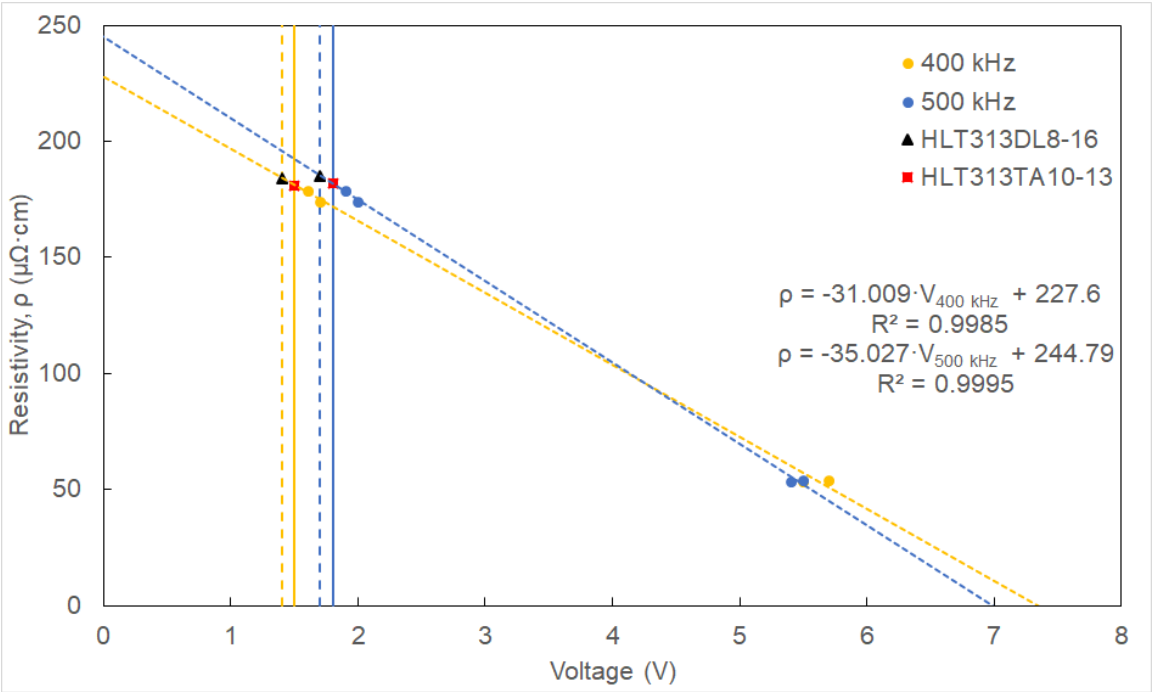

Figure 3.10: Calibration curves of probe voltage versus electrical resistivity at $400\,\mathrm{kHz}$ and $500\,\mathrm{kHz}$. Linear regression fits (dashed lines) were used to extrapolate the resistivity of HLT313TA10-13 and HLT313DL8-16 titanium fasteners from measured voltage responses. Vertical dashed lines indicate the corresponding voltage positions used to determine the extrapolated resistivity values.

The extracted resistivity values were evaluated across multiple excitation frequencies. The mean value, standard deviation, and percentage difference relative to the book value are summarized in Table 3.8.

Table 3.8: Resistivity of titanium fasteners measured via ET ($\mu\Omega \cdot \mathrm{cm}$).

Sample	**Mean** ($\mu\Omega \cdot \mathrm{cm}$)	**Standard Deviation**	**Difference** (%)
HLT313TA10-13	181.5	0.33	4.2
HLT313DL8-16	184.5	0.53	6.0

The variation across excitation frequency was less than $1\,\mu\Omega \cdot \mathrm{cm}$, indicating minimal frequency dependence within the tested range and good measurement repeatability. The low standard deviation further confirms that the calibration response was stable over the selected frequency band.

3.7.2 Resistivity Measurements Using the Four-Point Probe Technique

The four-point probe method is commonly used for measuring the resistivity of uniform conductive samples [108]. In this configuration, a known current is passed through the outer probes, while the voltage drop is measured across the inner probes. This arrangement minimizes the influence of contact resistance, since the voltage measurement circuit draws negligible current and therefore does not include the resistance of the electrical contacts. To reduce thermoelectric effects and instrumentation offsets, the applied current was reversed during each measurement, and the corresponding voltages were averaged. For cylindrical fasteners, resistivity was calculated using Equation 3.1, where the cross-sectional area was determined from the measured diameter of each specimen.

The experimental setup is shown in Figure 3.11. Each fastener was mounted in a custom 3D-printed holder, and electrical contact was established using copper foils clamped to the specimen ends. Care was taken to ensure consistent probe placement and stable mechanical contact throughout the measurement process.

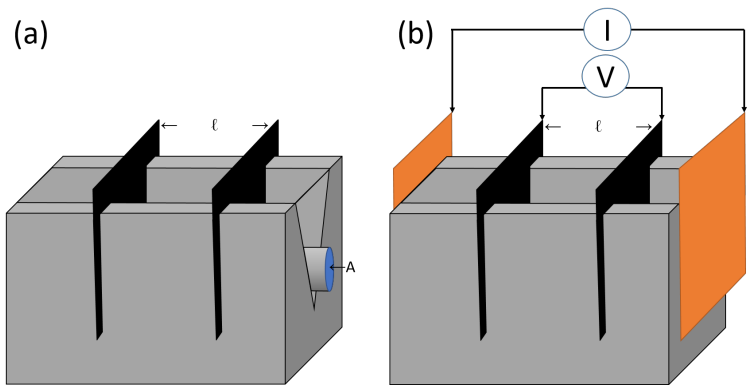

Figure 3.11: Four-point probe setup used for fastener resistivity measurements: (a) sample mounted in a 3D-printed holder and (b) electrical contact via copper foils clamped to the sample.

The geometric dimensions of the cylindrical fasteners used in the calculations are summarized in Table 3.9.

Table 3.9: Dimensions of cylindrical fasteners used in four-point probe measurements.

Sample	**Diameter** (cm)	**Length** (cm)	**Cross-sectional Area** (cm^2)
HLT313TA10-13	0.6536	1.4954	0.3355
HLT313DL8-16	0.5090	1.4954	0.2035

Five voltage measurements were obtained for each fastener at $\pm 100\,\mathrm{mA}$, and the averaged results are presented in Table 3.10, along with the calculated resistance and resistivity values.

Table 3.10: Four-point probe resistivity measurements of Ti–6Al–4V fasteners.

Sample	**Voltage** (mV)	**Resistance** ($\mathrm{m\Omega}$)	**Resistivity** ($\mu\Omega \cdot \mathrm{cm}$)
HLT313TA10-13	0.1259	0.126	172.9
HLT313DL8-16	0.0771	0.077	171.3

The repeatability of the four-point probe measurements was approximately $\pm 1\,\mu\Omega \cdot \mathrm{cm}$, indicating stable electrical contact and minimal measurement drift.

A comparison between the four-point probe results and the ET measurements is provided in Table 3.11.

Table 3.11: Comparison of resistivity values obtained using ET and four-point probe methods.

Sample	**ET Mean** ($\mu\Omega \cdot \mathrm{cm}$)	**Four-Point** ($\mu\Omega \cdot \mathrm{cm}$)	**Difference** ($\%$)
HLT313TA10-13	181.5	172.9	7.6
HLT313DL8-16	184.5	171.3	6.4

The ET measurements exhibit higher resistivity values compared to the four-point probe results. This is attributed to the surface-sensitive nature of ET, where the response is governed primarily by near-surface material properties and calibration against reference standards. As a result, surface condition, oxidation, and local material variation at the fastener head can increase the apparent resistivity.

Additional factors specific to the measurement configuration can further increase the apparent resistivity, including the presence of letter stamps and the proximity of edges during pencil probe measurements, both of which enhance the local eddy current response. Measurements were performed as close as possible to the centre of the fastener head on a flat, clear region; however, the fastener geometry can further affect the ET response. Unlike calibration standards, which are typically large and uniform, fasteners have finite dimensions and curved surfaces that can alter the distribution of induced eddy currents, leading to deviations from ideal calibration conditions.

In contrast, the four-point probe provides a bulk measurement of resistivity by directly relating current and voltage using Equation 3.1. This approach reduces sensitivity to surface conditions and

geometry and is therefore more representative of the intrinsic material properties.

The discrepancy between the two techniques is consistent with the expected difference between a surface-sensitive, comparative method and a direct bulk measurement.

Magnetic Permeability Effects

In addition to electrical conductivity, the magnetic permeability of the fastener materials influences the ET and PEC response. The titanium alloy Ti-6Al-4V (HLT313) is non-ferromagnetic, with a relative permeability close to unity ($\mu_r \approx 1.00005$), and therefore does not significantly perturb the magnetic field distribution [107].

In contrast, the precipitation-hardened stainless steel alloy PH13-8Mo used in HLT53 and HLT265 fasteners exhibits ferromagnetic behaviour, with a relative permeability that can range from approximately $46-127$, depending on the applied magnetic field and material condition [111]. This elevated permeability increases magnetic flux concentration and modifies the induced eddy current distribution, resulting in observable differences in signal response between fastener types.

4 Signal Processing and Analysis

4.1 General

This chapter outlines the signal processing and analysis methods used to evaluate PEC data for flaw detection. The procedure involves three main steps: selecting a time window of interest through signal gating, reducing dimensionality using MPCA, and classifying signals via discriminant analysis. These steps are first applied to calibration data from known flaw conditions and subsequently to signals from unknown samples. The objective is to extract and classify signal variations attributable to defects, while minimizing the influence of unrelated sources of variation.

4.2 Signal Gating

The transient response of a PEC signal is inherently complex, characterized by multiple overlapping features influenced by both material properties and experimental conditions. Since PCA-based analysis captures variance across the entire signal rather than relying on isolated features, selecting a segment of the response that contains the most relevant variation attributable to flaws is essential.

Figure 4.1 shows representative PEC signals acquired from fastener sites with and without known defects. The initial rise of the signal, dominated by the inductive response of the excitation coil, is largely consistent across all samples due to the uniform excitation pulse. However, signal decay patterns diverge significantly beyond the primary peak, which occurs at approximately $t \approx 0.22\,\mathrm{ms}$. This divergence, extending to $t \approx 0.82\,\mathrm{ms}$, is attributed to differences in electromagnetic diffusion associated with underlying material discontinuities, such as cracks or notches. A secondary feature at approximately $0.45\,\mathrm{ms}$ is attributed to non-ideal probe construction, including finite coil geometry and pickup coil asymmetry. As it appears in both defect and non-defect signals, it does not contribute to flaw discrimination.

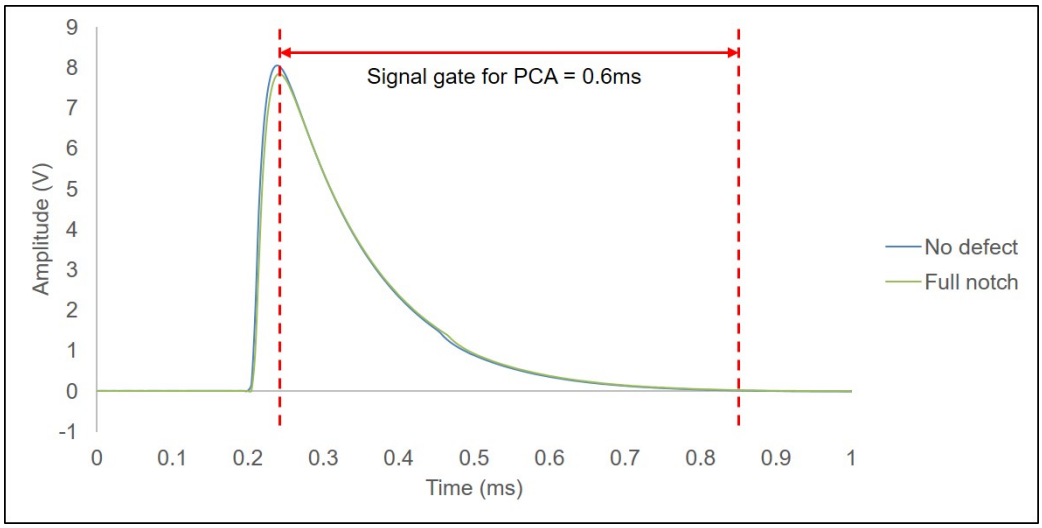

Figure 4.1: Representative PEC signals showing defect-induced variations and gated interval.

While the precise timing and amplitude of defect-induced variations are not known in advance, applying PCA within this targeted time window enables the unsupervised extraction of signal components most relevant to classification. The signal gate is defined to begin shortly after the primary peak and extend until the response has substantially decayed, terminating at $t = 0.82\,\mathrm{ms}$. This gating is applied to the absolute values of the pickup coil signals to eliminate polarity variations arising from differential coil orientation and to maintain consistency across measurements.

Focusing on this region yields a signal segment with a smoother, more predictable decay profile, which is more amenable to low-dimensional reconstruction using PCA eigenvectors. This approach minimizes the approximation error, quantified by the RSS, and ultimately enhances the sensitivity and specificity of flaw detection, as defined in Equation 2.70.

4.3 Signal Smoothing and Noise Reduction

At increased lift-off heights, the amplitude of both ET and PEC responses decreases, and the signals become increasingly susceptible to noise, making reliable peak identification more challenging. To address this, a Savitzky-Golay filter was applied to the raw time-domain responses to improve the SNR [112]. This is particularly important at larger lift-offs, where reduced signal amplitude increases the relative influence of measurement noise on feature extraction.

The Savitzky-Golay filter smooths the data by fitting a low-degree polynomial to a moving window of data points using a least-squares approach [112]. This method preserves important waveform characteristics, such as peak amplitude, peak width, and zero-crossing behaviour, unlike simple moving-average filters, which can distort these features.

The effectiveness of the filter depends on the choice of window size and polynomial order. Larger window sizes provide greater smoothing but may introduce distortion in rapidly varying regions of the signal, while higher-order polynomials can better capture waveform curvature but may also fit noise. In this work, the filter parameters were selected to balance noise reduction and feature preservation, ensuring that key transient characteristics relevant to subsequent analysis were not significantly altered.

4.4 Signal Processing Algorithm

A two-phase signal processing framework enables SHM using the PEC system, particularly for inspecting aircraft wing spars under unknown conditions. The first phase involves *calibration* using known flaw conditions to build a reference model, while the second phase—*real-time inspection*—applies this model to classify new measurements.

4.4.1 Calibration

The calibration process, illustrated in Figure 4.2, involves analyzing signals from specimens with known flaw conditions to establish a reference model for classification. A representative set of eigenvectors is extracted using MPCA, as described in Section 2.9.1, to capture signal variations attributable to flaws. Simultaneously, discriminant analysis (Section 2.10) is used to compute regression coefficients that define a linear boundary between notched and unnotched responses in the reduced principal component space. The resulting eigenvectors and coefficients are stored and used during subsequent inspections for flaw classification.

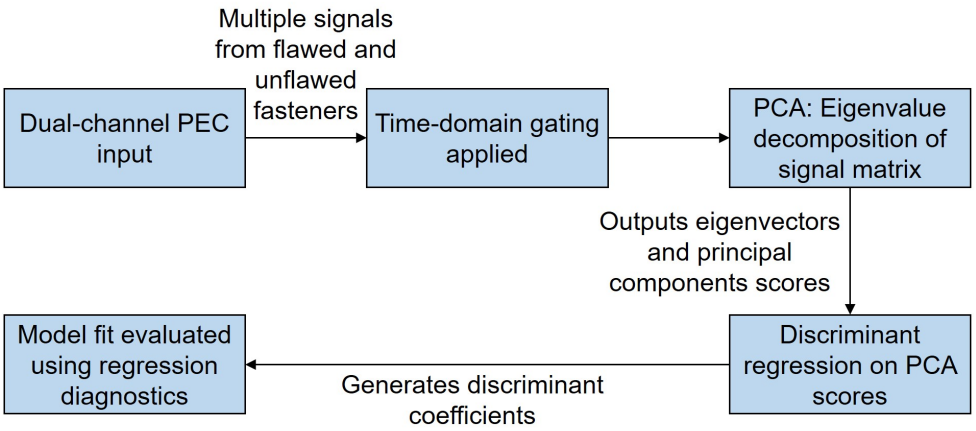

Figure 4.2: Signal processing workflow for calibration.

4.4.2 Real-Time Inspection

The second phase applies the stored calibration model to classify new PEC signals acquired during real-time field inspections. As shown in Figure 4.3, each incoming signal is gated and projected onto the precomputed principal component space. Discriminant scores are then calculated using the stored regression coefficients to classify each response as either notched or unnotched.

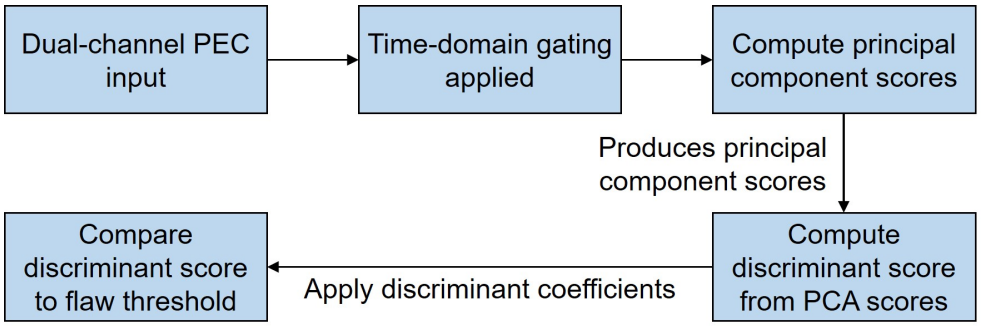

Figure 4.3: Signal processing workflow for real-time inspection.

This process is implemented in LabVIEW, which supports real-time visualization of PCA score scatter plots and automated flaw classification. The result is provided immediately after signal acquisition, enabling rapid go/no-go decisions in operational NDE environments.

5 Analytical Model

5.1 General

Analytical modelling is fundamental to understanding and predicting the behaviour of complex physical systems. In NDT applications such as PEC, analytical models can be formulated and solved in both the time and frequency domains [84]. These models provide closed-form solutions that enable rapid preliminary assessments of system behaviour, though they are often constrained by simplifying assumptions and idealized geometries.

As discussed in Section 3.2, a vertically differential transient eddy current probe configuration produces two oppositely signed response peaks, whose maximum signal separation improves the effective SNR at the extrema, simplifying signal interpretation. However, as lift-off—the distance between the probe and the material surface—increases, the SNR decreases, and the separation between signal peaks becomes less distinct, making signal analysis more challenging. Optimizing the transient eddy current probe dimensions for a given inspection geometry can enhance signal amplitude and thereby improve the effective SNR, facilitating evaluations at greater lift-offs and enabling more reliable transient signal interpretation. Consequently, both analytical and numerical models should be developed to optimize probe performance for the intended inspection configuration.

Analytical and numerical modelling approaches each provide distinct yet complementary advantages for system analysis and design optimization. Analytical models provide closed-form expressions that enable direct control over critical parameters, such as probe geometry and lift-off distance. This capability supports the development of optimized probe designs tailored to specific inspection geometries, improving signal clarity and reducing noise. Analytical models also offer strong generalization potential, enabling their application across a wide range of inspection conditions without recalibration, whereas FEM models are typically evaluated individually for each geometry and material configuration. Furthermore, they are computationally efficient, providing immediate results without requiring iterative simulations, and they yield valuable physical insight into how geometric and material parameters influence inspection outcomes.

Despite these advantages, analytical models are inherently limited by simplifying assumptions that can restrict their accuracy under realistic conditions. Approximations involving homogeneous

material properties, idealized boundary conditions, and simplified geometries can result in discrepancies when compared with experimental data. These limitations become more significant for systems with non-uniform geometries, multi-layered structures, or probe components incorporating ferrite cores, which exhibit non-linear magnetic behaviour and frequency-dependent losses, particularly at elevated lift-offs, where reduced probe–specimen coupling lowers the SNR and amplifies the influence of probe-related non-idealities.

In contrast, FEM modelling offers a flexible numerical framework capable of addressing such complexities. FEM can accommodate non-linear material behaviour, multi-layered configurations, and frequency-dependent losses, providing a more representative simulation of real-world inspection environments. This capability makes FEM particularly effective for investigating complex electromagnetic interactions in PEC systems and for validating analytical predictions. However, FEM models are computationally intensive during evaluation. They are less suited to rapid evaluations, as they rely on iterative meshing and solving procedures that can become time-consuming, particularly when applied across wide frequency ranges or multiple material configurations. By contrast, although developing analytical solutions to the underlying BVP may be time-consuming, their subsequent evaluation enables efficient parameter sweeps across wide frequency ranges and multiple material configurations.

5.2 Analytical Model Geometry

The analytical model geometry is illustrated in Figure 5.1. Two pickup coils are positioned symmetrically about the axis of an encircling driver coil located above a conducting plate of finite thickness. This vertically differential configuration forms the basis for the analytical formulation developed in this section.

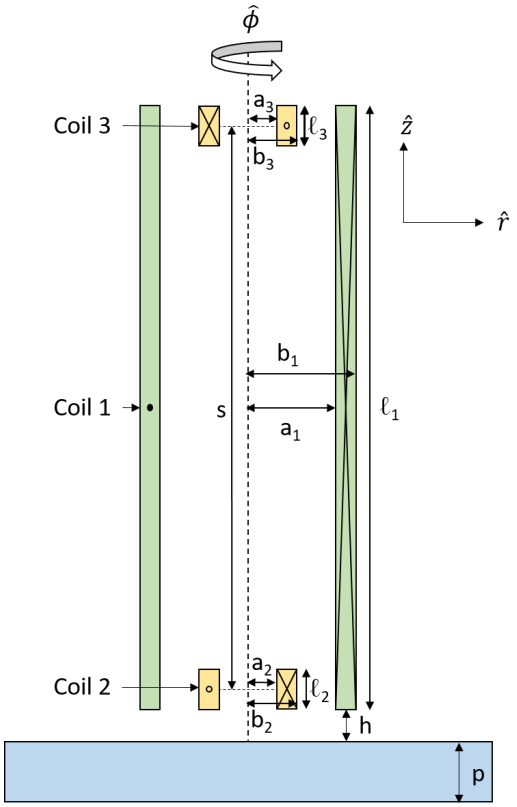

Figure 5.1: Driver coil, vertically differential pickup coils, and a flat conducting plate of finite thickness.

According to Faraday's law, Equation 2.2, time-varying currents flowing in the driver and pickup coils induce eddy currents within the conducting plate. These induced eddy currents, in turn, generate transient magnetic fields that couple back into the coils, altering their effective impedances. This feedback arises from Ampère's law, whereby the induced currents act as secondary current sources that modify the magnetic flux linking the coils and, through Equation 2.42, change the effective self and mutual inductances. The circuit representation describing the time-dependent currents $i_1(t)$ and $i_2(t)$ in the driver and pickup coils, respectively, is shown in Figure 5.2, with each coil represented by an effective impedance comprising its resistance and a time-dependent inductive component.

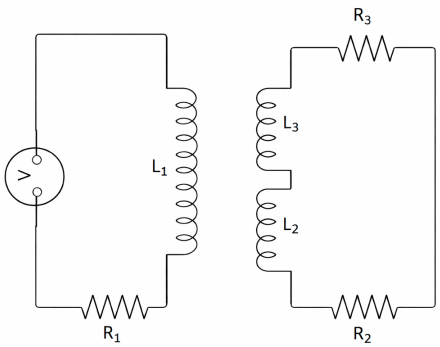

Figure 5.2: Equivalent circuit diagram for a driver coil and two vertically differential pickup coils.

The analytical formulation is based on the coupled differential equations derived from the circuit model in Figure 5.2. These equations incorporate complex self- and mutual inductance terms that describe the electromagnetic interactions between the driver coil, the pickup coils, and the conducting plate. The inductance functions are expressed in terms of frequency-dependent impedance components, which account for the influence of eddy currents on the probe response. The system of equations is solved using Fourier transform techniques, enabling a unified description of transient behaviour in both time and frequency domains.

To obtain expressions for the complex self- and mutual inductances, BVPs are formulated under the boundary conditions defined by the probe geometry and material interfaces.

A key element of the analytical solution is the Fourier series representation of the square-wave excitation signal applied to the driver coil. By decomposing the square wave into its harmonic components, the frequency-domain response can be used to reconstruct the time-domain eddy current behaviour through inverse summation. This approach enables precise computation and visualization of transient responses, providing a robust foundation for comparing analytical predictions with numerical simulations and experimental measurements.

5.3 Circuit Solution

The analytical model is formulated using differential circuit equations derived from interactions between the driver and pickup coils, as shown in Figure 5.2. These equations incorporate complex self- and mutual inductance functions that account for interactions between the probe's magnetic fields and the eddy currents in the conducting plate. Time-domain convolutions are denoted by $*$, as described in Section 2.8.

5.3.1 Time-Domain Circuit Equations

Using the self- and mutual inductance terms first introduced in Section 2.4.1 and the equivalent-circuit representation shown in Figure 5.2, the governing equation for the driver-coil circuit is

$$v_1(t) \;=\; R_1\, i_1(t) \;+\; \big(L_1 + \mathcal{L}_1(t)\big) * \frac{\partial i_1(t)}{\partial t} \;+\; \big(M_{21} + \mathcal{M}_{21}(t)\big) * \frac{\partial i_2(t)}{\partial t} \\ -\; \big(M_{31} + \mathcal{M}_{31}(t)\big) * \frac{\partial i_2(t)}{\partial t}. \quad (5.1)$$

Here, $v_1(t)$ is the applied excitation voltage, $i_1(t)$ is the current in the driver-coil circuit (Circuit 1), and $i_2(t)$ is the current in the pickup circuit (Circuit 2). R_i denotes the resistance of coil i, where $i \in \{1, 2, 3\}$. Similarly, L_i represents the self-inductance of coil i, and M_{ij} denotes the mutual inductance between coils i and j, where $i, j \in \{1, 2, 3\}$ and $i \neq j$. The quantities $\mathcal{L}_i(t)$ and $\mathcal{M}_{ij}(t)$ depend on the geometry and material properties of the probe and test specimen. Specifically, $\mathcal{L}_i(t)$ represents the time-dependent complex self-inductance of coil i arising from eddy current diffusion in the conducting specimen, while $\mathcal{M}_{ij}(t)$ is the corresponding time-dependent complex mutual inductance induced by the specimen response.

For the pickup coils,

$$0 \;=\; R_2\, i_2(t) + R_3\, i_2(t) + \big(L_2 + \mathcal{L}_2(t)\big) * \frac{\partial i_2(t)}{\partial t} + \big(L_3 + \mathcal{L}_3(t)\big) * \frac{\partial i_2(t)}{\partial t} \\ -\; \big(M_{23} + \mathcal{M}_{23}(t)\big) * \frac{\partial i_2(t)}{\partial t} \;-\; \big(M_{32} + \mathcal{M}_{32}(t)\big) * \frac{\partial i_2(t)}{\partial t} \\ +\; \big(M_{12} + \mathcal{M}_{12}(t)\big) * \frac{\partial i_1(t)}{\partial t} \;-\; \big(M_{13} + \mathcal{M}_{13}(t)\big) * \frac{\partial i_1(t)}{\partial t}. \quad (5.2)$$

Assuming identical, symmetrically placed pickup coils—an assumption supported by the measured pickup coil resistances in Table 3.1, which agree within $1\,\%$, and by the close agreement (within $4\,\%$) between the measured and analytically predicted pickup self-inductance values—the following relations hold:

$$R_2 = R_3, \qquad L_2 = L_3, \qquad M_{21} = M_{12}, \quad (5.3)$$

$$M_{31} = M_{13}, \qquad M_{23} = M_{32}, \qquad \mathcal{M}_{23}(t) = \mathcal{M}_{32}(t). \quad (5.4)$$

Under these assumptions, Equation 5.1 and Equation 5.2 reduce to:

$$v_1(t) \;=\; R_1\, i_1(t) + \big(L_1 + \mathcal{L}_1(t)\big) * \frac{\partial i_1(t)}{\partial t} + \big(\mathcal{M}_{21}(t) - \mathcal{M}_{31}(t)\big) * \frac{\partial i_2(t)}{\partial t}, \quad (5.5)$$

and

$$0 \;=\; 2R_2\, i_2(t) + \big(2L_2 + \mathcal{L}_2(t) + \mathcal{L}_3(t) - 2\big(M_{23} + \mathcal{M}_{23}(t)\big)\big) * \frac{\partial i_2(t)}{\partial t} \\ +\; \big(\mathcal{M}_{12}(t) - \mathcal{M}_{13}(t)\big) * \frac{\partial i_1(t)}{\partial t}. \quad (5.6)$$

5.3.2 Frequency-Domain Form and Solutions

Applying the Fourier transform from Section 2.6 to Equation 5.5 and Equation 5.6, the frequency-domain equations are obtained:

$$v_1(\omega) \;=\; \big(R_1 + \mathrm{j}\omega(L_1 + \mathcal{L}_1)\big)\, i_1(\omega) + \mathrm{j}\omega\big(\mathcal{M}_{21} - \mathcal{M}_{31}\big)\, i_2(\omega), \tag{5.7}$$

and

$$0 \;=\; \big(2R_2 + \mathrm{j}\omega(2L_2 + \mathcal{L}_2 + \mathcal{L}_3 - 2(M_{23} + \mathcal{M}_{23}))\big)\, i_2(\omega) + \mathrm{j}\omega\big(\mathcal{M}_{12} - \mathcal{M}_{13}\big)\, i_1(\omega), \tag{5.8}$$

where $\mathcal{L}_i = \mathcal{L}_i(\omega)$ and $\mathcal{M}_{ij} = \mathcal{M}_{ij}(\omega)$ denote complex, frequency-dependent self- and mutual inductance functions.

The solutions for $i_1(\omega)$ and $i_2(\omega)$ are derived from Equation 5.7 and Equation 5.8:

$$i_1(\omega) = \frac{\big(2R_2 + \mathrm{j}\omega(2L_2 + \mathcal{L}_2 + \mathcal{L}_3 - 2(M_{23} + \mathcal{M}_{23}))\big)\, v_1(\omega)}{\omega^2\big(\mathcal{M}_{12} - \mathcal{M}_{13}\big)^2 + \big(R_1 + \mathrm{j}\omega(L_1 + \mathcal{L}_1)\big)\big(2R_2 + \mathrm{j}\omega(2L_2 + \mathcal{L}_2 + \mathcal{L}_3 - 2(M_{23} + \mathcal{M}_{23}))\big)}, \tag{5.9}$$

and

$$i_2(\omega) = \frac{-\,\mathrm{j}\omega\big(\mathcal{M}_{12} - \mathcal{M}_{13}\big)\, v_1(\omega)}{\omega^2\big(\mathcal{M}_{12} - \mathcal{M}_{13}\big)^2 + \big(R_1 + \mathrm{j}\omega(L_1 + \mathcal{L}_1)\big)\big(2R_2 + \mathrm{j}\omega(2L_2 + \mathcal{L}_2 + \mathcal{L}_3 - 2(M_{23} + \mathcal{M}_{23}))\big)}. \tag{5.10}$$

5.3.3 Simplifications for Weak Couplings

If the coupling of Coil 3 to the sample is negligible, such that

$$\mathcal{L}_3 \ll 2L_2 + \mathcal{L}_2, \qquad \mathcal{M}_{31} = \mathcal{M}_{13} \ll \mathcal{M}_{12}, \qquad \mathcal{M}_{32} = \mathcal{M}_{23} \ll 2L_2 + \mathcal{L}_2, \tag{5.11}$$

the corresponding inductive terms may be neglected:

$$\mathcal{L}_3 \approx 0, \qquad \mathcal{M}_{31} = \mathcal{M}_{13} \approx 0, \qquad \mathcal{M}_{32} = \mathcal{M}_{23} \approx 0. \tag{5.12}$$

In addition, if the mutual coupling between Coils 2 and 3 is negligible due to their separation ($M_{23} \approx 0$), Equation 5.9 and Equation 5.10 simplify to:

$$i_1(\omega) = \frac{\big(2R_2 + \mathrm{j}\omega(2L_2 + \mathcal{L}_2)\big)\, v_1(\omega)}{\omega^2\mathcal{M}_{12}^2 + \big(R_1 + \mathrm{j}\omega(L_1 + \mathcal{L}_1)\big)\big(2R_2 + \mathrm{j}\omega(2L_2 + \mathcal{L}_2)\big)}, \tag{5.13}$$

and

$$i_2(\omega) = \frac{-\,\mathrm{j}\omega\mathcal{M}_{12}\, v_1(\omega)}{\omega^2\mathcal{M}_{12}^2 + \big(R_1 + \mathrm{j}\omega(L_1 + \mathcal{L}_1)\big)\big(2R_2 + \mathrm{j}\omega(2L_2 + \mathcal{L}_2)\big)}. \tag{5.14}$$

5.4 Boundary Value Problem Solutions for Inductance Derivation

To derive analytical expressions for the probe's self- and mutual inductances, the governing BVPs must be solved. Starting from the MQS Poisson equation for the azimuthal component of the magnetic vector potential, A_ϕ, in a homogeneous non-conducting region (Equation 2.18),

$$\nabla^2 A_\phi(r,z) = -\mu_0 j_\phi(r,z). \tag{5.15}$$

Assuming a linear, isotropic, and homogeneous medium, a total driving current i_0 in a filamentary loop located at (r_0, z_0) produces a current density $j_\phi(r,z) = \frac{i_0}{r}\,\delta(r-r_0)\,\delta(z-z_0)$. Substituting this into Equation 5.15 yields the differential form [14]:

$$\left(\frac{\partial^2}{\partial r^2} + \frac{1}{r}\frac{\partial}{\partial r} - \frac{1}{r^2} + \frac{\partial^2}{\partial z^2}\right) A_\phi(r,z) = -\mu_0 \frac{i_0\,\delta(r-r_0)\,\delta(z-z_0)}{r}. \tag{5.16}$$

Given the symmetry of the system in the azimuthal direction (ϕ), a first-order Hankel transform (parameter k_r) is applied to the radial coordinate r, and a Fourier cosine transform (parameter k_z) is applied to the axial coordinate z, as described in Section 2.6. The transformed equation obtained from Equation 5.16 becomes:

$$A_\phi(k_r,k_z) = \mu_0 i_0\,\frac{r_0 J_1(k_r r_0)\cos(k_z z_0)}{k_r^2 + k_z^2}. \tag{5.17}$$

Applying the inverse Hankel and inverse Fourier cosine transforms, as described in Section 2.6, to Equation 5.17 gives the spatial-domain solution for a filamentary source:

$$A_\phi(r,z) = \frac{\mu_0 i_0}{\pi}\int_0^\infty\!\!\int_0^\infty k_r J_1(k_r r)\cos(k_z z)\,\frac{r_0 J_1(k_r r_0)\cos(k_z z_0)}{k_r^2+k_z^2}\,\mathrm{d}k_z\,\mathrm{d}k_r. \tag{5.18}$$

To obtain the A_ϕ for a finite coil, the filamentary solution in Equation 5.18 is integrated over the coil cross-section and multiplied by the turn density $n = N/[l(b-a)]$, where N is the number of turns, l is the coil length, and a and b are the inner and outer radii. Consistent with the geometry used in Figure 5.4, the coil occupies $z_0 \in [0,l]$ and $r_0 \in [a,b]$, yielding:

$$A_\phi(r,z) = \frac{2\mu_0 n i_0}{\pi}\int_0^\infty\!\!\int_0^\infty k_r J_1(k_r r)\cos(k_z z)\,\frac{\displaystyle\int_a^b r_0 J_1(k_r r_0)\,\mathrm{d}r_0\,\sin\!\left(\frac{k_z l}{2}\right)}{k_z(k_r^2+k_z^2)}\,\mathrm{d}k_z\,\mathrm{d}k_r. \tag{5.19}$$

This double integral is convergent for all r and z, including points within the coil boundaries. To simplify, one of the inverse transforms can be performed analytically, though this restricts the regions of convergence of the resulting solutions.

Figure 5.3 illustrates two representative boundary configurations encountered in eddy current modelling: (a) a vertical interface, where the coil encircles a bounded region, and (b) a horizontal interface, where the coil is positioned above a planar conductive plate. These geometries represent two common configurations encountered in axisymmetric and layered domain analyses [20], [55].

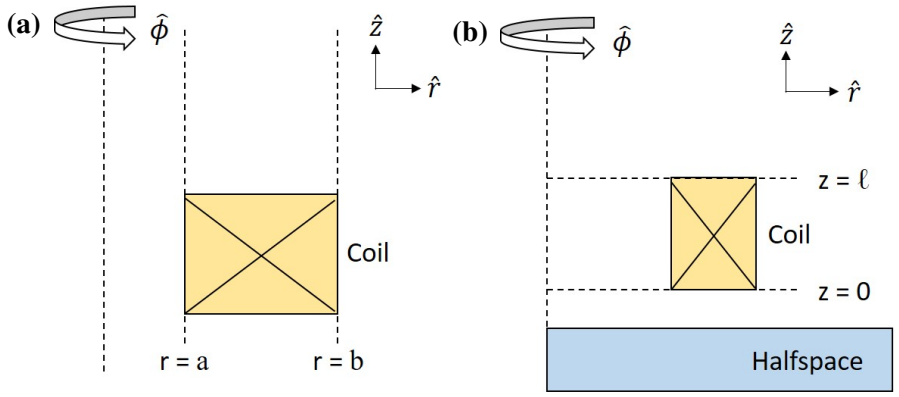

Figure 5.3: Cross-sectional view of two boundary configurations in eddy current modelling: (a) a vertical interface where the coil encircles a bounded region, and (b) a horizontal interface where the coil is positioned above a conductive plate.

For vertical interfaces, such as in Figure 5.3(a), performing the inverse Fourier cosine transform in Equation 5.19 first and applying the relevant boundary conditions yields the piecewise solution:

$$A_\phi(r,z) = \frac{2\mu_0 n i_0}{\pi}\int_0^\infty \frac{\cos(k_z z)\sin\left(\frac{k_z l}{2}\right)}{k_z}\begin{cases} I_1(k_z r)\int_a^b r_0 K_1(k_z r_0)\,\mathrm{d}r_0, & r<a,\\ K_1(k_z r)\int_a^b r_0 I_1(k_z r_0)\,\mathrm{d}r_0, & r>b,\end{cases}\mathrm{d}k_z, \tag{5.20}$$

where I_1 and K_1 are the modified Bessel functions of the first and second kinds. The solution is expressed for regions external to the current-carrying coil ($r < a$ and $r > b$), where the governing equation is homogeneous.

For horizontal interfaces, as shown in Figure 5.3(b), performing the inverse Hankel transform of Equation 5.19 yields:

$$A_\phi(r,z) = \frac{\mu_0 n i_0}{2}\int_0^\infty J_1(k_r r)\left(\frac{\int_a^b r_0 J_1(k_r r_0)\,\mathrm{d}r_0}{k_r}\right)\begin{cases} e^{-k_r(z-l)}(1-e^{-k_r l}), & z>l,\\ e^{k_r z}(1-e^{-k_r l}), & z<0,\end{cases}\mathrm{d}k_r. \tag{5.21}$$

5.4.1 Derivation for Self- and Mutual Inductances

Using the solutions in Equation 5.19, Equation 5.20, and Equation 5.21, the self- and mutual inductances are obtained by integrating the magnetic vector potential over the coil volume. Using the flux-linkage definition $L = \lambda/i_0$, with $\lambda = \iiint J_\phi A_\phi \,\mathrm{d}V$, and modelling the winding as a homogenized conductor with uniform azimuthal current density $J_\phi = n i_0$, the self-inductance reduces to [20], [73]:

$$L \equiv 2\pi n \iint_{\text{coil}} r\, A_\phi^{(\text{coil})}(r,z)\,\mathrm{d}r\,\mathrm{d}z. \tag{5.22}$$

Substituting Equation 5.19 into Equation 5.22 and performing the radial, axial, and azimuthal integrations, the self-inductance becomes:

$$L = 8n^2\mu_0 \int_0^\infty \int_0^\infty \frac{k_r}{k_z^2(k_r^2+k_z^2)} \left(\int_a^b r_0 J_1(k_r r_0)\,\mathrm{d}r_0 \right)^2 \sin^2\!\left(\frac{k_z l}{2}\right) \mathrm{d}k_z\,\mathrm{d}k_r. \tag{5.23}$$

For two identical coaxial coils (Coil 2 and Coil 3) with $a_2 = a_3$, $b_2 = b_3$, $l_2 = l_3$, and $n_2 = n_3$, separated by a distance of s, the mutual inductance is [20], [73]:

$$M_{23} \equiv 2\pi n_3 \iint_{\text{coil 3}} r\, A_\phi^{(\text{coil 2})}(r,z)\,\mathrm{d}r\,\mathrm{d}z. \tag{5.24}$$

Substituting Equation 5.21 into Equation 5.24, evaluating the radial, axial, and azimuthal integrals, and simplifying, the following result is obtained:

$$M_{23} = \mu_0 \pi n^2 \int_0^\infty \left(\int_a^b r J_1(k_r r)\,\mathrm{d}r \right)^2 \left(\frac{1-e^{-k_r l}}{k_r} \right)^2 e^{-k_r s}\,\mathrm{d}k_r. \tag{5.25}$$

Similarly, for coaxial coils where Coil 2 lies entirely within Coil 1, the mutual inductance is:

$$M_{12} \equiv 2\pi n_2 \iint_{\text{coil 2}} r\, A_\phi^{(\text{coil 1})}(r,z)\,\mathrm{d}r\,\mathrm{d}z. \tag{5.26}$$

Substituting the vertical-interface form of Equation 5.20 into Equation 5.26, and evaluating the radial, axial, and azimuthal integrals before simplifying yields:

$$M_{12} = 8n_2 n_1 \mu_0 \int_0^\infty \frac{\sin\!\left(\frac{k_z l_2}{2}\right)\sin\!\left(\frac{k_z l_1}{2}\right)}{k_z^2} \left(\int_{a_1}^{b_1} r_0 K_1(k_z r_0)\,\mathrm{d}r_0 \right) \left(\int_{a_2}^{b_2} r I_1(k_z r)\,\mathrm{d}r \right) \mathrm{d}k_z. \tag{5.27}$$

5.4.2 Complex Self- and Mutual Inductances for Conductive Plates

For the horizontal interface geometry in Figure 5.3(b), the A_ϕ for a coil in the air region ($z < 0$) derived from Equation 5.21 is:

$$A_\phi^{(\text{coil})}(k_r, z) = \Phi_{\text{coil}} e^{k_r z}, \qquad \Phi_{\text{coil}} = \frac{\mu_0 n}{2}\frac{1}{k_r}\left(\frac{\int_a^b r_0 J_1(k_r r_0)\,\mathrm{d}r_0}{k_r} \right)\left(1 - e^{-k_r l}\right). \tag{5.28}$$

where l denotes the axial extent of the coil.

Starting from the diffusion equation, Equation 2.17, expressed in cylindrical coordinates, the governing equation for a conducting plate of finite thickness p is

$$\left(\frac{\partial^2}{\partial z^2} + \frac{\partial^2}{\partial r^2} + \frac{1}{r}\frac{\partial}{\partial r} - \frac{1}{r^2} \right) A_\phi(r,z,t) = \mu\sigma \frac{\partial A_\phi(r,z,t)}{\partial t}. \tag{5.29}$$

Equation 5.29 can be transformed into a second-order Ordinary Differential Equation (ODE) by applying integral transforms to the spatial variables. Applying a temporal Fourier transform and a Hankel transform in the radial direction to Equation 5.29 yields:

$$\left(\frac{\partial^2}{\partial z^2} + k_r^2\right) A_\phi(k_r, z, \omega) = \mathrm{j}\omega\mu\sigma\, A_\phi(k_r, z, \omega). \tag{5.30}$$

Rearranging yields:

$$\frac{\partial^2}{\partial z^2} A_\phi(k_r, z, \omega) = (\mathrm{j}\omega\mu\sigma + k_r^2) A_\phi(k_r, z, \omega). \tag{5.31}$$

The general solution to Equation 5.31 is therefore

$$A_\phi^{(\mathrm{gen})}(k_r, z, \omega) = Ce^{\alpha z} + De^{-\alpha z}, \tag{5.32}$$

where $\alpha = \sqrt{k_r^2 + \mathrm{j}\omega\mu\sigma}$ and the constants C and D are determined by the boundary conditions. Different forms of this general solution apply depending on the region.

Figure 5.4 illustrates the BVP used to determine the magnetic vector potential for a finite-length coil positioned above a conducting plate. The geometry is divided into five regions: Region I is the air above the coil, Region II contains the coil volume, Region III is the air gap between the coil and the plate, Region IV is the conducting plate, and Region V is the air below the plate.

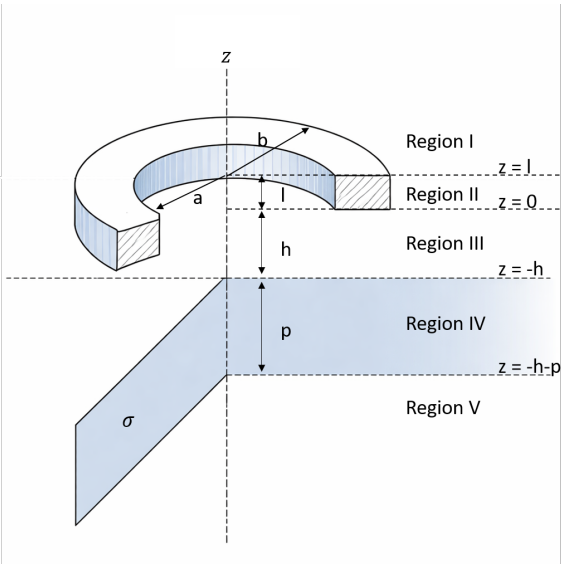

Figure 5.4: Multi-region BVP for a finite-length coil above a conducting plate.

In Region I, the magnetic vector potential consists of the contribution from the coil and a reflected component due to the presence of the conducting plate. Region II contains the distributed coil current and is therefore governed by a forced diffusion equation. Region III is source-free air and admits bidirectional exponentially varying solutions. Region IV describes diffusion within

the conducting plate, while Region V contains only exponentially decaying components to ensure bounded behaviour as $z \to -\infty$. Let h denote the lift-off distance between the base of the coil and the top surface of the plate, p the plate thickness, and $\mu_r = \mu/\mu_0$. The corresponding spectral solutions in each region are written as:

$$A_\phi^{(\mathrm{I})}(k_r, z) = \Phi_{\text{coil}} e^{-k_r(z-l)} + c_1 e^{-k_r z}, \qquad z > l, \tag{5.33}$$

$$A_\phi^{(\mathrm{II})}(k_r, z) = A_\phi^{(\text{coil})}(k_r, z) + c_2 e^{-k_r z} + c_3 e^{k_r z}, \qquad 0 < z < l, \tag{5.34}$$

$$A_\phi^{(\mathrm{III})}(k_r, z) = \Phi_{\text{coil}} e^{k_r z} + c_4 e^{k_r z} + c_5 e^{-k_r z}, \qquad -h < z < 0, \tag{5.35}$$

$$A_\phi^{(\mathrm{IV})}(k_r, z) = c_6 e^{\alpha z} + c_7 e^{-\alpha z}, \qquad -h - p < z < -h, \tag{5.36}$$

$$A_\phi^{(\mathrm{V})}(k_r, z) = c_8 e^{k_r z}, \qquad z < -h - p. \tag{5.37}$$

Since the coil current is distributed over a finite volume, no surface current sheets are present at the interfaces. Following the formulation of Dodd and Deeds [20], both A_ϕ and its normal derivative scaled by permeability remain continuous across all interfaces. The interfaces between regions are located at $z = l$ (Regions I–II), $z = 0$ (Regions II–III), $z = -h$ (Regions III–IV), and $z = -(h+p)$ (Regions IV–V). Substituting the regional solutions into the corresponding continuity conditions yields a system of linear equations for the unknown coefficients c_i, which is solved to obtain the reflected and transmitted field components required for the evaluation of the complex self- and mutual inductances.

At the interface between Regions I and II, corresponding to the air region above the coil and the coil volume, located at $z = l$, the continuity conditions are

$$A_\phi^{(\mathrm{I})}(k_r, l) = A_\phi^{(\mathrm{II})}(k_r, l), \tag{5.38}$$

$$\left.\frac{\partial A_\phi^{(\mathrm{I})}}{\partial z}\right|_{z=l} = \left.\frac{\partial A_\phi^{(\mathrm{II})}}{\partial z}\right|_{z=l}. \tag{5.39}$$

At the interface between Regions II and III, corresponding to the bottom of the coil and the air gap, located at $z = 0$, the continuity conditions are

$$A_\phi^{(\mathrm{II})}(k_r, 0) = A_\phi^{(\mathrm{III})}(k_r, 0), \tag{5.40}$$

$$\left.\frac{\partial A_\phi^{(\mathrm{II})}}{\partial z}\right|_{z=0} = \left.\frac{\partial A_\phi^{(\mathrm{III})}}{\partial z}\right|_{z=0}. \tag{5.41}$$

At the interface between Regions III and IV, corresponding to the air region above the conducting plate, located at $z = -h$, the continuity conditions are

$$A_\phi^{(\mathrm{III})}(k_r, -h) = A_\phi^{(\mathrm{IV})}(k_r, -h), \tag{5.42}$$

$$\left.\frac{1}{\mu_0}\frac{\partial A_\phi^{(\mathrm{III})}}{\partial z}\right|_{z=-h} = \left.\frac{1}{\mu}\frac{\partial A_\phi^{(\mathrm{IV})}}{\partial z}\right|_{z=-h}. \tag{5.43}$$

At the interface between Regions IV and V, corresponding to the bottom surface of the conducting plate and the air region below, located at $z = -(h + p)$, the continuity conditions are

$$A_\phi^{(\mathrm{IV})}(k_r, -h-p) = A_\phi^{(\mathrm{V})}(k_r, -h-p), \tag{5.44}$$

$$\frac{1}{\mu}\frac{\partial A_\phi^{(\mathrm{IV})}}{\partial z}\bigg|_{z=-h-p} = \frac{1}{\mu_0}\frac{\partial A_\phi^{(\mathrm{V})}}{\partial z}\bigg|_{z=-h-p}. \tag{5.45}$$

In the finite air regions (Regions I–III), the solutions are expressed as linear combinations of $e^{\pm k_r z}$; although one branch grows with z, both remain bounded over the finite intervals and the coefficients are determined by the interface conditions. Substituting the regional solutions given in Equation 5.33–Equation 5.37 into the continuity conditions at $z = l$, $z = 0$, $z = -h$, and $z = -(h + p)$ yields a coupled system of eight linear equations for the unknown coefficients c_i.

$$0 = c_1 e^{-k_r l} - c_2 e^{-k_r l} - c_3 e^{k_r l}, \tag{5.46}$$

$$0 = -c_1 e^{-k_r l} + c_2 e^{-k_r l} - c_3 e^{k_r l}, \tag{5.47}$$

$$0 = c_2 + c_3 - c_4 - c_5, \tag{5.48}$$

$$0 = -c_2 + c_3 - c_4 + c_5, \tag{5.49}$$

$$0 = \Phi_{\text{coil}} e^{-k_r h} + c_4 e^{-k_r h} + c_5 e^{k_r h} - c_6 e^{-\alpha h} - c_7 e^{\alpha h}, \tag{5.50}$$

$$0 = k_r\left(\Phi_{\text{coil}} e^{-k_r h} + c_4 e^{-k_r h} - c_5 e^{k_r h}\right) - \frac{\alpha}{\mu_r}\left(c_6 e^{-\alpha h} - c_7 e^{\alpha h}\right), \tag{5.51}$$

$$0 = c_6 e^{-\alpha(h+p)} + c_7 e^{\alpha(h+p)} - c_8 e^{-k_r(h+p)}, \tag{5.52}$$

$$0 = \frac{\alpha}{\mu_r}\left(c_6 e^{-\alpha(h+p)} - c_7 e^{\alpha(h+p)}\right) - k_r c_8 e^{-k_r(h+p)}. \tag{5.53}$$

Solving this system provides the unknown coefficients c_1–c_8 as follows:

$$c_1 = c_2 = c_5 = \Phi_{\text{coil}}\,\frac{(1 - e^{2\alpha p})(\alpha^2 - k_r^2\mu_r^2)e^{-2k_r h}}{(\alpha + k_r\mu_r)^2 e^{2\alpha p} - (\alpha - k_r\mu_r)^2}, \tag{5.54}$$

$$c_3 = c_4 = 0, \tag{5.55}$$

$$c_6 = \Phi_{\text{coil}}\,\frac{2k_r\mu_r(\alpha + k_r\mu_r)e^{\alpha(h+2p)-k_r h}}{(\alpha + k_r\mu_r)^2 e^{2\alpha p} - (\alpha - k_r\mu_r)^2}, \tag{5.56}$$

$$c_7 = \Phi_{\text{coil}}\,\frac{2k_r\mu_r(\alpha - k_r\mu_r)e^{-h(\alpha+k_r)}}{(\alpha + k_r\mu_r)^2 e^{2\alpha p} - (\alpha - k_r\mu_r)^2}, \tag{5.57}$$

$$c_8 = \Phi_{\text{coil}}\,\frac{4\alpha k_r\mu_r e^{p(\alpha+k_r)}}{(\alpha + k_r\mu_r)^2 e^{2\alpha p} - (\alpha - k_r\mu_r)^2}. \tag{5.58}$$

Using Equation 5.28 for Φ_{coil} and substituting c_5 into the air-gap potential in Region III Equation 5.35, the reflected field in the air region above the plate becomes:

$$A_{\phi}^{(\text{above})}(k_r, z) = \Phi_{\text{coil}}\left(e^{k_r z} + \frac{(1-e^{2\alpha p})(\alpha^2 - k_r^2\mu_r^2)e^{-2k_r h}}{(\alpha + k_r\mu_r)^2 e^{2\alpha p} - (\alpha - k_r\mu_r)^2} e^{-k_r z}\right). \tag{5.59}$$

The complex mutual inductance between two coaxial coils with their bases positioned at $z = 0$ along a shared axis can then be determined by integrating Equation 5.59 over the volume of the second coil, resulting in:

$$\mathcal{M}_{12} = 2\pi n_2 \int_0^{\infty} \Phi_{\text{coil1}} \frac{(1-e^{2\alpha p})(\alpha^2 - k_r^2\mu_r^2)e^{-2k_r h}}{(\alpha + k_r\mu_r)^2 e^{2\alpha p} - (\alpha - k_r\mu_r)^2} \left(\int_{a_2}^{b_2} r J_1(k_r r)\,\mathrm{d}r\right)\left(\frac{1-e^{-k_r l_2}}{k_r}\right)\mathrm{d}k_r. \tag{5.60}$$

Substituting the coil potential term Φ_{coil} from Equation 5.28 into Equation 5.60 yields the final closed-form expression:

$$\mathcal{M}_{12} = \pi n_1 n_2 \mu_0 \int_0^{\infty} \left(\int_{a_1}^{b_1} r_0 J_1(k_r r_0)\,\mathrm{d}r_0\right)\left(\frac{1-e^{-k_r l_1}}{k_r}\right) \frac{(1-e^{2\alpha p})(\alpha^2 - k_r^2\mu_r^2)e^{-2k_r h}}{(\alpha + k_r\mu_r)^2 e^{2\alpha p} - (\alpha - k_r\mu_r)^2} \times \left(\int_{a_2}^{b_2} r J_1(k_r r)\,\mathrm{d}r\right)\left(\frac{1-e^{-k_r l_2}}{k_r}\right)\mathrm{d}k_r. \tag{5.61}$$

Similarly, the complex mutual inductance between two coaxially aligned coils, located at a distance $l_2 + s$ above the plate along a shared axis, is given by:

$$\mathcal{M}_{13} = \pi n_1 n_3 \mu_0 \int_0^{\infty} \left(\int_{a_1}^{b_1} r_0 J_1(k_r r_0)\,\mathrm{d}r_0\right)\left(\frac{1-e^{-k_r l_1}}{k_r}\right) \frac{(1-e^{2\alpha p})(\alpha^2 - k_r^2\mu_r^2)e^{-2k_r h}}{(\alpha + k_r\mu_r)^2 e^{2\alpha p} - (\alpha - k_r\mu_r)^2} \times \left(\int_{a_3}^{b_3} r J_1(k_r r)\,\mathrm{d}r\right)\left(\frac{1-e^{-k_r l_3}}{k_r}\right) e^{-k_r(l_3+s)}\,\mathrm{d}k_r. \tag{5.62}$$

For two identical pickup coils ($a_2 = a_3$, $b_2 = b_3$, $l_2 = l_3$, $n_2 = n_3$) separated by a distance s above the plate, the mutual inductance simplifies to:

$$\mathcal{M}_{23} = \pi n_2^2 \mu_0 \int_0^{\infty} \left(\int_{a_2}^{b_2} r J_1(k_r r)\,\mathrm{d}r\right)^2 \left(\frac{1-e^{-k_r l_2}}{k_r}\right)^2 \frac{(1-e^{2\alpha p})(\alpha^2 - k_r^2\mu_r^2)e^{-2k_r h}}{(\alpha + k_r\mu_r)^2 e^{2\alpha p} - (\alpha - k_r\mu_r)^2} \times e^{-k_r(l_2+s)}\,\mathrm{d}k_r. \tag{5.63}$$

Finally, using the same formulation, the complex self-inductance of a single coil above a conductive plate is expressed as:

$$\mathcal{L} = \pi n^2 \mu_0 \int_0^{\infty} \left(\int_a^b r J_1(k_r r)\,\mathrm{d}r\right)^2 \left(\frac{1-e^{-k_r l}}{k_r}\right)^2 \frac{(1-e^{2\alpha p})(\alpha^2 - k_r^2\mu_r^2)e^{-2k_r h}}{(\alpha + k_r\mu_r)^2 e^{2\alpha p} - (\alpha - k_r\mu_r)^2}\mathrm{d}k_r. \tag{5.64}$$

5.5 Fourier Series Representation of Square Wave Excitation for Time-Domain Computation

In analyzing PEC systems, obtaining time-domain solutions for the induced currents is essential for understanding the transient response. This is facilitated by applying the inverse Fourier transform to the frequency-domain expressions derived from the governing circuit equations. The inverse Fourier transform is defined in Equation 2.53 and applied to the current expressions in Equation 5.13 and Equation 5.14. The resulting time-domain currents are:

$$i_1(t) = \frac{1}{2\pi}\int_{-\infty}^{\infty} \frac{\left(2R_2 + \mathrm{j}\omega(2L_2 + \mathcal{L}_2)\right) v(\omega)}{\omega^2\mathcal{M}_{12}^2 + \left(R_1 + \mathrm{j}\omega(L_1 + \mathcal{L}_1)\right)\left(2R_2 + \mathrm{j}\omega(2L_2 + \mathcal{L}_2)\right)} e^{\mathrm{j}\omega t}\,\mathrm{d}\omega, \tag{5.65}$$

and

$$i_2(t) = -\frac{1}{2\pi}\int_{-\infty}^{\infty} \frac{\mathrm{j}\omega\mathcal{M}_{12}\, v(\omega)}{\omega^2\mathcal{M}_{12}^2 + \left(R_1 + \mathrm{j}\omega(L_1 + \mathcal{L}_1)\right)\left(2R_2 + \mathrm{j}\omega(2L_2 + \mathcal{L}_2)\right)} e^{\mathrm{j}\omega t}\,\mathrm{d}\omega, \tag{5.66}$$

where $v_1(\omega)$ is the Fourier transform of the excitation $v_1(t)$.

5.5.1 Fourier Series Representation of the Square-Wave Excitation

In this PEC system, the excitation is a $50\,\%$-duty unipolar square wave. This square wave can be represented as a Fourier series, simplifying the analysis of the system's behaviour in both the frequency and time domains. Its Fourier series for the period $2T_0$ (T_0 is the length of the pulse) and amplitude v_0 is:

$$v(t) = \frac{v_0}{2} + \frac{2v_0}{T_0}\sum_{k=1}^{\infty} \frac{\sin(\varpi_k t)}{\varpi_k}, \tag{5.67}$$

with harmonic angular frequencies:

$$\varpi_k = (2k-1)\,\frac{\pi}{T_0}. \tag{5.68}$$

The Fourier transform of Equation 5.67 is described in Equation 2.64 and rewritten below:

$$v(\omega) = \pi v_0\delta(\omega) + \frac{2\pi v_0}{T_0}\sum_{k=1}^{\infty} \frac{\delta(\omega - \varpi_k) - \delta(\omega + \varpi_k)}{\mathrm{j}\varpi_k}, \tag{5.69}$$

where $\delta(\omega)$ is the Dirac delta function.

Substituting Equation 2.64 into Equation 5.65 and Equation 5.66 and using the delta function sifting property [88] yields sums over the harmonics, effectively reducing the problem to a summa-

tion of trigonometric functions. The expressions for the time-domain currents become:

$$i_1(t) = \frac{v_0}{2}\int_{-\infty}^{\infty}\sum_{k=1}^{\infty}\frac{\big(2R_2 + \mathrm{j}\omega(2L_2+\mathcal{L}_2)\big)\delta(\omega)}{\omega^2\mathcal{M}_{12}^2 + \big(R_1+\mathrm{j}\omega(L_1+\mathcal{L}_1)\big)\big(2R_2+\mathrm{j}\omega(2L_2+\mathcal{L}_2)\big)}e^{\mathrm{j}\omega t}\,\mathrm{d}\omega$$
$$+\frac{v_0}{T_0}\int_{-\infty}^{\infty}\sum_{k=1}^{\infty}\frac{2R_2+\mathrm{j}\omega(2L_2+\mathcal{L}_2)}{\omega^2\mathcal{M}_{12}^2 + \big(R_1+\mathrm{j}\omega(L_1+\mathcal{L}_1)\big)\big(2R_2+\mathrm{j}\omega(2L_2+\mathcal{L}_2)\big)}e^{\mathrm{j}\omega t}$$
$$\left(\frac{\delta(\omega-\varpi_k)-\delta(\omega+\varpi_k)}{\mathrm{j}\varpi_k}\right)\mathrm{d}\omega, \quad (5.70)$$

and

$$i_2(t) = -\frac{v_0}{2}\int_{-\infty}^{\infty}\sum_{k=1}^{\infty}\frac{\mathrm{j}\omega\mathcal{M}_{12}\,\delta(\omega)}{\omega^2\mathcal{M}_{12}^2 + \big(R_1+\mathrm{j}\omega(L_1+\mathcal{L}_1)\big)\big(2R_2+\mathrm{j}\omega(2L_2+\mathcal{L}_2)\big)}e^{\mathrm{j}\omega t}\,\mathrm{d}\omega$$
$$-\frac{v_0}{T_0}\int_{-\infty}^{\infty}\sum_{k=1}^{\infty}\frac{\mathrm{j}\omega\mathcal{M}_{12}}{\omega^2\mathcal{M}_{12}^2 + \big(R_1+\mathrm{j}\omega(L_1+\mathcal{L}_1)\big)\big(2R_2+\mathrm{j}\omega(2L_2+\mathcal{L}_2)\big)}e^{\mathrm{j}\omega t}\left(\frac{\delta(\omega-\varpi_k)-\delta(\omega+\varpi_k)}{\mathrm{j}\varpi_k}\right)\mathrm{d}\omega. \quad (5.71)$$

These integrals, once simplified, reduce to:

$$i_1(t) = \frac{v_0}{2R_1} + \frac{v_0}{T_0}\sum_{k=1}^{\infty}\left(\frac{2R_2+\mathrm{j}\varpi_k(2L_2+\mathcal{L}_2)}{\mathrm{j}\varpi_k\big(\varpi_k^2\mathcal{M}_{12}^2 + \big(R_1+\mathrm{j}\varpi_k(L_1+\mathcal{L}_1)\big)\big(2R_2+\mathrm{j}\varpi_k(2L_2+\mathcal{L}_2)\big)\big)}e^{\mathrm{j}\varpi_k t}\right)$$
$$-\frac{v_0}{T_0}\sum_{k=1}^{\infty}\left(\frac{2R_2-\mathrm{j}\varpi_k(2L_2+\mathcal{L}_2)}{\mathrm{j}\varpi_k\big(\varpi_k^2\mathcal{M}_{12}^2 + \big(R_1-\mathrm{j}\varpi_k(L_1+\mathcal{L}_1)\big)\big(2R_2-\mathrm{j}\varpi_k(2L_2+\mathcal{L}_2)\big)\big)}e^{-\mathrm{j}\varpi_k t}\right), \quad (5.72)$$

and

$$i_2(t) = -\frac{v_0}{T_0}\sum_{k=1}^{\infty}\left(\frac{\mathcal{M}_{12}}{\varpi_k^2\mathcal{M}_{12}^2 + \big(R_1+\mathrm{j}\varpi_k(L_1+\mathcal{L}_1)\big)\big(2R_2+\mathrm{j}\varpi_k(2L_2+\mathcal{L}_2)\big)}e^{\mathrm{j}\varpi_k t}\right)$$
$$+\frac{v_0}{T_0}\sum_{k=1}^{\infty}\left(\frac{\mathcal{M}_{12}}{\varpi_k^2\mathcal{M}_{12}^2 + \big(R_1-\mathrm{j}\varpi_k(L_1+\mathcal{L}_1)\big)\big(2R_2-\mathrm{j}\varpi_k(2L_2+\mathcal{L}_2)\big)}e^{-\mathrm{j}\varpi_k t}\right). \quad (5.73)$$

The second sums in Equation 5.72 and Equation 5.73 are complex conjugates of the first. The sum of a function and its complex conjugate equals twice the real part of that function [88]. Hence, these equations can be reformulated as:

$$i_1(t) = \frac{v_0}{2R_1} + \frac{2v_0}{T_0}\sum_{k=1}^{\infty}\Re\left\{\frac{e^{\mathrm{j}\varpi_k t}}{\mathrm{j}\varpi_k}\frac{2R_2+\mathrm{j}\varpi_k(2L_2+\mathcal{L}_2)}{\varpi_k^2\mathcal{M}_{12}^2 + \big(R_1+\mathrm{j}\varpi_k(L_1+\mathcal{L}_1)\big)\big(2R_2+\mathrm{j}\varpi_k(2L_2+\mathcal{L}_2)\big)}\right\}, \quad (5.74)$$

and

$$i_2(t) = -\frac{2v_0}{T_0}\sum_{k=1}^{\infty}\Re\left\{\frac{\mathcal{M}_{12}\,e^{\mathrm{j}\varpi_k t}}{\varpi_k^2\mathcal{M}_{12}^2 + \big(R_1+\mathrm{j}\varpi_k(L_1+\mathcal{L}_1)\big)\big(2R_2+\mathrm{j}\varpi_k(2L_2+\mathcal{L}_2)\big)}\right\}, \quad (5.75)$$

where $\mathcal{L}_1(\omega)$, $\mathcal{L}_2(\omega)$, and $\mathcal{M}_{12}(\omega)$ are evaluated at $\omega = \varpi_k$.

5.5.2 Trigonometric Expansion of the Time-Domain Response

To express the solutions in terms of trigonometric functions, the exponential term is expanded using Euler's identity [88]:

$$e^{\mathrm{j}\varpi_k t} = \cos(\varpi_k t) + j\sin(\varpi_k t), \tag{5.76}$$

which separates the expression into its real and imaginary components. Next, consider the fraction's denominator in the time-domain current Equation 5.74 and Equation 5.75. It is defined as:

$$D_k = \varpi_k^2 \mathcal{M}_{12}^2 + \big(R_1 + \mathrm{j}\varpi_k(L_1 + \mathcal{L}_1)\big)\big(2R_2 + \mathrm{j}\varpi_k(2L_2 + \mathcal{L}_2)\big), \tag{5.77}$$

its real and imaginary parts are:

$$\begin{aligned} A_k = \Re\{D_k\} = \varpi_k^2\big(\Re\{\mathcal{M}_{12}\}^2 - \Im\{\mathcal{M}_{12}\}^2\big) + (R_1 - \varpi_k\Im\{\mathcal{L}_1\})(2R_2 - \varpi_k\Im\{\mathcal{L}_2\}) \\ - \varpi_k^2\,(L_1 + \Re\{\mathcal{L}_1\})(2L_2 + \Re\{\mathcal{L}_2\})\,, \end{aligned} \tag{5.78}$$

$$\begin{aligned} B_k = \Im\{D_k\} = 2\varpi_k^2\Re\{\mathcal{M}_{12}\}\Im\{\mathcal{M}_{12}\} + \varpi_k\,(L_1 + \Re\{\mathcal{L}_1\})(2R_2 - \varpi_k\Im\{\mathcal{L}_2\}) \\ + \varpi_k\,(2L_2 + \Re\{\mathcal{L}_2\})(R_1 - \varpi_k\Im\{\mathcal{L}_1\})\,. \end{aligned} \tag{5.79}$$

Now, consider the numerator in the current expression for $i_1(t)$, given by:

$$N_k = 2R_2 + \mathrm{j}\varpi_k(2L_2 + \mathcal{L}_2), \tag{5.80}$$

with real and imaginary components given, respectively, as:

$$\Re\{N_k\} = 2R_2 - \varpi_k\Im\{\mathcal{L}_2\}, \qquad \Im\{N_k\} = \varpi_k\big(2L_2 + \Re\{\mathcal{L}_2\}\big) \tag{5.81}$$

Thus, by applying complex division, the fraction in Equation 5.74 can be rewritten as:

$$\frac{N_k}{A_k + jB_k} = \frac{\Re\{N_k\}A_k + \Im\{N_k\}B_k}{A_k^2 + B_k^2} + j\,\frac{\Im\{N_k\}A_k - \Re\{N_k\}B_k}{A_k^2 + B_k^2}. \tag{5.82}$$

The denominator $\mathrm{j}\varpi_k$ introduces both a division by frequency and a multiplication by $-j$, as $\frac{1}{j} = -j$. Thus, Euler's formula Equation 5.76 is reformulated as:

$$\frac{e^{\mathrm{j}\varpi_k t}}{\mathrm{j}\varpi_k} = \frac{\sin(\varpi_k t)}{\varpi_k} - j\,\frac{\cos(\varpi_k t)}{\varpi_k}, \tag{5.83}$$

Equation 5.74 becomes:

$$\begin{aligned} i_1(t) = \frac{v_0}{2R_1} + \frac{2v_0}{T_0}\sum_{k=1}^{\infty}\Bigg[\frac{(2R_2 - \varpi_k\Im\{\mathcal{L}_2\})A_k + \varpi_k(2L_2 + \Re\{\mathcal{L}_2\})B_k}{\varpi_k(A_k^2 + B_k^2)}\sin(\varpi_k t) \\ + \frac{\varpi_k(2L_2 + \Re\{\mathcal{L}_2\})A_k - (2R_2 - \varpi_k\Im\{\mathcal{L}_2\})B_k}{\varpi_k(A_k^2 + B_k^2)}\cos(\varpi_k t)\Bigg]. \end{aligned} \tag{5.84}$$

Similarly, Equation 5.75 can be expressed as:

$$i_2(t) = -\frac{2v_0}{T_0}\sum_{k=1}^{\infty}\left[\frac{\Re\{\mathcal{M}_{12}\}A_k + \Im\{\mathcal{M}_{12}\}B_k}{A_k^2+B_k^2}\cos(\varpi_k t)\right.$$
$$\left. - \frac{\Im\{\mathcal{M}_{12}\}A_k - \Re\{\mathcal{M}_{12}\}B_k}{A_k^2+B_k^2}\sin(\varpi_k t)\right]. \quad (5.85)$$

For Equation 5.84, the harmonic term can be expressed as:

$$S_k\sin(\varpi_k t) + C_k\cos(\varpi_k t), \quad (5.86)$$

where the coefficients S_k and C_k are defined as

$$S_k = \frac{(2R_2 - \varpi_k\Im\{\mathcal{L}_2\})A_k + \varpi_k(2L_2 + \Re\{\mathcal{L}_2\})B_k}{\varpi_k(A_k^2+B_k^2)}, \quad (5.87)$$

$$C_k = \frac{\varpi_k(2L_2 + \Re\{\mathcal{L}_2\})A_k - (2R_2 - \varpi_k\Im\{\mathcal{L}_2\})B_k}{\varpi_k(A_k^2+B_k^2)}. \quad (5.88)$$

Each term in Equation 5.86 may be rewritten as a single sinusoid using the phase-shift identity:

$$S_k\sin(\varpi_k t) + C_k\cos(\varpi_k t) = A'_k\sin(\varpi_k t + \phi_k), \quad (5.89)$$

where

$$A'_k = \sqrt{S_k^2 + C_k^2}, \qquad \phi_k = \arg\big(S_k + j\,C_k\big). \quad (5.90)$$

The resulting expression for the driver-coil current is therefore

$$i_1(t) = \frac{v_0}{2R_1} + \frac{2v_0}{T_0}\sum_{k=1}^{\infty}\frac{1}{\varpi_k}\sqrt{\frac{(2R_2 - \varpi_k\Im\{\mathcal{L}_2\})^2 + \varpi_k^2(2L_2 + \Re\{\mathcal{L}_2\})^2}{A_k^2+B_k^2}}$$
$$\times\sin\big(\varpi_k t \;+\; \arg\big(S_k + j\,C_k\big)\big)\,. \quad (5.91)$$

For the pickup-coil current, analogous sine and cosine coefficients are defined as

$$\tilde{S}_k = -\frac{\Im\{\mathcal{M}_{12}\}A_k - \Re\{\mathcal{M}_{12}\}B_k}{A_k^2+B_k^2},$$
$$\tilde{C}_k = \quad\frac{\Re\{\mathcal{M}_{12}\}A_k + \Im\{\mathcal{M}_{12}\}B_k}{A_k^2+B_k^2},$$

yielding the compact expression

$$i_2(t) = -\frac{2v_0}{T_0}\sum_{k=1}^{\infty}\sqrt{\frac{\Re\{\mathcal{M}_{12}\}^2 + \Im\{\mathcal{M}_{12}\}^2}{A_k^2+B_k^2}}$$
$$\times\sin\Big(\varpi_k t \;+\; \arg\big(\tilde{S}_k + j\,\tilde{C}_k\big)\Big)\,. \quad (5.92)$$

Note: $\arg(\cdot)$ denotes the complex argument (phase) and is equivalent to $\mathrm{atan2}(\Im\{\cdot\}, \Re\{\cdot\})$, ensuring the correct quadrant for ϕ_k.

Equation 5.91 and Equation 5.92 represent the final time-domain solutions for the driver and pickup coil currents, respectively, under square-wave excitation of amplitude v_0 and period $2T_0$, assuming linear magnetic permeability.

6 Numerical Implementation and Validation

6.1 General

This chapter presents results obtained from analytical modelling, FEM simulations, and experimental measurements conducted on the specimens introduced in Section 3.3. Analytical expressions for the driver and pickup coil currents, given in Equation 5.91 and Equation 5.92, were evaluated using the probe parameters listed in Table 3.1 and compared directly against corresponding FEM simulations and experimental data.

The objectives of this chapter are to assess the accuracy of the analytical model in reproducing the transient PEC response across a range of materials and lift-off conditions, and to quantify the agreement between analytical, numerical, and experimental signals using physically meaningful time-domain features.

6.2 Experimental Time-Domain Signal Acquisition

Experimental pickup-coil voltage responses were acquired using the PEC inspection system described in Chapter 3. For each specimen and lift-off condition, a unipolar square-wave excitation was applied to the driver coil, and the resulting differential pickup voltage was recorded over multiple excitation periods using a high-speed data acquisition system. The recorded waveforms were averaged over repeated pulses to improve SNR and were subsequently exported for post-processing. Lift-off was varied from 0 mm to 10 mm in 1 mm increments using a computer-controlled translation stage, ensuring consistent probe alignment and repeatable lift-off distances across all measurements.

6.3 Analytical Model Implementation

6.3.1 Numerical Implementation of the Analytical Reconstruction

The analytical reconstruction of the time-domain PEC response was implemented in Python using the closed-form expressions developed in Chapter 5. The implementation evaluates the frequency-domain driver and pickup currents given by Equation 5.13 and Equation 5.14, together with the complex self- and mutual inductance functions defined in Equation 5.61–Equation 5.64, and reconstructs the corresponding time-domain currents via the Fourier-series formulations in Equation 5.91 and Equation 5.92.

Numerical integration was performed using the Gauss–Kronrod adaptive quadrature routine `scipy.integrate.quad`, while harmonic-domain operations were vectorized using NumPy to improve computational efficiency. All probe geometry and DC circuit parameters (coil radii, lengths, turn counts, and resistances) were fixed to match the experimentally measured values of the physical probe described in Section 3.6, ensuring consistency across analytical, FEM, and experimental comparisons.

A complete description of the computational structure, including algorithm flow, data management, and harmonic summation procedures, is provided in Appendix E.

Lift-Off Configuration and Material Properties

Lift-off was varied from 0 to $10\,\mathrm{mm}$ in $1\,\mathrm{mm}$ increments to mirror the experimental scan conditions. In the analytical model, a fixed structural offset of $1.27\,\mathrm{mm}$ was added to all nominal lift-off values to account for the probe construction, such that a nominal lift-off of $0\,\mathrm{mm}$ corresponds to a physical coil–surface separation of $1.27\,\mathrm{mm}$.

For each lift-off and material, the frequency-dependent complex self-inductances $\mathcal{L}_1(\omega)$ and $\mathcal{L}_2(\omega)$, and the mutual inductance $\mathcal{M}_{12}(\omega)$, were computed at all retained harmonic frequencies and used to reconstruct both the driver current $i_1(t)$ and the pickup current $i_2(t)$. Material properties were specified using experimentally measured plate thicknesses and conductivities listed in Table 3.5.

Numerical Integration Tolerances and Convergence Controls

The evaluation of the frequency-dependent inductance expressions requires nested numerical integration, consisting of an inner radial integral and an outer wave number integral. Separate adaptive integration controls were applied to each layer to accommodate their differing numerical behaviour.

The inner integral was evaluated using absolute and relative tolerances of 10^{-9} and 10^{-7}, respectively, while the outer integral employed an absolute tolerance of 10^{-9} and a relative tolerance

of 10^{-6}, along with an increased subdivision limit to resolve the oscillatory Bessel-function behaviour. These settings were found to provide stable convergence at a low computational cost.

Caching and Computational Efficiency

The evaluation of $\mathcal{L}_1(\omega)$, $\mathcal{L}_2(\omega)$, and $\mathcal{M}_{12}(\omega)$ involves numerically expensive nested integrations for each harmonic and lift-off. To reduce computational cost, the implementation caches each inductance as a function of lift-off h and frequency f. Once computed, values are reused for all subsequent calls involving the same parameters. The cache is cleared and rebuilt whenever material properties change. This strategy reduces computation time by more than an order of magnitude and enables practical evaluation across all materials and lift-off conditions.

Harmonic Truncation and Time-Domain Reconstruction

The square-wave driver excitation is modelled as in Section 5.5: a unipolar $50\,\%$-duty waveform of amplitude v_0 and pulse length T_0. The code uses the odd-harmonic angular frequencies

$$\varpi_k = (2k-1)\,\frac{\pi}{T_0},$$

and reconstructs the currents according to the trigonometric series in Equation 5.84 and Equation 5.85. For each harmonic k, the denominator

$$D_k = \varpi_k^2 \mathcal{M}_{12}^2 + \big(R_1 + j\varpi_k(L_1 + \mathcal{L}_1)\big)\big(2R_2 + j\varpi_k(2L_2 + \mathcal{L}_2)\big),$$

is evaluated using the numerically computed inductances, and its real and imaginary parts, A_k and B_k, are formed as in Equation 5.78 and Equation 5.79. These are then used to construct the sine and cosine coefficients S_k and C_k for the driver current (Equation 5.87) and the corresponding coefficients for the pickup current in Equation 5.85. A small regularization term is applied to $|D_k|^2 = A_k^2 + B_k^2$ in the code to ensure numerical stability near resonant conditions. Additional numerical treatments, including finite excitation rise times and stable evaluation of exponential and complex-valued terms, were implemented to avoid numerical instabilities and ensure physically consistent behaviour of the reconstructed time-domain response.

The harmonic summation is truncated at a material-dependent maximum frequency $f_{\max}$. This limit is chosen using a skin depth-based criterion derived from the diffusion equation Equation 5.29, ensuring that the highest retained harmonic penetrates at least several skin depths into the plate. For highly conductive materials (e.g., copper), this results in a larger number of harmonics, whereas low-conductivity materials (e.g., titanium) require fewer terms. A global upper bound of $f_{\max} = 80\,\mathrm{kHz}$ is imposed to truncate the harmonic summation once additional high-frequency components contribute negligibly to the reconstructed time-domain waveform. The time grid spans one full excitation period $2T_0$. It is sampled at a rate of approximately 10–12 $f_{\max}$, providing a margin

above the Nyquist requirement and reducing discretization error in the steep leading edge and early-time diffusion region. These numerical choices were verified through convergence checks in $f_{\max}$ and Δt, for which further refinement produced negligible changes in the waveform and extracted features.

A detailed convergence study, including harmonic truncation, time-step refinement, and numerical integration tolerance verification, is presented in Appendix E.

For each material and lift-off, the code assembles the complete time-domain responses by combining the DC term and the Fourier series:

$$i_1(t) = \frac{v_0}{2R_1} + \frac{2v_0}{T_0} \sum_{k=1}^{k_{\max}} \big(S_k \sin(\varpi_k t) + C_k \cos(\varpi_k t)\big), \tag{6.1}$$

$$i_2(t) = -\frac{2v_0}{T_0} \sum_{k=1}^{k_{\max}} \big(\tilde{S}_k \sin(\varpi_k t) + \tilde{C}_k \cos(\varpi_k t)\big), \tag{6.2}$$

which are the discrete counterparts of Equation 5.84 and Equation 5.85. The resulting time traces $i_1(t)$ and $i_2(t)$ are stored for all lift-offs and exported to spreadsheet files, with time in the first column and each subsequent column corresponding to a distinct lift-off. These data sets form the analytical inputs used throughout Chapter 6 for comparison with the FEM simulations and experimental measurements.

Finally, the implementation includes verification checks to confirm that the reconstructed currents are effectively real-valued (imaginary parts are several orders of magnitude smaller than the real part) and that the mean value of $i_1(t)$ over one period matches the expected DC level $v_0/(2R_1)$ from Equation 5.74. These checks provide confidence that the numerical implementation is consistent with the analytical formulation and that the reconstructed time-domain signals are suitable for direct comparison with measured PEC responses.

6.3.2 Post-Processing and Quantitative Comparison of Analytical, FEM, and Experimental Signals

The analytical, FEM, and experimental time-domain responses were compared using a dedicated Python post-processing framework. For each material, the time traces were exported to spreadsheet files with time in the first column and individual lift-off heights in the remaining columns. The validation script imports this data into NumPy and pandas, organizes it into matrices of size $N_h \times N_t$ (rows corresponding to lift-off h, columns to time samples), and parses the lift-off values directly from the column headers. All subsequent analysis is performed on this common representation for the analytical, FEM, and experimental data sets.

Feature Extraction and Temporal Alignment

To enable a fair comparison of waveform morphology, a set of key time-domain features is extracted for each trace. A Savitzky–Golay filter is first applied to suppress high-frequency noise, while preserving the primary peak shape, as described in Section 4.3. From the smoothed waveform, the algorithm identifies the primary peak amplitude A_p and its occurrence time t_p, the first zero-crossing time t_0 following the peak, and the secondary minimum amplitude and time (A_s, t_s) associated with the first undershoot. In addition, a rise-time marker is computed as the time at which the waveform first exceeds a fixed fraction of the primary peak (e.g., 5%) above the baseline, and the full-width-at-fractional-maximum W is obtained by interpolating the times at which the waveform crosses a specified fraction of the peak amplitude (e.g., 10% or 50%) on the rising and falling edges.

Because the analytical reconstruction and FEM simulations may differ slightly in both amplitude and effective time scaling relative to the experimental data, the script applies a two-stage alignment procedure. First, a single global gain factor is determined for the analytical signals by minimizing the least-squares error between the analytical and experimental primary peak amplitudes across all common lift-offs,

$$g = \frac{\sum_h A_{p,\mathrm{EXP}}(h)\, A_{p,\mathrm{ANA}}(h)}{\sum_h A_{p,\mathrm{ANA}}^2(h)},$$

and the analytical traces are scaled by this factor. The FEM traces are left unscaled in amplitude.

Table 6.1: Global amplitude scaling factor applied to the analytical signals to match experimental primary peak amplitudes.

Material	Thickness (mm)	Global Scaling Factor
2024-T4	2.87	7171
2024-T4	5.30	19860
6061-T6	3.12	8975
6061-T6	9.55	141398
Cu	3.30	22322
Ti-2	4.06	3745
Ti-6Al-4V	3.12	2240

The magnitude of the gain factors reflects the unknown overall transfer function of the experimental signal chain (including amplifier gain and coil sensitivity), rather than a deficiency in the analytical formulation; the gain is applied uniformly across all lift-offs for a given material and does not affect relative trends or timing features.

Second, a global temporal shift Δt is estimated so that, on average, the analytical rise times coincide with the experimental rise times,

$$\Delta t \approx \frac{1}{N_h} \sum_h \big(t_{\mathrm{rise,EXP}}(h) - t_{\mathrm{rise,ANA}}(h)\big),$$

and all analytical traces are shifted by Δt via interpolation onto the experimental time grid.

Table 6.2: Global temporal shift applied to align analytical and FEM rise times with experimental data.

Material	**Thickness (mm)**	**Time Shift** Δt (ms)
2024-T4	2.87	0.042
2024-T4	5.30	0.024
6061-T6	3.12	0.035
6061-T6	9.55	-0.014
Cu	3.30	0.021
Ti-2	4.06	0.053
Ti-6Al-4V	3.12	0.051

To account for residual differences in effective temporal scaling that vary systematically with lift-off, a per-lift temporal normalization factor was computed based on the ratio of experimental to model peak widths,

$$a(h) \approx \frac{W_{\text{EXP}}(h)}{W_{\text{MOD}}(h)},$$

and rescales time for each lift-off according to

$$t_{\text{src}} = \frac{t_{\text{EXP}} - \Delta t}{a(h)}.$$

This yields temporally aligned analytical and FEM traces, whose primary lobe widths match the experimental response for each lift-off.

6.4 Finite Element Method Model

A FEM model was developed in COMSOL Multiphysics® version 6.2 to simulate the transient pulsed eddy current (PEC) response of the vertically differential probe. The *Magnetic Fields* (`mf`) interface under the *AC/DC* module was employed using the *Induction Currents* formulation. All geometric, electrical, and material parameters were defined to match the experimentally manufactured probe described in Chapter 3, ensuring direct comparability between the analytical model, the FEM simulations, and the experimental measurements.

6.4.1 Geometry and Coil Representation

A two-dimensional axisymmetric formulation was adopted to exploit the inherent rotational symmetry of the coaxial probe geometry, while significantly reducing computational cost. The model geometry comprised rectangular cross-sections representing the driver coil, two vertically separated pickup coils, the surrounding air domain, and the conductive test specimen. All coil dimensions and relative positions were parameterized using experimentally measured values listed in Table 3.1.

The final simulation configuration included three multi-turn coil features:

- **Driver coil (coil1):** $N = 966$ turns,
- **Upper pickup coil (coil2):** $N = 417$ turns,
- **Lower pickup coil (coil3):** $N = 417$ turns.

All coils were represented as homogenized multi-turn conductors using an AWG-based conductor area corresponding to AWG 36 copper magnet wire, consistent with the physical probe construction. This representation balances numerical stability with electromagnetic fidelity, while avoiding excessive meshing complexity associated with explicit wire geometries.

6.4.2 Materials and Boundary Conditions

Material properties for each specimen were defined using the experimentally measured electrical conductivities, as outlined in Table 3.5. All materials were assigned a relative permeability of $\mu_r = 1$. The surrounding air domain was modelled explicitly with $\sigma = 0$ and $\mu_r = 1$.

Magnetic insulation boundary conditions were applied at the outer radial, top, and bottom boundaries of the computational domain,

$$\mathbf{n} \times \mathbf{A} = \mathbf{0},$$

ensuring that the magnetic vector potential vanishes at the domain limits. An axisymmetric boundary condition was enforced along $r = 0$. The radial extent of the air domain was chosen to be at least five times the outer coil radius, and the axial extent was at least three times the plate thickness, ensuring that boundary truncation did not influence the solution.

6.4.3 Mesh Strategy

The computational mesh was generated by COMSOL's free triangular meshing algorithm with targeted refinement in regions of high electromagnetic field gradients, including the coil domains, the air–plate interface, and the upper surface of the conducting plate, where eddy currents are concentrated. Mesh resolution was guided by the expected electromagnetic skin depth (see Equation 2.32). A refined free-triangular mesh was employed in regions of high field gradients, including the coil domains and air–plate interface. Mesh convergence was verified through refinement studies, in which further mesh densification produced negligible changes in the simulated currents and fields, confirming that the solution is mesh-independent.

Although boundary-layer or mapped meshes are often employed for lift-off studies, a refined free-triangular mesh was found to provide sufficient resolution across all lift-off values without introducing numerical artefacts or mesh-induced discontinuities between parametric steps, as verified through mesh-refinement tests in which further mesh densification produced negligible changes in the simulated currents and fields.

6.4.4 Excitation and Coil Output Definition

The driver coil was excited directly within COMSOL's `mf` physics using a smoothed unit step current with a location of 5×10^{-7} s and a smoothing width of 1×10^{-6} s. This finite rise time avoids numerical instabilities associated with ideal discontinuities and more accurately reflects the experimental square-wave excitation circuitry.

The induced voltage in each pickup coil was computed using COMSOL's *Multi-Turn Coil* formulation, which evaluates the time derivative of the magnetic flux linkage. The vertically differential pickup signal was obtained by subtracting the voltages of the upper and lower pickup coils, consistent with the experimental probe design.

6.4.5 Time-Dependent Study and Parametric Sweep

Two studies were included in the final model configuration:

1. a *Frequency Domain* study at 0.1, 1, and 10 kHz for cross-validation of analytically computed inductances; and
2. a *Time Dependent* study resolving the transient response to the applied current step.

The time-dependent simulations employed COMSOL's variable-step, variable-order backward differentiation formula solver with automatic time-step control. The simulated time window extended from early microseconds to 1 ms, capturing both the rapid rise of the induced response and the subsequent diffusion-dominated decay.

A parametric sweep was applied to the lift-off parameter,

$$\mathrm{LO} = 0, 1, 2, \ldots, 10,$$

with units corresponding to millimetre-scale experimental lift-off distances. For each lift-off value, the full transient pickup-coil waveform was computed, yielding a dataset directly comparable to the experimental measurement matrix.

6.4.6 Computational Resources and Output Quantities

All simulations were performed on a workstation equipped with dual Intel® Xeon® Gold 6258R processors operating at 2.70 GHz and 256 GB of memory. Typical runtimes ranged from 10 to 25 minutes per material, depending on mesh density.

Global evaluations were used to extract the driver current, pickup-coil voltages, and magnetic flux quantities. The complete set of FEM results for all materials and lift-off values is provided in Appendix B.

6.5 Results

6.5.1 Raw Time-Domain Signal Comparison

The analytical and FEM models were first assessed at the level of the raw time-domain waveforms. For each material and lift-off configuration, the driver and pickup coil currents were reconstructed over a single period of the unipolar square-wave excitation using the harmonic summations in Equation 5.91 and Equation 5.92. The analytical model employed the same coil geometries, turn counts, and resistances as the experimentally manufactured probe, with air-core self-inductances L_1 and L_2 obtained from the double-integral expressions in Equation 5.23 and Equation 5.64. Plate conductivities were taken from the experimentally measured values to ensure a like-for-like comparison across analytical, FEM, and experimental responses.

Lift-off, defined as the distance between the probe and the plate surface, was parameterized from 0 to $10\,\mathrm{mm}$ in $1\,\mathrm{mm}$ increments. In the analytical model, this was implemented as an incremental offset relative to a baseline geometric lift-off of $1.27\,\mathrm{mm}$, which accounts for the physical location of the coils above the 3D-printed probe body. Thus, a nominal $0\,\mathrm{mm}$ lift-off in the results corresponds to the coil bases being $1.27\,\mathrm{mm}$ above the plate, consistent with the experimental configuration.

6.5.2 Raw Time-Domain Signal Analysis

A direct comparison of the experimental, analytical, and FEM pickup-coil responses in the time domain provides an essential first assessment of model fidelity prior to quantitative feature extraction. Figure 6.1 presents the reconstructed responses of Copper at three representative lift-off distances: 0, 5, and 10 mm, while Figure 6.2 represents Titanium Grade 2 at the same three lift-offs. These values span the practical operating range of the vertically differential probe and illustrate how lift-off influences transient eddy current behaviour.

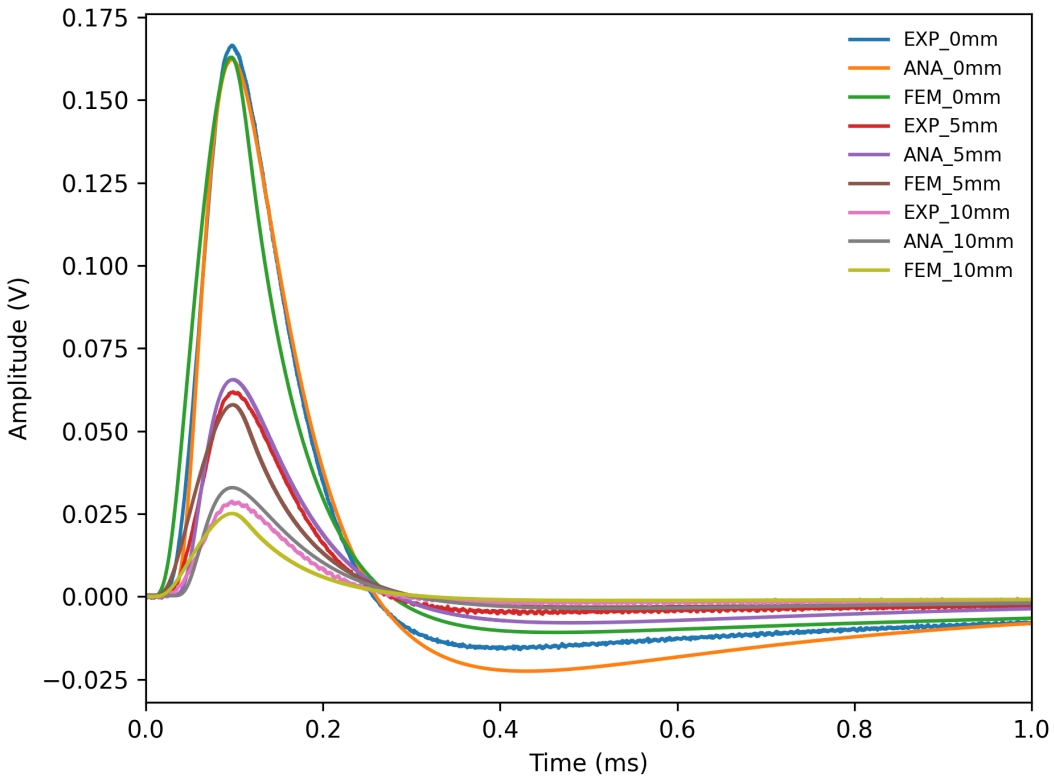

Figure 6.1: Stacked time-domain comparison of experimental, analytical, and FEM pickup-coil responses for Copper at lift-offs of 0, 5, and 10 mm.

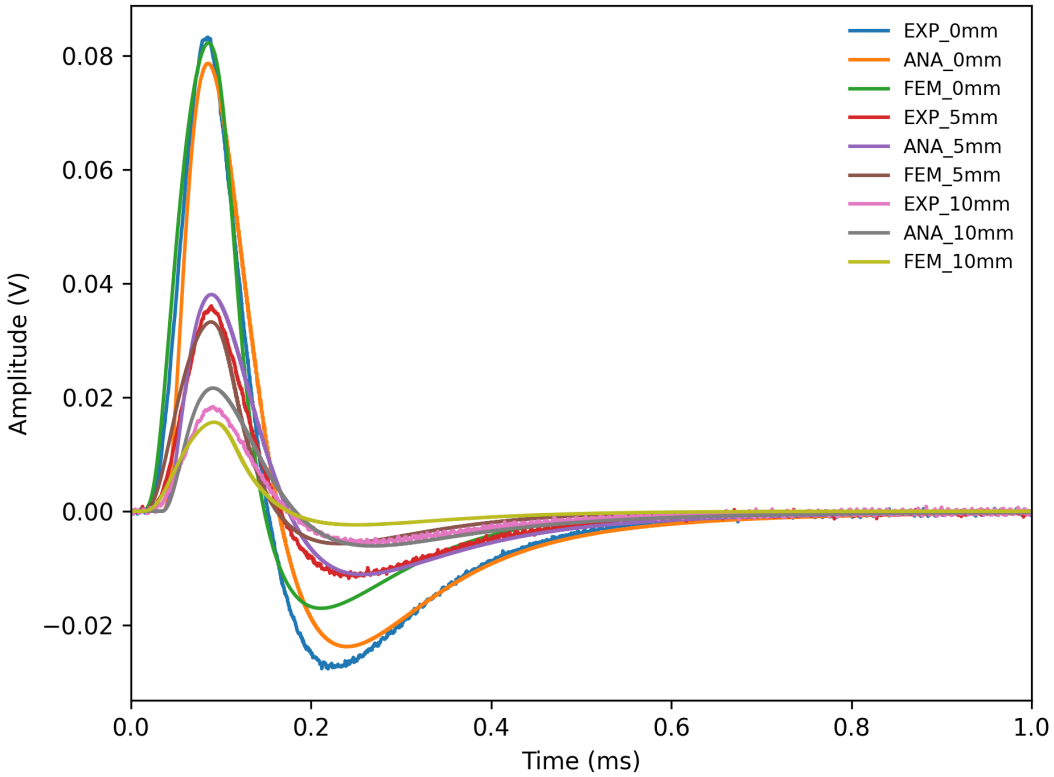

Figure 6.2: Stacked time-domain comparison of experimental, analytical, and FEM pickup-coil responses for Titanium Grade 2 at lift-offs of 0, 5, and 10 mm.

At 0 mm lift-off, the probe–sample coupling is strongest, yielding the highest signal amplitude. All three responses exhibit good agreement in their rise behaviour, primary peak timing, and early diffusion-driven decay. The analytical model accurately reproduces the steep rise and dominant transient structure, while the FEM results align closely with the experimental decay rate.

At $5\,\mathrm{mm}$ lift-off, the reduced magnetic coupling results in lower peak amplitude and broader transient features. The analytical model continues to match the temporal morphology of the waveform, but exhibits a slight positive bias in peak amplitude relative to the experiment at this lift-off, even after global amplitude normalization. In contrast, the FEM model slightly underestimates the peak magnitude while more closely reproducing the experimental peak timing and early decay behaviour.

At 10 mm lift-off, the effects of reduced SNR and increased lift-off sensitivity become more pronounced. Although the analytical solution captures the expected temporal waveform shape, it exhibits an increasing positive amplitude deviation relative to the experiment. The FEM solution underestimates the absolute amplitude but more accurately reproduces the experimental timing characteristics across the full transient response. These trends and their underlying causes are dis-

cussed further in Chapter 7.

Overall, the time-domain comparison demonstrates that both models capture the essential physics of the PEC response. The analytical model performs strongly at low and moderate lift-offs, while the FEM formulation exhibits superior robustness at elevated lift-offs, where experimental signals are more sensitive to noise and geometric uncertainties.

For each lift-off, the time-domain pickup response exhibits the expected behaviour: a rapid rise following the leading edge of the excitation pulse, a well-defined primary peak, a secondary peak, and a gradual decay towards zero as the induced eddy currents diffuse and dissipate. Both the analytical and FEM solutions reproduce this waveform morphology across all eleven lift-off values. At low lift-off (0–2 mm), the primary peak is largest in amplitude and occurs slightly earlier in time, with the decay portion of the waveform being strongly influenced by the plate conductivity. As lift-off increases, the peak amplitude decreases and the response broadens, resulting in longer rise and fall times and a reduced SNR in the experimental measurements.

Global waveform agreement was quantified using full-window Root-Mean-Square Error (RMSE), Normalized Root-Mean-Square Error (NRMSE), the coefficient of determination R^2, and Pearson correlation between the modelled and experimental pickup signals. Across all lift-offs and materials, the analytical model achieved a full-window $R^2 \approx 0.95$ with an NRMSE of approximately $5.2\,\%$ and a correlation coefficient of 0.99, indicating that the overall waveform shape is captured with good fidelity. The FEM model performed slightly better at this level, with $R^2 \approx 0.98$, NRMSE $\approx 3.5\,\%$, and correlation exceeding 0.99, reflecting the additional geometric and material detail that can be accommodated in the numerical simulation, while the analytical model relies on inherent simplifying assumptions that can influence detailed waveform agreement.

To further characterize shape similarity, cosine similarity, normalized cross-correlation, and Dynamic Time Warping (DTW) distance were computed between each modelled waveform and its experimental counterpart over the full time window. DTW is a similarity measure that non-linearly aligns two time series in time to minimize cumulative distance, thereby accounting for local temporal shifts, while preserving the overall waveform shape [113]. Averaged over lift-off, the analytical waveforms yielded a cosine similarity of approximately 0.985 and a cross-correlation of 0.997, while the FEM waveforms achieved ≈ 0.995 and 0.998, respectively. The DTW distance, which penalizes local timing and shape mismatches, was modest for both models but consistently lower for the FEM solution, again indicating that the FEM results provide a slightly closer match to the detailed experimental decay behaviour. Overall, these raw time-domain metrics confirm that the analytical model captures the dominant transient behaviour of the pickup response across all lift-offs, while the FEM model offers an incremental improvement in waveform fidelity.

Full lift-off dependent time-domain responses for all materials and thicknesses, including analytical, FEM, and experimental comparisons, are provided in Appendix B.

6.5.3 Salient Time-Domain Feature Extraction

While global error metrics provide a compact measure of agreement, they do not explicitly describe how well the models reproduce the key time-domain features that are most relevant for PEC inspection and classification. For this reason, a small set of physically meaningful scalar features was extracted from each pickup waveform:

- A_p [V]: primary peak amplitude of the pickup voltage.
- t_p [ms]: time of the primary peak, measured from the onset of the excitation pulse.
- t_0 [ms]: characteristic rise time, defined here as the time at which the waveform first crosses a fixed fraction of A_p on the leading edge (equivalently, the end of the fast-rising portion).
- A_s [V]: secondary extremum amplitude (typically, the most prominent negative excursion following the primary peak).
- t_s [ms]: time of the secondary extremum.
- W [ms]: effective peak width, defined as the time difference between the two crossings of a selected fraction of A_p (a half-amplitude criterion was used in this work).

These features were computed in a consistent manner for the experimental, analytical, and FEM waveforms. First, the experimental pickup signal was smoothed using a low-order Savitzky–Golay filter to reduce high-frequency noise while preserving peak locations, as described in Section 4.3. The primary peak A_p and its time t_p were then identified as the global maximum within a predefined early-time window following the excitation edge. The rise time t_0 and width W were obtained by linearly interpolating the time instants at which the waveform reached the specified fraction of A_p on the rising and falling flanks, respectively. The secondary extremum (A_s, t_s) was located as the most prominent opposite-polarity extremum in the subsequent decay window. The same algorithm, including smoothing parameters and search windows, was applied to the analytical and FEM outputs to ensure that any differences in extracted features arise from model discrepancies rather than from the feature-extraction procedure.

Table 6.3 lists the representative extracted features at three lift-off values (0, 5, and 10 mm) for the experimental, analytical, and FEM waveforms. These examples illustrate the typical behaviour observed across the full lift-off range: a strong monotonic reduction in A_p with increasing lift-off, a slow drift of t_p and t_0 towards later times, and a gradual broadening of the response (W). The analytical and FEM models reproduce both the trend and the absolute magnitude of these features with small deviations, which are quantified in the following subsection.

Table 6.3: Representative time-domain pickup features at selected lift-offs for the experimental, analytical, and FEM responses.

Lift-off (mm)	Experimental			Analytical			FEM		
	A_p (V)	t_p (ms)	W (ms)	A_p (V)	t_p (ms)	W (ms)	A_p (V)	t_p (ms)	W (ms)
0	0.16646	0.0975	0.18525	0.16228	0.0925	0.18534	0.16293	0.1010	0.19639
5	0.06173	0.0975	0.19754	0.06552	0.0880	0.19772	0.05794	0.1040	0.21164
10	0.02861	0.0975	0.20843	0.03292	0.0850	0.20807	0.02509	0.1030	0.21694

As seen in Table 6.3, both models closely reproduce the experimental peak width across the representative lift-off values, with only modest differences observed in peak amplitude and timing. While the general lift-off trends are well captured, small systematic deviations remain between the modelled and experimental features. These differences are quantified more rigorously in the following subsection by evaluating feature errors across all eleven lift-off values.

6.5.4 Quantitative Feature-Based Comparison

To quantify model performance in terms of the salient features defined above, feature-level errors were computed between each model and the experimental reference across all lift-offs from 0 mm to 10 mm. For the primary peak amplitude A_p and width W, the relative error was expressed as a percentage,

$$\Delta A_p(\%) = 100 \times \frac{A_{p,\text{model}} - A_{p,\text{EXP}}}{A_{p,\text{EXP}}}, \qquad \Delta W(\%) = 100 \times \frac{W_{\text{model}} - W_{\text{EXP}}}{W_{\text{EXP}}}. \tag{6.3}$$

For the peak time t_p and rise time t_0, absolute timing differences were reported in milliseconds,

$$\Delta t_p = t_{p,\text{model}} - t_{p,\text{EXP}}, \qquad \Delta t_0 = t_{0,\text{model}} - t_{0,\text{EXP}}. \tag{6.4}$$

The resulting per-lift-off errors were then summarized by their mean and standard deviation over all eleven lift-offs. Table 6.4 reports these statistics for both the analytical and FEM models.

Table 6.4: Summary of time-domain feature errors between modelled and experimental pickup responses, averaged over all lift-offs (0–10 mm). Positive values indicate that the model overestimates the corresponding feature relative to experiment.

Model	$\overline{\Delta A_p}$ (%)	$\overline{\Delta W}$ (%)	$\overline{\Delta t_p}$ (ms)	$\overline{\Delta t_0}$ (ms)
	$\pm\,\sigma_{\Delta A_p}$	$\pm\,\sigma_{\Delta W}$	$\pm\,\sigma_{\Delta t_p}$	$\pm\,\sigma_{\Delta t_0}$
Analytical	$+5.46 \pm 6.48$	-0.05 ± 0.20	-0.0100 ± 0.0031	-0.00266 ± 0.00187
FEM	-7.21 ± 2.96	$+6.08 \pm 0.85$	$+0.00459 \pm 0.00094$	$+0.0316 \pm 0.00361$

The feature-based statistics in Table 6.4 show that the analytical model reproduces the peak width W to within approximately $0.05\,\%$ on average, with a standard deviation of only $0.20\,\%$

across lift-off. The FEM model tends to over-predict W by about $6\,\%$, although this overestimation is consistent and exhibits relatively low variability. In terms of peak amplitude, the analytical model slightly overestimates A_p by an average of $5.5\,\%$, whereas the FEM results underestimate A_p by around $7.2\,\%$. The larger standard deviation in ΔA_p for the analytical model reflects the increasing positive bias at larger lift-offs, where the analytical waveform decays slightly more slowly than the experimental trace. This behaviour is consistent with simplifying assumptions in the analytical formulation, which become more influential as reduced coupling and lower SNRs amplify small discrepancies in the late-time decay. These effects are discussed further in Chapter 7. The near-zero bias in peak width suggests that the dominant diffusion physics governing the transient envelope is well captured by the analytical formulation, even when small amplitude and timing offsets are present.

The timing features provide additional insight into subtle differences in transient behaviour. On average, the analytical peak occurs $\Delta t_p \approx -0.010$ ms earlier than the experimental peak, with a relatively small spread ($\sigma_{\Delta t_p} \approx 0.003$ ms). The corresponding rise time t_0 is also slightly underestimated by about 2.7 μs. By contrast, the FEM peak is delayed by roughly 4.6 μs on average, and the rise time is overestimated by approximately 32 μs. These timing offsets are small compared to the absolute time scale of the response (sub-millisecond rise, millisecond-scale decay), but they are detectable in the early transient and consistent with the raw time-domain observations: the analytical waveforms tend to rise and peak marginally faster than the measurements, whereas the FEM waveforms lag slightly behind.

Overall, the feature-level analysis confirms the conclusions drawn from the raw time-domain comparison. The analytical model provides an accurate and computationally efficient prediction of the salient time-domain characteristics across all lift-offs, with peak amplitude and width errors generally within a few percent and timing errors on the order of a few microseconds. The FEM model delivers slightly superior global waveform agreement and more accurate reproduction of the overall decay shape, at the cost of a small systematic bias in peak width and timing. From a practical PEC inspection perspective, both models are sufficiently accurate to support probe optimization and the interpretation of lift-off trends; the analytical formulation is particularly attractive for rapid parametric studies, while the FEM model provides a high-fidelity benchmark for complex geometries and material stacks.

7 Model Performance Analysis

7.1 Accuracy of the Analytical Model

This section examines the results presented in Section 6.5.2–Section 6.5.4, to assess the accuracy of the analytical PEC model relative to both FEM simulations and experimental measurements. Emphasis is placed on the model's ability to reproduce the salient temporal characteristics of the pickup-coil response, including waveform morphology, amplitude scaling, timing behaviour, and sensitivity to lift-off height. Unlike earlier qualitative assessments, the present discussion is guided by quantitative waveform metrics and feature-level comparisons that directly reflect inspection-relevant signal behaviour.

As a limiting case, the analytical formulation was also evaluated in the absence of a conductive plate by setting $\sigma = 0$. In this configuration, the frequency-dependent plate-induced inductance terms $\mathcal{L}_1(\omega)$, $\mathcal{L}_2(\omega)$, and $M_{12}(\omega)$ vanish identically, and no eddy currents are generated. The pickup response therefore reduces to zero in the absence of conductive coupling (neglecting direct coil-to-coil mutual coupling), while the driver current follows the air-core R–L circuit transient, governed solely by the coil self-inductance. The model reproduces this behaviour exactly, confirming that the dual-circuit formulation collapses correctly to the uncoupled limit in the absence of conductive interaction.

In addition to global waveform metrics, particular attention is given to inspection-relevant scalar features, including the primary peak amplitude A_p, the characteristic rise time t_0, the time to zero-crossing, and the effective peak width W. These features govern lift-off estimation and material characterization in practical PEC inspection scenarios and, therefore, provide a more physically meaningful measure of model fidelity than global error metrics alone. The close agreement in these transient characteristics further confirms the validity of the dual-circuit formulation developed in Chapter 5, in which the coupled driver–pickup system is represented through frequency-dependent self- and mutual inductance terms. The preservation of the expected lift-off dependence further confirms that the circuit-level representation captures the dominant electromagnetic coupling mechanisms governing the transient response.

Overall, the analytical model demonstrates a strong predictive capability across the full lift-off

range investigated. As shown by the raw time-domain comparisons in Figure 6.1, the analytical waveforms closely reproduce the experimentally observed rise behaviour, primary peak structure, and diffusion-driven decay at low and moderate lift-offs. This agreement is supported by global waveform metrics, including coefficients of determination approaching $R^2 \approx 0.95$, low normalized root-mean-square error (NRMSE $\approx 5\%$), and Pearson correlation coefficients near unity. While the FEM model provides marginally improved global agreement, the analytical solution captures the dominant transient physics with substantially reduced computational cost, making it particularly suitable for parametric studies and probe optimization. Accordingly, the FEM solution serves as a high-fidelity numerical benchmark, bridging the idealized analytical formulation and the experimental measurements.

7.1.1 Inductance-Level Validation

The accuracy of the analytical model was further assessed by comparing analytically computed self- and mutual inductance values with corresponding FEM and experimental measurements. Table 7.1 summarizes the driver and pickup coil self-inductances, as well as the mutual inductance between the driver and the two pickup coils for the ARES probe.

Table 7.1: Comparison of inductance values from FEM, analytical, and experimental approaches for the ARES probe

Parameter	**FEM**	**Analytical**	**Experimental**
Driver self-inductance (mH)	6.02	6.27	6.27
Pickup self-inductance (mH)	inf	2.02	2.09
Mutual inductance (Driver–Pickup 1) (mH)	–	0.81	0.64
Mutual inductance (Pickup 1–Pickup 2) (mH)	–	$1.60 \cdot 10^{-3}$	$5.84 \cdot 10^{-3}$

The driver-coil self-inductance demonstrates strong agreement across all three approaches, validating both the analytical formulation and the FEM implementation. The analytical value closely matches the experimentally measured inductance defined according to Equation 2.42, confirming that the magnetic vector potential solution yields physically consistent flux linkage when integrated over the coil volume. The slightly lower value predicted by the FEM model is consistent with the finite computational domain employed in the simulation. Since self-inductance is defined by the flux linkage per unit current (Equation 2.42), accurate evaluation requires that the computational domain capture the majority of the magnetic flux produced by the coil. For an air-cored winding, a substantial portion of this flux resides in the surrounding air region. Truncation of the external field domain and the use of magnetic insulation boundary conditions can therefore reduce the computed flux linkage, leading to a modest underestimation of L.

For the pickup coils, the analytically computed self-inductance also agrees well with experi-

mental measurements. However, FEM simulations were unable to reliably resolve the pickup coil self-inductance due to numerical instabilities and mesh sensitivity associated with the thin-wire approximation and the floating nature of air-cored coils. The infinite value reported by the FEM solver reflects a numerical singularity under the selected formulation rather than a physical divergence in inductance.

It is noted that, in a simple $R-L$ circuit interpretation, the transient rise time is governed by the relaxation time constant; see Equation 2.45. A lower inductance would nominally reduce τ_c and accelerate the transient response. However, the small differences in air-core self-inductance observed here are insufficient to account for the subtle timing offsets identified in the waveform comparisons. These timing differences are more strongly influenced by frequency-dependent inductive behaviour and reconstruction effects than by static inductance variations.

Mutual inductance between the driver and Pickup 1 shows reasonable agreement between the analytical and experimental values, given the inherent difficulty of isolating mutual coupling in a coupled transient system. The mutual inductance between the two pickup coils is several orders of magnitude smaller, falling in the microhenry range. In the analytical time-domain reconstruction, pickup–pickup coupling is neglected based on the small magnitude of M_{23} relative to the dominant self- and driver–pickup inductances. As shown in Table 7.1, M_{23} is negligible compared to L and M_{12}, and its contribution to the transient response is therefore expected to be minimal within the resolution of the present measurements. Neither mutual inductance term could be resolved reliably in the FEM simulations, owing to domain-coupling limitations and the challenge of separating mutual contributions from the total coil response.

The discrepancies observed between analytically computed and experimentally measured mutual inductances can be attributed to several factors. The analytical formulation assumes idealized conditions, including a perfectly defined coil geometry, a uniform current distribution, and ideal magnetic coupling in free space. In contrast, experimental measurements are influenced by finite wire thickness and insulation, coil misalignment, lift-off variability, edge effects, and finite-domain fringing behaviour. Instrumentation limitations, including measurement noise and calibration uncertainty, further contribute to the observed deviations. Within these bounds, the level of agreement achieved is consistent with the expected modelling and measurement uncertainty.

Importantly, agreement at the inductance level provides independent validation of the underlying magnetic vector potential solution prior to time-domain reconstruction. This confirms that the analytical field formulation produces physically realistic coupling parameters and supports the reliability of the subsequent transient waveform predictions.

Frequency-Dependent Inductance Behaviour

The frequency-dependent behaviour of the self- and mutual inductances provides insight into the electromagnetic coupling between the probe and the conductive plate. Figures 7.1 and 7.2 show

the real and imaginary components of the inductances as a function of frequency for representative lift-off values.

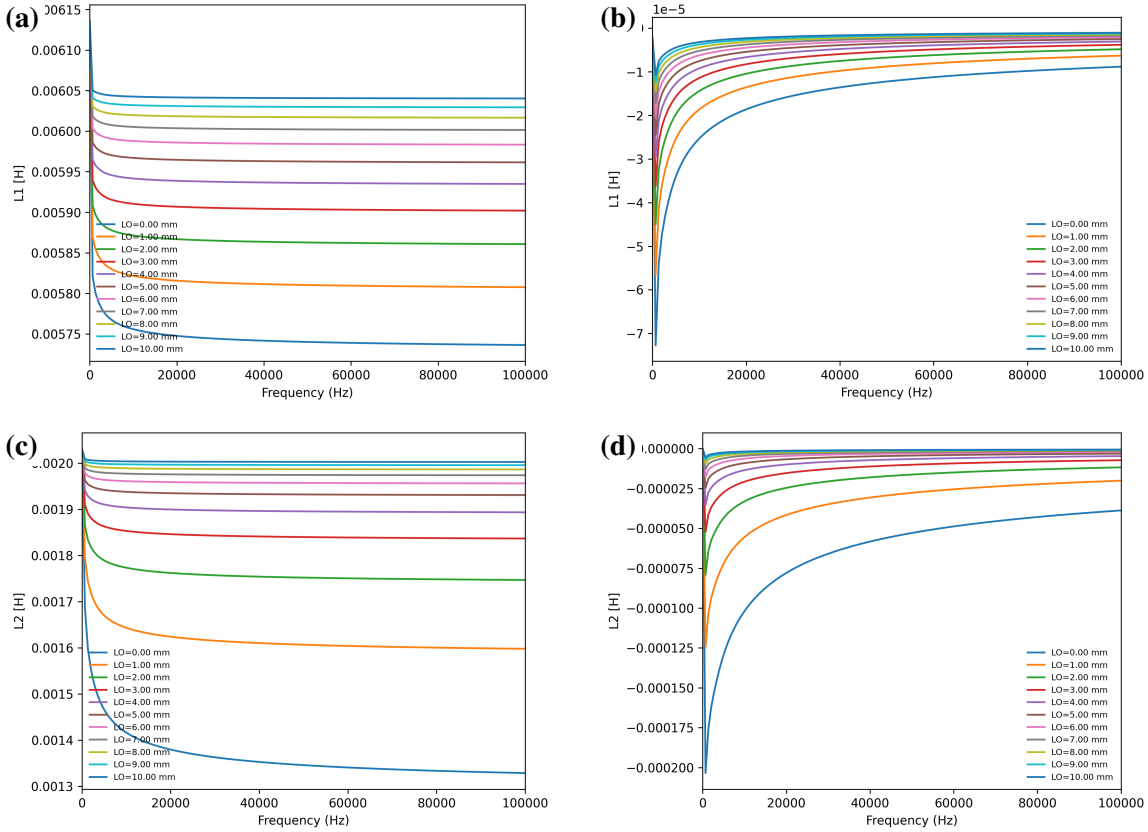

Figure 7.1: Frequency-dependent self-inductance components: (a) $\Re\{\mathcal{L}_1\}$, (b) $\Im\{\mathcal{L}_1\}$, (c) $\Re\{\mathcal{L}_2\}$, and (d) $\Im\{\mathcal{L}_2\}$.

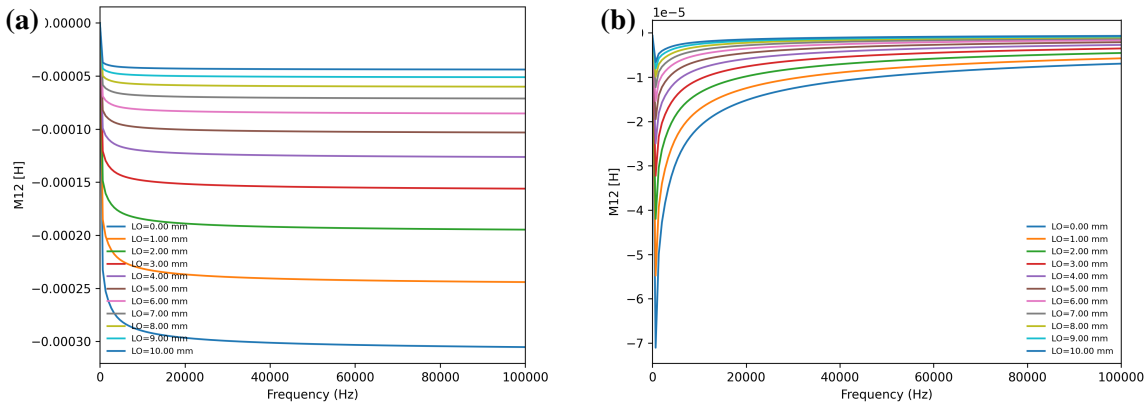

Figure 7.2: Frequency-dependent mutual inductance components: (a) $\Re\{\mathcal{M}_{12}\}$ and (b) $\Im\{\mathcal{M}_{12}\}$.

The real components represent stored magnetic energy, while the imaginary components reflect

the effect of eddy current diffusion within the conducting plate. As frequency increases, induced eddy currents oppose the primary magnetic field, reducing magnetic coupling. This is observed as a decrease in the mutual inductance magnitude at higher frequencies due to increased shielding. The self-inductance components exhibit similar behaviour, with frequency-dependent changes arising from the interaction between the probe field and the conductive specimen.

7.1.2 Interpretation of Feature Behaviour in the Context of the Dual-Circuit Model

The feature-level trends reported in Section 6.5.4 can be interpreted directly in the context of the dual-circuit formulation used to reconstruct the time-domain response. In the analytical model, the pickup waveform arises from the coupled interaction between the driver and pickup coils through frequency-dependent self- and mutual inductance terms. Consequently, each extracted feature reflects a specific physical mechanism within the equivalent circuit representation.

The monotonic decrease in primary peak amplitude A_p with increasing lift-off is consistent with the reduction in mutual inductive coupling between the driver coil and the conductive plate. As lift-off increases, the magnetic flux linking the plate decreases, reducing the induced eddy current density and, in turn, the back-coupled voltage measured in the pickup coil. The analytical model reproduces this trend with a modest positive bias in A_p, particularly at larger lift-offs. This behaviour is consistent with the simplified treatment of field truncation and coil-to-plate coupling in the analytical formulation. In contrast, the FEM model exhibits a systematic negative bias in A_p, which may be attributed to finite-domain truncation of magnetic flux and the resulting slight underestimation of inductive coupling.

The timing features t_p and t_0 are governed primarily by the effective circuit time constant,

$$\tau = \frac{L_{\text{eff}}}{R_{\text{eff}}}, \tag{7.1}$$

which follows directly from Equation 2.45. Here, L_{eff} includes both the air-core self-inductance defined in Equation 2.42 and the frequency-dependent plate contribution $\mathcal{L}(\omega)$. As summarized in Table 6.4, the small negative bias in Δt_p and Δt_0 for the analytical model indicates a slightly reduced effective time constant relative to the experiment, consistent with a marginal underestimation of the total flux linkage at early times. Conversely, the FEM solution produces a small positive timing offset, suggesting a slightly larger effective inductance or reduced effective resistance in the reconstructed transient.

The effective peak width W is primarily influenced by the diffusion-driven redistribution of eddy currents within the conductive plate. The near-zero mean error in ΔW for the analytical model demonstrates that the dominant diffusion physics are accurately captured by the frequency-domain inductance expressions and preserved through the inverse Fourier reconstruction. Although the FEM model overestimates W by approximately 6%, this bias is consistent and does not alter the overall lift-off dependence of the transient envelope.

Importantly, the secondary extremum (A_s, t_s) and zero-crossing behaviour depend on the balance between early-time magnetic coupling and late-time diffusion decay. The preservation of these features across all lift-offs confirms that the dual-circuit representation adequately captures both the inductive coupling mechanism and the diffusion-controlled plate response, even when small amplitude and timing biases are present.

Taken together, the feature-based analysis reinforces that the analytical model does not merely approximate the waveform globally, but preserves the physically meaningful characteristics that govern lift-off sensitivity, material discrimination, and probe optimization in practical PEC inspection.

7.1.3 Effect of Lift-off on Signal Amplitude

As illustrated in Figures 6.1 and 6.2, increasing lift-off height produces a monotonic reduction in signal amplitude due to magnetic field attenuation and the corresponding decrease in induced eddy current density within the conducting plate. As the separation distance increases, the magnetic flux linking the sample is reduced, leading to diminished probe–plate coupling and a lower maximum transient amplitude. This behaviour is consistently observed across experimental, analytical, and FEM responses, with the analytical model accurately reproducing the exponential-like amplitude decay trends evident in the experimental data. The same monotonic trend persists across the full lift-off range (0–10 mm) and for all investigated materials, as shown in Appendix B.

The secondary extrema in the pickup response exhibit greater inter-model variation, particularly at elevated lift-offs. These features arise from the redistribution and diffusion of induced eddy currents following the primary transient and are therefore more sensitive to material conductivity, plate thickness, and modelling assumptions related to probe geometry. As lift-off increases and the overall signal magnitude decreases, small discrepancies in diffusion modelling become more pronounced in the late-time response. Nevertheless, the analytical model preserves the relative lift-off trends and overall morphology of the transient minima across all tested conditions, demonstrating robustness in capturing lift-off-dependent behaviour even when small absolute amplitude deviations from experiment remain.

7.1.4 Time-Domain Reconstruction and Signal Shape

Reconstruction of the time-domain signals via inverse Fourier summation proved successful across all cases examined. As shown in Figure 6.1, the analytical model accurately reproduces both the sharp initial peak and the subsequent diffusion-dominated decay of the PEC response. The stability of extracted timing and width features across the full lift-off range confirms that truncation of the Fourier series at 500 harmonics preserves the dominant spectral content of the excitation and system response while maintaining computational efficiency.

Importantly, the close agreement in peak timing and effective width demonstrates that the inverse reconstruction does not introduce significant temporal distortion, further validating the analytical formulation as a reliable means of obtaining high-resolution time-domain responses from frequency-domain inductance expressions.

7.1.5 Sources of Discrepancy

While the analytical model demonstrates good agreement with the FEM simulations and experimental measurements, residual discrepancies remain, particularly at larger lift-offs and in the vicinity of secondary signal features. These deviations arise from several sources. First, the analytical formulation assumes spatially uniform material properties and idealized geometric boundaries. In practice, the test specimens may exhibit small variations in thickness, surface condition, and finite plate dimensions, all of which influence the local eddy current distribution. Second, the reduced magnetic coupling and finite-domain field effects between the coils and the conductive plate are not explicitly represented in the analytical solution. These effects become increasingly significant at larger lift-offs, where reduced magnetic coupling amplifies the relative influence of fringing fields in the finite plate geometries listed in Table 3.5. The FEM model partially captures these phenomena through its full geometric representation. Third, experimental measurements are subject to high-frequency noise and digitization artefacts introduced by the DAQ, particularly in late-time regions where the SNR decreases.

Finally, the analytical model neglects frequency-dependent skin and proximity effects within the probe windings. At higher harmonic frequencies, current crowding within the conductors increases the effective AC resistance of the coils and slightly alters the internal flux distribution [53], [79]. This modifies the amplitude and phase of the reconstructed transient response and contributes to small systematic differences between the analytical predictions and the measured signals.

Together, these factors explain the modest amplitude and timing biases observed in the feature-level comparisons. Nonetheless, the analytical model consistently reproduces the dominant transient behaviour and lift-off trends most relevant to PEC inspection.

7.1.6 Uncertainty Analysis and Propagation

A sensitivity study was performed to evaluate how uncertainties in physical and geometric parameters influence the PEC signal, following and extending the approach of Klein *et al.* [114]. Details are provided in Appendix C. Electrical conductivity σ and plate thickness p were found to be the most influential parameters, particularly for timing-related features, while geometric parameters such as pickup width b_2 exhibited more localized effects on amplitude metrics. These findings place the observed model–experiment discrepancies within the broader context of physical uncertainty and further support the analytical model's suitability for predictive and interpretive use.

Although the uncertainty analysis was not intended as a direct flaw-classification tool, it provides important insight into the physical mechanisms governing detectability. In particular, the dominant influence of electrical conductivity and plate thickness on timing-related features helps explain the variability observed in flaw contrast across different substrates. When material-dependent parameters significantly alter the effective diffusion behaviour, flaw-induced perturbations can be partially masked by global shifts in waveform timing or amplitude.

For this reason, uncertainty propagation alone is insufficient for reliable flaw discrimination. While it quantifies the sensitivity of individual scalar features to physical parameters, it does not account for correlated variations across the full transient response. Flaw detection requires distinguishing localized perturbations from global parameter-driven variability, which becomes increasingly challenging under weak-coupling or high lift-off conditions.

These observations motivate the transition to multivariate statistical approaches in the following chapter. By analyzing the entire waveform rather than isolated scalar features, the subsequent framework aims to separate flaw-induced signal structure from material- and geometry-induced variability, thereby improving robustness to uncertainty and enhancing classification performance.

8 Fastener Inspection Results

8.1 General

This chapter presents a structured evaluation of eddy current inspection, beginning with conventional ET for probe alignment and fastener localization. Results highlight the limitations of amplitude-based defect detection at elevated lift-offs. Raw time-domain signals from PEC probes are analyzed to address this, revealing diminished flaw separability under low-conductivity conditions. PCA is applied to extract dominant signal modes, enabling compact representation and improved robustness. Discriminant analysis is then used to classify notched and unnotched fasteners, with statistically derived confidence thresholds supporting reliable detection across varied materials, geometries, and probe configurations.

8.2 Conventional ET Inspection

Accurate probe alignment and effective signal interpretation are critical in ET inspections, particularly when locating fasteners and detecting subtle defects such as notches beneath surface coatings or RAM. Both misalignment and elevated lift-off distances can significantly degrade signal quality, adversely affecting fastener localization and defect characterization.

8.2.1 Probe Alignment Methodology

When fasteners are concealed beneath RAM, precise probe positioning is essential because visual alignment is unavailable, leaving electromagnetic feedback as the only alignment cue. To address this challenge, ET inspections were performed with a NORTEC 600D on the HLT313DL8–16 standard. As introduced in Section 3.2, the ZEUS, THOR, and ODIN probes were evaluated to assess sensitivity to lateral misalignment and positioning repeatability under varying lift-off conditions. The lateral misalignment was applied with respect to the fastener-centre standard shown in Figure 3.4.

Figure 8.1 illustrates the variation in ET response due to lateral displacement at lift-offs of 2 mm and 10 mm. In each plot, colour encodes the probe's lateral displacement along the y-direction

relative to the fastener centre: red denotes accurate alignment, blue indicates a 5 mm offset, and green indicates a 10 mm offset.

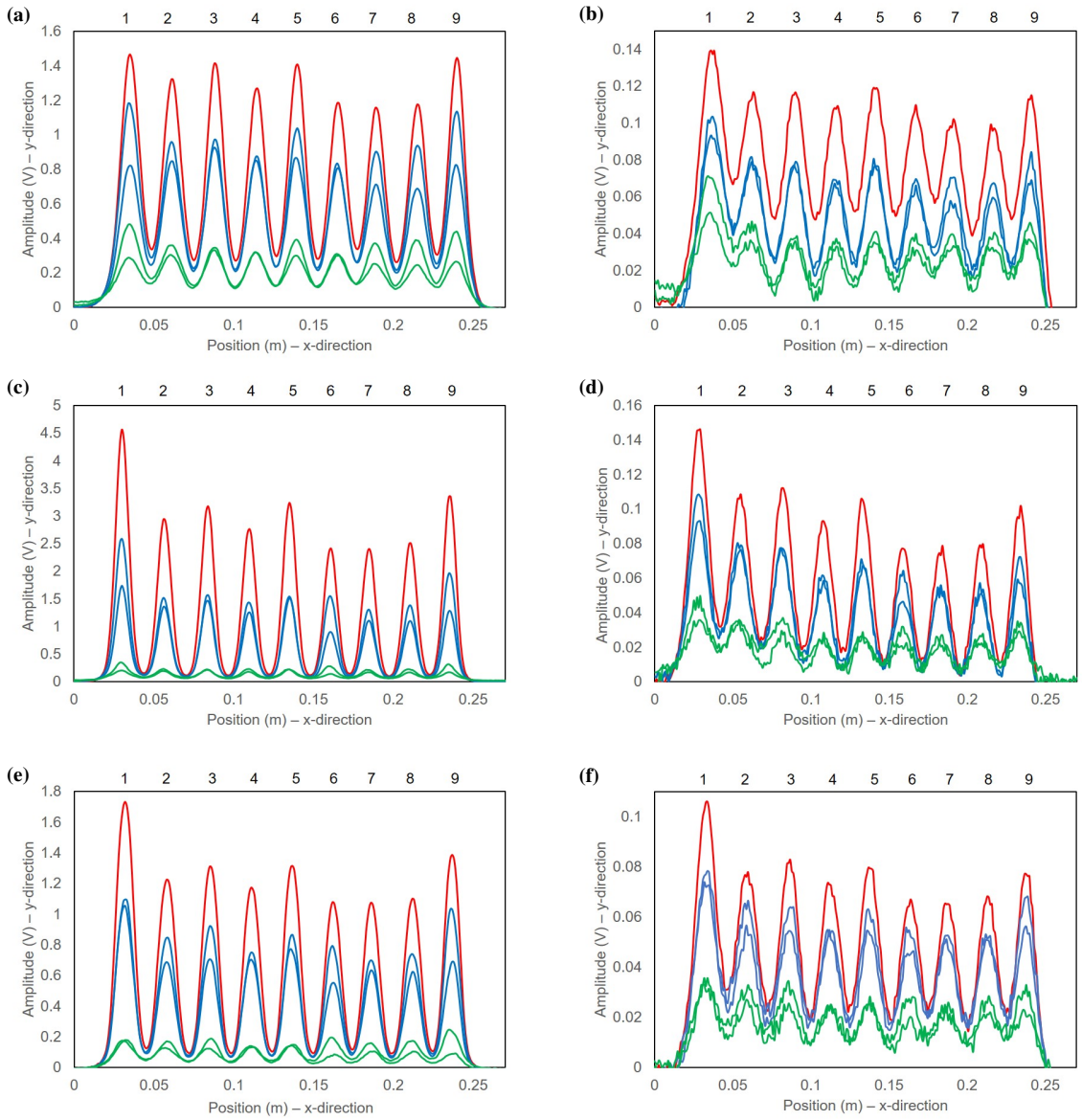

Figure 8.1: ET responses from THOR, ODIN, and ZEUS probes on the HLT313DL8–16 standard at nominal probe heights of 2 mm and 10 mm. (a)–(b) THOR, (c)–(d) ODIN, and (e)–(f) ZEUS. Colour indicates lateral displacement: red (centered), blue (5 mm), green (10 mm).

As shown in Figure 8.1, the impact of lateral misalignment increases with lift-off due to reduced electromagnetic coupling. The consequent loss of spatial resolution complicates accurate fastener localization. These observations underscore the need for precise and repeatable probe positioning, particularly in field scenarios involving concealed fasteners and RAM or thick surface coatings.

To facilitate alignment, a program was developed in LabVIEW 2021 to automatically identify each fastener centre irrespective of initial probe placement. The algorithm used real-time peak amplitude and phase-shift metrics, thereby mitigating lift-off and surface-condition variability. Alignment accuracy was verified by drilling small reference holes at the geometric centres of selected fasteners, as depicted in Figure 8.2.

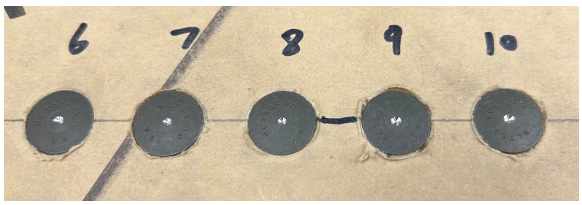

Figure 8.2: Drilled reference holes at fastener centres for alignment verification.

A borescope camera embedded within a crosshair probe (Figure 8.3) provided visual confirmation. When correctly centered, the drilled hole was not visible, as illustrated in Figure 8.4(a); misalignment brought the hole into the field of view, as shown in Figure 8.4(b), confirming the positional offset.

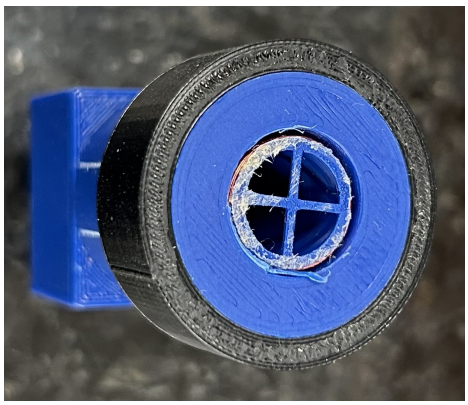

Figure 8.3: Crosshair probe with embedded borescope for visual alignment verification.

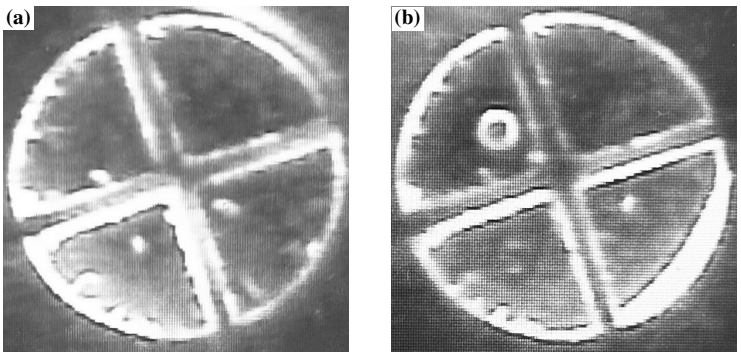

Figure 8.4: Borescope images showing (a) correct alignment, and (b) misalignment (hole visible).

Repeated measurements across ten fasteners demonstrated positioning repeatability within ± 0.5 mm, confirming the robustness of the alignment procedure. This precision was maintained across varying lift-offs and surface conditions, supporting its suitability for field inspections where manual alignment is impractical.

8.2.2 Fastener Localization and Notch Detection Performance

To evaluate conventional ET under realistic inspection conditions, scans were conducted using the ZEUS probe at a nominal probe height of 1 mm above the sample surface, corresponding to an effective lift-off of 2.3 mm above the fasteners. For the HLT265 ferromagnetic and HLT313 titanium specimens, this further translates to lift-offs of 8.7 mm and 15.7 mm above the angled aluminum, respectively. Time-domain signals were smoothed using a Savitzky-Golay filter implemented in Python to improve SNR and feature clarity, as described in Section 4.3.

Figure 8.5 presents results for HLT265 ferromagnetic fasteners: (a) HLT265TB8–6 (6.4 mm) and (b) HLT265TB10–18 (13.4 mm), as shown in Table 3.3. The 100 kHz response (orange) was used for fastener localization, and the 10 kHz response (blue) was used for notch detection. Grey vertical lines mark fastener positions; detected notches are indicated in red, consistent with Figure 3.4.

Figure 8.5 presents results for the HLT265 ferromagnetic fasteners, where Figure 8.5 (a) corresponds to the 6.4 mm thick sample (HLT265TB8-6) and Figure 8.5 (b) corresponds to the 13.4 mm thick sample (HLT265TB10-18), as shown in Table 3.3. The 100 kHz response (orange) was used for fastener localization, and the 10 kHz response (blue) was used for notch detection. Grey vertical lines mark fastener positions; detected notches are indicated in red, consistent with Figure 3.4

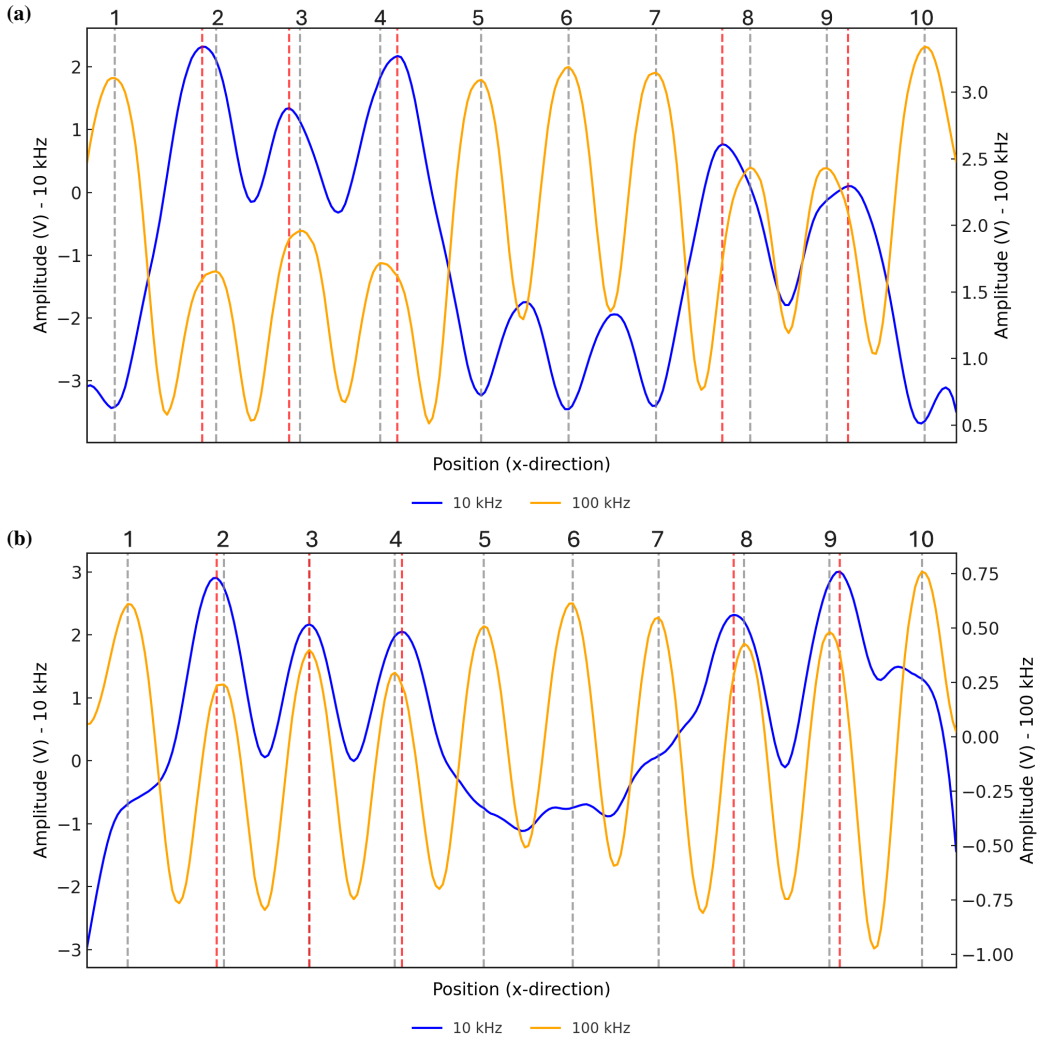

Figure 8.5: Conventional ET notch detection and fastener localization for HLT265 samples: (a) HLT265TB8-6 (6.4 mm) and (b) HLT265TB10-18 (13.4 mm). Grey vertical lines indicate fastener positions; red vertical lines indicate detected notches.

For the 6.4 mm specimen (Figure 8.5(a), the 10 kHz signal clearly reveals notches near Fasteners 2, 3, 4, 8, and 9; the 100 kHz response also highlights these locations, though the lower frequency provides stronger notch contrast. For the 13.4 mm specimen (Figure 8.5(b), the 10 kHz response still indicates notches near Fasteners 2, 3, 4, 8, and 9, while the 100 kHz response is attenuated and is useful primarily for fastener localization. Increasing thickness thus impairs high-frequency notch sensitivity, motivating lower-frequency excitation for enhanced penetration and defect visibility. This suggests that increasing material thickness impairs notch detection at higher frequencies, motivating lower-frequency excitation for penetration and defect visibility.

Figure 8.6 shows analogous results for the HLT313 titanium series: (a) HLT313DL8–9 (6.4 mm)

and (b) HLT313TA10–13 (13.4 mm) per Table 3.3. As above, 10 kHz was used for notch detection and 100 kHz for fastener localization.

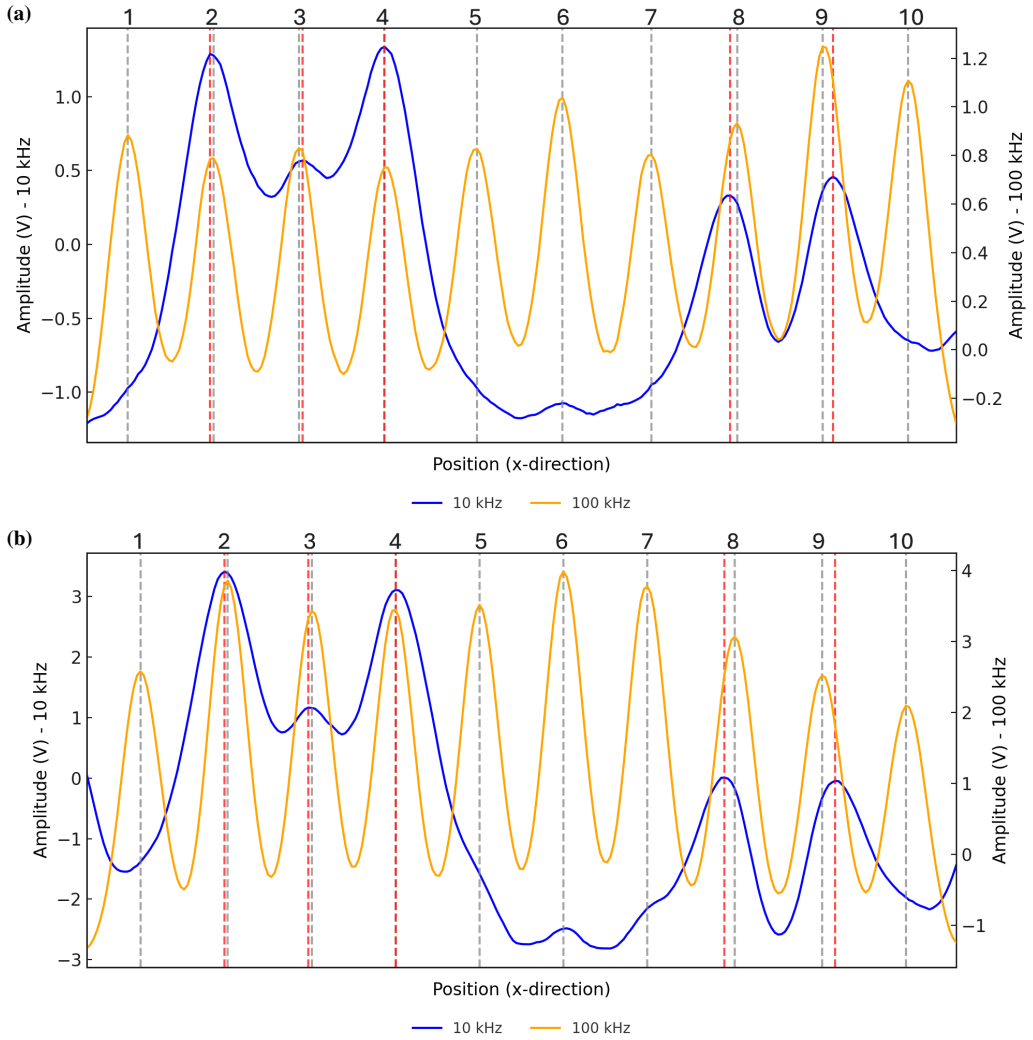

Figure 8.6: Conventional ET notch detection and fastener localization for HLT313 samples: (a) HLT313DL8-9 (6.4 mm) and (b) HLT313TA10-13 (13.4 mm). Grey vertical lines indicate fastener positions; red vertical lines indicate detected notches.

As shown in Figure 8.6, the 10 kHz signal consistently identifies notch locations near Fasteners 2, 3, 4, 8, and 9 for both thicknesses. The 100 kHz signal primarily indicates fastener positions with negligible notch sensitivity, reinforcing the need for lower frequencies to achieve reliable notch detection in thicker or lower-conductivity materials. In comparison, higher frequencies remain advantageous for fastener localization due to their enhanced resolution near the surface.

8.2.3 Limitations at Elevated Lift-Offs

To establish the operational limits of conventional ET, additional inspections were performed at increased lift-offs on the 13.4 mm titanium fastener sample (HLT313TA10–13). Scans were acquired at nominal probe heights of 5 mm and 10 mm above the sample surface, corresponding to effective lift-offs of 6.3 mm and 11.3 mm above the fasteners, and 19.7 mm and 24.7 mm above the angled aluminum, respectively. Figure 8.7 summarizes the results: (a) 19.7 mm and (b) 24.7 mm above the angled aluminum.

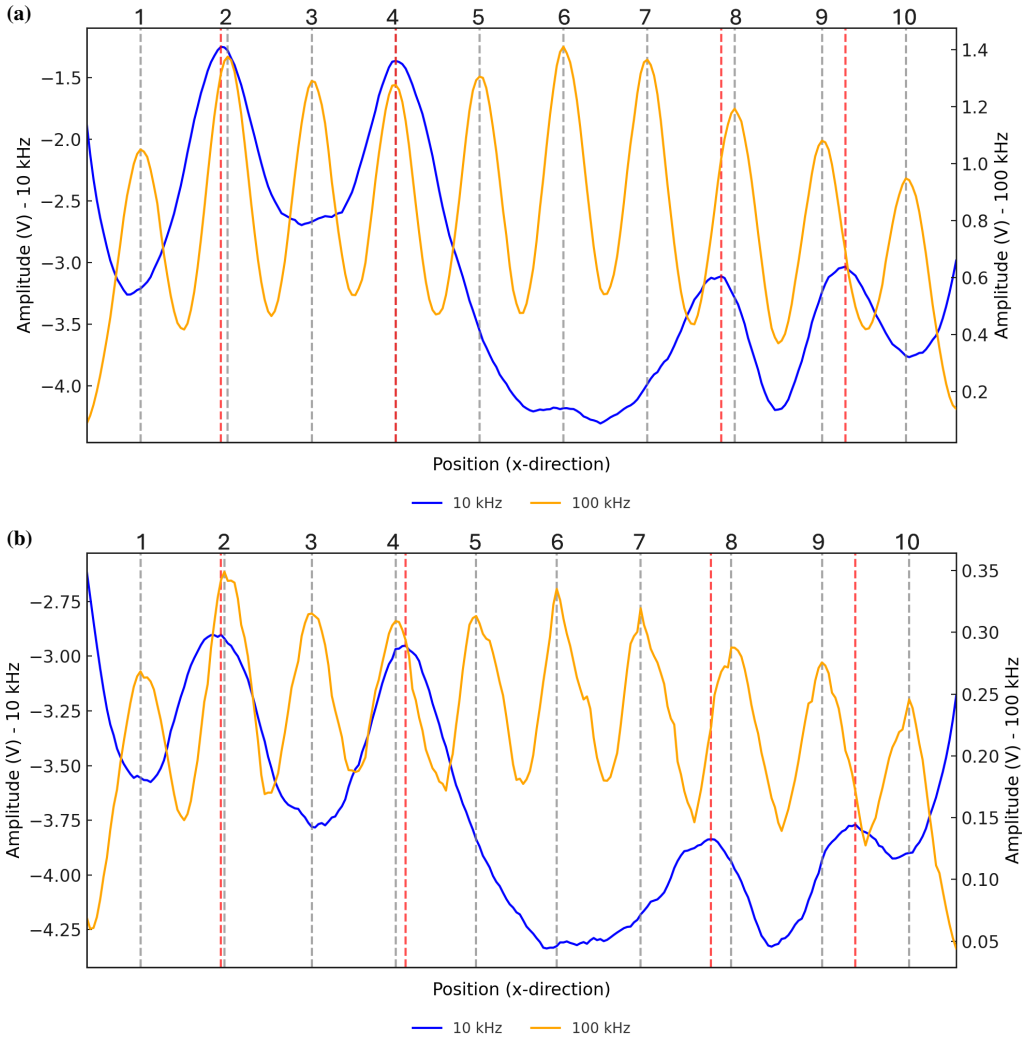

Figure 8.7: Conventional ET notch detection and fastener localization for HLT313TA10-13 sample at lift-offs above the angle aluminum of (a) 19.7 mm and (b) 24.7 mm. Grey vertical lines indicate fastener positions; red vertical lines indicate detected notches.

At both lift-offs, the 10 kHz signal indicates notches near Fasteners 2, 4, 8, and 9, but no distinct peak near Fastener 3; however, the amplitude remains elevated. The missing indication is plausibly

due to overlapping eddy current fields from Fasteners 2 and 4; broadened interaction zones can coalesce into a single ambiguous peak at high lift-off, a known artefact in which field spread and interference dominate [53]. The 100 kHz response remains effective for fastener localization but exhibits negligible notch sensitivity at these lift-offs.

These results demonstrate that fasteners are reliably detected at lift-offs of up to 11.3 mm, whereas notch detection is feasible only under favourable conditions (observed up to 24.7 mm). However, the SNR degrades markedly as lift-off increases, limiting the reliability of conventional ET for notch characterization, especially at greater lift-offs and in thicker or more complex geometries.

In summary, conventional ET is effective for fastener localization and, under moderate lift-offs, for notch detection. Performance degrades with increased lift-off and material complexity, motivating the adoption of advanced inspection methodologies, such as PEC, which offer enhanced sensitivity and robustness in scenarios involving variable lift-off, concealed fasteners, and low-conductivity fasteners with high-conductivity aluminum wing spars.

8.3 Raw Time-Domain Signal Analysis

Time-domain analysis forms the foundation of most traditional PEC inspection techniques. These methods typically involve extracting discrete features from the voltage response induced in the pickup coil, such as the initial peak amplitude, zero-crossing time, and exponential decay rate, with certain features exhibiting a LOI. Such features are linked to the electromagnetic diffusion behaviour within the test specimen and are sensitive to variations in geometry, material properties, and the presence of flaws. However, the diagnostic utility of these features diminishes at elevated lift-off distances due to increased signal attenuation, extended electromagnetic field penetration, and the resultant superposition of multiple response components.

This limitation is especially critical in aircraft inspection, where conductive skins and additional surface layers—such as corrosion-inhibiting primers, paint systems, or RAM coatings—often produce lift-offs exceeding several millimetres. In composite airframe structures, additional lift-off is introduced by CFRP layers, with thicknesses approaching 0.8 in. ($\sim$ 20 mm) in the CF-18 aircraft [9], [10]. In this study, raw time-domain signals were acquired from fasteners embedded in specimens with a 6.4 mm skin thickness. The probes were positioned at a nominal lift-off of 1 mm above the outer surface, resulting in a total effective lift-off of approximately 2.3 mm above the fastener heads. Four representative fastener positions were selected for analysis based on the presence or absence of manufactured notches, as indicated in Figure 3.4.

Figure 8.8 presents representative signals acquired using the ZEUS probe, which employs a vertically differential pair of pickup coils to enhance lift-off sensitivity, as described in Section 3.2. Per Table 3.3, Figure 8.8(a) corresponds to the HLT265TB10-12 specimen containing ferrous steel fas-

teners, while Figure 8.8(b) shows data from the HLT313DL8-9 specimen with non-ferrous titanium fasteners. For the steel sample, signals from notched Fasteners 4 and 8 (see Figure 3.4) display a consistent reduction in primary peak amplitude and a modified decay profile relative to unnotched Fasteners 6 and 10, enabling reliable discrimination. In contrast, although amplitude-based differences persist in the titanium sample, they are less pronounced, and the overlap between notched and unnotched responses becomes more pronounced. Subtle differences in secondary features—such as zero-crossing timing and trailing decay slope—remain detectable but are increasingly ambiguous.

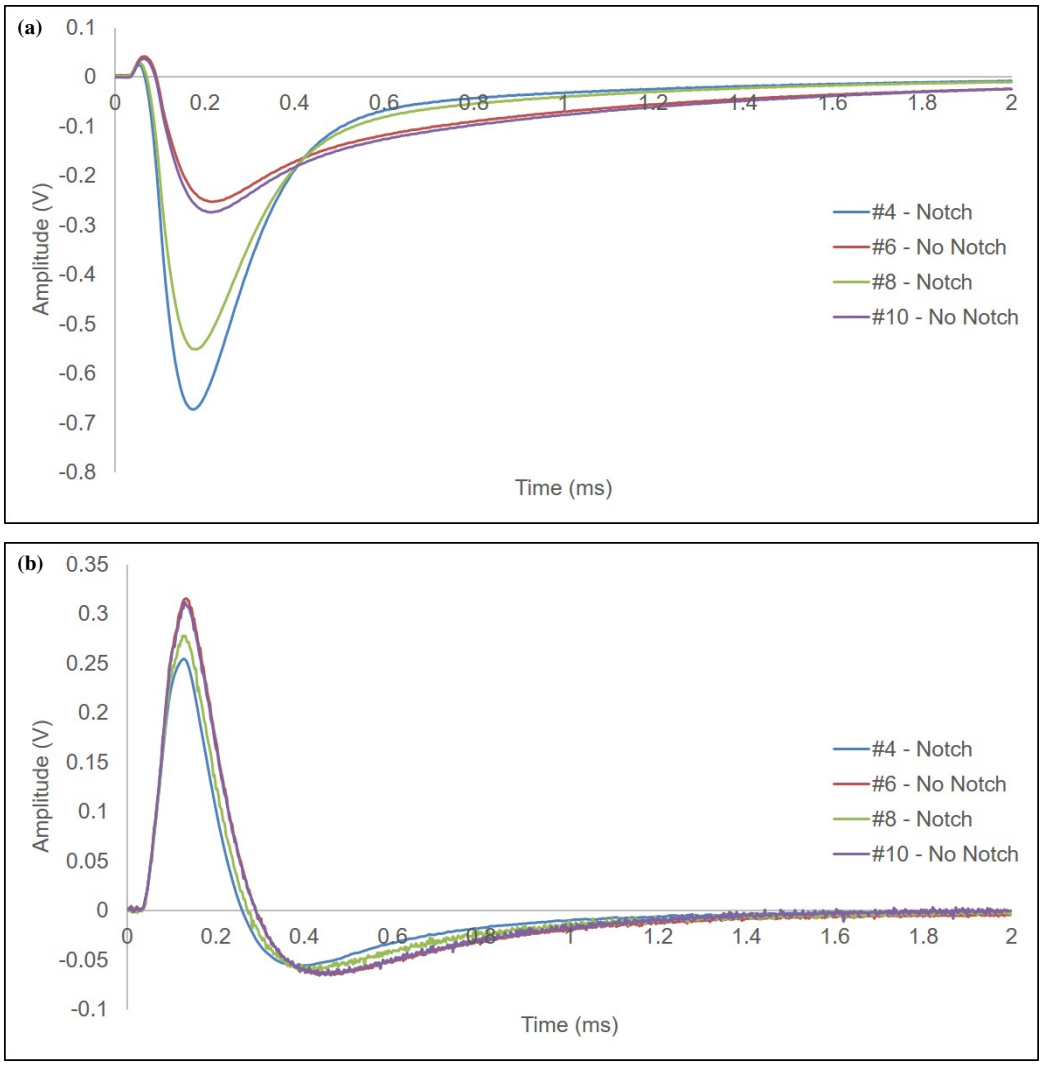

Figure 8.8: Raw time-domain responses using the ZEUS probe at four fastener locations for standard (a) HLT265TB10-12 and (b) HLT313DL8-9.

Figure 8.9 illustrates the corresponding responses acquired with the THOR probe under identical conditions. Unlike ZEUS, THOR employs a single pickup coil configuration with orthogonal

magnetic field orientation, as described in Section 3.2. As shown in Figure 8.9(a), signals from notched Fasteners 4 and 8 and unnotched Fasteners 6 and 10 (Figure 3.4) in the steel specimen exhibit minimal separation, particularly between Fasteners 6 and 8, whose amplitudes are nearly identical despite the presence of a notch. Figure 8.9(b) further underscores the limitations of scalar time-domain features in titanium specimens, where signal amplitudes and decay profiles converge within experimental uncertainty. These results demonstrate the reduced sensitivity of traditional single-feature metrics under high lift-off and low-conductivity conditions. A feature at approximately $0.3\,\mathrm{ms}$ in Figure 8.9(a) and $0.48\,\mathrm{ms}$ in Figure 8.9(b) is attributed to non-ideal probe construction, including finite coil geometry and pickup coil asymmetry. As it appears in both defect and non-defect signals, it does not contribute to flaw discrimination.

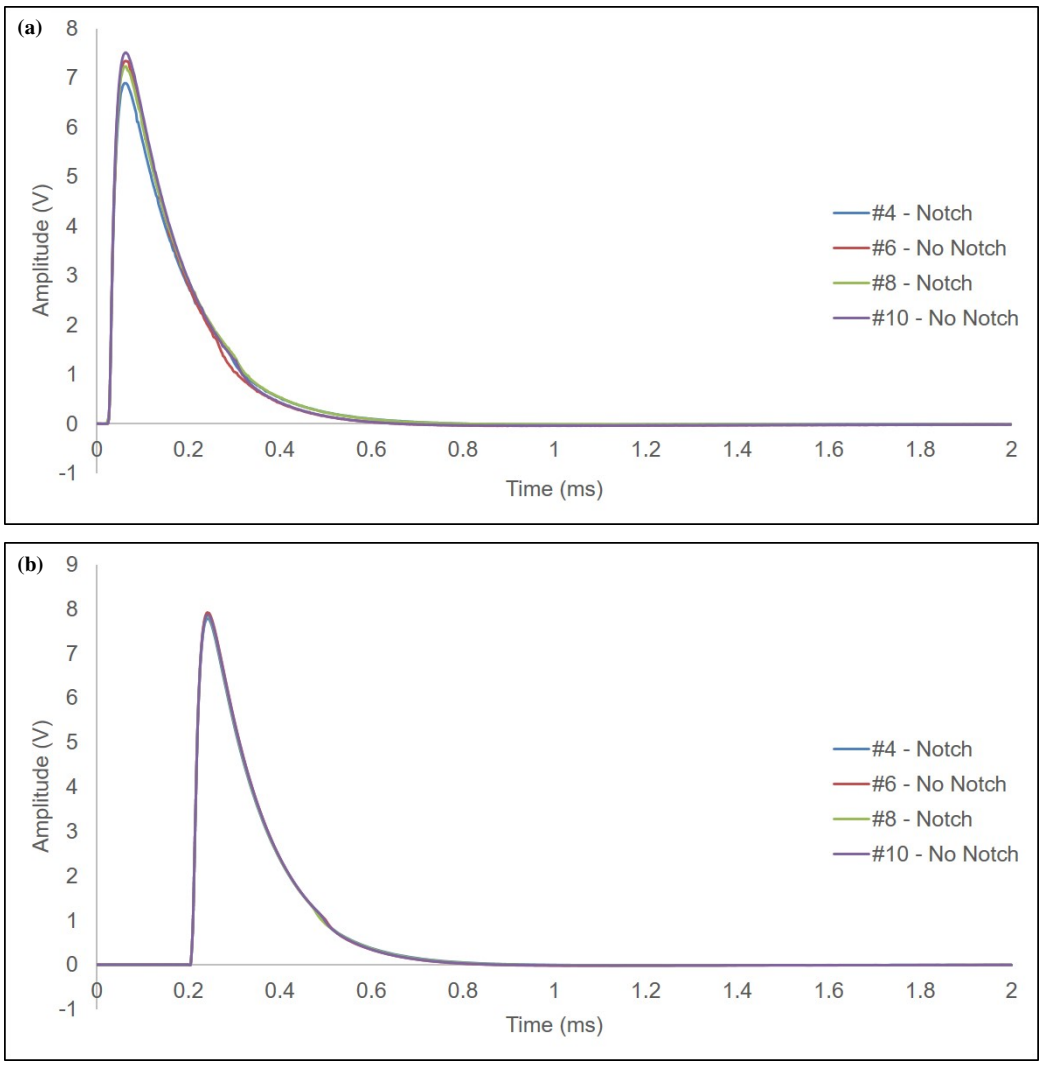

Figure 8.9: Raw time-domain responses using the THOR probe at four fastener locations for standard (a) HLT265TB10-12 and (b) HLT313DL8-9.

Figure 8.10 presents results obtained using the ODIN probe, as described in Section 3.2. Consistent with the previous findings, peak-based analysis in the steel specimen (Figure 8.10(a)) yields inconsistent classification performance, with substantial overlap between notched and unnotched responses. For the titanium specimen (Figure 8.10(b)), the inability of amplitude and decay-based features to resolve notch presence is evident, reflecting the combined effects of low permeability, reduced signal amplitude, and an elevated noise floor.

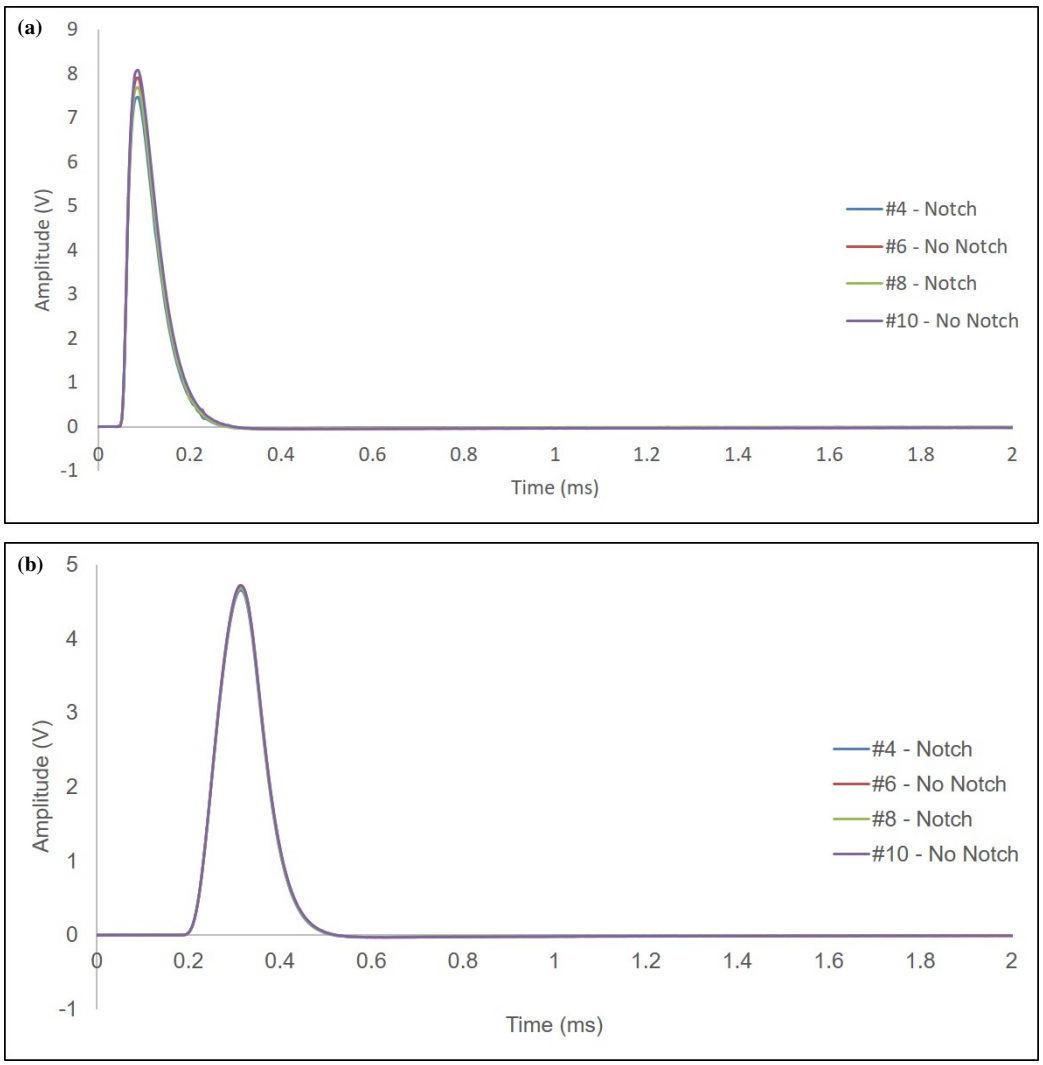

Figure 8.10: Raw time-domain responses using the ODIN probe at four fastener locations for standard (a) HLT265TB10-12 and (b) HLT313DL8-9.

These results reveal a common limitation across probe architectures: the inability of conventional time-domain feature-extraction techniques to provide robust, repeatable flaw classification under operational lift-off conditions, particularly in non-ferrous environments. While differential

configurations such as ZEUS offer improved resolution, their performance still degrades in low-conductivity materials or when defect contrast is minimal.

These findings motivate transitioning to multivariate signal analysis approaches that leverage the full temporal structure of the waveform rather than reducing it to a limited set of scalar descriptors. Techniques such as PCA and MPCA enable this transition by capturing global variance patterns across the entire signal, facilitating dimensionality reduction prior to classification. The following section explores the implementation of these techniques within a discriminant analysis framework, offering enhanced detection sensitivity and specificity under challenging inspection conditions.

8.4 Principal Component Analysis Process

The initial phase of the PCA workflow entails signal gating to isolate the region of interest where signal variation attributable to flaw presence is most pronounced. As outlined in Section 4.2, the selected time window spans 0.05–0.60 ms. Signals are sampled at 100 kHz, yielding 275 samples per pickup coil for the axisymmetric coil configuration in the THOR probe described in Section 3.2. The two coil signals are concatenated to form a 550-element column vector, thereby capturing two consecutive PEC decays in a single feature vector suitable for principal component analysis.

An illustrative example of a gated signal from the ferromagnetic standard HLT265TB8-6 described in Table 3.3, acquired using the THOR probe, is shown in Figure 8.11. This sample highlights the repeatable transient characteristics that encode lift-off and flaw information, which are subsequently leveraged in the eigenvalue decomposition.

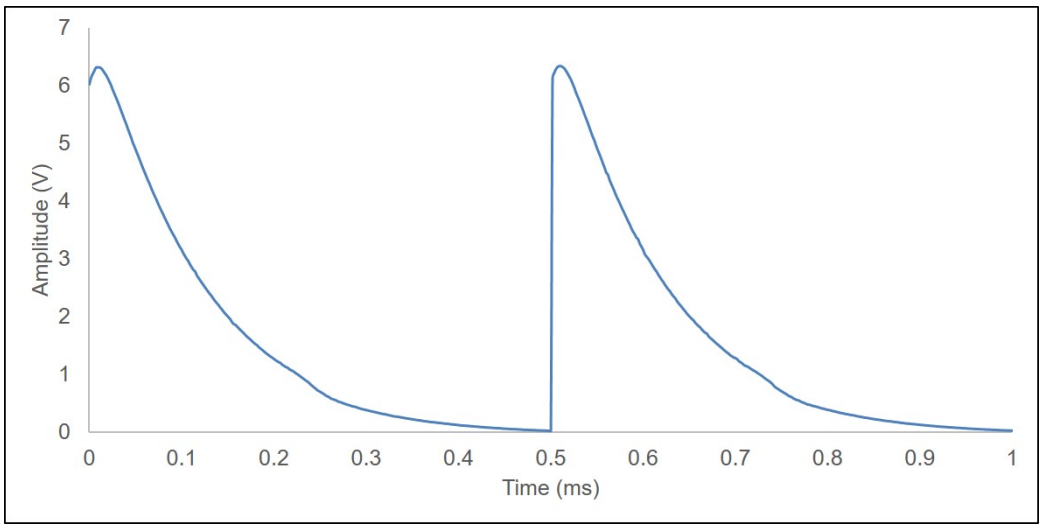

Figure 8.11: Gated PEC signal from THOR probe for specimen HLT265TB8-6, used in PCA analysis.

Eigenvalue decomposition is applied to the gated signals collected for a given sample, produc-

ing an orthonormal basis of eigenvectors (principal components) and associated eigenvalues that quantify the proportion of variance each component explains. Each eigenvector retains the same dimensionality as the input signals (i.e., 550 elements) and represents a time-domain waveform capturing a distinct axis of uncorrelated signal variation. For the HLT265TB8-6 sample described in Table 3.3, measurements were acquired at nominal probe heights of 1 mm, 2 mm, and 3 mm (two measurements per height). The first five eigenvectors derived from these measurements are presented in Figure 8.12.

It is important to note that the nominal probe height specified here refers to the vertical lift-off of the probe housing relative to the surface reference and does not directly correspond to the effective lift-off above the angled aluminum fastener surface. Owing to the probe geometry and the inclination of the aluminum specimen, a nominal probe height of 1 mm corresponds to effective lift-offs of approximately 7.4 mm and 14.4 mm above the aluminum surface for the THOR and ODIN probes. Increasing the nominal probe height to 3 mm increases the corresponding effective lift-offs to approximately 9.4 mm and 16.4 mm.

For the ZEUS probe, a nominal probe height of 1 mm corresponds to effective lift-offs of approximately 8.7 mm and 15.7 mm above the angled aluminum surface, while a nominal height of 3 mm corresponds to effective lift-offs of approximately 10.7 mm and 17.7 mm. As a result, even modest nominal probe lift-offs span effective lift-off distances approaching or exceeding 15 mm, rendering additional nominal lift-off increments unnecessary for this configuration.

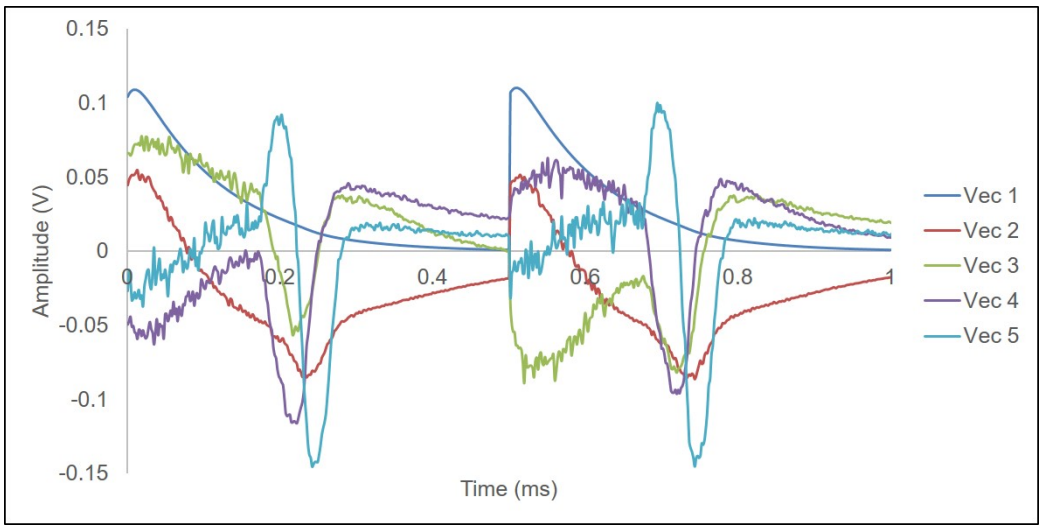

Figure 8.12: First five eigenvectors for the THOR probe derived from specimen HLT265TB8-6.

The corresponding eigenvalues λ_i are reported in Table 8.1. The first eigenvalue dominates the variance structure, indicating that its eigenvector closely approximates the average waveform shape, as seen in Figure 8.12. This observation is consistent with the average signal behaviour in Figure 8.11 and with PCA theory described in Section 2.9. Subsequent eigenvectors capture

progressively smaller, orthogonal sources of variation not explained by prior components. Based on the cumulative variance explained—exceeding 95.3% across the first five components—these five eigenvectors are retained for dimensionality reduction and subsequent classification, as they capture diagnostically relevant signal variation, while minimizing noise and redundancy.

Table 8.1: Eigenvalues corresponding to the first five eigenvectors for HLT265TB8-6.

Eigenvalue	λ_1	λ_2	λ_3	λ_4	λ_5
Value	182294	51.5669	6.39781	6.25306	2.20223

Each gated signal is projected onto this eigenbasis, producing a vector of principal component scores (i.e., PCA coefficients), as defined in Equation 2.74. These scores quantify how strongly each eigenvector is expressed in an individual signal. Retaining only the first five scores enables a compact yet high-fidelity representation that supports noise suppression and computational efficiency.

A scatter plot of the first two scores (Z_1, Z_2) is shown in Figure 8.13. The plot reveals strong clustering and minimal overlap between notched and unnotched signal groups, indicating good class separability. Notably, the second principal component (Z_2) exhibits the clearest separation, with the mean scores of the two classes differing by several standard deviations, indicating that Z_2 captures a dominant portion of defect-related variance.

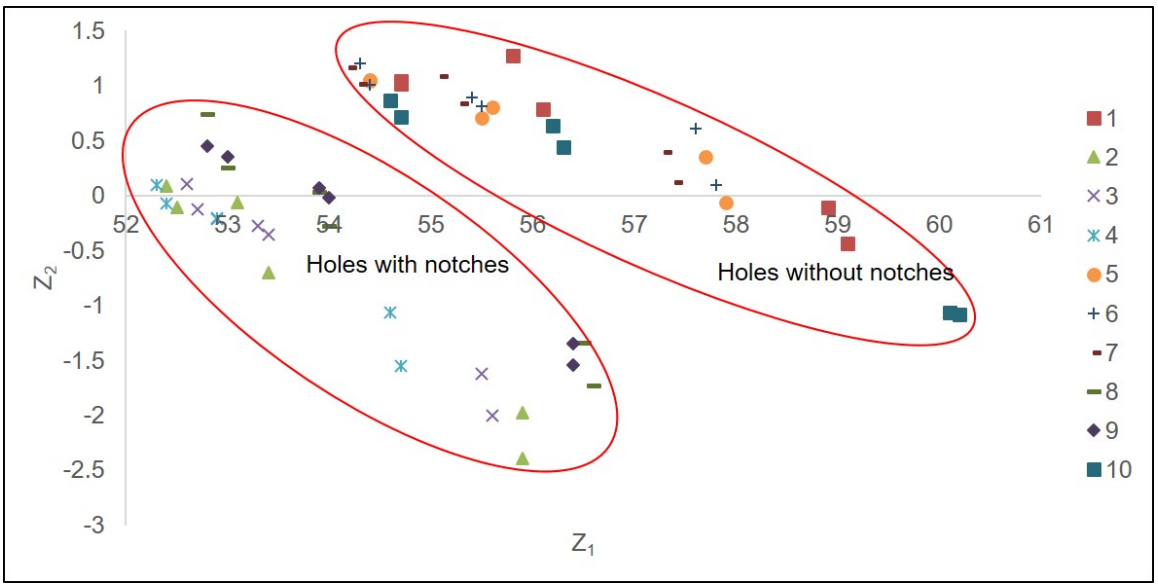

Figure 8.13: Principal component scatter plot of Z_1 versus Z_2 for THOR probe signals from HLT265TB8-6.

The effectiveness of this projection lies in its ability to preserve diagnostically relevant variation, while discarding noise and redundancy. While higher-order components (Z_3 through Z_5)

contribute less to defect discrimination, they capture subtler waveform features that may be useful in downstream statistical classification. Components beyond Z_5, which together explain less than 4.7% of the variance, are excluded to maintain model simplicity and reduce the risk of overfitting.

This five-dimensional feature set serves as the input to the subsequent discriminant analysis procedures described in Section 2.10, which formalize the classification of signal responses based on principal component structure.

8.5 Discriminant Analysis

The discriminant analysis process, introduced in Section 2.10, builds upon the principal component space (e.g., Figure 8.13) to enable quantitative classification of PEC signals. A multiple linear regression model is constructed using the first five principal components of each signal, with regression targets of zero and one assigned to unnotched and notched fasteners, respectively. As first implemented by Horan *et al.* [9], [10], this supervised learning approach effectively maps multidimensional PCA scores into a scalar discriminant score that reflects defect likelihood.

Applying this methodology to the HLT265TB8-6 dataset yields the regression coefficients defined in Equation 2.82. The resulting discriminant scores, shown in Figure 8.14, are plotted for each probe type. These scores provide a continuous output metric representing the degree of similarity between a measured signal and the characteristic response of a known defect condition.

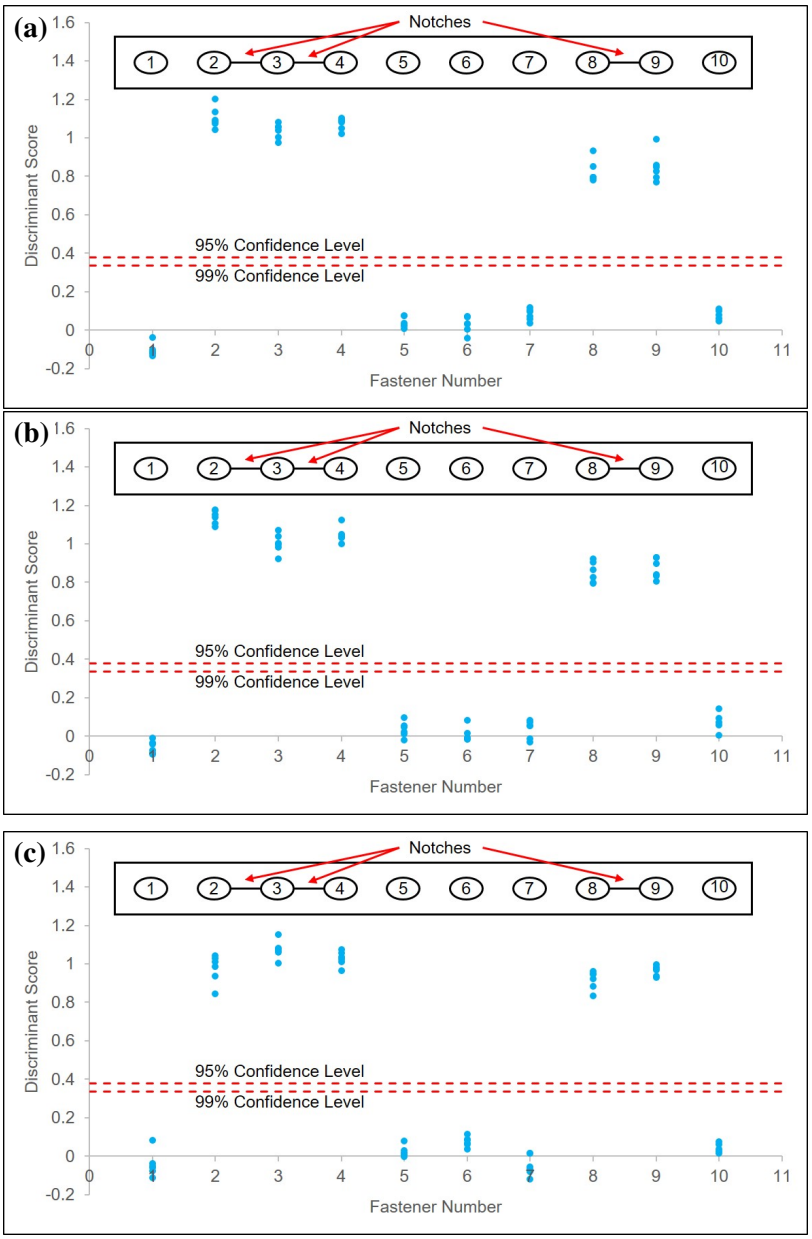

Figure 8.14: Discriminant scores for HLT265TB8-6 fasteners using (a) THOR, (b) ZEUS, and (c) ODIN probes.

The plots clearly illustrate the separation between clusters corresponding to unnotched fasteners (scores near zero) and those containing notches (scores near one), confirming the regression model's discriminative capability. This binary classification framework provides an interpretable and scalable means for real-time defect assessment across diverse inspection conditions.

8.5.1 Discriminant Score Thresholds for False Call Mitigation

The discriminant score thresholds $\hat{D}_{\text{decision}}$ for the ODIN, THOR, and ZEUS probes—computed using Equation 2.83—are summarized in Table 8.2. Thresholds were established at both 95% and 99% confidence levels based on the standard deviation of the scores associated with unnotched fasteners. These thresholds define quantitative decision boundaries beyond which a signal is classified as defective, providing statistical rigour to minimize false negatives and false positives.

Because the regression model is trained with an ideal target of zero for unnotched fasteners, lower threshold values closer to zero correspond to higher confidence in the absence of defects. In contrast, larger threshold values indicate greater overlap between the score distributions of the notched and unnotched classes—typically caused by lower SNR or more subtle flaw signatures.

Table 8.2: Discriminant score thresholds $\hat{D}_{\text{decision}}$ for ODIN, THOR, and ZEUS probes at 95% and 99% confidence levels. Materials: SS = stainless steel, Ti = titanium. "—" indicates not evaluated.

Fastener	**Material**	**Skin (mm)**	**ODIN**		**THOR**		**ZEUS**	
			95%	**99%**	**95%**	**99%**	**95%**	**99%**
HLT53DL8-10	SS	6.4	0.380	0.338	0.383	0.342	0.379	0.336
HLT53TB10-8	SS	6.4	0.381	0.339	0.380	0.338	—	—
HLT53YC10-15	SS	13.4	0.380	0.338	0.382	0.340	0.377	0.334
Family average (HLT53)			0.381	0.338	0.382	0.340	0.378	0.335
HLT265TB8-6	SS	6.4	0.378	0.335	0.380	0.338	0.379	0.337
HLT265TB10-12	SS	6.4	0.379	0.336	0.380	0.337	0.380	0.337
HLT265TB10-18	SS	13.4	0.378	0.335	0.381	0.339	0.378	0.335
Family average (HLT265)			0.378	0.335	0.380	0.338	0.379	0.336
HLT313DL8-9	Ti	6.4	0.380	0.337	0.385	0.345	0.384	0.343
HLT313TA10-13	Ti	13.4	0.390	0.350	0.337	0.380	0.386	0.345
Family average (HLT313)			0.385	0.344	0.383	0.341	0.385	0.344

8.5.2 Family of Fasteners: Classification Performance

To evaluate the robustness of the discriminant analysis approach across varying structural conditions, classification performance was assessed for three families of fasteners: HLT53, HLT265, and HLT313. Each family introduces distinct challenges due to differences in material composition, geometric complexity, and electromagnetic properties. The discriminant scores, derived from the principal component projections of gated PEC signals, quantify the model's ability to differentiate between notched and unnotched conditions.

HLT53 (stainless steel). The HLT53 fasteners, per Figure A.1, consist of stainless-steel bolts embedded in non-conductive skins. The high magnetic permeability of the ferrous fasteners, combined

with the negligible conductivity of the overlay, enables strong inductive coupling and deep magnetic field penetration. These favourable electromagnetic conditions yield highly separable signal characteristics. Among the probes, the ZEUS probe demonstrates exceptional classification performance, with minimal intra-class variance and a pronounced gap between notched and unnotched populations. The THOR and ODIN probes exhibit similar behaviour, with discriminant scores contained within the 95% confidence thresholds listed in Table 8.2. These findings underscore the importance of probe design and optimization in achieving reliable classification performance in layered aerospace structures. *Detailed per-measurement discriminant score plots for all three probes are provided in Appendix D.4 (Figure D.1).*

HLT265 (stainless steel with borehole). The HLT265 fastener family, per Figure A.3, employs stainless-steel fasteners with a central axial borehole designed for sealant injection. Despite this additional geometric complexity, all three probes demonstrate excellent classification performance. The separation between notched and unnotched signals remains highly distinct, with minimal overlap and score distributions that lie well within the 95% and 99% decision thresholds reported in Table 8.2. This consistent separation indicates that the central borehole does not substantially diminish the discriminative capability of the PEC signals. Overall, the HLT265 results exhibit the most uniform and reliable classification boundaries among all families, underscoring the robustness of the discriminant model under moderate structural variation and the reliability of all three probe designs for flaw detection in stainless-steel assemblies. *Complete per-measurement plots for HLT265 fasteners are presented in Appendix D.4 (Figure D.2).*

HLT313 (titanium). The HLT313 fasteners, per Figure A.2, are composed of titanium—a non-ferrous material characterized by low electrical conductivity and negligible magnetic permeability, as discussed in Section 3.7. These material properties inherently limit eddy current induction and magnetic field coupling, reducing the amplitude and contrast of the PEC signal. Despite these challenges, the ZEUS probe maintains a clear separation between notched and unnotched fasteners, with all scores well outside the classification threshold. The THOR and ODIN probes exhibit greater ambiguity, with several unnotched fasteners producing elevated discriminant scores that approach or exceed the 99% confidence boundary. This behaviour reflects the reduced SNR and increased lift-off sensitivity typical of low-conductivity alloys. *Detailed discriminant score distributions for the HLT313 family are shown in Appendix D.4 (Figure D.3).*

These results highlight the influence of material properties and sample geometry on flaw detectability when applying principal component-based discriminant analysis. As discussed in Section 3.7, variations in electrical conductivity and magnetic permeability can substantially alter eddy current penetration depth and signal contrast. When implementing such methods in field applica-

tions, it is essential to account for differences in fastener composition, structural configuration, and lift-off conditions to maintain consistent and reliable defect classification performance.

8.5.3 ODIN Results

Comparison Across Fastener Families Using Family-Based Eigenvectors

Figure 8.15 summarizes the discriminant scores (mean ± SD) for each fastener using family-based eigenvectors specific to each fastener type. The grouped chart provides an overview of classification trends across all materials and lift-offs, while the detailed per–fastener scatter plots are included in Appendix D.4 (Figure D.1, Figure D.2, Figure D.3). The term *family* refers to an aggregated dataset comprising all specimens of a given fastener type (e.g., HLT53, HLT265, HLT313) measured across multiple nominal lift-off heights. For each lift-off condition, two repeated measurements were acquired per fastener, expanding the dataset to capture geometric and positional variability. The corresponding family-level summary statistics are provided in Table 8.3, while full numerical results are available in Appendix D.1 (Table D.1) for completeness.

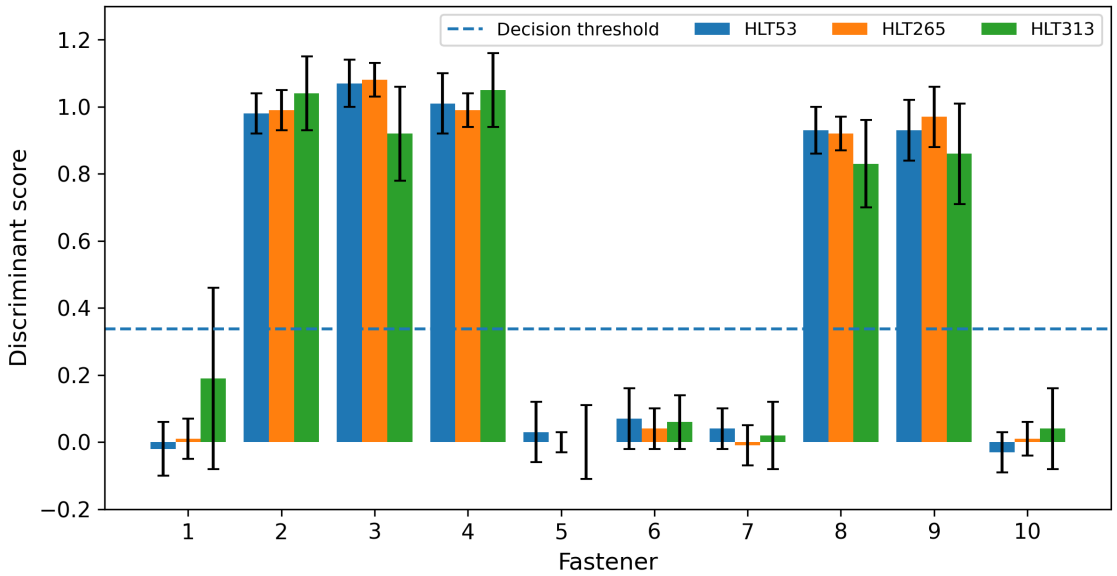

Figure 8.15: Grouped bar chart of discriminant scores (mean ± SD) by fastener and family using family-based eigenvectors; the dashed line indicates the 99% decision threshold.

Table 8.3: Summary statistics across fastener families using family-based eigenvectors.

Family	Mean ($\bar{x}$)	SD	Correct Classification (%)
HLT53	0.501	0.076	100
HLT265	0.500	0.056	100
HLT313	0.501	0.132	97.8

The HLT53 ferromagnetic fasteners exhibit strong electromagnetic coupling and low geometric complexity, leading to consistently high discriminant scores for notched Fasteners 2–4 and 8–9 and low scores for unnotched Fasteners 1, 5–7, 10 (see Figure 3.4 and Appendix D.1, Table D.3). Standard deviations remain small (typically below 0.09), indicating robust and repeatable classification under the family-based eigenvector framework. The HLT265 fasteners, also ferromagnetic but incorporating a central borehole, maintain comparable discrimination performance—again showing elevated means for notched fasteners and near-zero means for unnotched ones—demonstrating the ODIN probe's ability to generalize across moderate geometric variations (see Appendix D.1, Table D.4). The HLT313 titanium fasteners present a more challenging scenario due to their low conductivity and near-unity relative permeability (Section 3.7). Notched Fasteners 2–4 and 8–9 remain above the decision boundary, although the associated standard deviations are higher (generally above 0.1), reflecting weaker coupling and increased uncertainty (see Appendix D.1, Table D.2). Edge-proximal Fastener 1 also shows greater variability, consistent with expected edge-effect behaviour.

Overall, the family-based eigenvector approach provides high classification fidelity across all materials, producing strong contrast between notched and unnotched conditions with modest within-class variation. These results validate the use of pooled eigenvector sets for field-deployable pulsed eddy current inspection where individual sample calibration is impractical.

Effect of Eigenvector Selection

To assess the influence of eigenvector generation, Table 8.4 reports the average change in mean and standard deviation between self-derived and family-based eigenvectors (Self − Family) across all fasteners. These averages were computed from the detailed per–fastener values listed in Appendix D.1 (Table D.3, Table D.2, Table D.4). The results demonstrate that family-based eigenvectors yield slightly lower variability and more stable classification boundaries, particularly for low-conductivity materials such as titanium. This advantage arises because pooled eigenvectors incorporate broader training diversity, mitigating overfitting effects observed when eigenvectors are derived from smaller, self-calibrated datasets.

Table 8.4: Change relative to family eigenvectors for self-derived sets (ΔSelf $-$ Family), averaged across fasteners.

Family	Self Set	ΔMean	ΔSD
HLT53	HLT53DL8-9	-0.002	-0.019
HLT53	HLT53DL10-8	-0.002	-0.012
HLT53	HLT53YC10-15	-0.002	0.001
HLT265	HLT265TB8-6	0	-0.017
HLT265	HLT265TB10-12	0.001	-0.015
HLT265	HLT265TB10-18	0.001	-0.009
HLT313	HLT313DL8-9	-0.001	-0.052
HLT313	HLT313TA10-13	-0.002	0.014

Effect of Nominal Probe Height (Lift-Off)

To evaluate lift-off sensitivity, Table 8.5 summarizes the mean discriminant scores for HLT265 fasteners measured at nominal probe heights of 1, 2, and 3 mm, averaged across all notched and unnotched conditions. Three separate datasets—HLT265TB8-6, HLT265TB10-12, and HLT265TB10-18—were analyzed to capture the influence of material thickness and geometry. The detailed fastener-level discriminant results for these datasets are provided in Appendix D.1 (Table D.4).

Table 8.5: Mean discriminant scores ($\bar{x}\pm$SD) for HLT265 across lift-offs of 1–3 mm (per fastener).

Fastener	HLT265TB8-6	HLT265TB10-12	HLT265TB10-18
1	-0.04 ± 0.03	0.03 ± 0.02	0.05 ± 0.01
2	0.97 ± 0.06	1.01 ± 0.01	0.98 ± 0.03
3	1.07 ± 0.03	1.13 ± 0.03	1.04 ± 0.03
4	1.03 ± 0.03	1.03 ± 0.02	0.95 ± 0.06
5	0.02 ± 0.02	-0.01 ± 0.02	-0.02 ± 0.01
6	0.07 ± 0.02	0.04 ± 0.04	-0.01 ± 0.01
7	-0.05 ± 0.05	-0.02 ± 0.02	0.03 ± 0.02
8	0.91 ± 0.03	0.87 ± 0.03	0.94 ± 0.01
9	0.96 ± 0.02	0.89 ± 0.01	1.05 ± 0.03
10	0.04 ± 0.01	0.03 ± 0.02	-0.04 ± 0.02

Across all lift-off conditions, classification remains stable. Notched Fasteners 2, 3, 4, 8, and 9 consistently produce elevated scores exceeding the 99% decision threshold ($\hat{D}_{\text{decision}} = 0.335$), while unnotched Fasteners 1, 5–7, 10 cluster near zero regardless of probe height. Minor reductions in score magnitude with increasing lift-off are observed for Fasteners 3 and 9, indicating

slight attenuation due to lift-off; however, these changes are within acceptable limits and do not compromise classification reliability. Overall, the ODIN probe demonstrates stable performance across fastener families, lift-offs, and eigenvector generation strategies, supporting its suitability for practical inspection scenarios involving both ferrous and non-ferrous fasteners.

8.5.4 THOR Results

Comparison Across Fastener Families Using Family-Based Eigenvectors

Figure 8.16 summarizes the per–fastener discriminant scores (mean ± SD) for HLT53, HLT265, and HLT313 using family-based eigenvectors. The grouped chart provides an overview of classification trends across all materials and lift-offs, while the detailed per–fastener scatter plots are included in Appendix D (Figure D.1, Figure D.2, Figure D.3). As with the ODIN probe, *family* denotes an aggregated dataset for each fastener type measured across multiple nominal lift-offs, with two repeated measurements per height to capture geometric and positional variability. A compact family-level summary is provided in Table 8.6, while full per–fastener tables are listed in Appendix D (Table D.6) for completeness.

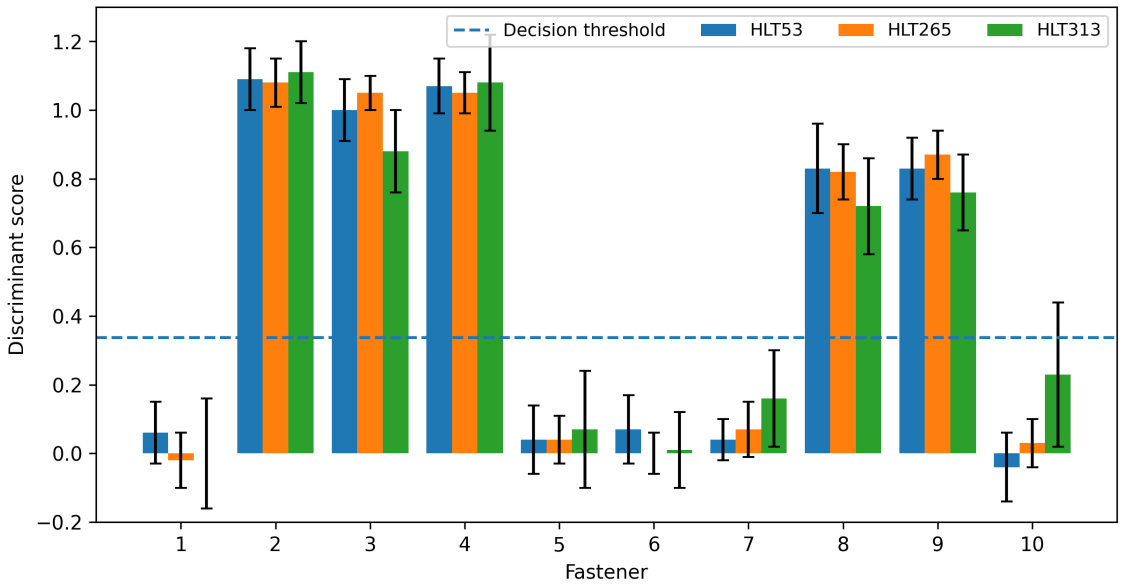

Figure 8.16: Grouped bar chart of discriminant scores (mean ± SD) by fastener and family using family-based eigenvectors for the THOR probe; the dashed line indicates the 99% decision threshold (Table 8.2).

Table 8.6: Summary statistics across fastener families using family-based eigenvectors (THOR).

Family	Mean ($\bar{x}$)	SD	Correct Classification (%)
HLT53	0.499	0.093	100.0
HLT265	0.500	0.056	100.0
HLT313	0.532	0.139	97.8

For the HLT53 and HLT265 ferromagnetic fasteners, THOR exhibits strong flaw detectability: notched Fasteners 2–4 and 8–9 consistently exceed the 99% decision threshold (Table 8.2), while unnotched Fasteners 1, 5–7, 10 remain near zero (see Appendix D, Table D.8, and Table D.9). Standard deviations are modest (generally < 0.10), indicating stable classification despite geometric variation and minor alignment changes. In contrast, HLT313 (titanium) yields lower average scores and increased variance. Notched fasteners still show elevated means, but SDs are typically $\gtrsim 0.12$, reflecting reduced SNR due to low conductivity and near-unity relative permeability (Appendix D, Table D.7). Variability at Fastener 10 also suggests edge-related artefacts. Overall, THOR performs robustly on ferromagnetic families; titanium classification remains achievable but with greater uncertainty.

Effect of Eigenvector Selection

To succinctly compare family-based and self-derived eigenvectors, Table 8.7 reports the average change (Self $-$ Family) in mean and SD across fasteners for each family. These averages are derived from the detailed per–fastener values reported in Appendix D (Table D.8, Table D.9, Table D.7). Family-based eigenvectors generally reduce within-class variability and provide more stable decision margins, whereas self-eigenvectors can tighten clustering locally but at the risk of elevated variance or occasional false-positive drift in unnotched cases.

Table 8.7: Change relative to family eigenvectors for self-derived sets (THOR; ΔSelf $-$ Family), averaged across fasteners.

Family	Self Set	ΔMean	ΔSD
HLT53	HLT53DL8-9	-0.001	-0.012
HLT53	HLT53DL10-8	-0.001	-0.041
HLT53	HLT53YC10-15	0.000	0.006
HLT265	HLT265TB8-6	0.003	-0.017
HLT265	HLT265TB10-12	0.000	0.002
HLT265	HLT265TB10-18	0.000	0.007
HLT313	HLT313DL8-9	-0.026	-0.054
HLT313	HLT313TA10-13	-0.032	-0.081

Effect of Nominal Probe Height (Lift-Off)

Lift-off sensitivity for HLT265 is summarized in Table 8.8 as the mean (and SD) across 1–3 mm for each fastener and self set (TB8-6, TB10-12, TB10-18). The full lift-off matrices and per–fastener discriminant score tables are available in Appendix D (Table D.10). Across all three sets, notched Fasteners 2, 3, 4, 8, 9 remain above the 99% threshold, while unnotched Fasteners 1, 5–7, 10 cluster around zero. Minor lift-off trends remain well within acceptable margins and do not impair classification reliability.

Table 8.8: Mean discriminant scores ($\bar{x}\pm$SD) across lift-offs of 1–3 mm for HLT265 (THOR).

Fastener	HLT265TB8-6	HLT265TB10-12	HLT265TB10-18
1	-0.10 ± 0.01	-0.01 ± 0.02	0.01 ± 0.07
2	1.10 ± 0.03	1.04 ± 0.03	1.15 ± 0.02
3	1.04 ± 0.01	1.09 ± 0.03	1.06 ± 0.02
4	1.07 ± 0.02	1.08 ± 0.02	0.99 ± 0.01
5	0.04 ± 0.01	0.01 ± 0.06	0.03 ± 0.03
6	0.03 ± 0.02	0.03 ± 0.04	-0.01 ± 0.01
7	0.08 ± 0.00	0.07 ± 0.05	0.07 ± 0.06
8	0.83 ± 0.03	0.84 ± 0.02	0.81 ± 0.06
9	0.85 ± 0.02	0.86 ± 0.07	0.84 ± 0.04
10	0.08 ± 0.02	-0.01 ± 0.02	0.06 ± 0.02

Overall, the THOR probe demonstrates high classification accuracy across material families, nominal lift-offs, and eigenvector strategies. Family-based eigenvectors offer robust generalization and noise suppression suitable for practical inspections where self-calibration may be infeasible.

8.5.5 ZEUS Results

Comparison Across Fastener Families Using Family-Based Eigenvectors

Figure 8.17 summarizes the per–fastener discriminant scores (mean $\pm$ SD) for HLT53, HLT265, and HLT313 using family-based eigenvectors. The grouped chart provides an overview of classification trends across all materials and lift-offs, while the detailed per–fastener scatter plots are included in Appendix D.4 (Figure D.1, Figure D.2, Figure D.3). As in prior sections, *family* denotes an aggregated dataset for each fastener type measured across nominal lift-offs of 1–3 mm, with two repeated measurements per height to capture geometric and positional variability. A compact family-level summary is provided in Table 8.9, while full per–fastener tables are presented in Appendix D.3 (Table D.11) for completeness.

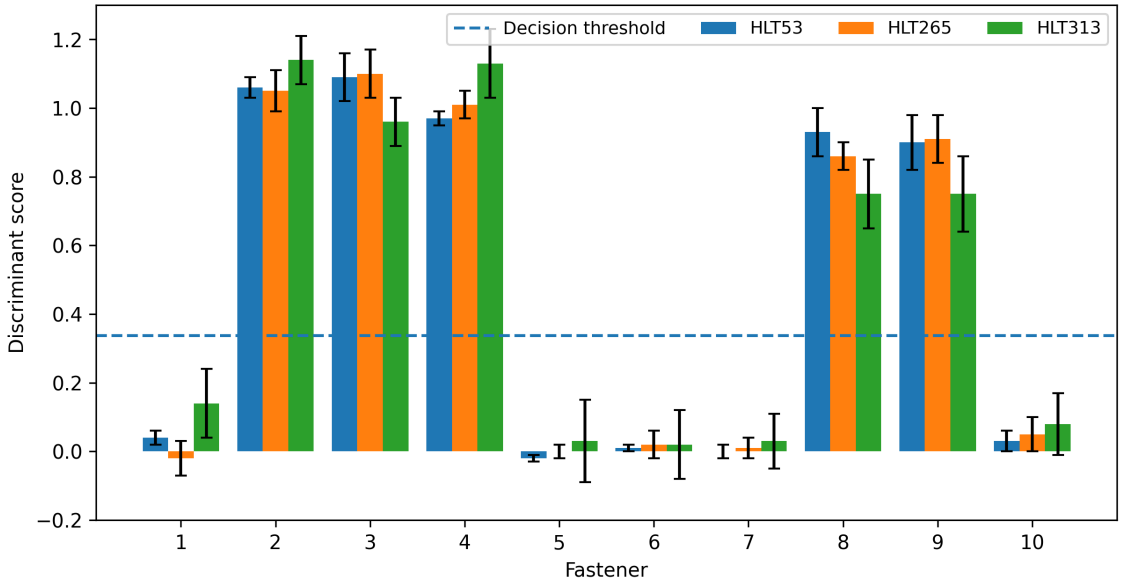

Figure 8.17: Grouped bar chart of discriminant scores (mean $\pm$ SD) by fastener and family using family-based eigenvectors for the ZEUS probe; the dashed line indicates the 99% decision threshold (Table 8.2).

Table 8.9: Summary statistics across fastener families using family-based eigenvectors (ZEUS).

Family	Mean ($\bar{x}$)	SD	Correct Classification (%)
HLT53	0.501	0.036	100.0
HLT265	0.499	0.047	100.0
HLT313	0.503	0.036	100.0

For HLT53 and HLT265, ZEUS demonstrates outstanding flaw classification: notched Fasteners 2–4 and 8–9 exceed the 99% decision threshold (Table 8.2), while unnotched Fasteners 1, 5–7, 10 remain near zero with low variance (typically < 0.08) (see Appendix D.3, Table D.13 and Table D.14). This reflects strong SNR arising from the combination of conductive, magnetically permeable materials and the ZEUS probe's ferrite-cored pickup coils. The HLT313 titanium fastener signals with notches remain separable but exhibit slightly reduced score margins and higher variability (SDs often > 0.10), consistent with weaker inductive coupling and increased sensitivity to lift-off and tilt (Appendix D.3, Table D.12). Overall, ZEUS exhibits high classification fidelity across all fastener families within the family-eigenvector framework.

Effect of Eigenvector Selection

To compare family-based and self-derived eigenvectors succinctly, Table 8.10 reports the average change (Self $-$ Family) in mean and SD across fasteners for each family. These averages were com-

puted from the detailed per–fastener results listed in Appendix D.3 (Table D.13, Table D.14, Table D.12). In general, family eigenvectors provide robust generalization and lower within-class variance, while self eigenvectors can tighten clustering locally, at the risk of occasional variance increases or small drifts for unnotched cases.

Table 8.10: Change relative to family eigenvectors for self-derived sets (ZEUS; ΔSelf $-$ Family), averaged across fasteners.

Family	Self Set	ΔMean	ΔSD
HLT53	HLT53DL8-9	-0.002	0.004
HLT53	HLT53YC10-15	-0.001	-0.024
HLT265	HLT265TB8-6	0.001	-0.006
HLT265	HLT265TB10-12	0.003	-0.012
HLT265	HLT265TB10-18	0.001	-0.029
HLT313	HLT313DL8-9	-0.002	-0.038
HLT313	HLT313TA10-13	0.002	0.006

Effect of Nominal Probe Height (Lift-Off)

Lift-off sensitivity for HLT265 is summarized in Table 8.11, which reports the mean (and SD) across 1–3 mm for each fastener and self set (TB8-6, TB10-12, TB10-18). The corresponding detailed per–fastener discriminant scores are available in Appendix D.3 (Table D.15). Notched Fasteners 2, 3, 4, 8, 9 remain above the decision threshold at all heights, while unnotched Fasteners 1, 5–7, 10 cluster near zero, indicating minimal impact from moderate lift-off changes.

Table 8.11: Mean discriminant scores ($\bar{x}\pm$SD) across lift-offs of 1–3 mm for HLT265 (ZEUS).

Fastener	HLT265TB8-6	HLT265TB10-12	HLT265TB10-18
1	-0.06 ± 0.03	0.04 ± 0.02	-0.03 ± 0.01
2	1.14 ± 0.02	1.02 ± 0.02	1.01 ± 0.01
3	1.00 ± 0.04	1.14 ± 0.03	1.12 ± 0.01
4	1.05 ± 0.03	1.08 ± 0.02	0.94 ± 0.01
5	0.04 ± 0.00	-0.03 ± 0.03	0.01 ± 0.01
6	0.01 ± 0.02	0.02 ± 0.04	0.03 ± 0.01
7	0.04 ± 0.04	0.05 ± 0.01	0.01 ± 0.01
8	0.85 ± 0.05	0.82 ± 0.02	0.91 ± 0.02
9	0.87 ± 0.04	0.84 ± 0.03	1.00 ± 0.01
10	0.06 ± 0.03	0.04 ± 0.02	0.00 ± 0.01

Overall, the ZEUS probe demonstrates high classification accuracy across material families, nominal lift-offs, and eigenvector strategies. Family-based eigenvectors offer a favourable balance of performance and generalization for field deployment where repeated self-calibration is impractical.

9 Fastener Inspection Analysis

9.1 Conventional Eddy Current Testing Performance

The results presented in Section 8.2 provide a comprehensive assessment of the capabilities and limitations of conventional ET for inspecting fasteners embedded beneath non-conductive layers and RAM. These experiments revealed strong dependencies on probe alignment, excitation frequency, material conductivity, and lift-off conditions. The following discussion integrates the findings for the ZEUS, THOR, and ODIN probes under realistic aerospace inspection scenarios.

Although the ZEUS, THOR, and ODIN probes were originally designed for pulsed excitation, their drive coils were repurposed for sinusoidal operation to facilitate conventional ET measurements in this study. This approach enabled a controlled evaluation of each probe's performance under conditions representative of legacy inspection systems.

9.1.1 Impact of Probe Misalignment and Alignment Methodology

Figure 8.1 highlights the sensitivity of all three probes to lateral displacement, particularly at higher lift-offs. At a nominal lift-off of $3.3\,\mathrm{mm}$, probe misalignment of $5\,\mathrm{mm}$ or more resulted in visible attenuation and waveform distortion. This degradation became more pronounced at $11.3\,\mathrm{mm}$ lift-off, where the broadened magnetic field distribution led to diminished amplitude contrast and a loss of spatial resolution. These effects were consistent across the THOR, ODIN, and ZEUS probes.

As discussed in Section 8.2, conventional ET systems exhibit substantial performance degradation under elevated lift-off and misalignment conditions. To address the practical challenges associated with manual probe positioning, a custom alignment program was developed in LabVIEW 2021. Visual verification using a borescope confirmed correct alignment when the drilled reference hole at the fastener centre disappeared from the field of view (Figure 8.4(a)). Conversely, when misaligned, the hole was visible (Figure 8.4(b)), qualitatively confirming positional offset. The system achieved an alignment repeatability within $\pm 0.5\,\mathrm{mm}$, demonstrating that conventional ET can be integrated into automated scanning platforms, provided the application remains within acceptable lift-off and material constraints. Although not a complete solution, this approach offers a practical interim improvement in repeatability for conventional ET systems prior to the full adop-

tion of PEC-based platforms. Nevertheless, the superior lift-off tolerance of PEC methods makes them a more robust long-term candidate for robotic NDT applications.

9.1.2 Crack Detection and Frequency Dependence

Crack detection performance was evaluated using the ZEUS probe with multi-frequency sinusoidal excitation. Figure 8.5 and Figure 8.6 illustrate the relationship between excitation frequency, skin depth, and flaw visibility. The 10 kHz signal consistently revealed crack indications at Fasteners 2, 3, 4, 8, and 9 for both the HLT265 and HLT313 families at an effective lift-off of $2.3\,\mathrm{mm}$, with skin thicknesses of $6.4\,\mathrm{mm}$ and $13.4\,\mathrm{mm}$, respectively. In contrast, the $100\,\mathrm{kHz}$ signal—while providing improved spatial resolution—was unable to resolve cracks in the thicker specimens due to the reduced penetration depth associated with higher frequencies. The chosen frequencies of $10\,\mathrm{kHz}$ and $100\,\mathrm{kHz}$ thus represent a compromise between sensitivity and spatial resolution. Frequencies below $5\,\mathrm{kHz}$ were excluded due to excessive low-frequency noise, whereas those above $200\,\mathrm{kHz}$ offered insufficient penetration for subsurface defect detection.

The advantage of low-frequency excitation for detecting buried flaws is consistent with electromagnetic diffusion theory, where skin depth increases as frequency decreases, as described in Equation 2.32. At $10\,\mathrm{kHz}$, the greater skin depth enabled the signal to interact more effectively with notches located beneath angled aluminum layers, particularly in low-conductivity materials such as titanium. However, this benefit was accompanied by reduced spatial resolution and amplitude response, requiring signal filtering to enhance interpretability.

9.1.3 Effect of Elevated Lift-Off on Signal Integrity

Figure 8.7 (a) and (b) quantify the effect of increased lift-off on detection performance. At lift-offs of $19.7\,\mathrm{mm}$ and $24.7\,\mathrm{mm}$ above the angled aluminum, crack indications remained visible at Fasteners 2, 4, 8, and 9; however, peak resolution was significantly reduced. Although the response at Fastener 3 remains elevated relative to the surrounding baseline, it no longer manifests as a distinct, well-localized peak. Instead, the signal appears broadened and spatially merged with neighbouring responses. This behaviour is attributed to increased magnetic field diffusion and reduced spatial confinement at large lift-offs, leading to responses from adjacent fasteners overlapping. Under sinusoidal excitation, this broadening of the magnetic field footprint is inherent to the narrowband nature of conventional ET. As a result, while measurable signal energy may persist at individual fastener locations, the loss of spatial resolution and reduced SNR limit reliable defect discrimination. These observations therefore define a practical detection limit for conventional ET, beyond which classification performance degrades at lift-offs approaching $25\,\mathrm{mm}$.

Despite these constraints, fastener localization remained achievable at $100\,\mathrm{kHz}$ up to a $24.7\,\mathrm{mm}$ lift-off. This outcome demonstrates that even under degraded SNR, conventional ET retains lim-

ited value for geometric feature tracking. However, its inability to distinguish individual cracks or estimate defect depth at elevated lift-offs underscores the inherent shortcomings of amplitude-based, single-feature analysis. As lift-off increases, the induced eddy current field becomes more diffuse, reducing spatial resolution and increasing overlap between signals from neighbouring fasteners or adjacent defect edges. Consequently, signal amplitude—strongly dependent on localized field–flaw interactions—loses both sensitivity and specificity. Moreover, because amplitude alone lacks temporal or phase information, subtle variations in flaw depth or orientation cannot be resolved, increasing the likelihood of misclassification or missed detections.

While conventional ET remains effective for fastener localization and crack detection at moderate lift-offs, its reliance on sinusoidal excitation imposes limitations under conditions of high lift-off, material heterogeneity, or geometric complexity. In contrast, PEC systems exploit transient excitation and broadband frequency content, enabling deeper field penetration and improved signal robustness. The inability of conventional ET to resolve flaw indications beyond approximately $25\,\mathrm{mm}$ lift-off reinforces the need for pulsed approaches in applications involving RAM-coated aircraft skins or recessed fasteners.

Given these constraints, even well-aligned conventional ET systems remain inherently limited when lift-off exceeds $20\,\mathrm{mm}$ or when complex geometries, composite skins, or stealth coatings restrict probe proximity. These results emphasize the need to transition to PEC-based inspection systems for next-generation aerospace platforms. Pulsed methods offer greater tolerance for lift-off variation, enhanced frequency diversity, and improved sensitivity to subsurface defects, making them better suited to the demanding inspection environments encountered in platforms such as the CF-188 and F-35.

The findings in this section highlight the intrinsic performance limitations of conventional ET when applied to modern aerospace structures. The subsequent sections evaluate PEC performance under comparable conditions, demonstrating its capability to overcome the deficiencies identified here.

9.2 Pulsed Eddy Current

The PEC technique employed in this study differs from conventional ET by using a voltage step function rather than a continuous sinusoidal waveform to excite the drive coil. A 10 V DC square wave with a 50% duty cycle and a pulse duration $P = 2$ ms was applied at 10 Hz. This excitation produced both forward and reverse transients in the test material and, consequently, a broadband transient magnetic field. The time-varying flux generated by the drive coil induces eddy currents in the specimen, which are sensed by one or more pickup coils. Pickup configurations may consist of single elements or differentials, with the latter offering enhanced noise suppression and increased lift-off sensitivity.

Accurate subtraction in differential configurations requires precise coil matching. Small mismatches in inductance, resistance, or placement introduce residual common-mode signals that can mask flaw responses. Such imbalances may also produce low-frequency drift or artificial peaks that are difficult to distinguish from legitimate defect signatures without filtering or statistical post-processing. Coil symmetry is, therefore, a central design consideration. In practice, achieving balance is non-trivial: signal amplitude is sensitive to small variations in winding geometry, core placement, and lift-off from the surface. These mechanical tolerances explain performance differences between nominally identical probes and underscore the need for repeatable fabrication.

Table 9.1 summarizes the key electrical parameters for the ZEUS, THOR, and ODIN probes, including measured and calculated inductances. Calculated values were obtained using the Wheeler approximation for air-core solenoids [115]. The Wheeler approximation [115] provides an empirical estimate of air-core coil inductance based on coil geometry, but does not account for magnetic core materials. Electrical resistance R was measured with a digital multimeter. The coil relaxation time $\tau_c = L/R$ (the time to $\approx 63\%$ reach steady-state current) is reported for each configuration as described in Section 2.4.1, and the corresponding steady-state transient current $i(t)$ was computed assuming an ideal voltage step, following Equation 2.44.

Table 9.1: Measured and calculated probe parameters for $10\,\mathrm{V}$ step excitation.

Probe	**Coil**	L (meas.) [mH]	L (calc.) [mH]	R [Ω]	$\tau_c = L/R$ [µs]	I_{ss} [A]
ZEUS	Drive	6.370	6.084	101.9	62.51	0.098
	Differential pair	6.920		47.5	145.68	0.211
ODIN	Drive	0.190	0.194	11.2	16.96	0.893
	Differential pair	2.441		83.0	29.41	0.120
	Single pickup (1)	1.222		42.4	28.82	0.236
	Single pickup (2)	1.221		42.1	29.00	0.238
THOR	Drive	1.851	0.261	21.7	85.30	0.461
	Differential pair	2.577		83.1	31.01	0.120
	Single pickup (1)	1.259		43.0	29.28	0.233
	Single pickup (2)	1.260		42.2	29.86	0.237

Measured and calculated inductances agree well for the air-cored drive coils in ZEUS and ODIN. In contrast, THOR's measured drive-coil inductance greatly exceeds the Wheeler [115] estimate due to the presence of a ferrite core, which increases the effective magnetic permeability and enhances flux linkage, as expected. Because Wheeler's formula [115] assumes a non-magnetic core, it does not capture the inductive amplification, nor the associated reduction in eddy current loss introduced by ferrite materials [116], [117], [118].

Differential pickup coil pairs exhibit an effective inductance approximately twice that of a single pickup coil, arising from the additive contributions of their self-inductances and mutual coupling.

This increased inductance leads to longer electrical relaxation times, consistent with the characteristic time constant (see Equation 2.45) in which the change in inductance dominates over the comparatively modest change in resistance.

The broadband content of the PEC excitation permits simultaneous interaction with multiple diffusion depths, capturing responses from near-surface to deeper subsurface regions. This spectral richness improves sensitivity and adaptability across varied inspection scenarios.

In summary, these measurements emphasize the importance of material selection and geometric symmetry in PEC probe design. Air-core coils afford predictable behaviour and straightforward analytical modelling, whereas ferrite cores increase sensitivity by concentrating flux and strengthening induced transient currents. Differential architectures can improve flaw detectability, but demand tight manufacturing tolerances and careful calibration to maintain balance.

These experimentally derived parameters provide the basis for the subsequent analytical and numerical models, enabling the simulation of the transient system response and its sensitivity to material, geometric, and defect-induced variations. Both the analytical and FEM formulations assume air-core coil behaviour; ferrite-core effects are not explicitly modelled and are considered a potential source of discrepancy between simulation and experiment.

9.2.1 Raw Pulsed Eddy Current Time-Domain Signal Analysis

Figure 8.8, Figure 8.9, and Figure 8.10 illustrate the limitations of conventional scalar feature–based approaches in PEC signal interpretation, particularly under elevated lift-off conditions and within low-conductivity substrates. Discrete time-domain features—such as peak amplitude, zero-crossing time, and exponential decay rate—have traditionally been used for flaw discrimination. However, their diagnostic reliability diminishes as SNR decreases or as electromagnetic coupling weakens due to reduced conductivity or permeability.

Among the probes evaluated, ZEUS (Figure 8.8) demonstrated the strongest contrast between notched and unnotched responses. Its vertically differential pickup architecture effectively suppresses common-mode background signals and enhances sensitivity to localized magnetic-field gradients. This is particularly evident in the steel sample (Figure 8.8(a)), where notched fasteners (Fasteners 4 and 8) exhibit clear reductions in primary peak amplitude and modified trailing-edge decay. Conversely, in the titanium sample (Figure 8.8(b)), the combination of low electrical conductivity and near-unity magnetic permeability significantly weakens coupling, producing overlapping signal traces and reduced flaw visibility.

It is useful to compare this behaviour with the differential probe architecture reported by Horan *et al.* [9]. Although their probe configuration differs from the vertically differential arrangement implemented in ZEUS, both approaches rely on differential measurement to enhance flaw-induced perturbations relative to the background response. In the present work, the vertical separation between pickup coils in ZEUS increases sensitivity to axial magnetic-field gradients produced by

localized eddy current disturbances. This geometry promotes improved common-mode suppression of the primary driver field and enhances contrast between notched and unnotched fasteners. By comparison, probe configurations that do not employ vertical differential separation rely more heavily on absolute amplitude variations, which become less reliable as coupling weakens or SNR decreases. The stronger peak separation observed in Figure 8.8 is therefore, consistent with the enhanced gradient sensitivity afforded by the vertically differential configuration.

Performance degradation is more pronounced in the single-pickup architectures of THOR and ODIN. In Figure 8.9, THOR shows negligible amplitude separation between notched and unnotched fasteners—even in the steel sample, where Fasteners 6 and 8 yield nearly identical responses. In the titanium sample, waveform convergence is even greater, reflecting the limited diagnostic utility of amplitude- or decay-based metrics under weak-coupling conditions. Similar behaviour is observed for ODIN (Figure 8.10), where variations in peak height and decay slope between notched and unnotched signals are minimal.

These results underscore a key finding: traditional scalar time-domain features are insufficient for reliable flaw classification when SNR is low or when intrinsic material properties produce weak contrast. The increasing signal ambiguity across probe types, materials, and lift-offs underscores the need to adopt multivariate analytical frameworks that capture global variance across the entire waveform rather than isolated feature points.

This motivates the transition toward statistical signal-analysis techniques, such as PCA, which leverage full waveform information to identify dominant modes of variation associated with flaw presence. By projecting time-domain responses into reduced-dimensional eigenspaces, these methods offer improved resilience to noise, enhanced generalization across inspection geometries, and the potential for automated, operator-independent flaw classification.

9.2.2 Discriminant Analysis Performance

The results presented in Section 8.5 demonstrate the effectiveness of principal component–based discriminant analysis applied to PEC signals for binary flaw classification across multiple aerospace fastener types. This approach reliably separates notched and unnotched fasteners by projecting gated time-domain signals into a reduced-dimensional eigenspace and applying a supervised multiple linear regression model. The method offers significant improvements over traditional scalar feature extraction—particularly under challenging conditions such as elevated lift-off or the inspection of low-conductivity, low-permeability materials (e.g., titanium fasteners).

A central strength of this framework lies in its resilience to signal degradation mechanisms. As lift-off increases, the SNR decreases, and electromagnetic field coupling becomes less distinct, making conventional metrics (e.g., peak amplitude and decay rate) increasingly unreliable. The proposed PCA-based method mitigates these effects by capturing global waveform variance and discarding non-informative components. The resulting discriminant score provides a continuous,

interpretable output that supports real-time, automated flaw classification—enabling deployment in autonomous scanning systems where operator-free decision-making is essential.

Influence of Probe Design

The comparative analysis of the ZEUS, THOR, and ODIN probes confirms that probe architecture plays a critical role in classification performance, particularly under demanding lift-off and material conditions. ZEUS consistently achieved the greatest class separation across all fastener types, including the titanium HLT313 family, where low conductivity and magnetic permeability typically degrade PEC signal quality. This enhanced performance is attributed to ZEUS's vertically differential pickup-coil configuration, which increases sensitivity to small variations in magnetic field gradients caused by flaws. Unlike axisymmetric configurations, ZEUS's vertically stacked pickup coils produce a lift-off–sensitive differential response that magnifies flaw-induced asymmetries. While this also increases sensitivity to lift-off variation, it improves notch detectability in high–lift-off scenarios by enhancing vertical-field discrimination.

By contrast, THOR and ODIN employ axisymmetric pickup-coil configurations, which are less sensitive to changes in vertical magnetic field gradients and, consequently, yield lower signal variation in the presence of shallow or subsurface flaws. Even so, THOR showed slightly better performance than ODIN in titanium inspections. This difference is attributed to THOR's ferrite-cored driver, which increases magnetic permeability and enables stronger flux penetration in low-conductivity materials. ODIN, by comparison, uses an air-cored driver and exhibits weaker overall signals in titanium—particularly in the thicker HLT313TA10-13 fastener set—where several unnotched fasteners scored above the $99\,\%$ confidence threshold, indicating an elevated false-positive rate due to insufficient contrast between notched and unnotched responses.

ODIN performed reliably within stainless-steel fastener families such as HLT53 and HLT265, achieving well-defined separation between notched and unnotched signals at both the $95\,\%$ and $99\,\%$ confidence thresholds. This supports the conclusion that ODIN's air-cored, axisymmetric configuration is sufficiently sensitive in high-permeability environments, where favourable magnetic coupling enhances signal amplitude and flaw contrast. Reduced classification performance was observed for both ODIN and THOR when inspecting the HLT53YC10-15 fastener. This specimen differs from others in the HLT53 series due to its surface finish code (Appendix A), specifically the presence of white paint applied to the fastener head, which introduces an additional effective lift-off between the probe and the conducting surface. This increased lift-off reduces magnetic coupling and signal amplitude, thereby degrading classification performance.

These findings reinforce the importance of tailoring probe architecture to material properties and inspection constraints. ZEUS, with its differential configuration, performs best under high lift-off and low-conductivity conditions. THOR and ODIN are more effective for stainless-steel applications, assuming surface finish and geometry are consistent with the calibration set. Notably,

THOR's improved performance in titanium samples highlights the advantages of ferrite-cored excitation when inspecting materials with limited induced current density.

Role of Eigenvector Basis

Using family-based eigenvectors consistently improved classification performance across all probes for the investigated fastener families. This approach captures inter-sample variability, while suppressing noise and irrelevant fluctuations by constructing a shared eigenspace from signals collected across multiple specimens within the same fastener family. Compared with self-based eigenvectors derived from individual samples, the family-based method improved the stability and generalization of the classification scores and yielded more consistent decision thresholds.

These differences are reflected in the eigenvectors themselves. Figure 9.1 presents the family-based eigenvectors for the HLT265 fastener group using probes (a) ZEUS, (b) THOR, and (c) ODIN. Each probe yields a distinct eigenvector set conditioned by its coil geometry and magnetic coupling. ZEUS exhibits the smoothest, most coherent eigenvector structure with minimal high-frequency content, suggesting strong SNR and consistent signal morphology across the fastener family, which likely contributes to superior discrimination. THOR shows a moderately increased level of high-frequency content relative to ZEUS, reflecting the influence of its ferrite-cored excitation and associated field shaping, which introduces additional spectral content while maintaining overall eigenvector coherence. While the eigenvectors remain well structured, increased spectral content indicates greater sensitivity to local variations in material response and geometry. In contrast, ODIN shows higher apparent eigenvector noise and sharper transitions, indicative of greater signal variability and reduced coherence across training samples. This elevated noise floor can hinder the isolation of defect-induced features, thereby reducing classification reliability in more challenging material scenarios.

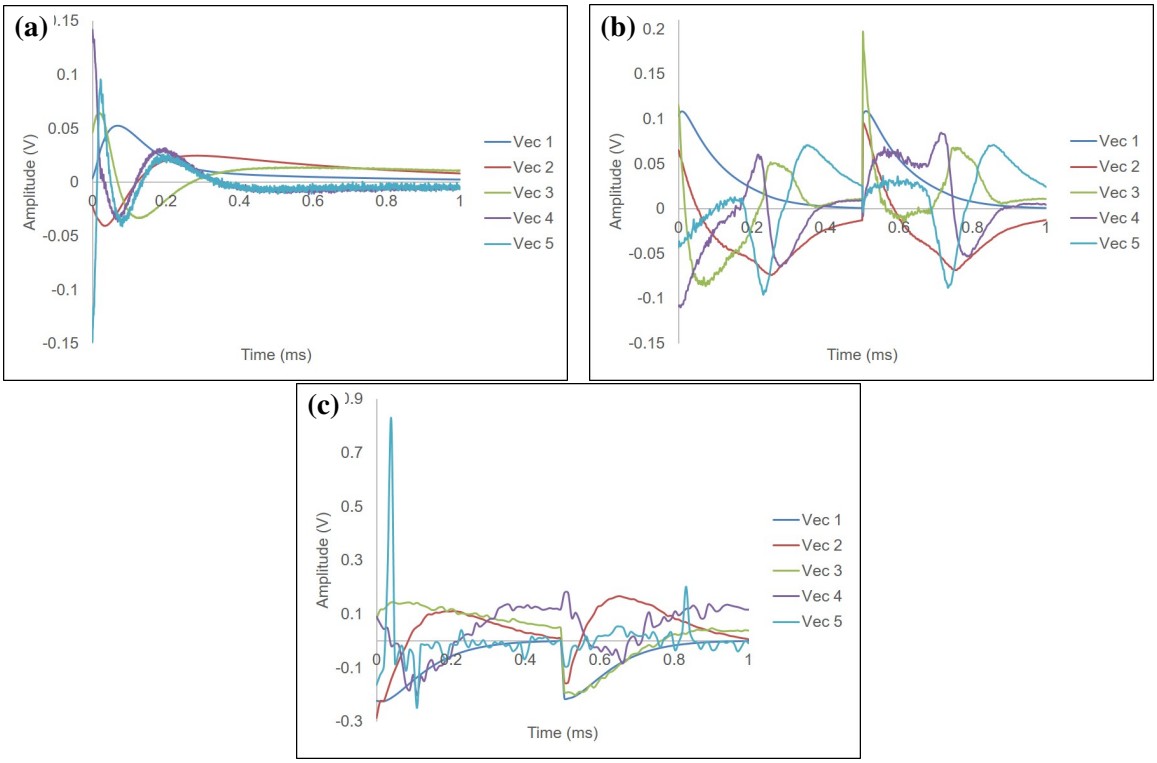

Figure 9.1: Family-based eigenvectors for the HLT265 fasteners using (a) ZEUS, (b) THOR, and (c) ODIN probes.

Figure 9.2 further illustrates this effect by comparing THOR's family-based eigenvector with self-based eigenvectors derived from three individual ferromagnetic HLT265 specimens. The family-based eigenvector exhibits lower high-frequency content and a smoother temporal profile than its self-based counterparts. This behaviour reflects the averaging effect of training on multiple representative signals, which suppresses specimen-specific fluctuations and yields a more stable, generalizable projection basis. As demonstrated in the discriminant analysis, this increased stability enhances classification consistency across structurally similar samples. These results support the conclusion that family-based eigenspaces improve discrimination between notched and unnotched fasteners within a given group by more effectively isolating flaw-related variance.

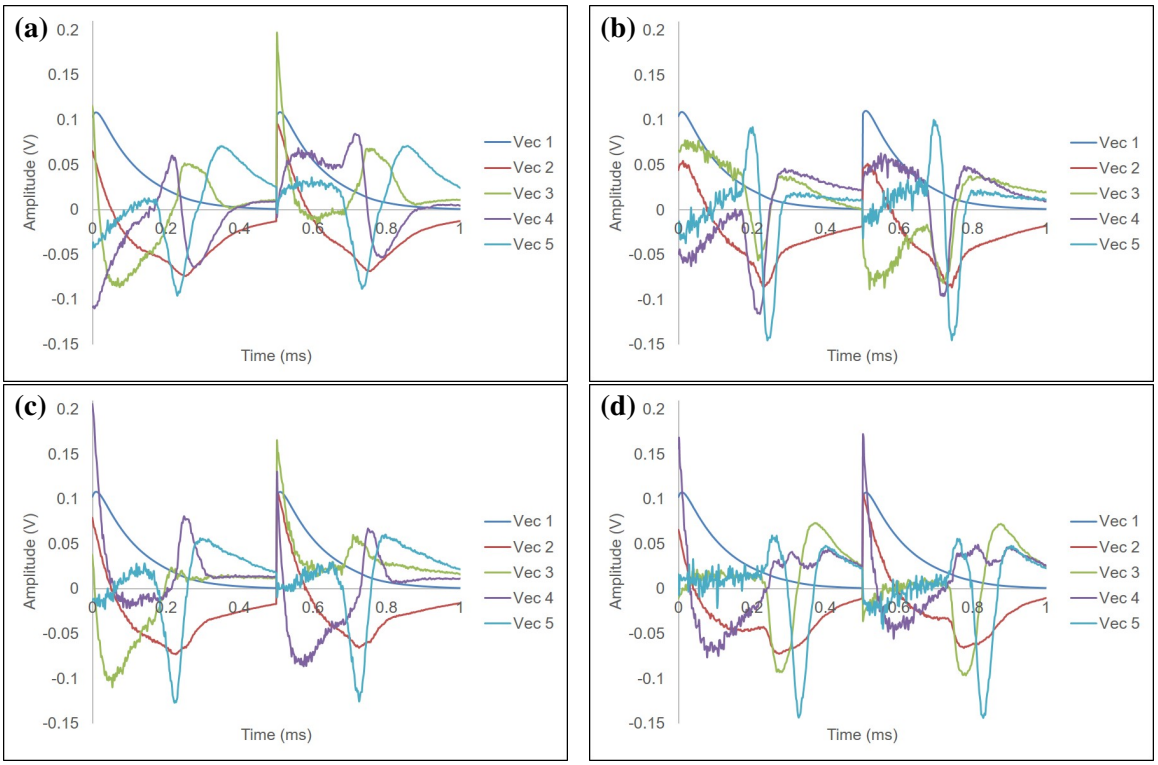

Figure 9.2: Comparison of THOR HLT265 family-based eigenvector (a) with self-based eigenvectors from individual HLT265 samples (b) HLT265TB8-6 self (c) HLT265TB10-12 self and (d) HLT265TB10-18.

The benefits of the family-based projection method are most apparent in the HLT265 fastener family, which showed the best class separation across all three probes (Figure D.2). Notched and unnotched fasteners were consistently distinguished with minimal score dispersion within the confidence bounds. This performance is attributed to the favourable material properties of HLT265 fasteners—namely, high magnetic permeability and moderate conductivity—which produce strong, repeatable PEC responses.

Conversely, the HLT313 titanium fastener family exhibited the weakest separation (Figure 8.14). For THOR and ODIN, several unnotched fasteners were misclassified above the 99 % confidence threshold, indicating a higher false-positive rate. This behaviour highlights the challenge of flaw detection in low-conductivity and low-permeability materials, where a larger skin depth does not directly translate into improved sensitivity. Despite increased penetration depth, the induced eddy current response remains governed by Equation 2.40, and the reduced conductivity results in a weaker secondary magnetic field and diminished signal response.

Interestingly, ODIN performed better than anticipated in the HLT313 set. Although ODIN uses an air-cored driver and axisymmetric pickup configuration—typically less effective in titanium—it produced only a single misclassified unnotched fastener at the sample edge, where boundary effects can alter flux paths and inflate scores. By comparison, THOR—despite its ferrite-cored

driver—produced four false positives distributed across the specimen, suggesting that improved coupling can also increase susceptibility to local geometric non-uniformities. Thus, while family-based eigenspaces generally outperform self-based counterparts, the optimal strategy can still depend on probe–material interactions and specimen variability.

Lift-off Robustness and Field Deployment

Classification performance across all probes and fastener families demonstrated strong resilience to lift-off variation, an essential consideration for operational deployment in aerospace maintenance environments. For nominal probe heights of 1 to $3\,\mathrm{mm}$—corresponding to lift-off distances of approximately 2.3 to $4.3\,\mathrm{mm}$ above the sample surface and up to $17.7\,\mathrm{mm}$ above the angled aluminum backplate—discriminant scores remained well separated between notched and unnotched fasteners. Score distributions showed negligible drift, confirming that classification accuracy is preserved under moderate vertical displacement.

Of particular note is the ZEUS probe, which maintained robust flaw discrimination at lift-offs approaching $18\,\mathrm{mm}$ from the angled aluminum layer—effectively simulating the inspection of subsurface fasteners through a thick composite stack-up. At this extreme lift-off, ZEUS continued to produce clean separation with no false positives, including in titanium specimens (HLT313) known for weak eddy current responses. This underscores the advantage of the vertically differential pickup-coil configuration, which enhances sensitivity to subtle field gradients, while rejecting common-mode interference and noise.

This level of robustness was not replicated using conventional ET with the same probe. As discussed in Section 8.2, ZEUS, operated under sinusoidal excitation at comparable lift-offs, exhibited considerable signal degradation, with ambiguous crack indications and diminished contrast between notched and unnotched fasteners—particularly in thicker or low-conductivity materials. These limitations, driven by reduced skin depth and low SNR at high lift-off, reinforce the comparative advantage of pulsed excitation and dimensionality-reduction–based analysis in demanding scenarios.

The fixed-eigenspace discriminant-scoring strategy employed here proved critical to lift-off tolerance. Even without re-optimizing the eigenspace for each lift-off, classification remained stable and repeatable, simplifying implementation and calibration. Future work may extend this framework to higher lift-offs using existing family-based eigenvectors, enabling inspection through thicker composite skins or non-conductive coatings without compromising detectability.

These results support the practicality of deploying PEC-based systems, such as ZEUS, on automated or portable NDT platforms for airframes with limited surface access. By maintaining detection accuracy at lift-offs approaching $25\,\mathrm{mm}$, the system demonstrates deployment-level capability for field applications (e.g., CF-188 and F-35 inner wing spars), where stealth materials and complex geometry impose lift-off constraints.

Discriminant Score Thresholds

The discriminant score thresholds established at the $95\,\%$ and $99\,\%$ confidence levels (Table 8.2) provide a statistically rigorous framework for binary flaw classification under varying inspection conditions. Derived from the distribution of scores associated with unnotched (baseline) specimens, these thresholds define upper bounds beyond which a signal is classified as notched. The $95\,\%$ threshold emphasizes sensitivity to reduce false negatives, whereas the more conservative $99\,\%$ threshold prioritizes specificity to limit false positives. In safety-critical inspection contexts, false positives can lead to unnecessary fastener removal, component replacement, or structural teardown, increasing inspection time, costs, and the risk of secondary damage without improving safety margins.

Thresholds were computed independently for each probe and fastener family, thereby accounting for material properties, geometric configuration, and probe architecture. This tailoring ensures that each decision boundary reflects the achievable classification margin for a given probe–sample pairing. For example, ZEUS consistently exhibited tighter score distributions and lower thresholds due to its vertically differential configuration, which improves signal contrast and reduces common-mode noise. Higher thresholds were observed for ODIN and THOR in titanium fastener groups, where reduced electromagnetic coupling diminishes flaw-related score separation.

In practice, these thresholds translate continuous discriminant scores into actionable maintenance criteria. Embedding confidence-based decision boundaries within automated analysis enables deterministic outputs—flagging fasteners for re-inspection, repair evaluation, or clearance for continued service—thus formalizing probabilistic risk management aligned with modern aerospace NDT. Moreover, decision thresholds can be selected based on the inspection context. More conservative criteria (e.g., a $99\,\%$ threshold) are appropriate for high-consequence regions or confirmatory inspections, where false positives must be minimized. Less restrictive criteria (e.g., a $95\,\%$ threshold) may be used during preliminary or wide-area screening to maximize sensitivity, with indications subsequently reviewed or re-inspected using stricter thresholds.

Overall, the thresholding framework provides a flexible, statistically defensible mechanism for converting data-rich PEC responses into practical decision logic. Future work may incorporate real-time uncertainty quantification or Bayesian updating to refine thresholds as additional inspection data become available.

10 Summary and Future Work

10.1 Summary

This thesis was motivated by the inspection challenges of the RCAF F-35 fleet, which features composite wing skins and RAM coatings that prevent direct access to structural components such as inner wing spars and, in many cases, preclude physical probe contact altogether. These constraints necessitate the development of a non-contact NDT method capable of detecting SCC adjacent to both ferrous and non-ferrous fasteners at lift-off distances exceeding 11 mm. To address this need, a PEC-based inspection system was developed and comprehensively evaluated. The system integrates a suite of custom-designed probes, advanced time-domain signal processing, and a discriminant classification framework based on MPCA. The three PEC probes—ZEUS, THOR, and ODIN—were designed with different core materials and coil configurations to investigate trade-offs between magnetic sensitivity, lift-off tolerance, and practical inspection performance.

Conventional ET was first evaluated to benchmark its performance under representative aerospace inspection conditions. While effective at identifying cracks and localizing fasteners under low to moderate lift-offs, performance degraded rapidly beyond an 11 mm lift-off from the wing skin. This degradation was primarily attributed to reduced magnetic-field coupling and declining SNR. In addition, sensitivity to probe misalignment and dependence on sinusoidal excitation limited the practicality of conventional ET for composite or stealth structures such as the F-35, where consistent lift-off and alignment cannot be guaranteed.

In contrast, the broadband transient excitation and time-domain nature of PEC provided enhanced robustness at elevated lift-offs and across materials with differing conductivity and magnetic permeability. Although conventional time-domain features—such as peak amplitude, zero-crossing time, and decay slope—offered limited reliability in low-SNR or low-conductivity environments (e.g., titanium), these shortcomings were addressed through the implementation of a multivariate framework based on MPCA. Each gated waveform was reduced to a small number of principal components that captured flaw-related variance, and these principal component scores were processed through linear discriminant analysis to generate a single, interpretable discriminant score. This approach, following the methodology originally proposed by Horan *et al.* [9], enabled quantitative

classification with statistical confidence.

Among the developed probes, ZEUS consistently demonstrated the highest classification accuracy. Its vertically differential pickup configuration enhanced sensitivity to vertical field gradients, while rejecting common-mode noise, resulting in superior flaw discrimination even at lift-offs of up to 17.7 mm above the angled aluminum substrate. This capability extended to titanium fasteners, where other probes exhibited reduced contrast. THOR, featuring a ferrite-cored driver and an axisymmetric pickup layout, provided stronger flux penetration and improved titanium response relative to ODIN, but exhibited greater score variance across fastener positions, likely due to spatial field nonuniformity introduced by the ferrite core. ODIN, employing an air-cored driver and axisymmetric pickups, performed reliably for stainless-steel fasteners but produced a higher rate of false positives in thicker titanium specimens (notably HLT313TA10-13), where electromagnetic coupling strength was limited by material properties.

The use of family-based eigenvectors significantly improved classification consistency for all probes. By constructing a shared eigenspace from multiple specimens within a fastener family, the approach captures inter-sample variability, while suppressing noise and specimen-specific artefacts. This methodology proved especially effective in the HLT265 stainless-steel family, which exhibited strong separation between notched and unnotched fasteners due to its favourable magnetic permeability and moderate conductivity. In comparison, the HLT313 titanium family presented greater classification challenges. ODIN misclassified only a single unnotched fastener located near a sample edge, while THOR misclassified four unnotched fasteners across the specimen, indicating heightened sensitivity to local field inhomogeneities and potential edge effects.

Discriminant score thresholds were defined at the 95% and 99% confidence levels, based on the distribution of unnotched training data. These thresholds were independently calibrated for each probe and fastener family, allowing statistically rigorous binary classification of new inspection signals. The incorporation of fixed decision thresholds supports integration into automated inspection pipelines, enabling real-time classification and re-inspection logic consistent with modern aerospace NDT practice.

In parallel with experimental efforts, a comprehensive analytical and numerical modelling framework was developed to simulate the time-domain response of PEC systems. The square-wave excitation was expressed as a truncated Fourier series containing odd harmonics, enabling inverse harmonic reconstruction of the transient response. Analytical simulations were performed using 500 harmonics across 2000 uniformly spaced time steps to ensure temporal fidelity. Frequency-dependent complex inductances—$\mathcal{L}_1$, $\mathcal{L}_2$, and $\mathcal{M}_{12}$—were employed to compute coil currents at each harmonic frequency, and the inverse Fourier transform was used to reconstruct the time-domain waveform. The analytical results successfully reproduced key physical behaviours, including polarity inversion between drive and pickup coils, monotonic amplitude decay with increasing lift-off, and material-dependent diffusion effects. Strong agreement was achieved with both FEM

simulations and experimental data, particularly at low lift-offs where the assumptions of planar geometry and homogeneous conductivity remain valid.

Residual discrepancies at higher lift-offs and in low-conductivity or thick specimens are attributed to simplified boundary representations and modelling assumptions, which become more influential under weak coupling conditions, as well as to experimental artefacts such as electrical noise and digitization distortion. Despite these limitations, the analytical model provides a computationally efficient and physically interpretable framework for predicting PEC system performance across a range of materials and geometries, while also enabling systematic evaluation of parameter sensitivity.

Overall, this thesis presents a fully integrated and experimentally validated PEC inspection methodology for detecting subsurface flaws around fasteners beneath composite and RAM-coated surfaces. The combination of custom probe architectures, multivariate classification, and analytical–numerical modelling demonstrates that PEC techniques can overcome the intrinsic limitations of conventional ET under high-lift-off and low-conductivity conditions. The resulting system enables reliable flaw detection, probabilistic classification, and scalable simulation capability—establishing a robust foundation for future non-contact NDT deployment on advanced aerospace platforms such as the F-35.

10.2 Future Work

While this work establishes a comprehensive PEC inspection framework for detecting SCC around aerospace fasteners, several opportunities remain to further enhance system capability, generalization, and readiness for operational deployment.

First, incorporating RAM coatings directly into experimental test specimens would significantly improve realism and provide a more accurate representation of operational aircraft surfaces. Such integration would enable a quantitative assessment of how stealth materials influence signal attenuation, magnetic field diffusion, and SNR, thereby informing optimized probe design and signal-processing strategies for next-generation stealth platforms.

Second, although the present combination of linear discriminant analysis and principal component projection has achieved high classification accuracy, future work should explore non-linear machine learning classifiers, such as support vector machines, random forests, or neural networks. These models can capture non-linear relationships between waveform structure and flaw state, offering improved classification performance in complex or low-SNR scenarios. Moreover, adaptive or ensemble approaches could leverage large inspection datasets to refine model performance over time, enhancing defect detection robustness across repeated inspections of structurally similar aircraft.

Third, a hybrid projection framework that dynamically selects between self-based and family-based eigenspaces depending on the inspection context—such as material type, probe configuration, or lift-off height—could further reduce misclassification rates. By tailoring the eigenspace to the prevailing signal characteristics, such an adaptive method would improve generalization across varying inspection conditions and material systems.

Fourth, integration of the PEC framework with automated or robotic scanning platforms represents a critical step toward operational implementation. Embedding the acquisition, gating, projection, and classification modules into portable embedded systems would enable real-time flaw detection and high-throughput inspection during flight-line maintenance, where inspections are performed directly on the aircraft, as well as during depot-level maintenance. Automated systems inherently produce structured, repeatable datasets under controlled geometric conditions, facilitating the development of robust statistical and learning-based models. Achieving real-time computational performance will be an essential requirement for such integration.

Fifth, expanding the experimental dataset to encompass a wider range of fastener materials, flaw geometries, lift-off conditions, environmental parameters (e.g., temperature, humidity), and operator variability would enable comprehensive POD studies. These expanded datasets would support validation under aerospace NDT certification standards and facilitate qualification for deployment on aircraft such as the F-35 and CF-188 fleets.

The analytical modelling framework developed in this thesis can also be extended to accommodate more complex geometrical configurations commonly found in aircraft structures. These include curved, layered, or stepped surfaces where planar approximations no longer hold. For geometries exhibiting cylindrical symmetry—such as riveted fuselage panels or fastener arrays along curved spars—solutions may be formulated in cylindrical coordinates using separable representations involving Bessel functions. Such extensions would retain computational efficiency, while accounting for realistic curvature and three-dimensional field behaviour.

For configurations involving edge boundaries, material transitions, or local truncations, the use of Truncated Region Eigenfunction Expansion (TREE) offers a powerful modelling approach [119]. TREE can efficiently solve BVPs in finite domains while enforcing field continuity across material interfaces, making it particularly well suited for simulating electromagnetic interactions at transitions between skin panels, spars, and stiffeners.

Finally, the analytical framework may be expanded to explicitly incorporate the effects of ferrite-cored pickup coils by introducing a permeability-dependent material region into the boundary value formulation [99], [116], [117]. This would require replacing the air-core assumption and adopting a finite-permeability core model, thereby modifying the magnetic vector potential solution and associated boundary conditions to account for flux concentration, non-uniform field distributions, and frequency-dependent magnetic losses within the ferrite [100]. The resulting formulation would yield permeability-dependent self- and mutual inductance expressions, enabling a more ac-

curate representation of ferrite-enhanced coupling while retaining the overall analytical structure of the model. Incorporating the frequency-dependent permeability of ferrite materials in the inductance and mutual coupling calculations would, therefore, improve modelling fidelity for probes such as ZEUS and THOR, which benefit from magnetic field concentration and enhanced sensitivity due to their ferrite cores.

Collectively, these directions define a clear roadmap for advancing PEC inspection capability. Continued research in advanced classification, adaptive eigenspace design, geometric generalization, and real-time implementation will accelerate the transition of PEC from laboratory research to fully deployable, high-performance NDT solutions for next-generation aerospace platforms.

References

[1] Federal Aviation Administration, *Guide for developing and evaluating repair station and quality control manuals*, Advisory Circular AC 145-9A, Federal Aviation Administration, 2017. [Online]. Available: https : / / www . faa . gov / documentLibrary / media / Advisory_ Circular/AC_145-9A.pdf.

[2] International Civil Aviation Organization, *Standard for aircraft inspection and repair management*, International Civil Aviation Organization, 2014. [Online]. Available: https://www.icao.int/APAC/Meetings/2019%20COSCAPSEA%20iSTARS/9760_cons_en.pdf#search=9760.

[3] P. J. Shull, *Nondestructive Evaluation: Theory, Techniques, and Applications* (Mechanical Engineering). CRC Press, 2002, ISBN: 9780203911068.

[4] C. Hellier, *Handbook of Nondestructive Evaluation*, 3rd. McGraw-Hill Education, 2020, ISBN: 9781260441437.

[5] Canadian General Standards Board (CGSB), "Non-destructive testing—qualification and certification of NDT personnel," Canadian General Standards Board, Ottawa, ON, Canada, Standard CAN/CGSB-48.9712-2022, 2022.

[6] P. Cawley, "Non-destructive testing: Current capabilities and future directions," *Proceedings of the Institution of Mechanical Engineers, Part L: Journal of Materials: Design and Applications*, vol. 215, no. 4, pp. 213–223, Oct. 2001. DOI: 10.1243/1464420011545058.

[7] H. Lemire, P. Underhill, T. Krause, M. Bunn, and D. Butcher, "Improving probability of detection of bolt hole eddy current inspection," *Research in Nondestructive Evaluation*, vol. 21, pp. 141–156, Jul. 2010. DOI: 10.1080/09349841003728951.

[8] A. Ahmad and L. J. Bond, Eds., *ASM Handbook, Volume 17: Nondestructive Evaluation of Materials*. Materials Park, Ohio, United States: ASM International, 2018, ISBN: 9781627081535.

[9] P. F. Horan, P. R. Underhill, and T. W. Krause, "Real time pulsed eddy current detection of cracks in f/a-18 inner wing spar using discriminant separation of modified principal components analysis scores," *IEEE Sensors Journal*, vol. 14, no. 1, pp. 171–177, 2014. DOI: 10.1109/JSEN.2013.2281368.

[10] P. Horan, P. R. Underhill, and T. W. Krause, "Pulsed eddy current detection of cracks in F/A-18 inner wing spar without wing skin removal using modified principal component analysis," *NDT & E International*, vol. 55, pp. 21–27, 2013. DOI: 10.1016/j.ndteint.2013.01.004.

[11] D. M. Butt, "Optimizing pulsed eddy current for inspection of second layer wing structure," M.A.Sc. thesis, Royal Military College of Canada, Kingston, Canada, May 2016.

[12] C. Uemura, "Probability of detection for pulsed eddy current inspection of second layer cracks in aircraft lap-joint structures," M.Sc. thesis, Royal Military College of Canada, Kingston, Canada, Jan. 2018.

[13] T. J. Cadeau, "Increased field depth penetration with pulsed eddy current," M.Sc. thesis, Royal Military College of Canada, Kingston, Canada, Apr. 2008.

[14] D. Desjardins, "Analytical modeling for transient probe response in eddy current testing," M.Sc. thesis, Royal Military College of Canada, Kingston, Canada, 2011.

[15] V. S. Cecco, G. van Drunen, and F. L. Sharp, *Eddy-Current Testing: Manual on Eddy-Current Method* (AECL-7523). Chalk River, Ontario: Atomic Energy of Canada Limited, 1981, vol. 1.

[16] Olympus IMS. "Eddy current testing: Complete guide." Accessed: December 17, 2023. [Online]. Available: https://www.olympus-ims.com/en/ndt-tutorials/eddy-current-testing/depth-of-penetration/.

[17] B. Lebrun, Y. Jayet, and J.-C. Baboux, "Pulsed eddy current signal analysis: Application to the experimental detection and characterization of deep flaws in highly conductive materials," *NDT & E International*, vol. 30, no. 3, pp. 163–170, 1997. DOI: 10.1016/S0963-8695(96)00072-2.

[18] C. Mandache and J. H. V. Lefebvre, "Transient and harmonic eddy currents: Lift-off point of intersection," *NDT & E International*, vol. 39, no. 1, pp. 57–60, 2006. DOI: 10.1016/j.ndteint.2005.06.003.

[19] B. v. Wwedensky, "Concerning the eddy currents generated by a spontaneous change of magnetization," *Annalen der Physik*, vol. 64, no. 17, pp. 609–620, 1921.

[20] C. V. Dodd and W. E. Deeds, "Analytical solutions to eddy-current probe-coil problems," *Journal of Applied Physics*, vol. 39, no. 6, pp. 2829–2838, May 1968. DOI: 10.1063/1.1656680.

[21] J. Bowler and T. Theodoulidis, "Coil impedance variation due to induced current at the edge of a conductive plate," *Journal of Physics D: Applied Physics*, vol. 39, no. 13, pp. 2862–2871, Jun. 2006. DOI: 10.1088/0022-3727/39/13/035.

[22] T. Theodoulidis and J. Bowler, "Eddy current interaction with a right-angled conductive wedge," *Proceedings of the Royal Society A: Mathematical, Physical and Engineering Science*, vol. 461, no. 2064, pp. 3123–3139, Aug. 2005. DOI: 10.1098/rspa.2005.1509.

[23] T. Theodoulidis and J. Bowler, "Interaction of an eddy-current coil with a right-angled conductive wedge," *IEEE Transactions on Magnetics*, vol. 46, no. 4, pp. 1034–1042, May 2010. DOI: 10.1109/TMAG.2009.2036724.

[24] N. Harfield and J. R. Bowler, "Solution of the two-dimensional problem of a crack in a uniform field in eddy-current non-destructive evaluation," *Journal of Physics D: Applied Physics*, vol. 28, no. 10, p. 2197, Oct. 1995. DOI: 10.1088/0022-3727/28/10/032.

[25] Y. Yoshida and J. R. Bowler, "Vector potential integral formulation for eddy-current probe response to cracks," *IEEE Transactions on Magnetics*, vol. 36, no. 2, pp. 461–469, 2000. DOI: 10.1109/20.825808.

[26] H. Sun, J. Bowler, and T. Theodoulidis, "Eddy currents induced in a finite length layered rod by a coaxial coil," *IEEE Transactions on Magnetics*, vol. 41, no. 10, pp. 2455–2461, 2005. DOI: 10.1109/TMAG.2005.855439.

[27] A. Simm, T. Theodoulidis, and N. Poulakis, "Investigation of the magnetic field response from eddy current inspection of defects," *The International Journal of Advanced Manufacturing Technology*, vol. 54, pp. 223–230, Apr. 2011. DOI: 10.1007/s00170-010-2919-5.

[28] G. M. Morozova, V. F. Polygalov, M. I. Epov, and V. S. Mogilatov, "Transient electromagnetic field of current circuit localized on the axis of a hollow magnetic cylinder (solution of the problem and applications)," *Russian Geology and Geophysics*, vol. 41, no. 11, pp. 1435–1444, Nov. 2000.

[29] J. Bi, C. Tian, Y. Fu, T. Jia, C. Bao, and Z. Xue, "Efficient and accurate pulsed eddy current modelling: Enhancing BPNN performance through box-cox transform," *Nondestructive Testing and Evaluation*, vol. 0, no. 0, pp. 1–19, 2025. DOI: 10.1080/10589759.2025.2474095.

[30] D. Desjardins, T. Krause, A. Tetervak, and L. Clapham, "Concerning the derivation of exact solutions to inductive circuit problems for eddy current testing," *NDT & E International*, vol. 68, pp. 128–135, Aug. 2014. DOI: 10.1016/j.ndteint.2014.07.008.

[31] D. Desjardins, T. W. Krause, and L. Clapham, "Transient response of a driver-pickup coil probe in transient eddy current testing," *NDT & E International*, vol. 75, pp. 8–14, Apr. 2015. DOI: 10.1016/j.ndteint.2015.04.008.

[32] M. Fan, P. Huang, B. Ye, D. Hou, G. Zhang, and Z. Zhou, "Analytical modeling for transient probe response in pulsed eddy current testing," *NDT & E International*, vol. 42, no. 5, pp. 376–383, 2009. DOI: 10.1016/j.ndteint.2009.01.005.

[33] X. Chen and Y. Lei, "Time-domain analytical solutions to pulsed eddy current field excited by a probe coil outside a conducting ferromagnetic pipe," *NDT & E International*, vol. 68, pp. 22–27, 2014. DOI: 10.1016/j.ndteint.2014.07.005.

[34] H. Sun, Y. Shi, and W. Zhang, "Time-domain modeling analysis of pulsed eddy current testing on ferromagnetic casing," *Review of Scientific Instruments*, vol. 91, no. 9, p. 094 702, Sep. 2020. DOI: 10.1063/5.0015264.

[35] T. Theodoulidis and A. Skarlatos, "Efficient calculation of transient eddy current response from multi-layer cylindrical conductive media," *Philosophical Transactions of the Royal Society A: Mathematical, Physical and Engineering Sciences*, vol. 378, no. 2182, p. 20 190 588, Jan. 2020. DOI: 10.1098/rsta.2019.0588.

[36] S. Giguère and S. J. M. Dubois, "Pulsed eddy current: Finding corrosion independently of transducer lift-off," *AIP Conference Proceedings*, vol. 509, no. 1, pp. 449–456, May 2000. DOI: 10.1063/1.1306083.

[37] S. Giguère, B. Lepine, and J. Dubois, "Pulsed eddy current technology: Characterizing material loss with gap and lift-off variations," *Research in Nondestructive Evaluation - RES NONDESTRUCT EVAL*, vol. 13, pp. 119–129, Sep. 2001. DOI: 10.1007/s00164-001-0014-x.

[38] G. Y. Tian and A. Sophian, "Reduction of lift-off effects for pulsed eddy current NDT," *NDT & E International*, vol. 38, no. 4, pp. 319–324, 2005. DOI: 10.1016/j.ndteint.2004.09.007.

[39] G. Y. Tian, Y. Li, and C. Mandache, "Study of lift-off invariance for pulsed eddy-current signals," *IEEE Transactions on Magnetics*, vol. 45, no. 1, pp. 184–191, 2009. DOI: 10.1109/TMAG.2008.2006246.

[40] C. Huang and X. Wu, "Probe lift-off compensation method for pulsed eddy current thickness measurement," in *Proceedings of the 2014 3rd Asia-Pacific Conference on Antennas and Propagation (APCAP)*, 2014, pp. 937–939. DOI: 10.1109/APCAP.2014.6992656.

[41] S. Sudirman, F. Natalia, A. Sophian, and A. Ashraf, "Pulsed eddy current signal processing using wavelet scattering and gaussian process regression for fast and accurate ferromagnetic material thickness measurement," *Alexandria Engineering Journal*, vol. 61, no. 12, pp. 11 239–11 250, 2022. DOI: 10.1016/j.aej.2022.04.028.

[42] X. Fu, C. Zhang, X. Peng, L. Jian, and Z. Liu, "Towards end-to-end pulsed eddy current classification and regression with CNN," in *2019 IEEE International Instrumentation and Measurement Technology Conference (I2MTC)*, Auckland, New Zealand, 2019, pp. 1–5. DOI: 10.1109/I2MTC.2019.8826858.

[43] Y. He, M. Pan, D. Chen, and F. Luo, "PEC defect automated classification in aircraft multi-ply structures with interlayer gaps and lift-offs," *NDT & E International*, vol. 53, pp. 39–46, Jan. 2013. DOI: 10.1016/j.ndteint.2012.10.007.

[44] Y. He, M. Pan, F. Luo, D. Chen, and X. Hu, "Support vector machine and optimised feature extraction in integrated eddy current instrument," *Measurement*, vol. 46, no. 1, pp. 764–774, 2013. DOI: 10.1016/j.measurement.2012.09.014.

[45] M. Pan, Y. He, G. Tian, D. Chen, and F. Luo, "PEC frequency band selection for locating defects in two-layer aircraft structures with air gap variations," *IEEE Transactions on Instrumentation and Measurement*, vol. 62, no. 10, pp. 2849–2856, 2013. DOI: 10.1109/TIM.2013.2239892.

[46] C. A. Stott, P. R. Underhill, V. K. Babbar, and T. W. Krause, "Pulsed eddy current detection of cracks in multilayer aluminum lap joints," *IEEE Sensors Journal*, vol. 15, no. 2, pp. 956–962, 2015. DOI: 10.1109/JSEN.2014.2354404.

[47] J. A. Buck, P. R. Underhill, J. E. Morelli, and T. W. Krause, "Simultaneous multiparameter measurement in pulsed eddy current steam generator data using artificial neural networks," *IEEE Transactions on Instrumentation and Measurement*, vol. 65, no. 3, pp. 672–679, 2016. DOI: 10.1109/TIM.2016.2514778.

[48] P. P. Whalen, "Transient eddy current inspection in the presence of ferrous fasteners in multi-layered aluminum structures," Ph.D. dissertation, Royal Military College of Canada, Kingston, 2010.

[49] D. Desjardins, G. Vallières, P. Whalen, and T. Krause, "Advances in transient (pulsed) eddy current for inspection of multi-layer aluminum structures in the presence of ferrous fasteners," *AIP Conference Proceedings*, vol. 1430, pp. 400–407, May 2012. DOI: 10.1063/1.4716256.

[50] V. Babbar, P. Underhill, C. Stott, and T. Krause, "Finite element modeling of second layer crack detection in aircraft bolt holes with ferrous fasteners present," *NDT & E International*, vol. 65, p. 110 006, Jul. 2014. DOI: 10.1016/j.ndteint.2014.03.005.

[51] W. Punter and R. Hughes, "Evaluation of pulsed eddy current generation through aerospace bolts using an internally mounted sensor," *Proceedings of the Annual British Conference on Non-Destructive Testing*, vol. 61, no. 1, pp. 45–52, 2024. DOI: 10.1784/ndt2024.2a3.

[52] B. A. Auld and J. C. Moulder, "Review of advances in quantitative eddy current nondestructive evaluation," *Journal of Nondestructive Evaluation*, vol. 18, pp. 3–36, 1999.

[53] J. Blitz, *Electrical and Magnetic Methods of Non-Destructive Testing* (Non-Destructive Evaluation Series). Springer Netherlands, 1997, ISBN: 9780412791505.

[54] M. S. Luloff, J. Morelli, and T. W. Krause, "Examination of dodd and deeds solutions for a transmit-receive eddy current probe above a layered planar structure," *AIP Conference Proceedings*, vol. 1806, no. 1, p. 110 004, Feb. 2017. DOI: 10.1063/1.4974682.

[55] J. Bowler and T. Theodoulidis, "Eddy currents induced in a conducting rod of finite length by a coaxial encircling coil," *Journal of Physics D: Applied Physics*, vol. 38, p. 2861, Aug. 2005. DOI: 10.1088/0022-3727/38/16/019.

[56] J. Bowler, T. Theodoulidis, H. Xie, and Y. Ji, "Evaluation of eddy-current probe signals due to cracks in fastener holes," *IEEE Transactions on Magnetics*, vol. 48, no. 3, pp. 1159–1170, Mar. 2012. DOI: 10.1109/TMAG.2011.2170084.

[57] T. Theodoulidis, "Developments in calculating the transient eddy-current response from a conductive plate," *IEEE Transactions on Magnetics*, vol. 44, no. 8, pp. 1894–1896, Aug. 2008. DOI: 10.1109/TMAG.2008.919482.

[58] S. Yan and X. Chen, "Time-domain analytical solutions to pulsed eddy current model of moving cylindrical conductor," *NDT & E International*, vol. 137, p. 102 863, Apr. 2023. DOI: 10.1016/j.ndteint.2023.102863.

[59] S. Giguere, *Pulsed Eddy-Currents for Corrosion Detection*. Ottawa, ON, Canada: National Library of Canada [Bibliotheque nationale du Canada], 2000.

[60] C. S. Angani, H. G. Ramos, A. L. Ribeiro, T. J. Rocha, and P. Baskaran, "Lift-off point of intersection feature in transient eddy-current oscillations method to detect thickness variation in stainless steel," *IEEE Transactions on Magnetics*, vol. 52, no. 6, pp. 1–8, 2016. DOI: 10.1109/TMAG.2016.2531024.

[61] Z. Liu, P. Ramuhalli, S. Safizadeh, and D. S. Forsyth, "Combining multiple nondestructive inspection images with a generalized additive model," *Measurement Science and Technology*, vol. 19, no. 8, p. 085 701, Jun. 2008. DOI: 10.1088/0957-0233/19/8/085701.

[62] J. H. V. Lefebvre and J. M. S. Dubois, "Lift-off point of intercept (LOI) behavior," in *AIP Conference Proceedings*, vol. 760, Apr. 2005, pp. 523–530. DOI: 10.1063/1.1916720.

[63] J. H. V. Lefebvre and C. Mandache, "Pulsed eddy current thickness measurement of conductive layers over ferromagnetic substrates," *International Journal of Applied Electromagnetics and Mechanics*, vol. 27, no. 1-2, pp. 1–8, 2008. DOI: 10.3233/JAE-2008-922.

[64] J. Kral, R. Šmíd, H. M. G. Ramos, and A. L. Ribeiro, "The lift-off effect in eddy currents on thickness modeling and measurement," *IEEE Transactions on Instrumentation and Measurement*, vol. 62, no. 7, pp. 2043–2049, 2013. DOI: 10.1109/TIM.2013.2251782.

[65] Y. Yu, Y. Yan, F. Wang, G. Tian, and D. Zhang, "An approach to reduce lift-off noise in pulsed eddy current nondestructive technology," *NDT & E International*, vol. 63, pp. 1–6, 2014. DOI: 10.1016/j.ndteint.2013.12.012.

[66] G. Y. Tian, Y. He, I. Adewale, and A. Simm, "Research on spectral response of pulsed eddy current and NDE applications," *Sensors and Actuators A: Physical*, vol. 189, pp. 313–320, 2013. DOI: 10.1016/j.sna.2012.10.011.

[67] V. Demers-Carpentier, M. Rochette, C. Tremblay, M. M. Sisto, and A. Potvin, "Pulsed eddy current array design and applications," *e-Journal of Nondestructive Testing*, vol. 24, no. 6, 2019, Presented at NDE 2018 Conference and Exhibition of the Indian Society for Non-Destructive Testing (ISNT), 19–21 December 2018, Mumbai, India. [Online]. Available: https://www.ndt.net/?id=24348.

[68] A. Sophian, G. Y. Tian, D. Taylor, and J. Rudlin, "A feature extraction technique based on principal component analysis for pulsed eddy current NDT," *NDT & E International*, vol. 36, no. 1, pp. 37–41, 2003. DOI: 10.1016/S0963-8695(02)00069-5.

[69] J. M. Lattin, J. D. Carroll, and P. E. Green, *Analyzing Multivariate Data* (Analyzing Multivariate Data 1). Thomson Brooks and Cole, 2003, ISBN: 9780534349745.

[70] D. Butt, P. Underhill, and T. Krause, "Examination of pulsed eddy current for inspection of second layer aircraft wing lap-joint structures using outlier detection methods," *CINDE Journal*, vol. 37, pp. 6–10, Sep. 2016.

[71] D. Butt, P. Underhill, and T. Krause, "Enhancing pulsed eddy current for inspection of P-3 Orion lap-joint structures," in *AIP Conference Proceedings*, vol. 1706, American Institute of Physics, Feb. 2016, p. 090 017. DOI: 10.1063/1.4940554.

[72] D. J. Griffiths, *Introduction to electrodynamics*, 4th ed. Cambridge University Press, 2017.

[73] J. Jackson, *Classical Electrodynamics*. Wiley, 1998, ISBN: 9780471309321.

[74] E. W. Weisstein. "Vector laplacian." From MathWorld–A Wolfram Web Resource. [Online]. Available: https://mathworld.wolfram.com/VectorLaplacian.html.

[75] T. W. Krause and P. R. Underhill, "Selecting the correct electromagnetic inspection technology," *Advanced Materials Letters*, vol. 10, no. 12, pp. 1–8, 2019. DOI: 10.5185/amlett.2019.2213.

[76] Iowa State University Center for Nondestructive Evaluation. "Nondestructive evaluation techniques: Eddy current testing," Accessed: Oct. 13, 2023. [Online]. Available: https://www.nde-ed.org/NDETechniques/EddyCurrent/AdvancedTechniques/pulsedecinspection.xhtml.

[77] H. C. Ohanian, "On the approach to electro- and magneto-static equilibrium," *American Journal of Physics*, vol. 51, no. 11, pp. 1020–1022, 1983. DOI: 10.1119/1.13364.

[78] T. W. Krause, C. Mandache, and J. H. V. Lefebvre, "Diffusion of pulsed eddy currents in thin conducting plates," *AIP Conference Proceedings*, vol. 975, no. 1, pp. 368–375, Feb. 2008. DOI: 10.1063/1.2902682.

[79] P. O. Moore and S. S. Upda, "Electromagnetic testing," in *Nondestructive Testing Handbook*, 3rd ed. American Society for Nondestructive Testing, 2004, vol. 5.

[80] H. D. Young and R. A. Freedman, *University Physics*. San Francisco: Pearson Education, 2004.

[81] G. Rizzoni and J. A. Kearns, *Principles and Applications of Electrical Engineering*. New York: McGraw-Hill Education, 2022, ISBN: 9781260596984.

[82] S. Goldman, *Transformation Calculus and Electrical Transients*. New York: Prentice Hall Inc., 1949.

[83] D. Desjardins, T. Krause, and L. Clapham, "Transient eddy current method for the characterization of magnetic permeability and conductivity," *NDT & E International*, vol. 80, pp. 65–70, 2016. DOI: 10.1016/j.ndteint.2016.02.010.

[84] A. Sophian, G. Y. Tian, and M. Fan, "Pulsed eddy current non-destructive testing and evaluation: A review," *Chinese Journal of Mechanical Engineering*, vol. 30, pp. 500–514, 2017.

[85] J. Ge, C. Yang, P. Wang, and Y. Shi, "Defect classification using postpeak value for pulsed eddy-current technique," *Sensors*, vol. 20, no. 12, 2020. DOI: 10.3390/s20123390.

[86] R. Miorelli and C. Reboud, "Fast simulation tools dedicated to pulsed eddy current applications," in *Electromagnetic Non-Destructive Evaluation (XXI)*. Amsterdam, Netherlands: IOS Press, 2018, pp. 25–32.

[87] M. S. Safizadeh, B. A. Lepine, D. S. Forsyth, and A. Fahr, "Time-frequency analysis of pulsed eddy current signals," *Journal of Nondestructive Evaluation*, vol. 20, no. 2, pp. 73–86, Jun. 2001. DOI: 10.1023/a:1012244208475.

[88] E. Kreyszig, *Advanced Engineering Mathematics*, 10th ed. John Wiley & Sons, 2011.

[89] L. C. Andrews, B. K. Shivamoggi, and S. of Photo-Optical Instrumentation Engineers, *Integral Transforms for Engineers*. SPIE Optical Engineering Press, 1999, ISBN: 9780819432322.

[90] E. W. Weisstein, *Bessel function of the first kind*, From MathWorld–A Wolfram Web Resource., 2024. [Online]. Available: https://mathworld.wolfram.com/BesselFunctionoftheFirstKind.html.

[91] D. W. Kammler, *A First Course in Fourier Analysis*. Cambridge University Press, 2007, ISBN: 9780521883405.

[92] I. T. Jolliffe, *Principal Component Analysis* (Springer Series in Statistics), 2nd ed. Springer New York, 2013, ISBN: 9781475719048.

[93] H. Abdi and L. J. Williams, "Principal component analysis," *Wiley Interdisciplinary Reviews: Computational Statistics*, vol. 2, no. 4, pp. 433–459, 2010. DOI: 10.1002/wics.101.

[94] S. Wold, K. Esbensen, and P. Geladi, "Principal component analysis," *Chemometrics and Intelligent Laboratory Systems*, vol. 2, no. 1, pp. 37–52, 1987, Proceedings of the Multivariate Statistical Workshop for Geologists and Geochemists. DOI: 10.1016/0169-7439(87)80084-9.

[95] G. Yang, P. Que, and T.-L. Chen, "Independent component analysis-based feature extraction technique for defect classification applied for pulsed eddy current NDE," *Research in Nondestructive Evaluation*, vol. 20, Oct. 2009. DOI: 10.1080/09349840903078996.

[96] R. A. Fisher, "The use of multiple measurements in taxonomic problems," *Annals of Eugenics*, vol. 7, no. 2, pp. 179–188, 1936. DOI: 10.1111/j.1469-1809.1936.tb02137.x.

[97] U.S. Department of Defense, *MIL-HDBK-1823A (notice-2): Nondestructive evaluation system reliability assessment*, Nov. 2018.

[98] D. Berry and B. Lindgren, *Statistics: Theory and Methods*. Duxbury Press, 1996, ISBN: 9780534504793.

[99] Y. Lu and J. Bowler, "An analytical model of eddy current ferrite-core probes," *AIP Conference Proceedings*, vol. 1430, pp. 387–392, May 2012. DOI: 10.1063/1.4716254.

[100] P. May, E. Zhou, and D. Morton, "The design of a ferrite-cored probe," *Sensors and Actuators A: Physical*, vol. 136, no. 1, pp. 221–228, 2007, 25th Anniversary of Sensors and Actuators A: Physical. DOI: 10.1016/j.sna.2006.11.031.

[101] T. Krause, R. J. McGregor, A. Tetervak, and R. Underhill, *Pulsed eddy current sensor for precision measurement at large lift-offs on metallic surfaces*, United States Patent 9091664B2, Jul. 2015.

[102] T. Krause, R. Underhill, and A. Tetervak, "Through-tile pressure-hull circularity/topology measurement and corrosion detection technology: Further development and qualification testing of pulsed eddy current offset-measurement technique-RMCC/DRDC-DRSI Annex-PRI0024," Nov. 2010, Accessed: December 12, 2024.

[103] JET-TEK, *HI-TIGUE™(HLT™) fasteners*, Accessed: 2024-06-24, Oct. 2022. [Online]. Available: https://jet-tek.com/product-specialties/hi-tigue-pins-hlt-fasteners/.

[104] Canadian Forces, *C-12-188-SRM / MM-02 CF-188 structural manual*, Canadian Forces Technical Order.

[105] L-3 MAS Canada, "New NDT techniques - project definition report," L-3 MAS Canada, Tech. Rep., 2007, F/A 18 Fleet Management.

[106] J. R. Davis, *ASM Specialty Handbook: Aluminum and Aluminum Alloys*. Materials Park, OH: ASM International, Jan. 1993, ISBN: 9780871704962.

[107] G. Welsch, R. Boyer, and E. Collings, *Materials Properties Handbook: Titanium Alloys* (Materials properties handbook). ASM International, 1993, ISBN: 9780871704818.

[108] F. M. Smits, "Measurement of sheet resistivities with the four-point probe," *The Bell System Technical Journal*, vol. 37, no. 3, pp. 711–718, 1958. DOI: 10.1002/j.1538-7305.1958.tb03883.x.

[109] F. Van Barr, J. Wyman, P. Ross Underhill, A. K. Krause, and T. W. Krause, "Eddy current method for inspecting foil-to-tab weld quality in li-ion batteries," *IEEE Transactions on Instrumentation and Measurement*, vol. 74, pp. 1–8, 2025. DOI: 10.1109/TIM.2025.3545707.

[110] M. Luloff, "Numerical modelling of eddy current probes for candu® fuel channel inspection," M.A.Sc. thesis, Queen's University, Kingston, Canada, Sep. 2016.

[111] Carpenter Technology Corporation, *Carpenter 13-8 stainless*, 2004. Accessed: Apr. 12, 2026. [Online]. Available: https://www.spacematdb.com/spacemat/manudatasheets/PH13-8Mo.pdf.

[112] A. Savitzky and M. J. E. Golay, "Smoothing and differentiation of data by simplified least squares procedures," *Analytical Chemistry*, vol. 36, no. 8, pp. 1627–1639, 1964.

[113] M. Müller, *Information Retrieval for Music and Motion*. Berlin, Germany: Springer, 2007. DOI: 10.1007/978-3-540-74048-3.

[114] G. Klein, "Comprehensive modelling for eddy current based pressure tube to calandria tube gap measurements," M.A.Sc. thesis, Queen's University, Kingston, ON, 2017.

[115] H. A. Wheeler, "Simple inductance formulas for radio coils," *Proceedings of the Institute of Radio Engineers*, vol. 16, no. 10, pp. 1398–1400, 1928.

[116] H. A. Sabbagh, J. R. Bowler, and L. D. Sabbagh, "A model of eddy-current probes with ferrite cores," *Nondestructive Testing and Evaluation*, vol. 5, no. 1, pp. 67–79, 1989. DOI: 10.1080/02780898908952955.

[117] F. Buvat, G. Pichenot, D. Prémel, D. Lesselier, M. Lambert, H. Voillaume, and J.-P. Choffy, "Eddy-current modeling of ferrite-cored probes," *AIP Conference Proceedings*, vol. 760, no. 1, pp. 463–470, Apr. 2005. DOI: 10.1063/1.1916712.

[118] M. Maaß, A. Griessner, V. Steixner, and C. Zierhofer, "Reduction of eddy current losses in inductive transmission systems with ferrite sheets," *BioMed Eng OnLine*, vol. 16, no. 3, 2017. DOI: 10.1186/s12938-016-0297-4.

[119] A. Skarlatos and T. Theodoulidis, "Study of the non-linear eddy-current response in a ferromagnetic plate: Theoretical analysis for the 2D case," *NDT & E International*, vol. 93, pp. 150–156, 2018. DOI: 10.1016/j.ndteint.2017.09.003.

[120] K. Hinkelmann and O. Kempthorne, *Design and Analysis of Experiments, Volume 1: Introduction to Experimental Design*, 2nd ed. Hoboken, NJ: John Wiley & Sons, 2008.

[121] J. R. Taylor, *An Introduction to Error Analysis: The Study of Uncertainties in Physical Measurements*, 2nd ed. Sausalito, CA: University Science Books, 1997.

Appendices

A Fastener Geometries

This appendix provides dimensional drawings of the aerospace fastener families evaluated in this work, including the HLT53 (Figure A.1), HLT313 (Figure A.2), and HLT265 (Figure A.3) series. The HLT53, HLT313, and HLT265 series represent common high-strength structural fasteners used in wing spar and multi-layer aircraft assemblies. Differences in head geometry, shank diameter, grip length, and countersink profile influence local electromagnetic field redistribution and therefore affect PEC signal behaviour. These drawings are included to provide geometric context for the flaw-detection results presented in Chapter 8 and Chapter 9.

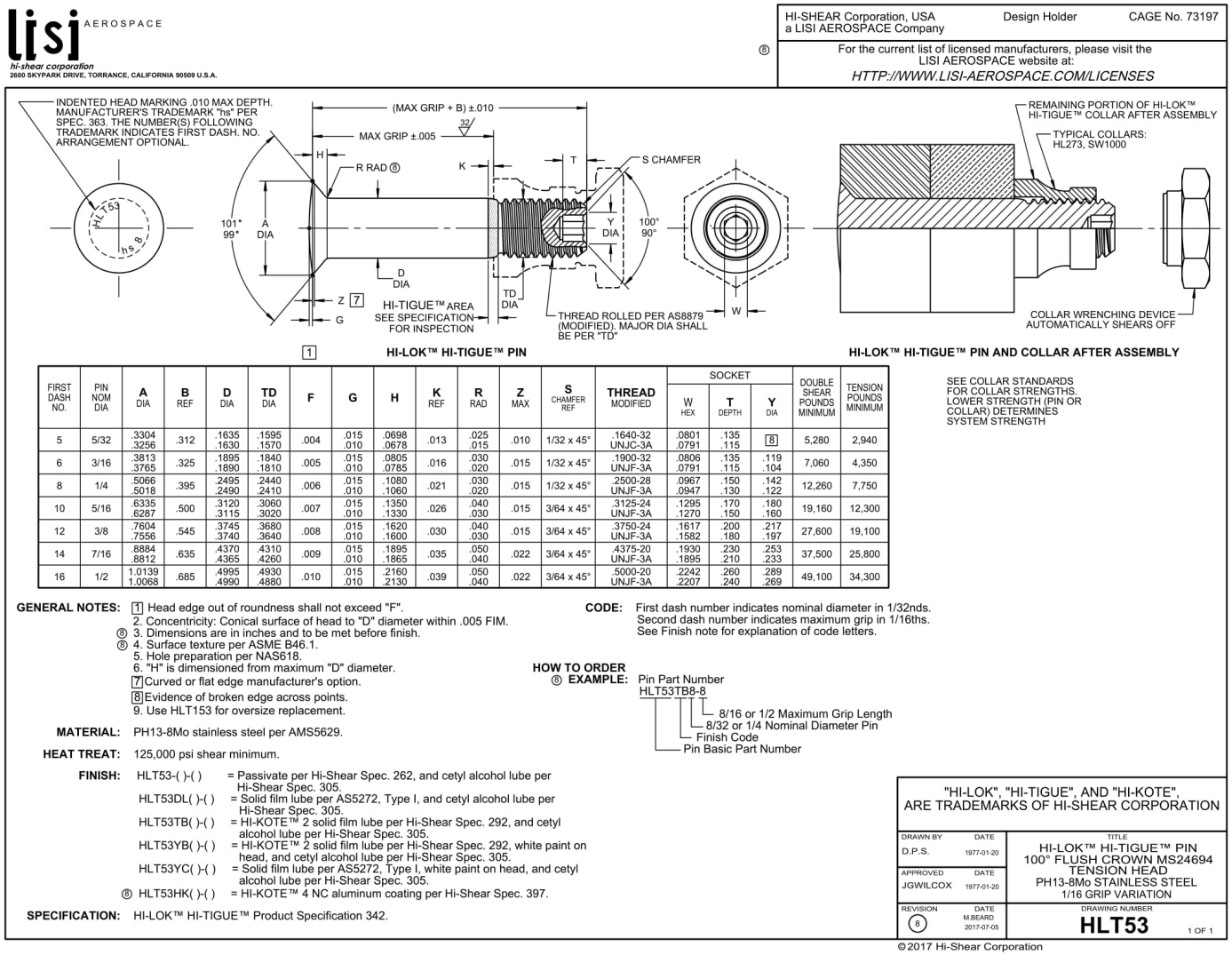

FIRST DASH NO.	PIN NOM DIA	A DIA	B REF	D DIA	TD DIA	F	G	H	K REF	R RAD	Z MAX	S CHAMFER REF	THREAD MODIFIED	SOCKET W HEX	SOCKET T DEPTH	SOCKET Y DIA	DOUBLE SHEAR POUNDS MINIMUM	TENSION POUNDS MINIMUM
5	5/32	.3304 .3256	.312	.1635 .1630	.1595 .1570	.004	.015 .010	.0698 .0678	.013	.025 .015	.010	1/32 x 45°	.1640-32 UNJC-3A	.0801 .0791	.135 .115	[8]	5,280	2,940
6	3/16	.3813 .3765	.325	.1895 .1890	.1840 .1810	.005	.015 .010	.0805 .0785	.016	.030 .020	.015	1/32 x 45°	.1900-32 UNJF-3A	.0806 .0791	.135 .115	.119 .104	7,060	4,350
8	1/4	.5066 .5018	.395	.2495 .2490	.2440 .2410	.006	.015 .010	.1080 .1060	.021	.030 .020	.015	1/32 x 45°	.2500-28 UNJF-3A	.0967 .0947	.150 .130	.142 .122	12,260	7,750
10	5/16	.6335 .6287	.500	.3120 .3115	.3060 .3020	.007	.015 .010	.1350 .1330	.026	.040 .030	.015	3/64 x 45°	.3125-24 UNJF-3A	.1295 .1270	.170 .150	.180 .160	19,160	12,300
12	3/8	.7604 .7556	.545	.3745 .3740	.3680 .3640	.008	.015 .010	.1620 .1600	.030	.040 .030	.015	3/64 x 45°	.3750-24 UNJF-3A	.1617 .1582	.200 .180	.217 .197	27,600	19,100
14	7/16	.8884 .8812	.635	.4370 .4365	.4310 .4260	.009	.015 .010	.1895 .1865	.035	.050 .040	.022	3/64 x 45°	.4375-20 UNJF-3A	.1930 .1895	.230 .210	.253 .233	37,500	25,800
16	1/2	1.0139 1.0068	.685	.4995 .4990	.4930 .4880	.010	.015 .010	.2160 .2130	.039	.050 .040	.022	3/64 x 45°	.5000-20 UNJF-3A	.2242 .2207	.260 .240	.289 .269	49,100	34,300

SEE COLLAR STANDARDS FOR COLLAR STRENGTHS. LOWER STRENGTH (PIN OR COLLAR) DETERMINES SYSTEM STRENGTH

GENERAL NOTES:
[1] Head edge out of roundness shall not exceed "F".
2. Concentricity: Conical surface of head to "D" diameter within .005 FIM.
® 3. Dimensions are in inches and to be met before finish.
® 4. Surface texture per ASME B46.1.
5. Hole preparation per NAS618.
6. "H" is dimensioned from maximum "D" diameter.
[7] Curved or flat edge manufacturer's option.
[8] Evidence of broken edge across points.
9. Use HLT153 for oversize replacement.

MATERIAL: PH13-8Mo stainless steel per AMS5629.

HEAT TREAT: 125,000 psi shear minimum.

FINISH:
HLT53-( )-( ) = Passivate per Hi-Shear Spec. 262, and cetyl alcohol lube per Hi-Shear Spec. 305.
HLT53DL( )-( ) = Solid film lube per AS5272, Type I, and cetyl alcohol lube per Hi-Shear Spec. 305.
HLT53TB( )-( ) = HI-KOTE™ 2 solid film lube per Hi-Shear Spec. 292, and cetyl alcohol lube per Hi-Shear Spec. 305.
HLT53YB( )-( ) = HI-KOTE™ 2 solid film lube per Hi-Shear Spec. 292, white paint on head, and cetyl alcohol lube per Hi-Shear Spec. 305.
HLT53YC( )-( ) = Solid film lube per AS5272, Type I, white paint on head, and cetyl alcohol lube per Hi-Shear Spec. 305.
® HLT53HK( )-( ) = HI-KOTE™ 4 NC aluminum coating per Hi-Shear Spec. 397.

SPECIFICATION: HI-LOK™ HI-TIGUE™ Product Specification 342.

CODE: First dash number indicates nominal diameter in 1/32nds. Second dash number indicates maximum grip in 1/16ths. See Finish note for explanation of code letters.

HOW TO ORDER
® **EXAMPLE:** Pin Part Number HLT53TB8-8
- 8/16 or 1/2 Maximum Grip Length
- 8/32 or 1/4 Nominal Diameter Pin
- Finish Code
- Pin Basic Part Number

"HI-LOK", "HI-TIGUE", AND "HI-KOTE", ARE TRADEMARKS OF HI-SHEAR CORPORATION

DRAWN BY	DATE	TITLE
D.P.S.	1977-01-20	HI-LOK™ HI-TIGUE™ PIN 100° FLUSH CROWN MS24694 TENSION HEAD PH13-8Mo STAINLESS STEEL 1/16 GRIP VARIATION
APPROVED JGWILCOX	DATE 1977-01-20	
REVISION (8)	DATE M.BEARD 2017-07-05	DRAWING NUMBER HLT53 1 OF 1

HLT53

Figure A.1: Dimensional drawing of the HLT53 fastener family used in this study. The geometry includes a protruding head configuration with defined grip length and shank diameter.

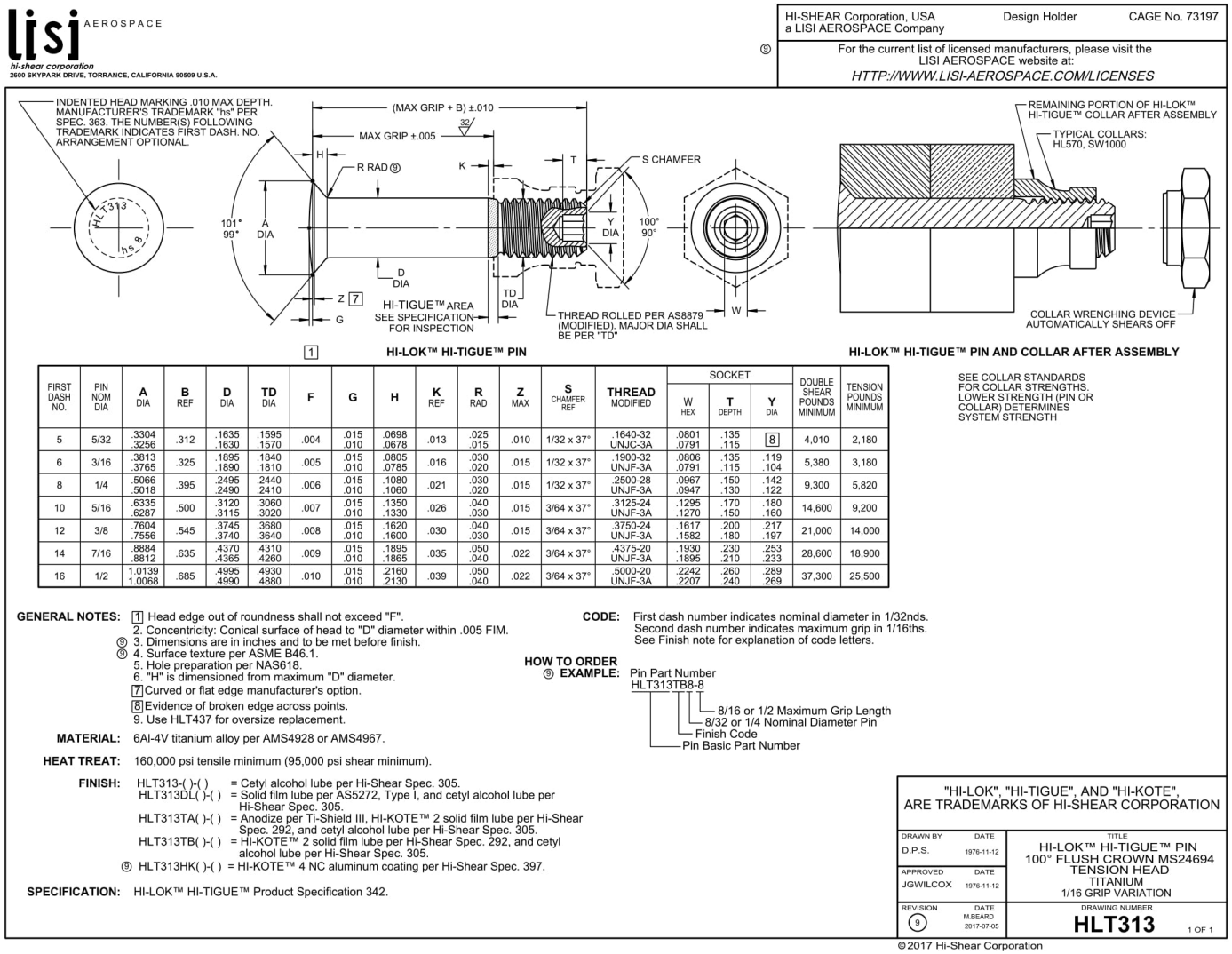

1 **HI-LOK™ HI-TIGUE™ PIN**

HI-LOK™ HI-TIGUE™ PIN AND COLLAR AFTER ASSEMBLY

FIRST DASH NO.	PIN NOM DIA	A DIA	B REF	D DIA	TD DIA	F	G	H	K REF	R RAD	Z MAX	S CHAMFER REF	THREAD MODIFIED	SOCKET W HEX	SOCKET T DEPTH	SOCKET Y DIA	DOUBLE SHEAR POUNDS MINIMUM	TENSION POUNDS MINIMUM
5	5/32	.3304 .3256	.312	.1635 .1630	.1595 .1570	.004	.015 .010	.0698 .0678	.013	.025 .015	.010	1/32 x 37°	.1640-32 UNJC-3A	.0801 .0791	.135 .115	8	4,010	2,180
6	3/16	.3813 .3765	.325	.1895 .1890	.1840 .1810	.005	.015 .010	.0805 .0785	.016	.030 .020	.015	1/32 x 37°	.1900-32 UNJF-3A	.0806 .0791	.135 .115	.119 .104	5,380	3,180
8	1/4	.5066 .5018	.395	.2495 .2490	.2440 .2410	.006	.015 .010	.1080 .1060	.021	.030 .020	.015	1/32 x 37°	.2500-28 UNJF-3A	.0967 .0947	.150 .130	.142 .122	9,300	5,820
10	5/16	.6335 .6287	.500	.3120 .3115	.3060 .3020	.007	.015 .010	.1350 .1330	.026	.040 .030	.015	3/64 x 37°	.3125-24 UNJF-3A	.1295 .1270	.170 .150	.180 .160	14,600	9,200
12	3/8	.7604 .7556	.545	.3745 .3740	.3680 .3640	.008	.015 .010	.1620 .1600	.030	.040 .030	.015	3/64 x 37°	.3750-24 UNJF-3A	.1617 .1582	.200 .180	.217 .197	21,000	14,000
14	7/16	.8884 .8812	.635	.4370 .4365	.4310 .4260	.009	.015 .010	.1895 .1865	.035	.050 .040	.022	3/64 x 37°	.4375-20 UNJF-3A	.1930 .1895	.230 .210	.253 .233	28,600	18,900
16	1/2	1.0139 1.0068	.685	.4995 .4990	.4930 .4880	.010	.015 .010	.2160 .2130	.039	.050 .040	.022	3/64 x 37°	.5000-20 UNJF-3A	.2242 .2207	.260 .240	.289 .269	37,300	25,500

SEE COLLAR STANDARDS FOR COLLAR STRENGTHS. LOWER STRENGTH (PIN OR COLLAR) DETERMINES SYSTEM STRENGTH

GENERAL NOTES:
1. Head edge out of roundness shall not exceed "F".
2. Concentricity: Conical surface of head to "D" diameter within .005 FIM.
⑨ 3. Dimensions are in inches and to be met before finish.
⑨ 4. Surface texture per ASME B46.1.
5. Hole preparation per NAS618.
6. "H" is dimensioned from maximum "D" diameter.
7. Curved or flat edge manufacturer's option.
8. Evidence of broken edge across points.
9. Use HLT437 for oversize replacement.

MATERIAL: 6Al-4V titanium alloy per AMS4928 or AMS4967.

HEAT TREAT: 160,000 psi tensile minimum (95,000 psi shear minimum).

FINISH:
HLT313-( )-( ) = Cetyl alcohol lube per Hi-Shear Spec. 305.
HLT313DL( )-( ) = Solid film lube per AS5272, Type I, and cetyl alcohol lube per Hi-Shear Spec. 305.
HLT313TA( )-( ) = Anodize per Ti-Shield III, HI-KOTE™ 2 solid film lube per Hi-Shear Spec. 292, and cetyl alcohol lube per Hi-Shear Spec. 305.
HLT313TB( )-( ) = HI-KOTE™ 2 solid film lube per Hi-Shear Spec. 292, and cetyl alcohol lube per Hi-Shear Spec. 305.
⑨ HLT313HK( )-( ) = HI-KOTE™ 4 NC aluminum coating per Hi-Shear Spec. 397.

SPECIFICATION: HI-LOK™ HI-TIGUE™ Product Specification 342.

CODE: First dash number indicates nominal diameter in 1/32nds. Second dash number indicates maximum grip in 1/16ths. See Finish note for explanation of code letters.

HOW TO ORDER
⑨ **EXAMPLE:** Pin Part Number
HLT313TB8-8
- 8/16 or 1/2 Maximum Grip Length
- 8/32 or 1/4 Nominal Diameter Pin
- Finish Code
- Pin Basic Part Number

"HI-LOK", "HI-TIGUE", AND "HI-KOTE", ARE TRADEMARKS OF HI-SHEAR CORPORATION

DRAWN BY	DATE	TITLE
D.P.S.	1976-11-12	HI-LOK™ HI-TIGUE™ PIN 100° FLUSH CROWN MS24694 TENSION HEAD TITANIUM 1/16 GRIP VARIATION
APPROVED JGWILCOX	DATE 1976-11-12	
REVISION ⑨	DATE M.BEARD 2017-07-05	DRAWING NUMBER HLT313 1 OF 1

Figure A.2: Dimensional drawing of the HLT313 fastener family. This configuration features a countersunk head profile that modifies near-surface field distribution relative to protruding-head designs.

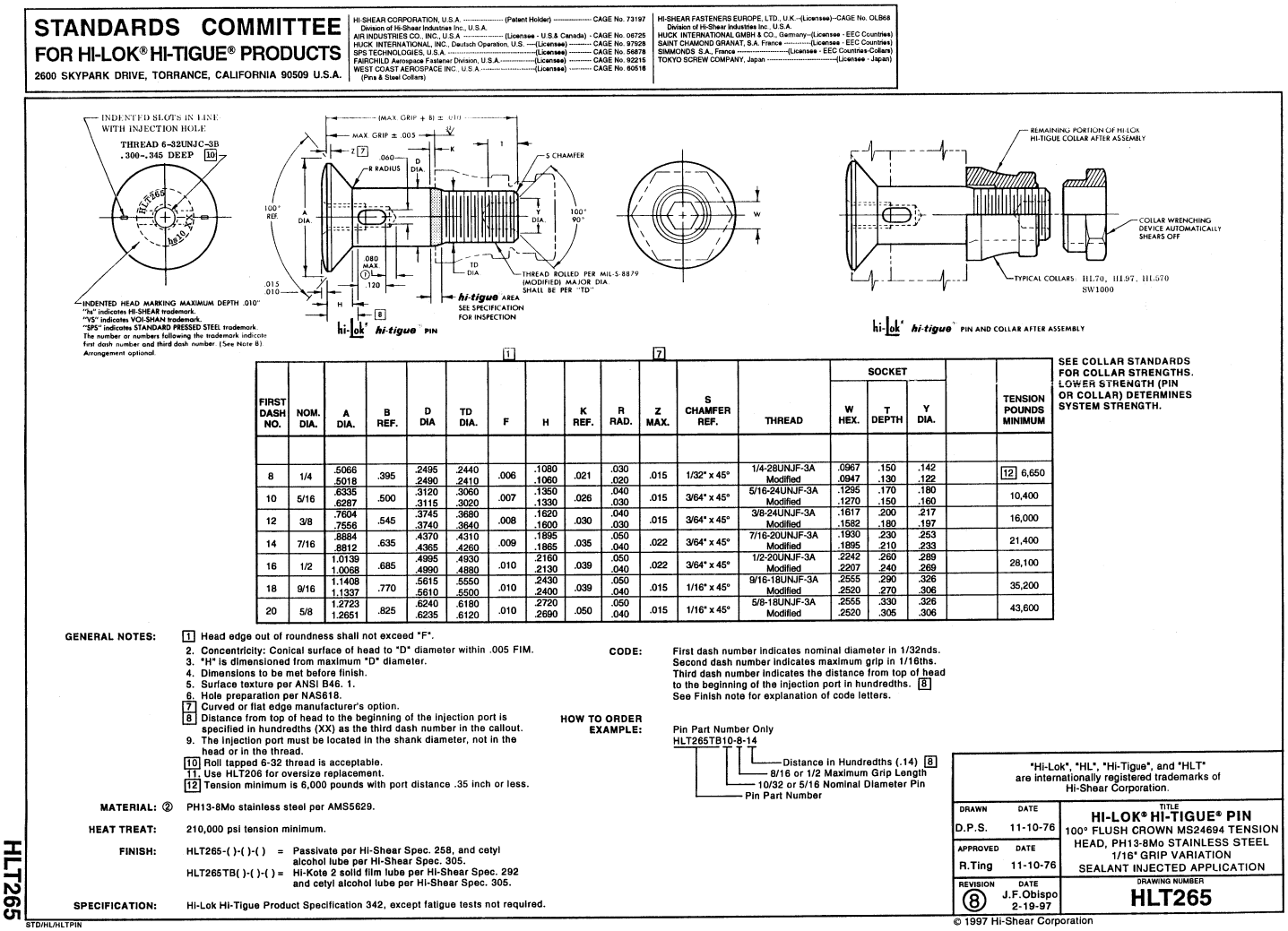

FIRST DASH NO.	NOM. DIA.	A DIA.	B REF.	D DIA	TD DIA.	F	H	K REF.	R RAD.	Z MAX.	S CHAMFER REF.	THREAD	SOCKET W HEX.	SOCKET T DEPTH	SOCKET Y DIA.		TENSION POUNDS MINIMUM
8	1/4	.5066 .5018	.395	.2495 .2490	.2440 .2410	.006	.1080 .1060	.021	.030 .020	.015	1/32" x 45°	1/4-28UNJF-3A Modified	.0967 .0947	.150 .130	.142 .122		12 6,650
10	5/16	.6335 .6287	.500	.3120 .3115	.3060 .3020	.007	.1350 .1330	.026	.040 .030	.015	3/64" x 45°	5/16-24UNJF-3A Modified	.1295 .1270	.170 .150	.180 .160		10,400
12	3/8	.7604 .7556	.545	.3745 .3740	.3680 .3640	.008	.1620 .1600	.030	.040 .030	.015	3/64" x 45°	3/8-24UNJF-3A Modified	.1617 .1582	.200 .180	.217 .197		16,000
14	7/16	.8884 .8812	.635	.4370 .4365	.4310 .4260	.009	.1895 .1865	.035	.050 .040	.022	3/64" x 45°	7/16-20UNJF-3A Modified	.1930 .1895	.230 .210	.253 .233		21,400
16	1/2	1.0139 1.0068	.685	.4995 .4990	.4930 .4880	.010	.2160 .2130	.039	.050 .040	.022	3/64" x 45°	1/2-20UNJF-3A Modified	.2242 .2207	.260 .240	.289 .269		28,100
18	9/16	1.1408 1.1337	.770	.5615 .5610	.5550 .5500	.010	.2430 .2400	.039	.050 .040	.015	1/16" x 45°	9/16-18UNJF-3A Modified	.2555 .2520	.290 .270	.326 .306		35,200
20	5/8	1.2723 1.2651	.825	.6240 .6235	.6180 .6120	.010	.2720 .2690	.050	.050 .040	.015	1/16" x 45°	5/8-18UNJF-3A Modified	.2555 .2520	.330 .305	.326 .306		43,600

SEE COLLAR STANDARDS FOR COLLAR STRENGTHS. LOWER STRENGTH (PIN OR COLLAR) DETERMINES SYSTEM STRENGTH.

GENERAL NOTES:

1. Head edge out of roundness shall not exceed "F".
2. Concentricity: Conical surface of head to "D" diameter within .005 FIM.
3. "H" is dimensioned from maximum "D" diameter.
4. Dimensions to be met before finish.
5. Surface texture per ANSI B46. 1.
6. Hole preparation per NAS618.
7. Curved or flat edge manufacturer's option.
8. Distance from top of head to the beginning of the injection port is specified in hundredths (XX) as the third dash number in the callout.
9. The injection port must be located in the shank diameter, not in the head or in the thread.
10. Roll tapped 6-32 thread is acceptable.
11. Use HLT206 for oversize replacement.
12. Tension minimum is 6,000 pounds with port distance .35 inch or less.

CODE: First dash number indicates nominal diameter in 1/32nds. Second dash number indicates maximum grip in 1/16ths. Third dash number indicates the distance from top of head to the beginning of the injection port in hundredths. 8 See Finish note for explanation of code letters.

HOW TO ORDER EXAMPLE: Pin Part Number Only HLT265TB10-8-14

- HLT265 — Pin Part Number
- TB — 10/32 or 5/16 Nominal Diameter Pin
- 10 — 8/16 or 1/2 Maximum Grip Length
- 8 — Distance in Hundredths (.14)

MATERIAL: ② PH13-8Mo stainless steel per AMS5629.

HEAT TREAT: 210,000 psi tension minimum.

FINISH: HLT265-( )-( )-( ) = Passivate per Hi-Shear Spec. 258, and cetyl alcohol lube per Hi-Shear Spec. 305.
HLT265TB( )-( )-( ) = Hi-Kote 2 solid film lube per Hi-Shear Spec. 292 and cetyl alcohol lube per Hi-Shear Spec. 305.

SPECIFICATION: Hi-Lok Hi-Tigue Product Specification 342, except fatigue tests not required.

HLT265

STD/HL/HLTPIN

DRAWN	DATE	TITLE
D.P.S.	11-10-76	HI-LOK® HI-TIGUE® PIN 100° FLUSH CROWN MS24694 TENSION HEAD, PH13-8Mo STAINLESS STEEL 1/16" GRIP VARIATION SEALANT INJECTED APPLICATION
APPROVED	DATE	
R.Ting	11-10-76	
REVISION	DATE	DRAWING NUMBER
⑧	J.F.Obispo 2-19-97	HLT265

Figure A.3: Dimensional drawing of the HLT265 fastener family. Variations in head geometry and shank dimensions relative to HLT53 and HLT313 influence eddy current redistribution and pickup-coil coupling.

B Comprehensive Model Comparison Figures

This appendix presents full time-domain PEC responses for all investigated materials and thicknesses, including analytical predictions, FEM simulations, and experimental measurements.

For each material configuration, responses are shown for lift-offs ranging from 0 mm to 10 mm in 1 mm increments. Figures are organized to facilitate direct qualitative comparison of waveform morphology, amplitude scaling, and diffusion-driven timing behaviour across modelling approaches.

All responses were processed using identical time bases and plotting scales to ensure direct visual comparison between modelling approaches. Analytical and FEM results were reconstructed using the same excitation waveform and material parameters employed in the experimental configuration. Experimental signals were peak-aligned to mitigate trigger-offset effects identified in Section 7.1.6. No amplitude normalization was applied unless otherwise stated, such that differences reflect true modelling and measurement deviations.

A summary of all model comparison figures provided in this appendix is listed in Table B.1.

Table B.1: Summary of full time-domain PEC model comparison figures provided in this appendix.

Material	Thickness (mm)	Figure Reference
2024-T4 Aluminum	5.30	Figure B.1
2024-T4 Aluminum	2.87	Figure B.2
6061-T6 Aluminum	3.12	Figure B.3
6061-T6 Aluminum	9.55	Figure B.4
Copper	3.30	Figure B.5
Ti-2	4.06	Figure B.6
Ti-6Al-4V	3.80	Figure B.7

Detailed waveform comparisons for each material configuration follow.

B.1 2024-T4 Aluminum

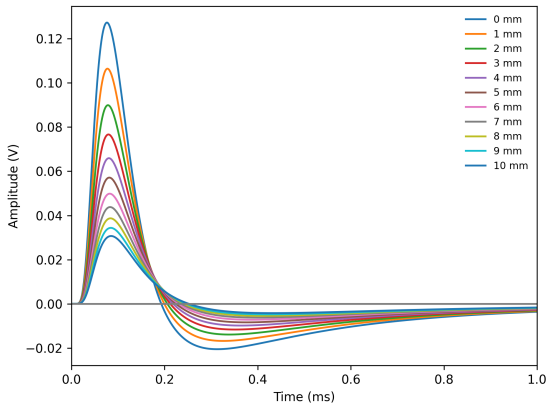

(a) Analytical

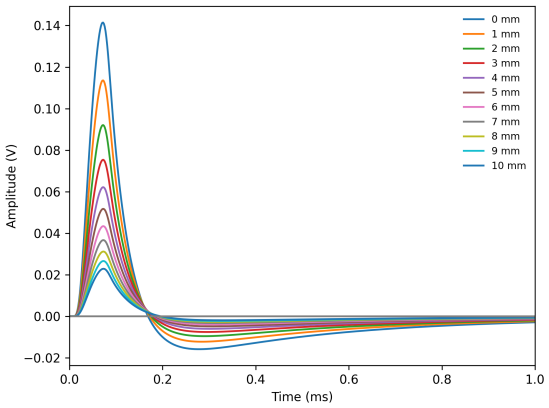

(b) FEM

8

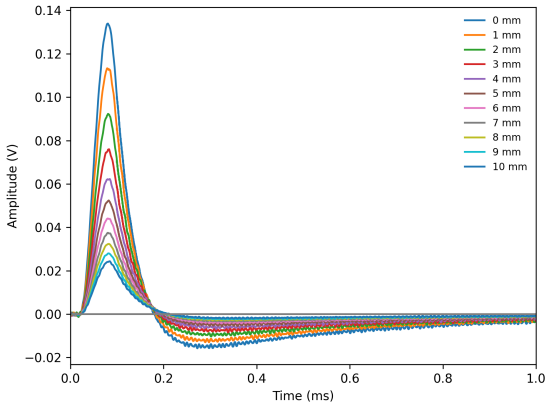

(c) Experimental

Figure B.1: Lift-off dependent PEC responses for 2024-T4 aluminum ($p = 5.3$ mm).

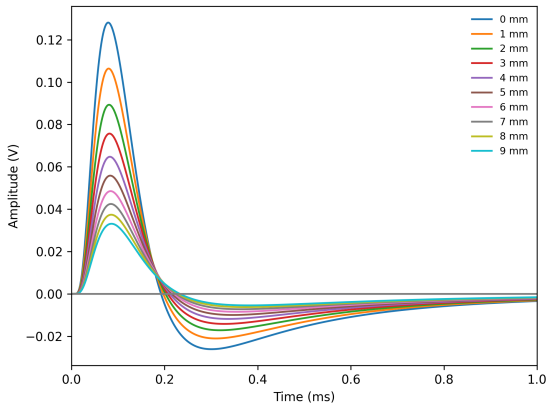

(a) Analytical

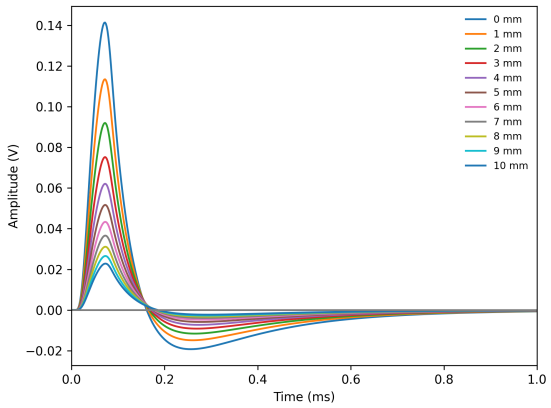

(b) FEM

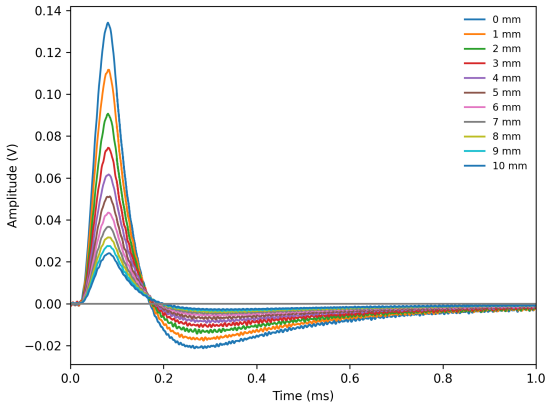

(c) Experimental

Figure B.2: Lift-off dependent PEC responses for 2024-T4 aluminum ($p = 2.87$ mm).

B.2 6061-T6 Aluminum

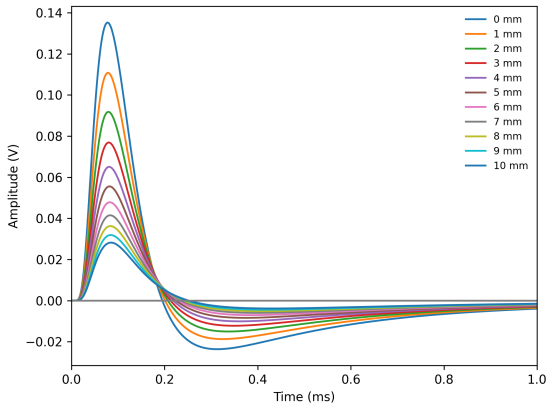

(a) Analytical

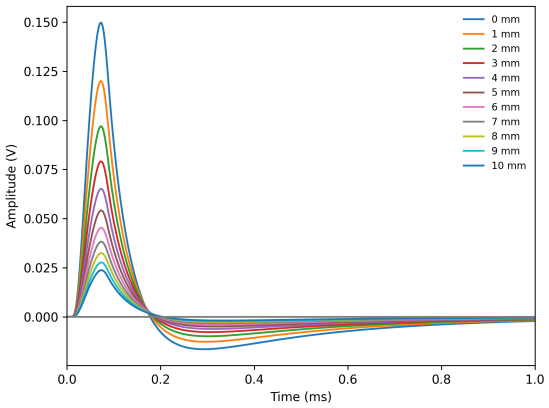

(b) FEM

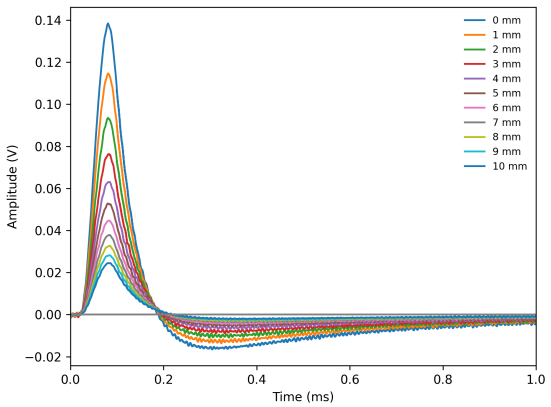

(c) Experimental

Figure B.3: PEC responses for 6061-T6 aluminum ($p = 3.12$ mm).

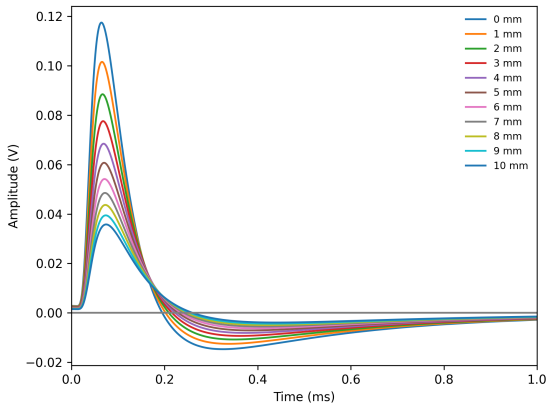

(a) Analytical

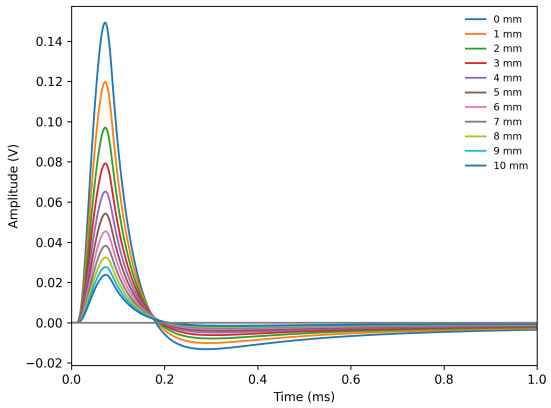

(b) FEM

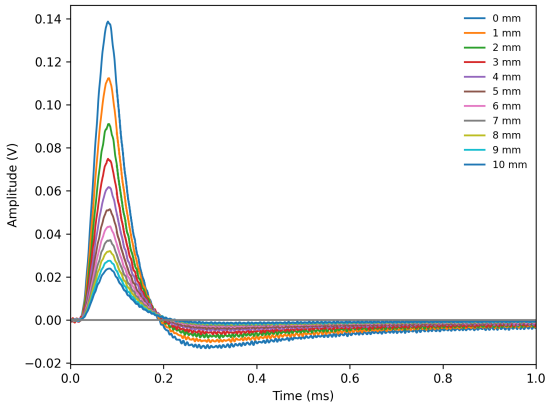

(c) Experimental

Figure B.4: PEC responses for 6061-T6 aluminum ($p = 9.55$ mm).

B.3 Copper

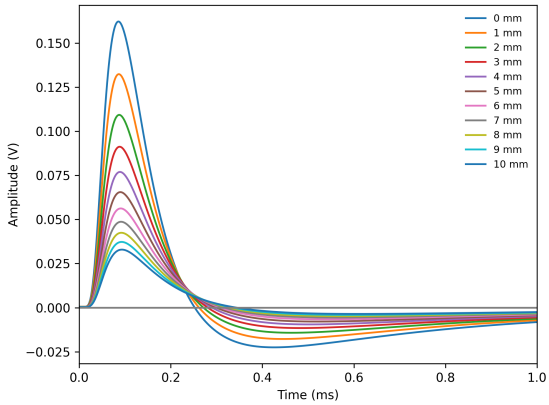

(a) Analytical

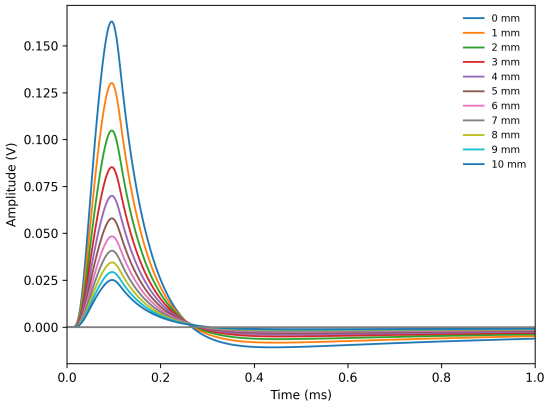

(b) FEM

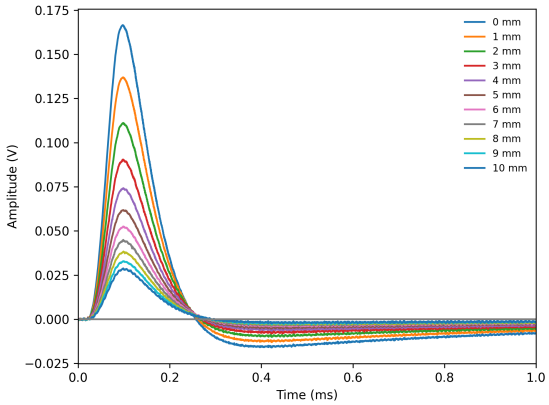

(c) Experimental

Figure B.5: PEC responses for copper plate.

B.4 Commercially Pure Titanium (Ti-2)

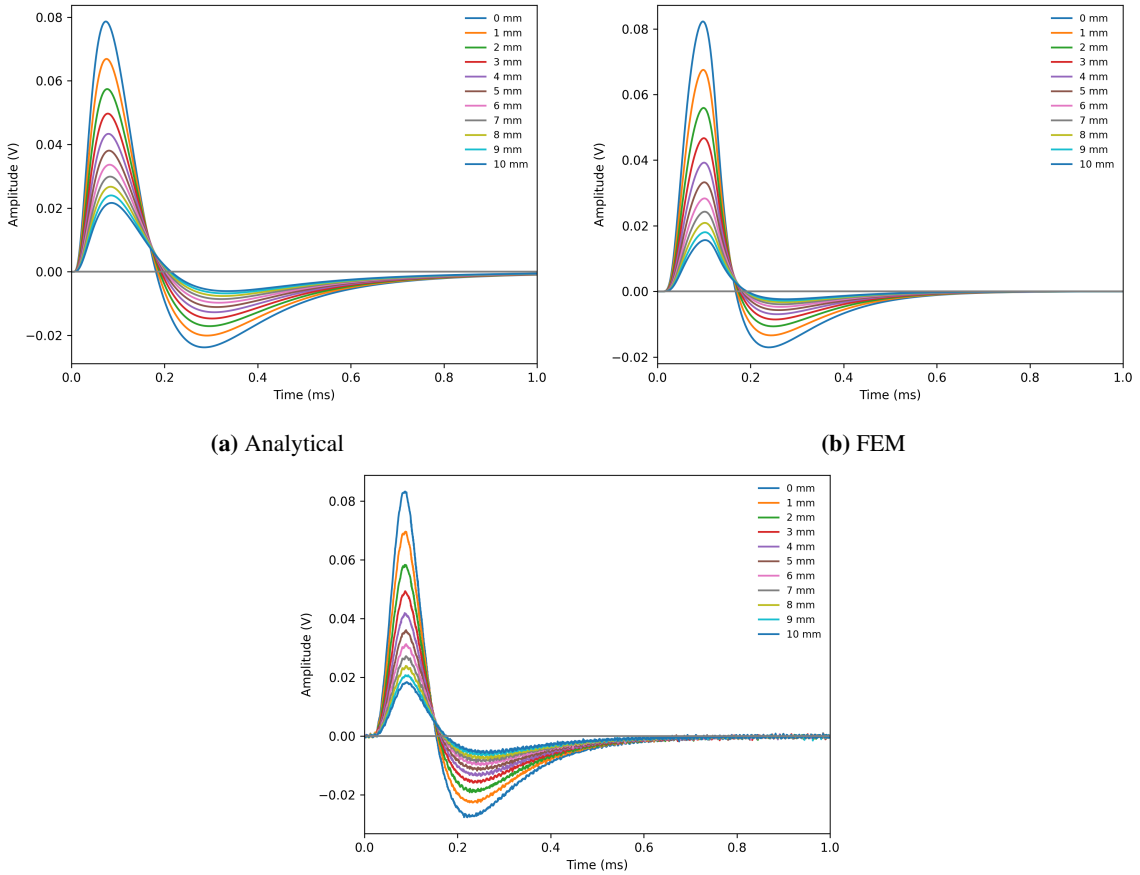

(a) Analytical

(b) FEM

(c) Experimental

Figure B.6: PEC responses for Ti-2 plate.

B.5 Ti-6Al-4V

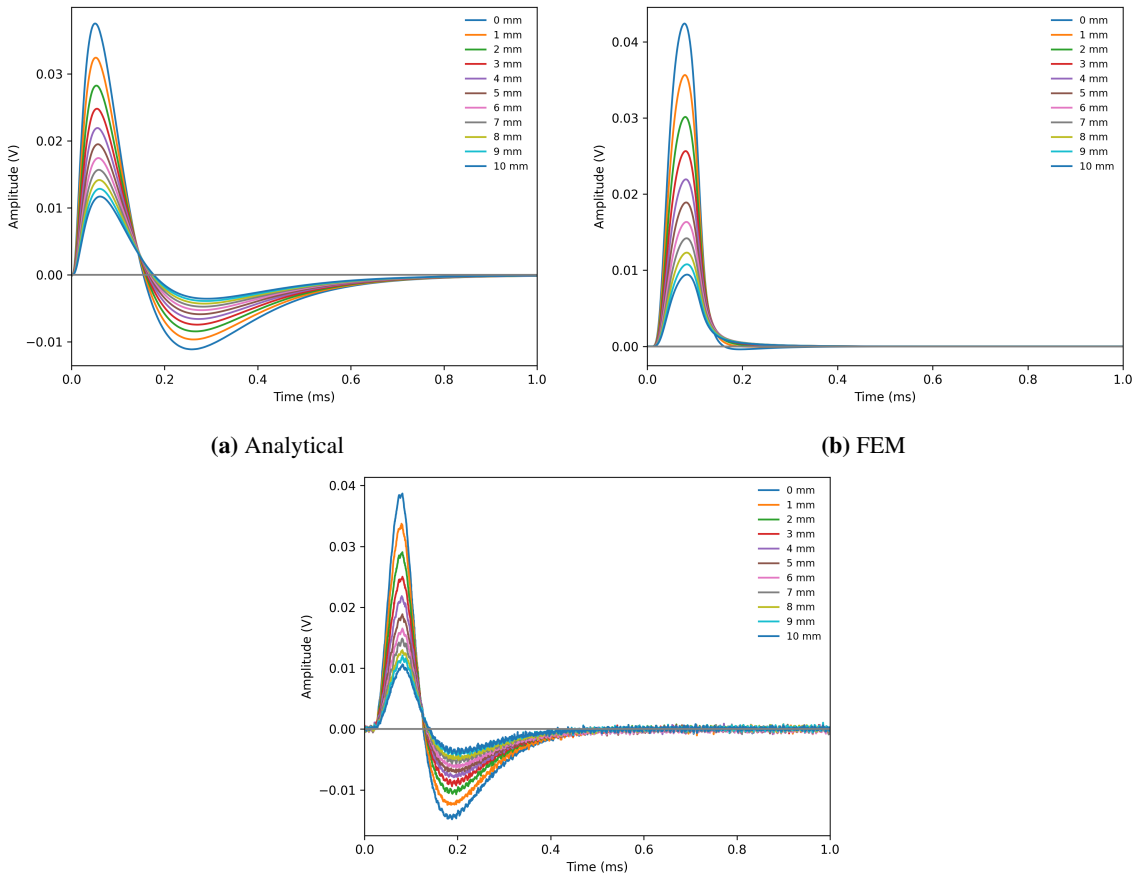

(a) Analytical

(b) FEM

(c) Experimental

Figure B.7: PEC responses for Ti-6Al-4V plate ($p = 3.8$ mm).

C Uncertainty Analysis and Propagation

Based on the analytical model developed in this work, a structured sensitivity analysis was conducted to quantify how uncertainties in physical and geometric parameters propagate through the reconstructed PEC signal. This study extends the methodology of Klein *et al.* [114] by incorporating additional geometric and material variables directly relevant to differential PEC probe configurations.

The analysis focused on six independent input parameters known to significantly affect the PEC response: electrical conductivity σ, lift-off distance h, coil separation s, driver coil radius b_1, pickup coil radius b_2, and plate thickness p. Each parameter was systematically varied at two coded levels—high $(+1)$ and low (-1)—relative to a nominal baseline condition coded as 0. Coded variable schemes are commonly used in sensitivity analysis and experimental design, as they facilitate the clear identification of main effects and interactions, while ensuring consistent numerical scaling across parameters [120].

Eight sensitivity analyses were designed, as summarized in Table C.1, to encompass a representative subset of the full 2^6 factorial design space. The selected eight-run fractional design captures the dominant main effects under the assumption of negligible higher-order interactions, while limiting computational cost, which is appropriate given the smooth and monotonic parameter dependence observed in the analytical model.

Table C.1: Coded experimental (Exp) design matrix used to investigate parameter sensitivity. Parameters indicating variation at high (+1) and low (-1) levels.

Input parameter	**Exp 1**	**Exp 2**	**Exp 3**	**Exp 4**	**Exp 5**	**Exp 6**	**Exp 7**	**Exp 8**
Electrical conductivity, σ (10^7 S/m)	+1	+1	+1	+1	-1	-1	-1	-1
Lift-off, h (mm)	+1	+1	-1	-1	+1	+1	-1	-1
Coil separation, s (mm)	+1	-1	+1	-1	+1	-1	+1	-1
Driver coil radius, b_1 (mm)	+1	+1	-1	-1	-1	-1	+1	+1
Pickup coil radius, b_2 (mm)	+1	-1	+1	-1	-1	+1	-1	+1
Plate thickness, p (mm)	+1	-1	-1	+1	+1	-1	-1	+1

Table C.2 provides the physical values corresponding to each coded level. This mapping enables the translation of coded sensitivities into practical engineering insights for probe fabrication and inspection configuration.

Table C.2: Decoded physical parameter levels corresponding to coded values $(-1, 0, +1)$.

Input parameter	-1 (low)	0 (nominal)	+1 (high)	Percent change
Electrical conductivity, σ (10^7 S/m)	1.67	1.75	1.83	$\pm 4.57\%$
Lift-off, h (mm)	1.22	1.27	1.32	$\pm 3.94\%$
Coil separation, s (mm)	60	65	70	$\pm 7.69\%$
Driver coil radius, b_1 (mm)	12.140	12.205	12.270	$\pm 0.53\%$
Pickup coil radius, b_2 (mm)	6.98	7.24	7.50	$\pm 3.59\%$
Plate thickness, p (mm)	2.77	2.87	2.97	$\pm 3.48\%$

The pronounced influence of conductivity σ and plate thickness p on time-based signal features reinforces the necessity of precise temporal alignment when comparing analytical, FEM, and experimental results. Since even small variations in these parameters can alter the arrival times and waveform shapes of the transient response, uncorrected timing discrepancies could obscure underlying model–data agreement. This is particularly relevant for early-time features such as the peak arrival and secondary peak timing, which are sensitive to electromagnetic diffusion rates governed by material properties. Peak-matching techniques ensured that comparisons were not confounded by trigger delays or phase offsets, enabling a more accurate and meaningful assessment of model fidelity. In this context, the sensitivity analysis provides quantitative justification for the alignment procedure, highlighting how small parameter deviations—especially in σ and p—can introduce observable phase shifts in the time-domain response.

To quantify the effect of parameter variability on PEC signal features, a first-order uncertainty propagation was performed using the standard Taylor series linearization approach. The total variance in a signal feature Y due to uncorrelated input uncertainties is given by [121]:

$$\sigma_Y^2 \approx \sum_{i=1}^{n} \left(\frac{\partial Y}{\partial x_i} \right)^2 \sigma_{x_i}^2, \tag{C.1}$$

where x_i denotes the i^{th} input parameter, $\frac{\partial Y}{\partial x_i}$ is the sensitivity of the output Y with respect to x_i, and σ_{x_i} is the standard uncertainty associated with x_i. This expression originates from a first-order Taylor series expansion of Y around nominal values x_i^0, assuming small, uncorrelated input variations.

Partial derivatives were numerically approximated using central finite differences applied to the coded experimental data. The uncertainty values σ_{x_i} were assigned based on each parameter's known manufacturing tolerances and measurement precision.

Five key time-domain PEC signal features were evaluated: peak amplitude, peak arrival time, secondary peak amplitude, secondary peak arrival time, and time-to-zero crossing. Figure C.1 presents the relative contribution of each input parameter in these signal features.

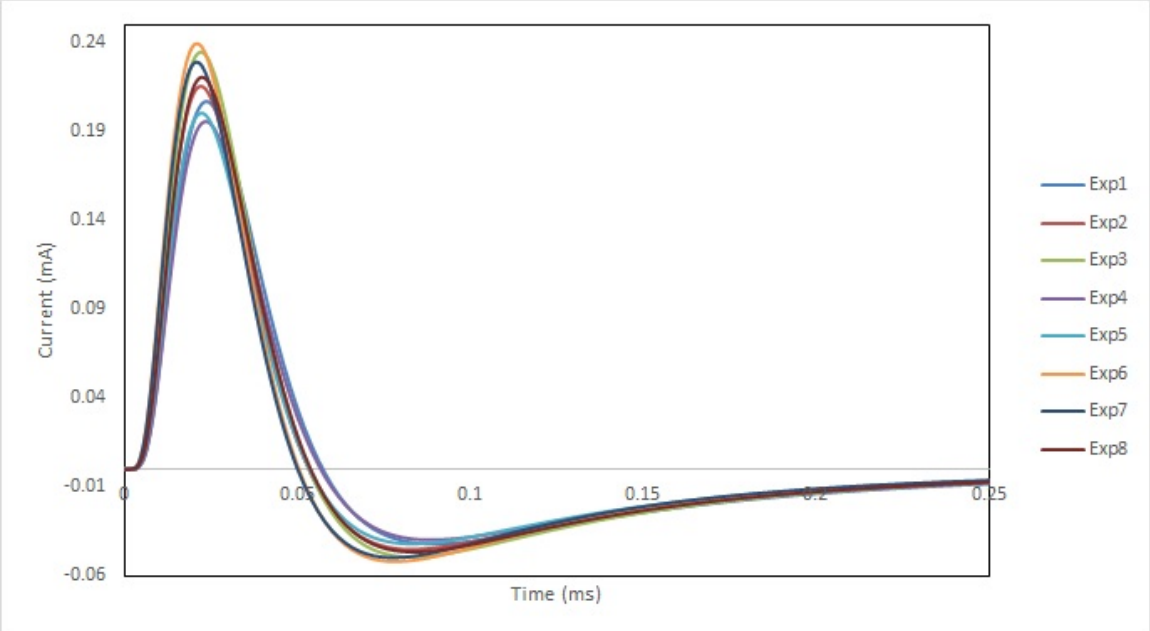

Figure C.1: Relative contribution of each input parameter to the total uncertainty in five time-domain PEC signal features, as computed using the analytical model.

In addition to relative contributions, absolute percentage changes in each signal feature due to parameter variations are summarized in Table C.3. The results indicate that electrical conductivity σ and plate thickness p exert the most significant influence, particularly on timing-related metrics. Pickup coil width b_2 and plate thickness p were dominant contributors to signal amplitude variation.

Table C.3: Percent change in extracted PEC features under coded parameter perturbations.

Input parameter	ΔA_p (%)	ΔA_s (%)	Δt_p (%)	Δt_s (%)	Δt_{zc} (%)
Electrical conductivity, σ (10^7 S/m)	-1.99	-2.19	2.22	0.02	3.26
Lift-off, h (mm)	1.00	-1.04	0	0	0.47
Coil separation, s (mm)	-0.01	-0.03	0	0	0.47
Driver coil radius, b_1 (mm)	0.09	0.09	0	0	0.47
Pickup coil radius, b_2 (mm)	3.52	3.51	0	0	0.47
Plate thickness, p (mm)	-5.39	-5.48	2.22	0.02	3.26

To apply Equation C.1 using the data in Table C.3, the partial derivative $\frac{\partial Y}{\partial x_i}$ for each parameter was estimated using a finite-difference approach. Since each parameter was perturbed across a full coded range from -1 to $+1$, the total change Δx_i equals two coded units. The sensitivity of a given output Y to a parameter x_i can thus be approximated as:

$$\frac{\partial Y}{\partial x_i} \approx \frac{\Delta Y}{\Delta x_i} = \frac{\Delta Y_{\text{coded}}}{2}. \tag{C.2}$$

For example, consider the influence of conductivity σ on peak amplitude. From Table C.3, the total change in peak amplitude over the full coded range is -1.99%, or -0.0199 in decimal form. The

derivative per coded unit is:

$$\left.\frac{\partial Y_{\text{peak}}}{\partial \sigma}\right|_{\text{coded}} \approx \frac{-0.0199}{2} = -0.0099.$$

This derivative must be scaled according to the physical variation associated with one coded unit to propagate uncertainty in physical units, since Equation C.1 requires derivatives expressed in dimensional form . For conductivity, one coded unit corresponds to $0.08 \times 10^7 = 8.0 \times 10^5$ S/m. The derivative in physical units is therefore:

$$\left.\frac{\partial Y}{\partial \sigma}\right|_{\text{physical}} = \frac{-0.0099}{8.0 \times 10^5} = -1.24 \times 10^{-8}\,\text{mA} \cdot \text{m/S}.$$

Assuming the standard uncertainty in conductivity is $\sigma_\sigma = 0.08 \times 10^7$ S/m, the contribution of conductivity to the total uncertainty in peak amplitude is:

$$\sigma_{Y,\sigma}^2 = \left(\frac{\partial Y}{\partial \sigma}\right)^2 \cdot \sigma_\sigma^2 = \left(-1.24 \times 10^{-8}\ \frac{\text{mA} \cdot \text{m}}{\text{S}}\right)^2 \cdot \left(0.08 \times 10^7\ \frac{\text{S}}{\text{m}}\right)^2.$$

This yields the squared contribution of conductivity uncertainty to the overall variance in the peak amplitude. Repeating this process for all parameters and summing the contributions yields the total propagated uncertainty σ_Y. The consolidated uncertainties for each signal feature, calculated using Equation C.1, are summarized in Table C.4.

Table C.4: Final uncertainty contributions (standard deviations) from each input parameter to each PEC signal feature.

Parameter	**Peak Amplitude**		**Peak Arrival Time**		**Time-to-Zero Crossing**
	Primary (mA)	Secondary (mA)	Primary (s)	Secondary (s)	(s)
σ (10^7 S/m)	9.86×10^{-5}	1.20×10^{-4}	1.23×10^{-4}	1.53×10^{-8}	2.65×10^{-4}
h (mm)	2.50×10^{-5}	2.69×10^{-5}	2.27×10^{-34}	1.15×10^{-34}	5.41×10^{-6}
s (mm)	6.28×10^{-10}	1.93×10^{-8}	0	0	5.41×10^{-6}
b_1 (mm)	2.09×10^{-7}	2.17×10^{-7}	2.27×10^{-34}	1.15×10^{-34}	5.41×10^{-6}
b_2 (mm)	3.10×10^{-4}	3.08×10^{-4}	0	0	5.41×10^{-6}
p (mm)	7.26×10^{-4}	7.52×10^{-4}	1.23×10^{-4}	1.53×10^{-8}	2.65×10^{-4}

To consolidate the uncertainty contributions from all parameters, a RSS approach was employed to compute the total propagated standard uncertainty for each PEC signal feature, as per [121]:

$$\sigma_Y = \sqrt{\sum_{i=1}^{n} \left(\frac{\partial Y}{\partial x_i} \cdot \sigma_{x_i}\right)^2}. \tag{C.3}$$

Table C.5 presents the final total uncertainties in absolute terms and percentages relative to the nominal signal values.

Table C.5: Total uncertainty in each PEC signal feature using root-sum-square propagation, expressed relative to nominal values.

Signal Feature	Total Uncertainty (RSS)	Nominal Value	Uncertainty (%)
Peak Amplitude (mA)	7.96×10^{-4}	2.17×10^{-1}	0.37%
Peak Arrival Time (s)	1.74×10^{-4}	2.20×10^{-1}	0.08%
Secondary Peak Amplitude (mA)	8.22×10^{-4}	4.57×10^{-2}	1.80%
Secondary Peak Arrival Time (s)	2.16×10^{-8}	8.40×10^{-1}	¡0.01%
Time-to-Zero Crossing (s)	3.75×10^{-4}	5.40×10^{-1}	0.07%

Notably, the secondary peak amplitude exhibited the highest relative uncertainty (1.80%), indicating that this feature is particularly sensitive to small variations in system parameters. In contrast, time-based features such as peak arrival and zero-crossing times demonstrated minimal uncertainty, reflecting their comparatively weaker dependence on geometric tolerances within the examined perturbation range.

These findings underscore the importance of precise control over material and geometric parameters when required for high-resolution PEC analysis. Furthermore, a coded experimental design proved effective for isolating dominant factors and informing parameter prioritization during model development and experimental calibration.

Overall, this uncertainty analysis supports the robustness of the PEC signal model and provides a valuable foundation for uncertainty-informed optimization and targeted parameter control in future PEC system design and implementation.

D Discriminant Analysis

This appendix provides the full per–fastener discriminant score tables and scatter plots used to generate the summarized results in Chapter 8. Tables report the mean discriminant score and standard deviation, $\bar{x} \pm \mathrm{SD}$, computed from repeated measurements at nominal lift-offs. Discriminant scores were obtained by projecting the time-domain responses into the specified PCA eigenspace (family-based or self-derived) and applying the same classification rule used in the main text.

Unless otherwise stated, boldface entries correspond to notched fasteners and are included to aid visual comparison with the decision-threshold discussion in the main chapter.

D.1 ODIN: Full Discriminant Score Tables

Table D.1–Table D.5 provide the complete ODIN discriminant score results used to support the family-level summaries and eigenvector-selection comparisons in the main chapter. Table D.1 consolidates results at the family level (HLT53, HLT265, HLT313), while Table D.2–Table D.4 resolve the same analysis by specific fastener configuration using both family-based and self-derived eigenspaces. Table D.5 reports lift-off-averaged values (1–3 mm) for HLT265 to emphasize configuration-to-configuration separability independent of small lift-off variation.

Table D.1: Representative discriminant scores ($\bar{x} \pm \mathrm{SD}$) using family-based eigenvectors for the ODIN probe over the HLT53, HLT265, and HLT313 test standards.

Fastener	HLT53	HLT265	HLT313
1	-0.02 ± 0.08	0.01 ± 0.06	0.19 ± 0.27
2	$\mathbf{0.98} \pm 0.06$	$\mathbf{0.99} \pm 0.06$	$\mathbf{1.04} \pm 0.11$
3	$\mathbf{1.07} \pm 0.07$	$\mathbf{1.08} \pm 0.05$	0.92 ± 0.14
4	$\mathbf{1.01} \pm 0.09$	$\mathbf{0.99} \pm 0.05$	$\mathbf{1.05} \pm 0.11$
5	0.03 ± 0.09	0.00 ± 0.03	0.00 ± 0.11
6	0.07 ± 0.09	0.04 ± 0.06	0.06 ± 0.08
7	0.04 ± 0.06	-0.01 ± 0.06	0.02 ± 0.10
8	0.93 ± 0.07	0.92 ± 0.05	0.83 ± 0.13
9	0.93 ± 0.09	0.97 ± 0.09	0.86 ± 0.15
10	-0.03 ± 0.06	0.01 ± 0.05	0.04 ± 0.12

Table D.2: Discriminant scores ($\bar{x} \pm$ SD) for the ODIN probe using family and self-derived eigenvectors on HLT313 titanium fasteners.

Fastener	HLT313 Family	HLT313DL8-9	HLT313TA10-13
1	0.19 ± 0.27	0.07 ± 0.08	0.30 ± 0.36
2	$\mathbf{1.04} \pm 0.11$	$\mathbf{1.04} \pm 0.05$	0.95 ± 0.07
3	0.92 ± 0.14	0.97 ± 0.08	0.92 ± 0.17
4	$\mathbf{1.05} \pm 0.11$	$\mathbf{1.06} \pm 0.10$	$\mathbf{1.00} \pm 0.09$
5	0.00 ± 0.11	-0.06 ± 0.05	0.11 ± 0.16
6	0.06 ± 0.08	0.01 ± 0.08	0.08 ± 0.09
7	0.02 ± 0.10	0.01 ± 0.08	0.01 ± 0.08
8	0.83 ± 0.13	0.87 ± 0.09	0.83 ± 0.14
9	0.86 ± 0.15	0.96 ± 0.07	0.84 ± 0.19
10	0.04 ± 0.12	0.07 ± 0.12	-0.05 ± 0.11

Table D.3: Discriminant scores ($\bar{x} \pm$ SD) for the ODIN probe using family and self-derived eigenvectors on HLT53 ferromagnetic fasteners.

Fastener	HLT53 Family	HLT53DL8-9	HLT53DL10-8	HLT53YC10-15
1	-0.02 ± 0.08	-0.04 ± 0.04	-0.03 ± 0.03	0.01 ± 0.07
2	0.98 ± 0.06	0.97 ± 0.06	0.97 ± 0.10	$\mathbf{1.00} \pm 0.07$
3	$\mathbf{1.07} \pm 0.07$	$\mathbf{1.09} \pm 0.02$	$\mathbf{1.09} \pm 0.07$	$\mathbf{1.04} \pm 0.10$
4	$\mathbf{1.01} \pm 0.09$	$\mathbf{1.04} \pm 0.05$	$\mathbf{1.03} \pm 0.06$	0.95 ± 0.11
5	0.03 ± 0.09	0.02 ± 0.06	0.02 ± 0.06	0.06 ± 0.12
6	0.07 ± 0.09	0.08 ± 0.08	0.17 ± 0.11	0.01 ± 0.06
7	0.04 ± 0.06	0.08 ± 0.06	-0.02 ± 0.04	0.03 ± 0.05
8	0.93 ± 0.07	0.95 ± 0.07	0.85 ± 0.11	0.95 ± 0.04
9	0.93 ± 0.09	0.86 ± 0.06	0.94 ± 0.03	0.98 ± 0.12
10	-0.03 ± 0.06	-0.06 ± 0.07	-0.03 ± 0.03	-0.04 ± 0.03

Table D.4: Discriminant scores ($\bar{x} \pm \mathrm{SD}$) for the ODIN probe using family and self-derived eigenvectors on HLT265 fasteners (ferromagnetic).

Fastener	HLT265 Family	HLT265TB8-6	HLT265TB10-12	HLT265TB10-18
1	0.01 ± 0.06	-0.04 ± 0.06	0.03 ± 0.04	0.05 ± 0.04
2	0.99 ± 0.06	0.97 ± 0.07	1.01 ± 0.02	0.98 ± 0.07
3	1.08 ± 0.05	1.07 ± 0.04	1.14 ± 0.03	1.04 ± 0.05
4	0.99 ± 0.05	1.03 ± 0.03	1.03 ± 0.04	0.96 ± 0.07
5	0.00 ± 0.03	0.02 ± 0.03	-0.01 ± 0.04	-0.02 ± 0.03
6	0.04 ± 0.06	0.08 ± 0.02	0.04 ± 0.05	0.00 ± 0.04
7	-0.01 ± 0.06	-0.05 ± 0.05	-0.02 ± 0.03	0.04 ± 0.05
8	0.92 ± 0.05	0.92 ± 0.05	0.87 ± 0.04	0.94 ± 0.04
9	0.97 ± 0.09	0.96 ± 0.02	0.89 ± 0.08	1.05 ± 0.05
10	0.01 ± 0.05	0.04 ± 0.02	0.03 ± 0.04	-0.03 ± 0.03

Table D.5: Mean discriminant scores ($\bar{x} \pm \mathrm{SD}$) for the ODIN probe over HLT265 fasteners averaged across lift-offs of 1–3 mm.

Fastener	HLT265TB8-6	HLT265TB10-12	HLT265TB10-18
1	-0.04 ± 0.03	0.03 ± 0.02	0.05 ± 0.01
2	0.97 ± 0.06	1.01 ± 0.01	0.98 ± 0.03
3	1.07 ± 0.03	1.13 ± 0.03	1.04 ± 0.03
4	1.03 ± 0.03	1.03 ± 0.02	0.95 ± 0.06
5	0.02 ± 0.02	-0.01 ± 0.02	-0.02 ± 0.01
6	0.07 ± 0.02	0.04 ± 0.04	-0.01 ± 0.01
7	-0.05 ± 0.05	-0.02 ± 0.02	0.03 ± 0.02
8	0.91 ± 0.03	0.87 ± 0.03	0.94 ± 0.01
9	0.96 ± 0.02	0.89 ± 0.01	1.05 ± 0.03
10	0.04 ± 0.01	0.03 ± 0.02	-0.04 ± 0.02

D.2 THOR: Full Discriminant Score Tables

Table D.6–Table D.10 provide the complete THOR discriminant score results supporting the summary in the chapter figures and tables. The same table structure as the ODIN appendix is used to enable direct comparison across probes: a family-level overview, followed by configuration-resolved results using family-based and self-derived eigenspaces, and finally, lift-off-averaged values for HLT265.

Table D.6: Representative discriminant scores ($\bar{x}\pm$SD) using family-based eigenvectors for THOR probe for HLT53, HLT265, and HLT313 test standards.

Fastener	HLT53	HLT265	HLT313
1	0.06 ± 0.09	-0.02 ± 0.08	0.00 ± 0.16
2	$\mathbf{1.09} \pm 0.09$	$\mathbf{1.08} \pm 0.07$	$\mathbf{1.11} \pm 0.09$
3	$\mathbf{1.00} \pm 0.09$	$\mathbf{1.05} \pm 0.05$	0.88 ± 0.12
4	$\mathbf{1.07} \pm 0.08$	$\mathbf{1.05} \pm 0.06$	$\mathbf{1.08} \pm 0.14$
5	0.04 ± 0.10	0.04 ± 0.07	0.07 ± 0.17
6	0.07 ± 0.10	0.00 ± 0.06	0.01 ± 0.11
7	0.04 ± 0.06	0.07 ± 0.08	0.16 ± 0.14
8	0.83 ± 0.13	0.82 ± 0.08	0.72 ± 0.14
9	0.83 ± 0.09	0.87 ± 0.07	0.76 ± 0.11
10	-0.04 ± 0.10	0.03 ± 0.07	0.23 ± 0.21

Table D.7: Discriminant scores ($\bar{x}\pm$SD) for THOR probe using family and self-derived eigenvectors for HLT313 titanium fasteners.

Fastener	HLT313 Family	HLT313DL8-9	HLT313TA10-13
1	0.00 ± 0.16	-0.08 ± 0.07	-0.01 ± 0.06
2	1.11 ± 0.09	1.08 ± 0.08	1.04 ± 0.06
3	0.88 ± 0.12	0.94 ± 0.07	1.08 ± 0.05
4	1.08 ± 0.14	1.15 ± 0.11	1.08 ± 0.04
5	0.07 ± 0.17	0.00 ± 0.07	0.02 ± 0.08
6	0.01 ± 0.11	0.06 ± 0.05	0.03 ± 0.06
7	0.16 ± 0.14	0.10 ± 0.07	0.07 ± 0.06
8	0.72 ± 0.14	0.79 ± 0.14	0.84 ± 0.03
9	0.76 ± 0.11	0.75 ± 0.11	0.86 ± 0.08
10	0.23 ± 0.21	0.27 ± 0.08	-0.01 ± 0.06

Table D.8: Discriminant scores ($\bar{x}\pm$SD) for THOR probe using family and self-derived eigenvectors for HLT53 ferromagnetic fasteners.

Fastener	HLT53 Family	HLT53DL8-9	HLT53DL10-8	HLT53YC10-15
1	0.06 ± 0.09	0.14 ± 0.08	0.03 ± 0.06	0.06 ± 0.10
2	1.09 ± 0.09	1.12 ± 0.08	1.00 ± 0.05	1.09 ± 0.09
3	1.00 ± 0.09	1.03 ± 0.06	1.06 ± 0.07	0.99 ± 0.07
4	1.07 ± 0.08	1.04 ± 0.05	1.14 ± 0.05	0.96 ± 0.09
5	0.04 ± 0.10	0.06 ± 0.08	0.03 ± 0.06	0.07 ± 0.14
6	0.07 ± 0.10	0.09 ± 0.12	-0.01 ± 0.06	0.04 ± 0.02
7	0.04 ± 0.06	-0.01 ± 0.05	0.05 ± 0.05	0.06 ± 0.04
8	0.83 ± 0.13	0.73 ± 0.10	0.89 ± 0.04	0.85 ± 0.20
9	0.83 ± 0.09	0.85 ± 0.05	0.80 ± 0.04	0.94 ± 0.16
10	-0.04 ± 0.10	-0.07 ± 0.14	0.01 ± 0.04	-0.07 ± 0.08

Table D.9: Discriminant scores ($\bar{x}\pm$SD) for THOR probe using family and self-derived eigenvectors for HLT265 ferromagnetic fasteners.

Fastener	HLT265 Family	HLT265TB8-6	HLT265TB10-12	HLT265TB10-18
1	0.01 ± 0.06	-0.10 ± 0.03	-0.01 ± 0.06	0.01 ± 0.13
2	0.99 ± 0.06	1.11 ± 0.05	1.04 ± 0.06	1.15 ± 0.05
3	1.08 ± 0.05	1.04 ± 0.04	1.08 ± 0.05	1.06 ± 0.02
4	0.99 ± 0.05	1.07 ± 0.03	1.08 ± 0.04	0.99 ± 0.07
5	0.00 ± 0.03	0.04 ± 0.03	0.02 ± 0.08	0.02 ± 0.06
6	0.04 ± 0.06	0.03 ± 0.04	0.03 ± 0.06	-0.01 ± 0.04
7	-0.01 ± 0.06	0.08 ± 0.03	0.07 ± 0.06	0.07 ± 0.06
8	0.92 ± 0.05	0.83 ± 0.05	0.84 ± 0.03	0.81 ± 0.07
9	0.97 ± 0.09	0.85 ± 0.07	0.86 ± 0.08	0.84 ± 0.05
10	0.01 ± 0.05	0.08 ± 0.02	-0.01 ± 0.06	0.06 ± 0.08

Table D.10: Average discriminant scores ($\bar{x}\pm$SD) for the THOR probe over HLT265 fasteners across lift-offs of 1–3 mm.

Fastener	HLT265TB8-6	HLT265TB10-12	HLT265TB10-18
1	-0.10 ± 0.01	-0.01 ± 0.02	0.01 ± 0.07
2	1.10 ± 0.03	1.04 ± 0.03	1.15 ± 0.02
3	1.04 ± 0.01	1.09 ± 0.03	1.06 ± 0.02
4	1.07 ± 0.02	1.08 ± 0.02	0.99 ± 0.01
5	0.04 ± 0.01	0.01 ± 0.06	0.03 ± 0.03
6	0.03 ± 0.02	0.03 ± 0.04	-0.01 ± 0.01
7	0.08 ± 0.00	0.07 ± 0.05	0.07 ± 0.06
8	0.83 ± 0.03	0.84 ± 0.02	0.81 ± 0.06
9	0.85 ± 0.02	0.86 ± 0.07	0.84 ± 0.04
10	0.08 ± 0.02	-0.01 ± 0.02	0.06 ± 0.02

D.3 ZEUS: Full Discriminant Score Tables

Table D.11–Table D.15 provide the complete ZEUS discriminant score results supporting the summarized in-chapter figures and tables. These results are included to document per–fastener behaviour within each family and to show how eigenvector selection (family vs. self) influences class separation across different fastener configurations and materials.

Table D.11: Representative discriminant scores ($\bar{x}\pm$SD) using family-based eigenvectors for the ZEUS probe over HLT53, HLT265, and HLT313 fastener standards.

Fastener	HLT53	HLT265	HLT313
1	0.04 ± 0.02	-0.02 ± 0.05	0.14 ± 0.10
2	1.06 ± 0.03	1.05 ± 0.06	1.14 ± 0.07
3	1.09 ± 0.07	1.10 ± 0.07	0.96 ± 0.07
4	0.97 ± 0.02	1.01 ± 0.04	1.13 ± 0.10
5	-0.02 ± 0.01	0.00 ± 0.02	0.03 ± 0.12
6	0.01 ± 0.01	0.02 ± 0.04	0.02 ± 0.10
7	0.00 ± 0.02	0.01 ± 0.03	0.03 ± 0.08
8	0.93 ± 0.07	0.86 ± 0.04	0.75 ± 0.10
9	0.90 ± 0.08	0.91 ± 0.07	0.75 ± 0.11
10	0.03 ± 0.03	0.05 ± 0.05	0.08 ± 0.09

Table D.12: Discriminant scores ($\bar{x}\pm$SD) for ZEUS probe using family and self-derived eigenvectors for HLT313 titanium fasteners.

Fastener	HLT313 Family	HLT313DL8-9	HLT313TA10-13
1	0.14 ± 0.10	0.05 ± 0.04	0.20 ± 0.06
2	1.14 ± 0.07	1.19 ± 0.02	1.08 ± 0.05
3	0.96 ± 0.07	0.96 ± 0.10	0.91 ± 0.05
4	1.13 ± 0.10	1.13 ± 0.08	1.17 ± 0.11
5	0.03 ± 0.12	0.02 ± 0.05	0.02 ± 0.17
6	0.02 ± 0.10	0.03 ± 0.06	0.00 ± 0.10
7	0.03 ± 0.08	0.09 ± 0.05	0.02 ± 0.07
8	0.75 ± 0.10	0.75 ± 0.05	0.75 ± 0.17
9	0.75 ± 0.11	0.72 ± 0.05	0.78 ± 0.11
10	0.08 ± 0.09	0.07 ± 0.06	0.12 ± 0.11

Table D.13: Discriminant scores ($\bar{x}\pm$SD) for ZEUS probe using family and self-derived eigenvectors for HLT53 ferromagnetic fasteners.

Fastener	HLT53 Family	HLT53DL8-9	HLT53YC10-15
1	0.04 ± 0.02	0.06 ± 0.05	0.01 ± 0.01
2	1.06 ± 0.03	1.05 ± 0.03	1.02 ± 0.01
3	1.09 ± 0.07	1.12 ± 0.05	1.03 ± 0.01
4	0.97 ± 0.02	0.99 ± 0.04	0.95 ± 0.01
5	-0.02 ± 0.01	-0.03 ± 0.02	-0.01 ± 0.01
6	0.01 ± 0.01	-0.02 ± 0.04	0.01 ± 0.01
7	0.00 ± 0.02	0.01 ± 0.04	0.00 ± 0.01
8	0.93 ± 0.07	0.91 ± 0.05	1.00 ± 0.01
9	0.90 ± 0.08	0.84 ± 0.03	0.99 ± 0.02
10	0.03 ± 0.03	0.06 ± 0.05	0.00 ± 0.02

Table D.14: Discriminant scores ($\bar{x}\pm$SD) for ZEUS probe using family and self-derived eigenvectors for HLT265 stainless steel fasteners.

Fastener	HLT265 Family	HLT265TB8-6	HLT265TB10-12	HLT265TB10-18
1	-0.02 ± 0.05	-0.06 ± 0.03	0.04 ± 0.05	-0.03 ± 0.01
2	1.05 ± 0.06	1.14 ± 0.03	1.02 ± 0.03	1.02 ± 0.01
3	1.10 ± 0.07	1.00 ± 0.05	1.14 ± 0.03	1.11 ± 0.02
4	1.01 ± 0.04	1.05 ± 0.04	1.08 ± 0.03	0.94 ± 0.01
5	0.00 ± 0.02	0.04 ± 0.04	-0.03 ± 0.03	0.01 ± 0.02
6	0.02 ± 0.04	0.01 ± 0.03	0.02 ± 0.05	0.03 ± 0.01
7	0.01 ± 0.03	0.04 ± 0.04	0.05 ± 0.01	0.01 ± 0.03
8	0.86 ± 0.04	0.85 ± 0.05	0.82 ± 0.03	0.91 ± 0.03
9	0.91 ± 0.07	0.87 ± 0.05	0.84 ± 0.04	1.00 ± 0.02
10	0.05 ± 0.05	0.06 ± 0.05	0.04 ± 0.05	0.00 ± 0.02

Table D.15: Average discriminant scores ($\bar{x}\pm$SD) for the ZEUS probe over HLT265 fasteners across lift-offs of 1–3 mm.

Fastener	HLT265TB8-6	HLT265TB10-12	HLT265TB10-18
1	-0.06 ± 0.03	0.04 ± 0.02	-0.03 ± 0.01
2	1.14 ± 0.02	1.02 ± 0.02	1.01 ± 0.01
3	1.00 ± 0.04	1.14 ± 0.03	1.12 ± 0.01
4	1.05 ± 0.03	1.08 ± 0.02	0.94 ± 0.01
5	0.04 ± 0.00	-0.03 ± 0.03	0.01 ± 0.01
6	0.01 ± 0.02	0.02 ± 0.04	0.03 ± 0.01
7	0.04 ± 0.04	0.05 ± 0.01	0.01 ± 0.01
8	0.85 ± 0.05	0.82 ± 0.02	0.91 ± 0.02
9	0.87 ± 0.04	0.84 ± 0.03	1.00 ± 0.01
10	0.07 ± 0.03	0.04 ± 0.02	0.00 ± 0.01

D.4 Full Discriminant Scatter Plots

Figure D.1–Figure D.3 show the full per-measurement discriminant score distributions used to compute the summary statistics reported in the appendix tables. Each panel corresponds to a single probe and fastener family, and includes the same decision thresholds used for classification in the main chapter. These plots are provided to illustrate within-class scatter, lift-off-driven variance, and the presence of any outliers that are not apparent in the mean $\pm$ SD summaries alone.

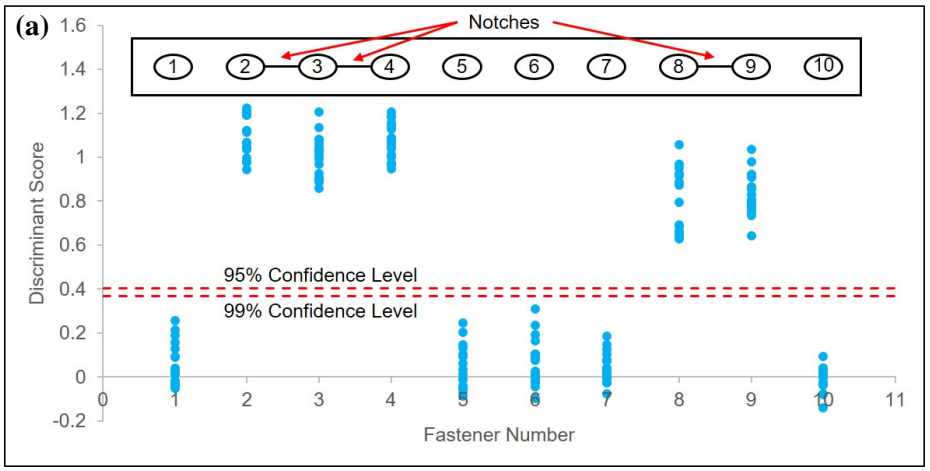

(a) THOR probe — HLT53 fasteners.

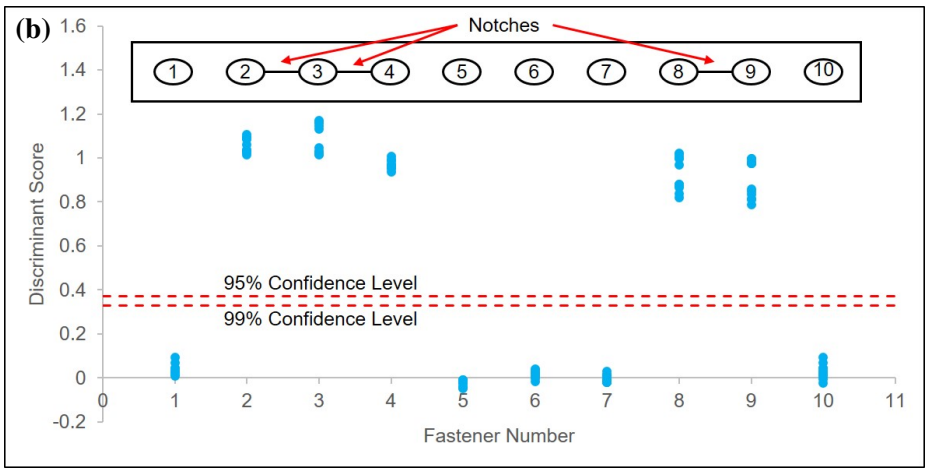

(b) ZEUS probe — HLT53 fasteners.

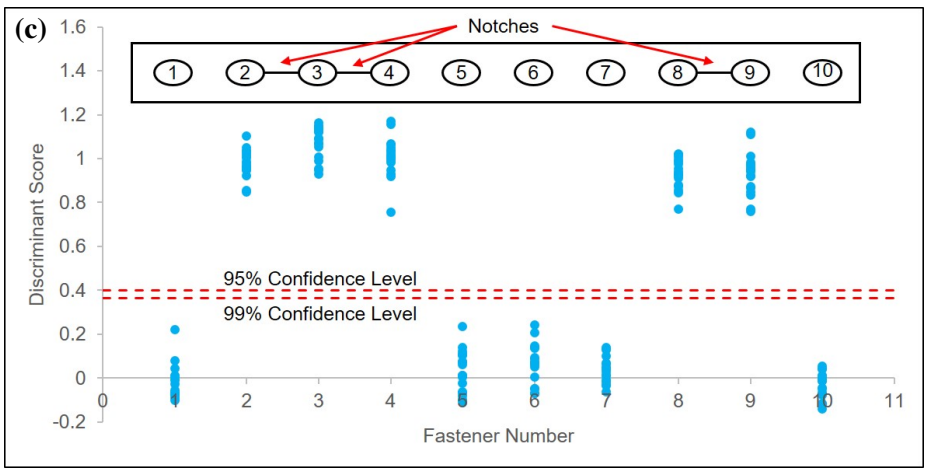

(c) ODIN probe — HLT53 fasteners.

Figure D.1: Per-measurement discriminant scores for the HLT53 family across 1–3 mm lift-offs. Panels (a)–(c) show THOR, ZEUS, and ODIN, respectively. Dashed lines indicate the 95% and 99% decision thresholds used for classification.

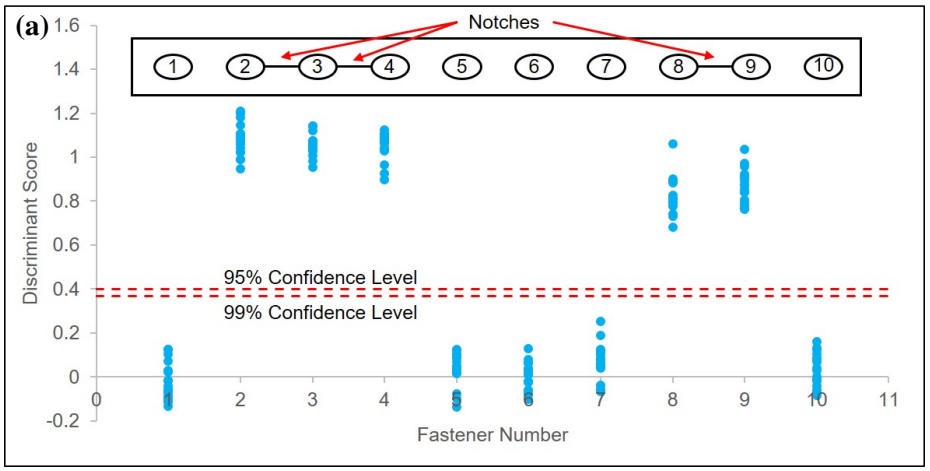

(a) THOR probe — HLT265 fasteners.

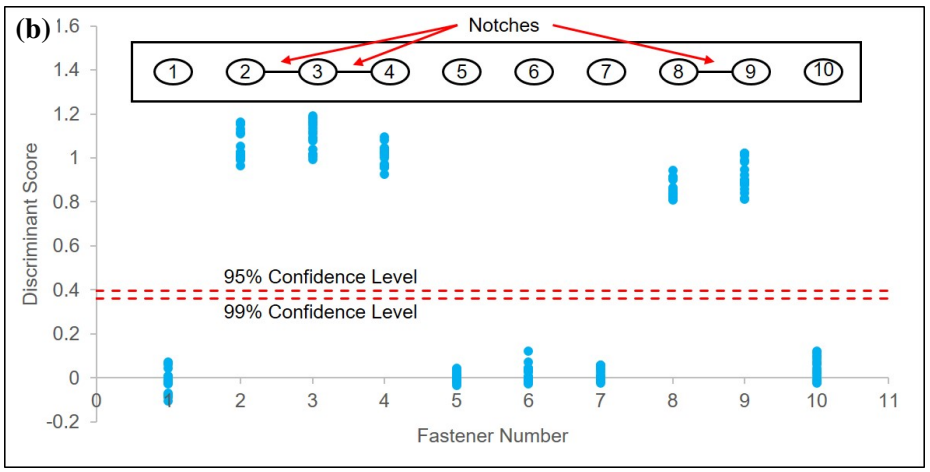

(b) ZEUS probe — HLT265 fasteners.

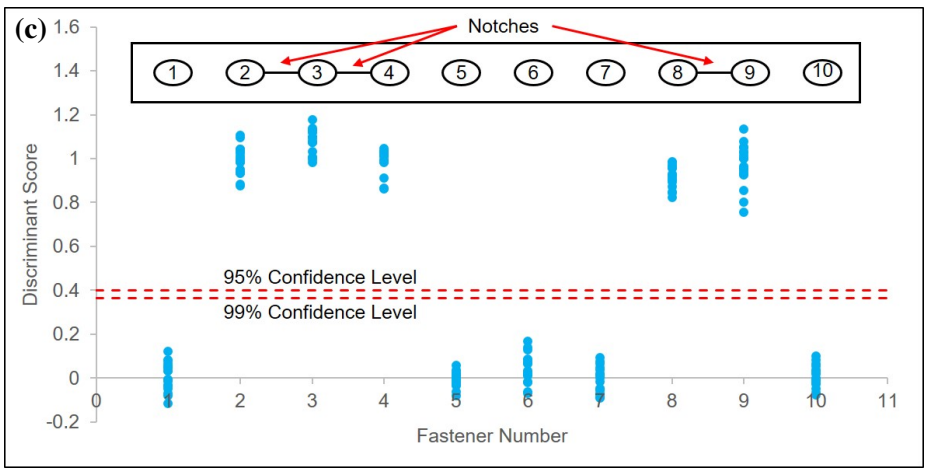

(c) ODIN probe — HLT265 fasteners.

Figure D.2: Per-measurement discriminant scores for the HLT265 family across 1–3 mm lift-offs. Panels (a)–(c) show THOR, ZEUS, and ODIN, respectively. Dashed lines indicate the 95% and 99% decision thresholds used for classification.

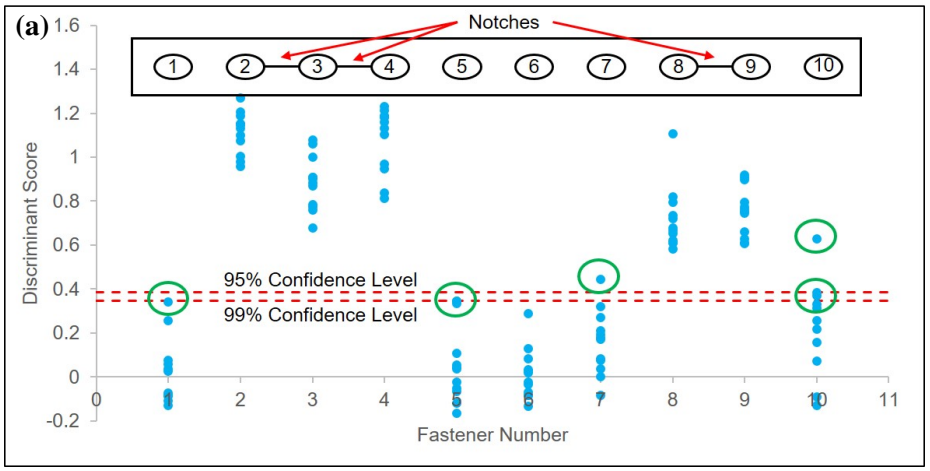

(a) THOR probe — HLT313 titanium fasteners.

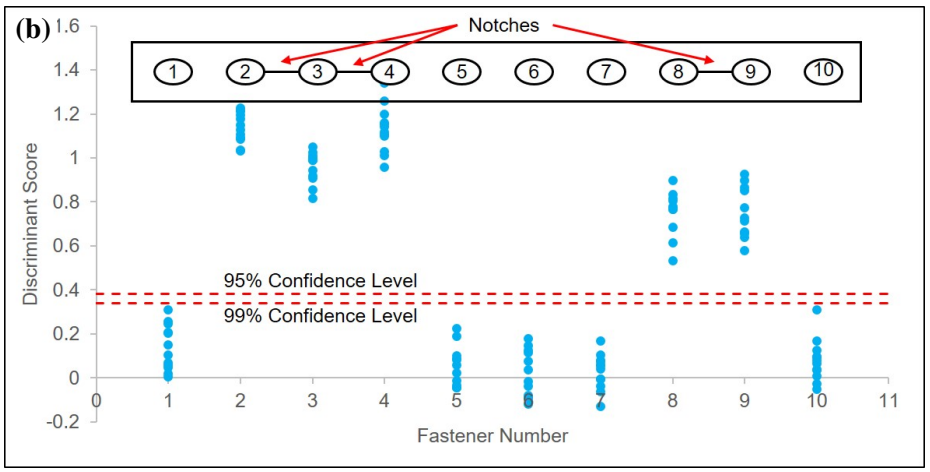

(b) ZEUS probe — HLT313 titanium fasteners.

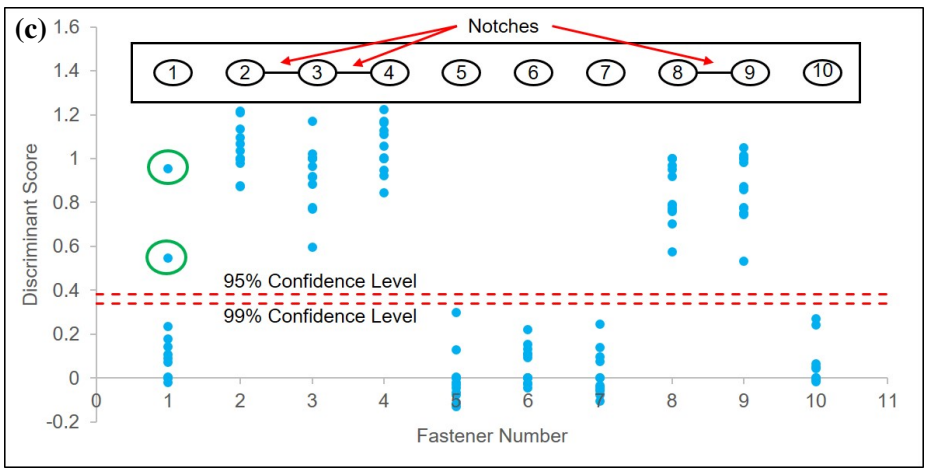

(c) ODIN probe — HLT313 titanium fasteners.

Figure D.3: Per-measurement discriminant scores for the HLT313 (titanium) family across 1–3 mm lift-offs. Panels (a)–(c) show THOR, ZEUS, and ODIN, respectively. Dashed lines indicate the 95% and 99% decision thresholds used for classification.

E Numerical Implementation and Convergence Verification

This appendix summarizes the numerical procedures used to implement the analytical PEC model and to reconstruct the time-domain responses from the derived frequency-domain expressions. The purpose of this appendix is to document the discretization strategy, convergence verification, and numerical safeguards employed to ensure stability and reproducibility of the results presented in Chapter 5–Chapter 6.

E.1 Fourier Harmonic Reconstruction

The time-domain coil currents were reconstructed from their complex frequency-domain representations using a truncated Fourier series corresponding to square-wave excitation. For a fundamental excitation frequency f_0, only odd harmonics were retained, consistent with the Fourier representation of a 50% duty-cycle square wave.

The reconstructed time-domain response was computed as

$$i(t) = \sum_{n=1,3,5,\ldots}^{N_h} \Re\left\{ I(\mathrm{j}\omega_n) e^{\mathrm{j}\omega_n t} \right\}, \tag{E.1}$$

where $\omega_n = 2\pi n f_0$ and N_h denote the maximum harmonic index.

Convergence with respect to harmonic truncation was verified by progressively increasing N_h until the change in peak amplitude and peak arrival time was less than 0.1% between successive truncation levels. In practice, convergence was achieved for $N_h \geq 150$ harmonics across all materials and lift-off conditions considered. Doubling the harmonic count beyond this value produced no observable change in waveform shape or extracted signal features.

E.2 Numerical Evaluation of Inductance Integrals

The analytical expressions for self- and mutual inductances involve improper integrals over radial wavenumber k_r and, where applicable, axial wavenumber k_z. These integrals were evaluated numerically using adaptive quadrature methods.

All integrations were performed using double-precision arithmetic with the following tolerances:

- Absolute tolerance: 10^{-9}
- Relative tolerance: 10^{-6}

Upper integration limits were selected such that further extension of the domain altered the computed inductance values by less than 0.05%. Convergence was verified by doubling the integration bounds and tightening tolerances to confirm the invariance of the results.

To avoid numerical instability at high wave numbers, exponential terms were evaluated using scaled representations where necessary. Complex square roots appearing in diffusion terms were computed using branch-consistent definitions to preserve physical causality and ensure continuity across the complex plane. The principal branch was selected such that the real part of the propagation constant remained non-negative, ensuring physically decaying fields within the conducting region.

E.3 Treatment of the Non-Conductive Limit

For validation purposes, the analytical model was evaluated in the limiting case $\sigma \to 0$ to represent a non-conductive medium. Assigning conductivity exactly equal to zero would eliminate the diffusion term and introduce singular behaviour in the complex propagation constant. Instead, a small finite conductivity of $10\,\mathrm{S/m}$ was used to approximate the non-conductive limit, while preserving numerical stability and continuity of the solution.

The resulting response converged to the expected air-core behaviour and matched the analytical free-space inductance expressions, confirming the correct implementation of the boundary conditions.

E.4 Finite-Difference Sensitivity Calculations

Partial derivatives required for uncertainty propagation (Appendix C) were computed using central finite differences. For a parameter x_i, the derivative was approximated as

$$\frac{\partial Y}{\partial x_i} \approx \frac{Y(x_i + \Delta x_i) - Y(x_i - \Delta x_i)}{2\Delta x_i}, \tag{E.2}$$

where Δx_i corresponds to one coded unit.

Step sizes were selected to balance truncation and round-off errors. Verification tests using halved perturbation magnitudes confirmed the stability of the derivative estimates within 1%.

E.5 Time Discretization and Feature Extraction

Time-domain signals were sampled at a resolution sufficient to capture early-time diffusion behaviour and peak structure. The sampling interval was selected such that further refinement did not alter extracted peak amplitudes or arrival times by more than 0.05%.

Peak detection and time-alignment procedures were applied consistently across analytical, FEM, and experimental datasets. Peak-matching ensured that comparisons were not influenced by trigger

delays or phase offsets. Sensitivity analysis results (Appendix C) quantitatively justified the necessity of this alignment, particularly for parameters affecting electromagnetic diffusion rates, such as conductivity σ and plate thickness p.

E.6 Verification Against FEM and Experimental Data

To ensure that the observed agreement between analytical, FEM, and experimental results was not influenced by numerical discretization artefacts, the following verification checks were performed:

- Harmonic truncation was doubled to confirm waveform invariance.
- Integration tolerances were tightened by one order of magnitude.
- Time resolution was increased to confirm the stability of extracted features.

In all cases, changes in extracted signal features remained below 0.1%, indicating that numerical error was negligible relative to physical parameter uncertainty.

E.7 Reproducibility

The analytical implementation was developed in Python using double-precision floating-point arithmetic. All scripts used to generate the results presented in this thesis are archived and available upon request. The numerical parameters, tolerances, and convergence criteria documented above are sufficient to reproduce the reported results independently.